UNIVERSITÄT
DUISBURG
ESSEN

Growth, Morphology, and Conductivity in Semimetallic/Metallic Films on Si(001)

Dissertation

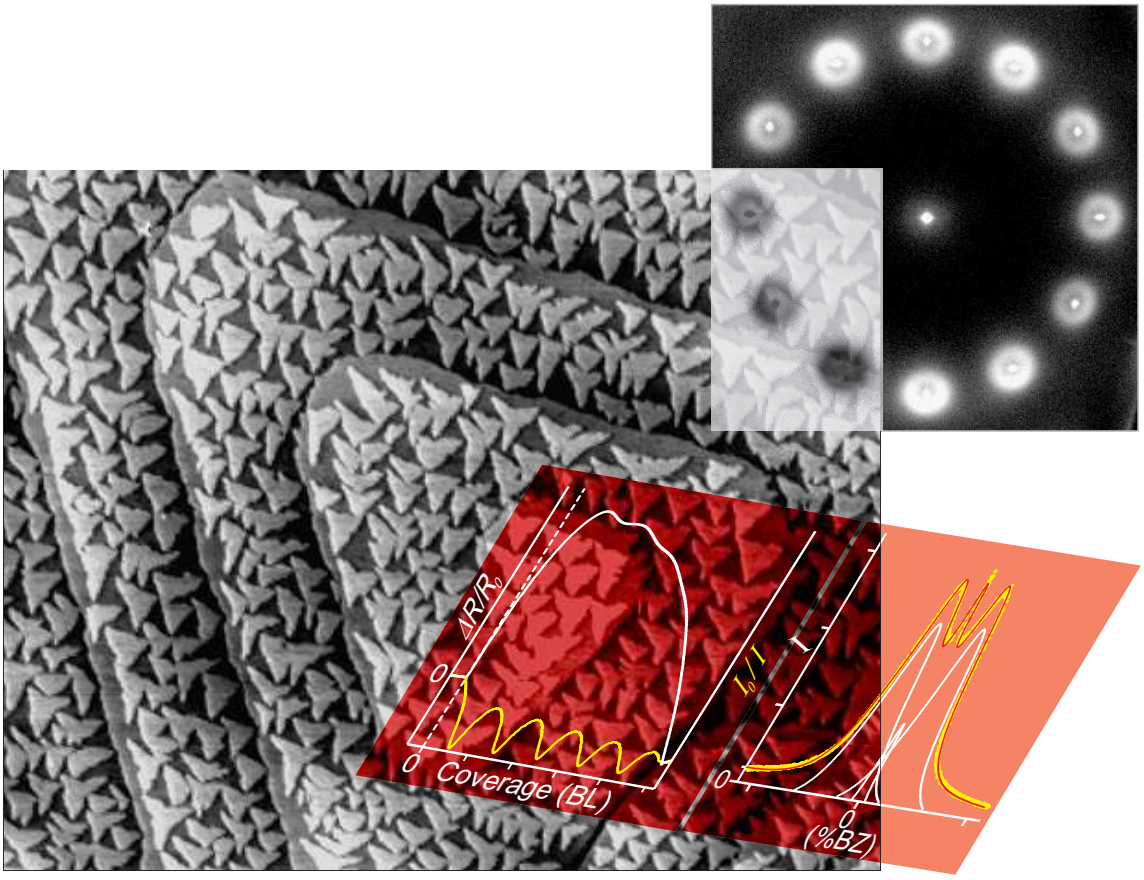

Giriraj Jnawali

Growth, Morphology, and Conductivity in Semimetallic/Metallic Films on Si(001)

Vom Fachbereich Physik
der Universität Duisburg-Essen
zur Erlangung des akademischen Grades
Doktor der Naturwissenschaften
Dr. rer. nat.

genehmigte

Dissertation

von

Dipl.-Phys. Giriraj Jnawali

geboren in *Nepal*

Duisburg, 2009

Referent:	:	Prof. Dr. M. Horn-von Hoegen
Korreferent	:	Prof. Dr. G. Dumpich
Korreferent		Prof. Dr. J. Wollschläger
Prüfungsvorsitzender	:	Prof. Dr. L. Schäfer
Tag der Disputation	:	9. Juni 2009

Schlagworte:

Si, Bi, Ag, WSi_2, Heteroepitaxie, Versetzungsnetzwerke, Homoepitaxie, Nukleation, SPA-LEED, STM, Oberfläche Leitfähigkeit

Keywords:

Si, Bi, Ag, WSi_2, Heteroepitaxy, Dislocation Network, Homoepitaxy, Nucleation, SPA-LEED, STM, Surface Conductivity

Abstract

This dissertation deals with the study of epitaxial growth of semimetallic (Bi) and metallic (Ag) films on Si(001) as well as *in situ* electrical transport study of those films via surface manipulation. The focus of the transport measurements is to study the influence of the surface morphology or structure on the resistance of the film. The most important challenge is the preparation of high quality films with well-defined morphology under ultra high vacuum conditions.

In spite of the large lattice mismatch and different lattice geometry, it is possible to grow epitaxial Bi(111) films on Si(001) substrates, which are surprisingly smooth, relaxed and almost free of defects. Due to the two-fold symmetry of the substrates, the Bi(111) film is composed of crystallites rotated by 90° with respect to each other. Annealing of 6 nm film from 150 K to 450 K enables the formation of a periodic interfacial misfit dislocations, which accommodates a remaining lattice mismatch of 2.3 %. The surface/interface roughness and the bulk defect density of the film found to be extremely low, indicating the high crystalline quality of the film with atomically smooth surface and abrupt interface. Similar to the Bi films, Ag grows in a (111) orientation on Si(001) with two 90° rotated domains. The remaining strain of 2.2 % (tensile) is accommodated by the formation of an ordered network of dislocations. The Ag film exhibits atomically smooth surface.

Those Bi films and Ag films were used as model systems to study the influence of the surface morphology on the electrical resistance. Surprisingly, all the Bi films (3 - 170 nm thicknesses) have shown an anomalous behavior of conductance with temperature and thickness. As in the case of doped semiconductor, the conductance increases exponentially from 150 K to 300 K and saturates at 350 K before finally decreasing with temperature. This behavior hints to the long predicted semimetal-to-semiconductor transition in the Bi films. However, the thickness dependent conductance behavior agrees with a previously observed metallic surface state, because the conductance does not change with thickness at 80 K. *In situ* measurements of the resistance during additional Bi deposition on the smooth Bi(111) films exhibit a square root dependent with coverage after a linear increase at very low coverage (1 % of a BL). Due to the extreme electronic properties of Bi, such as a large Fermi wavelength and a large electron mean free path, this behavior is not supported by the classical electron scattering model of Fuchs-Sondheimer. Since the Bi(111) surface state possesses two orders of magnitude higher number of carriers than in the bulk, the surface acts as a dominant channel of electron transport. During additional deposition of Bi, carriers are scattered at the adatoms and small islands, resulting in dramatic increase of surface resistance. Experimental results of nucleation and growth behavior at initial stages in Bi(111) homoepitaxy and the concept of 2D metallic surface states allow to explain the square root dependent of the resistance with coverage. Additionally, from the initial rise of resistance, a 2D surface state conductivity was determined, assuming that the surface states are completely destroyed after additional 0.5 BL Bi deposition. Applying the Boltzmann equation, the scattering mean free path at the 2D surface states was roughly estimated to be 15 nm.

The situation becomes much simpler in the case of the resistance behavior during deposition of Ag on a smooth Ag(111) film. The Fuchs-Sondheimer model works quite well and qualitatively demonstrate the increase of film resistance due to the diffuse scattering caused by surface roughness. Furthermore, in a complex situation such as surface alloying via Au deposition on Ag films, the resistance increases dramatically even at room temperature, suggesting that the scattering efficiency in this case is even higher than the case of normal surface roughness.

Zusammenfassung

In dieser Dissertation wird das epitaktische Wachstum dünner halbmetallischer Wismut- bzw. metallischer Silberfilme auf Si(001) sowie der elektrische Transport durch diese Filme untersucht. Im Fokus der Transportmessungen steht die Untersuchung des Einflusses von Oberflächenmorphologie bzw. -struktur auf die Leitfähigkeit. Hierfür sind Filme mit hoher Kristallqualität unter Ultrahochvakuum-Bedingungen eine entscheidende Voraussetzung.

Trotz des großen Unterschieds der beiden Gitterkonstanten und der verschiedenen Gittergeometrie ist es möglich, Bi(111) Filme auf Si(001) Substrate aufzuwachsen, die überraschend glatt, entspannt und praktisch frei von Defekten sind. Bedingt durch die 2-zählige Symmetrie des Substrates besteht der Bi(111) Film aus Mikrometer großen (111) Kristalliten, die jeweils um 90° gegeneinander verdreht sind. Eine verbleibende Gitterfehlanpassung von 2.3% wird durch die Ausbildung eines periodischen Netzwerks von Versetzungen an der Grenzfläche angepasst. Die Oberflächen- bzw. Grenzflächenrauhigkeit und die Volumendefektdichte des Films sind extrem gering, was die hohe Kristallgüte des Films mit einer atomar glatten Oberfläche und einer abrupten Grenzfläche widerspiegelt. Ähnlich wie für Wismut wachsen auch Silber-Filme mit einer (111) Orientierung und um jeweils 90° gedrehten Domänen auf Si(001). Auch hier passt ein Netzwerk von Versetzungen eine verbleibende Gitterfehlanpassung von 2.2% an. Auch hier ist der Silberfilm atomar glatt.

Diese Silber- und Wismut-Filme wurden dann als Modellsystem für die Untersuchung des Einflusses der Oberflächenmorphologie auf den elektrischen Widerstand verwendet. Überraschenderweise zeigten alle Wismutfilme (3 - 170 nm Dicke) ein anomales Verhalten als Funktion der Schichtdicke und Temperatur. Wie im Fall eines dotierten Halbleiters stieg die Leitfähigkeit zwischen 150 und 300 K exponentiell an, zeigte ein Plateau bei 350 K bevor sie mit steigender Temperatur abfiel. Dieses Verhalten ließe sich mit dem lang vorhergesagten Halbleiter/Halbmetallübergang für dünne Bi-Filme erklären. Die zusätzlich beobachtete schichtdickenunabhängige Leitfähigkeit bei 80 K ist mit einem in der Literatur beschriebenen metallischen Oberflächenzustand zu erklären. Bei weiterem Bedampfen mit Wismut werden die Ladungsträger an den dabei entstehenden Wismutinseln gestreut und eine Erhöhung des Widerstands beobachtet, die nach einem linearen Anstieg eine wurzelförmige Abhängigkeit von der zusätzlichen Bedeckung aufweist. Auf Grund der besonderen elektronischen Eigenschaften von Wismut - wie eine große Fermiwellenlänge und eine große freie Weglänge der Elektronen - kann dieses Verhalten nicht durch ein klassisches Streumodell nach Fuchs-Sondheimer erklärt werden. Da jedoch der metallische Oberflächenzustand von Bi(111) bis zu zwei Größenordnungen mehr Ladungsträger aufweist wie das Filmvolumen stellt dieser den dominanten elektronischen Transportkanal dar. Bei weiterem Aufdampfen von Wismut bei 80 K werden die Elektronen an den isolierten Adatomen bzw. 2dim. Inseln gestreut, was einen deutlichen Anstieg des Widerstands bewirkt. Mit einer STM Analyse der Inseldichte und -größe in diesem Wachstumsbereich konnte der beobachtete wurzelförmige Anstieg des Oberflächenwiderstands erklärt werden. Unter der Annahme, dass der Oberflächenzustand nach Aufdampfen einer halben Atomlage Wismut vollständig zerstört ist, konnte die Leitfähigkeit im Oberflächenzustand auch quantitativ bestimmt werden. Die mittlere freie Streulänge für Transport im Oberflächenzustand konnte zu 15 nm bestimmt werden.

Die Erklärung des Widerstandsanstiegs bei der Abscheidung weiteren Silbers auf ultradünne Silberfilme bei tiefen Temperaturen ist wesentlich einfacher. Die Beschreibung über Fuchs-Sondheimer erklärt den durch das Aufrauhen der Oberfläche bewirkten Widerstandsanstieg qualitativ sehr gut. Im Falle der Abscheidung von Gold auf die Silberfilme bewirkt die Oberflächenlegierung einen auch bei Zimmertemperatur deutlichen Anstieg des Widerstands. Offensichtlich ist die Streueffizienz in diesem Fall deutlich höher als für rauhe Oberflächen ist.

Abbreviations

4PP	4-Point Probe
AFM	Atomic Force Microscopy
Ag	Silver
Au	Gold
Bi	Bismuth
BL	Bilayer
BZ	Brillouin Zone
CTR	Crystal Truncation Rod
DAS	Dimer-Adatom-Stacking faults
fcc	Face Centered Cubic
FM	Frank-van der Merwe
FWHM	Full Width at Half Maximum
GIXRD	Grazing Incidence X-Ray Diffraction
LDLRSEM	Long Distance Low-Resolution Scanning Electron Microscope
LEED	Low-Energy Electron Diffraction
LEEM	Low-Energy Electron Microscopy
LPCVD	Low-Pressure Chemical Vapor Deposition
MBE	Molecular Beam Epitaxy
MOSFET	Metal-Oxide-Semiconductor Field-Effect Transistor
PEEM	Photo-Emission Electron Microscopy
PSD	Position Sensitive Detector
RHEED	Reflection High-energy Electron Diffraction
RT	Room Temperature ($\approx$300 K)
SEM	Scanning Electron Microscopy
Si	Silicon
SPA-LEED	Spot Profile Analyzing Low-Energy Electron Diffraction

Contents

1 Introduction

Solid state materials display a wide range of physical phenomena, which are driven by their electronic, structural and size dependent properties. Depending on their electrical conductivity, materials are classified into metals, semiconductors and insulators. However, this simple classification ignores some intriguing phenomena of semimetals. In some cases the properties may not even be isotropic. The crystallographic orientation, the experimental conditions (such as sample temperature) and the surface and interface structure of the material change the electrical behavior. In extreme cases, we encounter materials conducting charge carriers in two dimensional (2D) planes or even one dimensional (1D) lines.

In the case of thin films, the conductivity is limited by the scattering at film boundaries, i.e., at the surface and interface and conductivity is reduced as compared to the bulk. If the film thickness is comparable or even smaller than the electron de Broglie wavelength λ_{el}, the conductivity oscillates with increasing thickness, where the period of the oscillation is equal to $\lambda_{el}/2$. This phenomena occurs due to the electron confinement effect, resulting in an energy band quantization perpendicular to the surface, which is known as the quantum size effect (QSE). In another case, if the metallic layers grow in a layer-by-layer fashion, the conductivity also oscillates, but the maxima of the oscillation are repeated at each integer order thickness of the layer. This phenomena originates due to the periodic variation of the step density at the surface, which also changes the probability of scattering events at terrace steps. Similarly, if the coverage is extremely low so that only single isolated adatoms are on the surface, the scattering of the charge carrier is enhanced so remarkably that the resistivity increases linearly with coverage. However, the resistivity deviates from the linear form to the quadratic form as the coverage increases and the surface topography changes from adatoms to 2D islands. The situation becomes even more complicated and challenging if the surface or interface is modified either via intrinsic defects or by surface manipulation and reconstruction. In heteroepitaxy, dislocation-like defects are often generated at the interface to match the lattice parameter of the growing film with the substrate lattice. Those defects can locally trap the electrons or holes, and eventually reduce the carrier density inside the film. Interestingly, the charge accumulation, which can be activated by changing the conditions such as the sample temperature, behaves as the donor or acceptor as in the case of extrinsic semiconductors. Similarly, by the adsorption of either solid atoms or organic molecules, each adatom can behave like a single scatterer. It can also be possible that there is either a charge transfer mechanism or electron filling. There are also some materials which have the tendency to alloy with the film materials via different kinds of diffusion mechanisms such as exchange diffusion. Such kinds of surface modifications can also result in a significant change in the

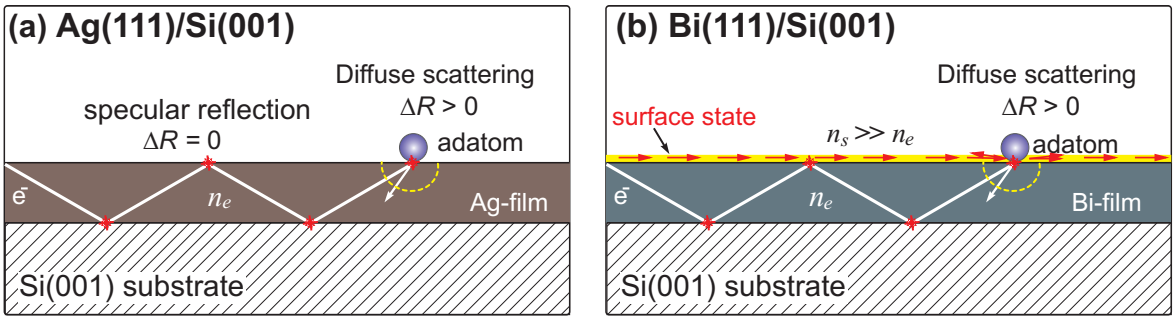

Figure 1.1: Schematic view of the scattering mechanism in Ag films and Bi films. (a) Smooth and continuous film does not contribute resistance, since the electrons are specularly scattered at the film boundaries. However, adatoms on the surface can increase the film resistance due to the diffuse scattering of electrons. (b) In the case of thin films of Bi, the electron transport occurs via 2D surface states, since the carrier density is higher at the surface than at the film. The surface resistance increases via adsorption due to the diffuse scattering of carriers at adatoms.

film resistivity. Direct evidence of some of those effects will also be explored in this thesis.

For metallic thin films, electrical conduction is especially dominated by electron scattering events at the film boundaries. Resistivity increase in thin films of thickness t, which is comparable to the electron mean free path ($\tau_{el} \leq t$), which occurs via the adsorption of metal atoms, because each adsorbate adds a scattering contribution and reduces the probability of the specular reflection of electrons at film boundaries. A theoretical formulation of this concept was postulated by Fuchs [1] in 1938 and later by Sondheimer in 1952 [2], which works extremely well in explaining resistivity in thin metallic films [3]. In 1995, A. Kaser and E. Gerlach further developed the theory of scattering in a quantum mechanical concept and put forward an expression for resistivity change caused by surface roughness [4]. This was experimentally supported by previous results [5]. This thesis will also show some results on the resistance increase via the additional deposition of Ag on well-defined smooth Ag(111) films. The above-mentioned theory of electron scattering at adatoms or island edges caused by the surface roughness, explains the resistance behavior with coverage. This investigation will be performed not only to test the simple scattering theory but also to compare it with complex scattering phenomena such as scattering due to surface alloying in a heteroepitaxial growth of Au on Ag(111). Additionally, it will also be shown whether the theory may be applied in a semimetallic system such as Bi on Bi(111), which has a smaller Fermi vector k_F as compared to metals. There are some additional reasons why bismuth (Bi) is so special.

Bi is a Group V semimetal and crystallizes into a rhombohedral structure with 2 atoms in the unit cell. Due to the slight structure distortion along the trigonal axis [$(111)_{rhom}$], the band structure becomes a semimetal with a band overlap of $\sim$ 40 meV [6]. Inherently, the density of states in bulk Bi is about five orders of magnitude lower than that of a good conductor [7]. The Fermi surface is highly anisotropic, which results in an anisotropic carrier effective mass m^* (the typical value is $\sim 0.001 m_e$). As a consequence of this, the carriers have a very long de Broglie wavelength λ_{el} ($\sim$ 30 nm) [8] and high mobility. This leads to the pronounced QSE in thin films, which was first observed for Bi in 1966 [9]. One important

prediction as a result of the QSE is the so-called semimetal-to-semiconductor (SMSC) transition, as predicted by Lutskii [10]. However, the existence of the SMSC transition still remains ambiguous. In addition, light cyclotron masses m_c in certain orientations of the Bi crystal result in higher cyclotron frequencies (eB/m_c) ensuring that quantum magneto-oscillations can be observed in moderate magnetic fields B [11]. In 1999, Yang *et al.* [12] observed very large magnetoresistance effects in a thin epitaxially grown Bi film. So, all its electronic properties favor achieving large spin-relaxation lengths and are useful for the realization of spin-based electronic devices such as magnetic-field sensing [13, 14, 15, 16]. Moreover, in recent years, the interest in Bi has increased dramatically because high quality Bi films have shown highly metallic surface states and Rashba-type spin-orbit splitting at the Fermi level. Thus, Bi surfaces can also be used as a quasi-2D metal with unique spin properties. These remarkable results, however, have questioned the validity of the semiconductor-semimetal transition because of the existence of the surface states that smear out any sharp features of the transition [17]. Bi has additionally, attracted a lot of interest because of its unusual structural and vibrational properties originating from its unique intermediate bonding character, between metallic and covalent bond [18, 19, 20]. It is a model system that demonstrates a rich variety of ultrafast dynamics in the limit of high density excitations, such as extremely large phonon amplitudes, electronic softening and phase transitions [19, 21].

Besides these renewed interests, tremendous efforts, and fascinating breakthroughs in recent years, Bi has shown a strong potential for future technological applications. However, to realize an electronic device, high quality films are demanded. In the most favorable case, if the Bi film could be prepared on a technologically relevant substrate of Si(001), it might be compatible with the present technology. In addition, a Si substrate becomes insulating at low temperatures, so it can be used to study electrical transport properties of Bi films. In addition, Bi is among the very few elements which are nonreactive with Si and which do not form a silicide. This property certainly provides a playground for studying fundamental physics.

Earlier studies [22, 23, 24] have shown that Bi grows epitaxially in a (111) direction on Si(111)-(7×7) substrates at room temperature with the occurrence of a so called “magic mismatch” between both lattices, resulting in high quality films. Later on Nagao *et al.* discovered a sharp transformation from one allotropic form, i.e., (110) to another one, i.e., bulk-like (111), at a 4 monolayer coverage of Bi film on Si(111)-(7×7). Those films, later on, were applied to study various electronic properties. In the case of a Si(001) substrate, previous attempts at growing Bi films suggested a Frank–van der Merwe mode at low temperatures $T < 280$ K and a Stranski–Krastanov mode at high temperatures $T > 280$ K [25]. The deposition at low temperatures, however, is accompanied by the formation of bulk defects and increasing surface roughness. Bi thin films made by evaporation and sputtering are often polycrystalline with small grains [26, 27]. Because of the lack of thorough investigations, little is known about the structural quality of the films. Most importantly, a proper recipe of growing high quality single crystalline Bi films on Si(001) is missing. This thesis supplies not only a recipe, but also some important aspects of growth such as the change of island shape and size during

growth, temperature dependent growth behavior, etc. The film morphology, strain state and crystalline quality are investigated by high-resolution low-energy electron diffraction (SPA-LEED), scanning tunneling microscopy (STM), atomic force microscopy (AFM) and x-ray diffraction (XRD), respectively. Additionally, a very first study on semimetallic homoepitaxy of Bi(111) by SPA-LEED and STM is presented, which determines important growth parameters such as adatom diffusion coefficient, attempt frequency and the terrace diffusion barrier. In the context of thin film growth, such fundamental parameters are extremely necessary to gain a microscopic understanding of the growth mechanisms. Those high quality Bi films served as virtual substrates to study the electrical transport behavior via the additional deposition of Bi at different temperatures.

Since electrical transport measurements are highly sensitive to the quality of the contacts, a contact, which is reliable, ohmic in nature, thermally stable and compatible to the Si surface is always desirable for surface sensitive resistance measurements. This thesis will present a novel method to fabricate surface science compatible WSi_2 contacts that can also be extended for technological applications.

Electrical measurements on Ag and Bi films will be accomplished using the silicide contacts in a 4PP technique. *In situ* characterization of surface roughness during deposition allows the simultaneous determination of film morphology and resistivity. Resistance behavior on Ag films will be discussed under the simple theory of the electron scattering model, as shown schematically in Fig. 1.1(a). The resistance of a smooth Ag film increases during additional deposition due to the diffuse scattering of electrons at the adsorbate. However, the resistance behavior of Bi films, during the additional deposition of Bi atoms, cannot be explained by this classical model. Since the Bi(111) surface has two orders of magnitude higher carrier density than the bulk Bi, a concept of 2D transport, as shown schematically in Fig. 1.1(b), is applied. A new approach, a combination of the Boltzmann transport equation in a 2D concept and an experimental observation of coverage dependent island density, will be presented to explain the experimental observation of the resistance behavior at the sub-bilayer coverage regime. At higher coverages, however, the resistance behavior agrees with the classical scattering model quite satisfactorily.

This thesis is organized as follows:

- In chapter 2, some basics of experimental methods will be described. More focus will be given to the electron diffraction theory, because LEED is used as the main tool for investigation in this work. STM, AFM, XRD, etc., will be introduced briefly.
- Chapter 3 deals with the experiment, where major experimental devices and the measurement setup are introduced. In this work, epitaxial films of metals (Ag, Au) or semimetal (Bi) are prepared on Si substrates via MBE under UHV conditions. The setup of the UHV system, including SPA-LEED and MBE tools, are schematically presented. The working principle of SPA-LEED will be explained in some detail.
- In chapter 4, a brief introduction of two basic materials used in this thesis will be

reported. As a substrate, Si(001) draws special attention in this work; its bulk and surface crystallographic structure and temperature dependent surface crystal phases are explained, showing some experimental results. Since Bi is the important material to be studied in this thesis, a brief introduction to its crystallographic structure will be schematically presented.

- Since this thesis also deals with various aspects of the epitaxial growth mechanism, a fundamental understanding of epitaxy is required. Chapter 5 discusses some insights on the theoretical basics and model of epitaxial growth. Emphasis will be given to only the relevant aspects of growth, specially in the case of homoepitaxy.

- Chapter 6 will report an important breakthrough of fabricating surface science compatible silicide (WSi_2) contacts on Si(001) substrate, which are used to measure surface resistance of epitaxial metal/semimetal films in a 4PP setup. A real time study of surface morphology by LEEM during silicide formation at high temperatures allows to understand the kinetics and the surface structure. Study of silicide structures by additional techniques such as *in situ* SPA-LEED and *ex situ* SEM and AFM provides rich information related to the surface contamination and the morphology. All the information about the morphology, along with the electrical characterization of the contacts, reported in this chapter, can be found in Ref. [28].

- Major experimental results will be presented in chapter 7 (Refs. [29, 30, 31, 32, 33, 34]), which will explain mainly an important recipe describing how to grow high quality Bi films on a Si(001) substrate. Since the generation of a highly periodic one-dimension dislocation network at the Bi(111)/Si(001) hetero-interface plays an effective role in relaxing the strained Bi film, the dislocation network is characterized quantitatively via the determination of surface height undulation by different techniques. The very first investigation of the simultaneous measurement of the strain state and the lattice relaxation of Bi(111) films with increasing the coverage of Bi on Si(001) will be presented. Finally, the quality of the films will be studied via quantitative determination of surface morphology parameters by various techniques such as SPA-LEED, STM, and AFM. Bulk crystallanity and the lattice relaxation will be characterized by laboratory XRD and synchroton XRD/XRR techniques. Some results on growth and morphology of Ag(111) films on Si(001) will also be presented in the second section of this chapter. The film preparation via a kinetic pathway allows us to achieve a very smooth surface on Ag(111) films, which is an important requirement for electrical transport study in thin films. Some morphological aspects of those Ag films will be discussed at the end of the chapter.

- In chapter 8 (Refs. [35, 36]), the very first study of the semimetallic homoepitaxy of Bi(111) will be reported. A combination of SPA-LEED and STM study at different temperatures allows us to determine diffusion parameters, which are key to understanding nucleation and growth mechanism in this system.

- Chapter 9 (Ref. [37]) presents results of resistance measurements in Bi(111) films. Various aspects responsible for changing the surface resistance, such as morphology, surface crystal phases, surface electronic properties, etc., are discussed. A new approach, which explains the resistance behavior during the initial stages of growth in Bi(111) homoepitaxy, will be presented. A 2D surface state conductivity in Bi(111) surface will be estimated via surface manipulation, which allows to roughly determine an important electronic parameter, the scattering mean free path l_{el} at the 2D surface states. In the next section, the influence of surface morphology on the resistance of smooth Ag(111) films will be presented. The observed behavior will be explained applying the Fuchs-Sondheimer model of the electron scattering. In the preceding section, the resistance behavior during adsorption of Au on Ag(111) surface will be studied. The resulting large increase of resistance at 300 K will be explained based on a simple model of surface alloying via exchange diffusion.

- Finally, some conclusions will be drawn in chapter 10, emphasizing important findings of this work. Some possibilities of future study will be suggested, which may produce exciting results, especially in the case of Bi.

2 The Basics of Experimental Methods

For the experimental investigation throughout this work, both *in situ* techniques such as spot profile analyzing low-energy electron diffraction (SPA-LEED), scanning tunneling microscopy (STM) and *ex situ* techniques such as atomic force microscopy (AFM), scanning electron microscopy (SEM) and x-ray diffraction (XRD) have been used as measurement methods. Among them, SPA-LEED and XRD are diffraction methods, probing the reciprocal space and the STM and AFM are the direct imaging techniques probing in the real space. Since SPA-LEED has been extensively used to study the surface structure and growth behaviors, the basics of the diffraction theory will be discussed exclusively. The remaining techniques and their theoretical background will also be introduced briefly in the preceding sections.

2.1 Low-energy electron diffraction

Low-energy electron diffraction (LEED)[38, 39] is one of the oldest and most reliable surface science technique to study the structure and morphology of two-dimensional (2D) plane surfaces of crystalline solids. The electrons are bombarded on the surface and the diffracted electrons are observed as spots on a phosphorescent screen. The relative position of the spots on the screen shows the surface crystallographic structure. The typical energy used in this technique lies between 10-200 eV, which carries a mean free path of $\sim$5 Å [40]. This results in a low penetration depth ($\sim$3-10 Å) in the solid material, and therefore electrons are highly sensitive to the surface. Besides that, electrons are non-destructive probes for metals and most semiconductors (except the insulator and weakly bound chemisorbed or physiosorbed systems). Since the electron de Broglie wavelength for the low-energy range is of the order of interatomic distances ($\sim$0.5-4 Å) of the solid, LEED can provide the information about the atomic arrangement within the surface unit cells of the crystals. The exact interpretation of the atomic arrangement is supported by the dynamic LEED theory, which considers the multiple scattering in the diffraction process. From the energy dependent spot intensity analysis, the so-called $I(V)$-analysis, one can get precise information about the atomic position within the unit cells.

Besides the intensity, the shape (profile) and the position of the diffraction spots contain important information related to the surface morphology and the defect structure. This can only be possible with the high resolution LEED (SPA-LEED), which will be discussed later in this section. Such spot profiles can be described well by the kinematic approximation.

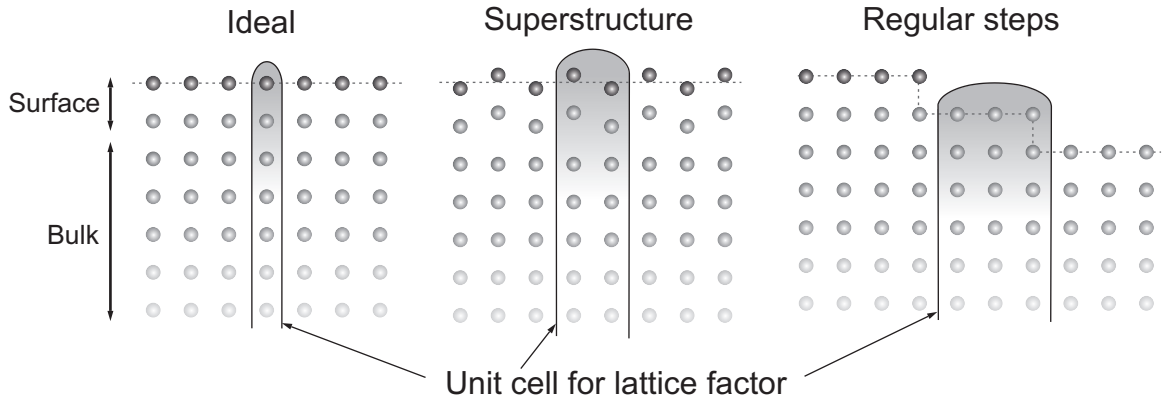

Figure 2.1: The unit cells as used in the kinematic approximation for different surfaces such as the ideal surface, the surface with superstructures, and the surface of regular atomic steps [41].

2.1.1 Kinematic diffraction theory

Although the multiple scattering events of low-energy electrons are important for the computation of LEED analysis, a single scattering consideration within the kinematic approximation can also provide important information. According to this approximation, a surface is described by an arrangement of identical units as shown in Fig. 2.1. The wave function of the diffracted electrons from the surface can be described by the sum of the electron waves scattered from the incident wave vector k_i into the final wave vector k_f by all surface atoms positioned at r_n, i.e., the position at n^{th} surface unit cell and expressed as:

$$\Psi(k, k_i) = \sum_n f_n(k, k_i)\, e^{ikr_n} \tag{2.1}$$

with $k = k_i - k_f$ the scattering vector and $f_n(k, k_i)$ the structure factor. The structure factor takes into account all the electron waves coming from the surface atom at r_n along with the underlying atoms in the column as shown in Fig. 2.1. The total intensity of the scattered wave, which is observable, can be written as:

$$I(k, k_i) = \mid \Psi(k, k_i) \mid^2 = \sum_{n,m} f_n(k, k_i)\, f_m^*(k, k_i)\, e^{ik(r_n - r_m)} \tag{2.2}$$

Let us assume that all atoms are on perfect lattice sites. The position vector r_n can be extended as:

$$r_n = r(n_x, n_y) = a_x n_x + a_y n_y + a_z h_n \tag{2.3}$$

where $n = (n_x, n_y)$ describes a unit mesh, a_x, a_y are the surface unit vectors, a_z is the unit vector perpendicular to the surface, with an absolute value of d, and h_n the height of the respective unit mesh. For a square lattice with the lattice parameter a, r_n is just given by $r_n = an + d_z h_n$. Separating the scattering vector k into the parallel component $k_\parallel$ and the perpendicular component $k_\perp$, Eq. 2.2 can be rearranged into:

$$I(k,k_i) = \sum_{n,m} \left\langle f_{(n+m)}(k,k_i)\, f_m^*(k,k_i)\, e^{idk_\perp(h_{n+m}-h_m)} \right\rangle_m e^{iak_\parallel n} \tag{2.4}$$

The symbol $\langle\,\rangle_m$ denotes the averaging with respect to m. From Eq. 2.4 it is obvious that the measured intensity of the scattered wave depends on both the arrangement of the atoms and their scattering amplitudes. Using the kinematic approximation, all the scattering amplitudes are replaced by a spatial average considering a single scattering cross-section within a unit cell. This approximation is more accurate for smooth surfaces, since the scattering amplitude differs between the steps and the terraces. Neglecting the small deviation of the scattering amplitude at various features at the surface, the intensity in Eq. 2.4 can be split into two parts as follows:

$$I(k,k_i) = F(k,k_i) \cdot G(k_\parallel,k_\perp) \tag{2.5}$$

with the dynamical form factor $F(k,k_i)$ and the long range cell contribution of lattice factor $G(K)$.

$$F(k,k_i) = \mid f(k,k_i) \mid^2 \tag{2.6}$$

$$G(k_\parallel,k_\perp) = \sum_n \left\langle e^{idk_\perp(h_{n+m}-h_m)} \right\rangle_m e^{iak_\parallel n} \tag{2.7}$$

Since the form factor strongly depends on the perpendicular component of the scattering vector $k_\perp (k_\perp \propto \sqrt{E}$, where E is the electron energy) and weakly dependent on the parallel component $k_\parallel$, Eq. 2.5 can be simplified as:

$$I(k,k_i) = F(E) \cdot G(k_\parallel,k_\perp) \tag{2.8}$$

where the dynamical effect is described by the form factor $F(E)$ and the shape of the spot profile can be described only by the lattice factor $G(k_\parallel,k_\perp)$. The lattice factor in Eq. 2.7 can be further modified to:

$$G(k_\parallel,k_\perp) = \sum_n \phi(n,k_\perp)\, e^{iak_\parallel n} \tag{2.9}$$

which concludes that the spot profile is the Fourier transform of the phase correlation $\phi(n,k_\perp)$. The phase correlation is often connected with the pair correlation function $C(n,h)$, which refers to the probability to find two surface atoms separated by a distance of na and a vertical distance dh (h denotes an integer), and described as:

$$\phi(n,k_\perp) = \sum_{-\infty}^{\infty} C(n,h)\, e^{ik_\perp dh} \tag{2.10}$$

$$C(n,h) = \int_0^{2\pi/d} dk_\perp\, \phi(n,k_\perp)\, e^{ik_\perp dh} \tag{2.11}$$

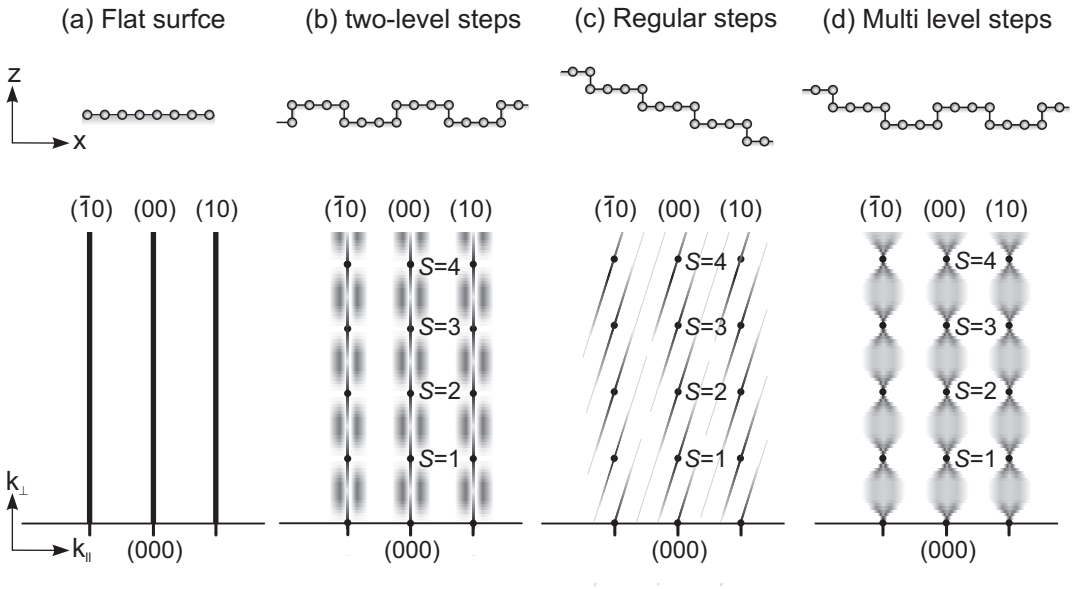

Figure 2.2: Diffraction rods from (a) a perfect surface (atomically smooth surface): spot profile does not change as a function of vertical scattering vector $k_\perp$. Spots show only the instrumental broadening. Diffraction rods from (b) a surface with two level steps: spot profile shows diffuse intensity (with distinct shoulder) for most energies. The spots are sharp at the in-phase condition ($S = n$, where n is integer), i.e., the 3D Bragg conditions. Diffraction rods from (c) a vicinal surface (surface with a regular step train): spot profile shows a spot splitting due to the linear phase grid of steps. The spots move in accordance to the inclination of the vicinal surface. Diffraction rods from (d) a surface with multilevel steps (rough surface): spot shows broadened (diffuse) profile for most energies. A sharp central spike is only observed at the exact in-phase condition [41].

The above equation clearly indicates that a complete information about the surface morphology requires a series of spot profiles from phase 0 to $2\pi/d$.

Unlike the structure factor $F(E)$, the lattice factor $G(k_\parallel, k_\perp)$ does not modify the integral intensity of the spot. It rather influences the intensity distribution in the reciprocal space. A perfect smooth, flat and defect free surface produces sharp spots, which are only instrumentally broadened. Due to the similar height in the atomically flat surface, which gives $(C(n,h) = \delta(h))$, the lattice factor $G(k_\parallel, k_\perp)$ can be described by the sum of δ-functions:

$$G_{ideal}(k_\parallel) = \sum_n \delta(k_\parallel - \frac{2\pi}{a}n) \tag{2.12}$$

If the perfect translational symmetry of the surface is modified by defects or surface roughness, the fundamental diffraction spots redistribute the intensity from the sharp to the diffuse spots, reflecting the long range order. Fig. 2.2 shows different surfaces and the respective diffraction spots in the reciprocal space. Sharp spots from the flat surface (Fig. 2.2(a)) change into diffuse shoulder for two-level regular steps (Fig. 2.2(b)), spot splitting for regular step arrays (Fig. 2.2(c)) and spot broadening for rough surface (Fig. 2.2(d)). However, the total integral intensity of the diffuse and peaked part of a particular spot i, j is always conserved and normalized to 1 by the number of surface unit cells and is independent on both the surface

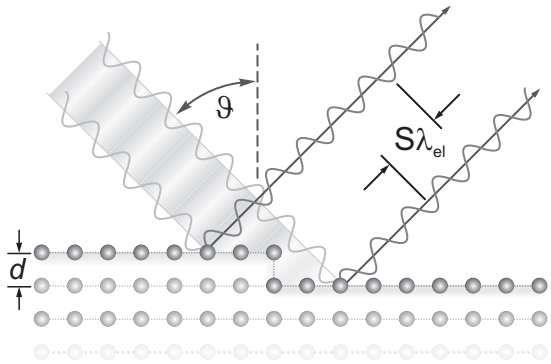

Figure 2.3: Phase shift due to scattering at a monatonic step edge: electrons scattered from stepped surfaces undergo a phase difference of $2\pi S$, i.e., a path difference given by the scattering phase S and the electron wavelength λ_{el}. For integer values of S the electrons interfere constructively and the sharp LEED spot appears. The electrons are insensitive to the surface roughness at the in-phase condition. For half integer values of S the electron interference is destructive and the sharp LEED spot disappears. The electrons are sensitive to the surface roughness at the out-of-phase condition.

morphology h_n and $k_\perp$:

$$\int_{BZ} dk_\parallel \, G_{ij}(k_\parallel, k_\perp) = 1, \tag{2.13}$$

where the lattice factor $G_{ij}(k_\parallel, k_\perp)$ is obtained from the intensity $I_{ij}(k)$ of the spot i, j. The actual lattice factor $G_{ij}(k_\parallel, k_\perp)$ can be extracted from the measured intensity profile by normalizing with the total integral intensity of the spots i, j.

$$\frac{I_{ij}(k_\parallel, k_\perp)}{I_{total}} = \frac{F(k, k_i) \cdot G(k_\parallel, k_\perp)}{\int_{BZ} dk_\parallel \, F(k, k_i) \cdot G(k_\parallel, k_\perp)} \cong \frac{F(k, k_i) \cdot G(k_\parallel, k_\perp)}{\overline{F}_{BZ} \int_{BZ} dk_\parallel \, G(k_\parallel, k_\perp)} \tag{2.14}$$

$$= \frac{F(k, k_i) \cdot G(k_\parallel, k_\perp)}{\overline{F}_{BZ}} \cong G(k_\parallel, k_\perp) \tag{2.15}$$

Since the variation of the form factor $F(k, k_i)$ with k is much smoother than the lattice factor $G(k_\parallel, k_\perp)$, the form factor $F(k, k_i)$ can be considered constant, i.e., $F(k, k_i) = \overline{F}_{BZ}$ around the spot i, j in reciprocal space, where diffuse intensity is observed. This indicates that the approximation works best for larger morphological features.

2.1.2 Scattering phase

The scattering phase S describes the phase difference in numbers of electron wavelength λ_{el}, when electrons are scattered from adjacent terraces separated by single atomic steps (step height = d), as shown in Fig. 2.3. It depends on the vertical scattering vector $k_\perp$ as:

$$S = \frac{k_\perp d}{2\pi}. \tag{2.16}$$

Electrons undergoes constructive interference for the integer values of scattering phase, i.e., $S = n$, where n is integer, known as the Bragg or in-phase condition, and destructive interference for half integer values, i.e., $S = n + \frac{1}{2}$, known as the anti-Bragg or out-of-phase condition. At the in-phase condition, electrons are not sensitive to the morphology and sharp LEED spots are expected. In contrast, at the out-of-phase condition, the intensity is redistributed into a diffuse part surrounding the sharp spot, and are sensitive to the morphology such as surface roughness.

For the (00)-spot, where $k_{\parallel} = 0$, the scattering phase depends on the electron wavelength as:

$$S = 2d \cos\vartheta/\lambda_{el} \tag{2.17}$$

with

$$\lambda_{el} = \frac{h}{p} = \left(\frac{h^2}{2mE}\right)^{\frac{1}{2}} \tag{2.18}$$

where h is Planck's constant, p is the electron momentum, m_e is the mass of electron, E is the primary energy of the incident electron, and ϑ is the angle of incidence with respect to the surface normal ($\cos\vartheta = 0.997 \approx 1$ for the SPA-LEED geometrical construction). Combining both Eq. 2.17 and Eq. 2.18 and substituting the values for fundamental constants, the scattering phase S can be further simplified into:

$$S = 2d \cos\vartheta\sqrt{E(eV)/150.4} \tag{2.19}$$

Additionally, from the knowledge of the electron energies of the in-phase conditions and the corresponding scattering phase S we can determine the step height d via the Laue condition. Constructive interference between adjacent levels is observed for the maxima of the $G(S)$ curve where the Laue condition is fulfilled. From the distance $\triangle S$ between two successive maxima or minima of the $G(S)$ function and the respective electron energies, the vertical layer distance can be easily calculated by combining Eqs. 2.17 and 2.18 [42]:

$$d = \frac{\triangle S}{2\cos\vartheta}\left(\frac{\lambda_e(E_1)\,\lambda_e(E_2)}{\lambda_e(E_1) - \lambda_e(E_2)}\right). \tag{2.20}$$

2.1.3 Two level system: spot profile analysis

If the surface is rough with small islands of single atomic steps (see Fig. 2.5), the spot consists of a sharp central spike $I_0(k_\perp)$ surrounded by a diffuse shoulder $I_{shd}(k_\perp, k_\parallel)$. The central spike is given by the constructive interference of electrons scattered from islands and the film surface. Its intensity depends only on the coverage in the first layer Θ, i.e., the fraction of scatterers in the first layer and oscillates with the scattering phase S as [43, 42]:

$$G(S,\Theta) = 1 - 2\Theta(1-\Theta)(1-\cos(2\pi S)). \tag{2.21}$$

For the in-phase condition, all intensity is confined to the central spike and the intensity distribution is the same as the perfect flat surface. In contrast, at the out-of-phase condition, the spot profile only shows the diffuse shoulder. Furthermore, the minima of the central spike also changes drastically with small changes in the coverage Θ. The overall behavior of the central spike intensity has been summarized in Fig. 2.4, where normalized central spike intensity $G(S,\Theta)$ has been plotted against the phase S and the coverage Θ, respectively. At $\Theta = \frac{1}{2}$, interference of scattered electrons from islands and the substrate is completely destructive in the out-of-phase condition. Substituting $\Theta = 0.5$ (half of a complete layer), Eq. 2.21 turns out to be

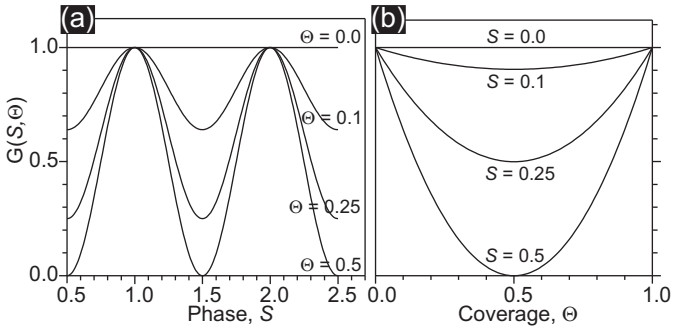

Figure 2.4: (a) $G(S, \Theta)$ of the (00)-spot profile as a function of scattering phase S for an ideal 2-level system, plotted for various coverages. (b) $G(S, \Theta)$ for an ideal layer-by-layer growth mode, plotted for various scattering phases S. Further deposition repeats the curve, showing a signature of layer-by-layer growth.

$$G(S) = \frac{1}{2}[1 + \cos(2\pi S)]. \tag{2.22}$$

2.1.4 Multilevel system: spot profile analysis

If a surface is rough with multiple islands growing one above the other as shown in Fig. 2.5, the spot profile shows a sharp central spike $G_{ideal}(k_\perp)$ surrounded by a broadening $\Phi_{diff}(k_\perp, k_\parallel)$, caused by the interference from different levels of the islands.

$$G(k) = G(k_\perp)\, G_{ideal}(k_\parallel) + [1 - G(k_\perp)]\ \Phi_{diff}(k_\perp, k_\parallel) \tag{2.23}$$

where $\Phi_{diff}(k_\perp, k_\parallel)$ is the diffuse profile,

$$\Phi_{diff}(k_\perp, k_\parallel) = \frac{I_{diff}(k_\perp, k_\parallel)}{\int_{BZ} I_{diff}(k_\perp, k_\parallel)\, dk_\parallel} \tag{2.24}$$

The amplitude of both central spike and broadening vary with $k_\perp$. Here the lattice factor $G(k_\parallel = 0, k_\perp)$ is given by the Fourier transform of the surface projection of all surface scatterers onto the surface normal and contains the information about the layer distribution p_h [44, ?], which is the probability of finding a surface atom in the level h and the phase-shift S.

$$G(k_\parallel = 0, S) = \sum_h C_h\, \cos(2\pi S h) \tag{2.25}$$

Here, C_h describes the vertical height correlation, defined by:

$$C_h = \sum_l p_l\, p_{h+l}. \tag{2.26}$$

The calculation of the $G(k_\parallel = 0, S)$ as a function of the phase S can be done by the Fourier transformation from the normalized central spike intensity, i.e., the lattice factor $G(k_\parallel, k_\perp)$ via Eq. 2.15. This calculation gives an important parameter of the statistical value of vertical

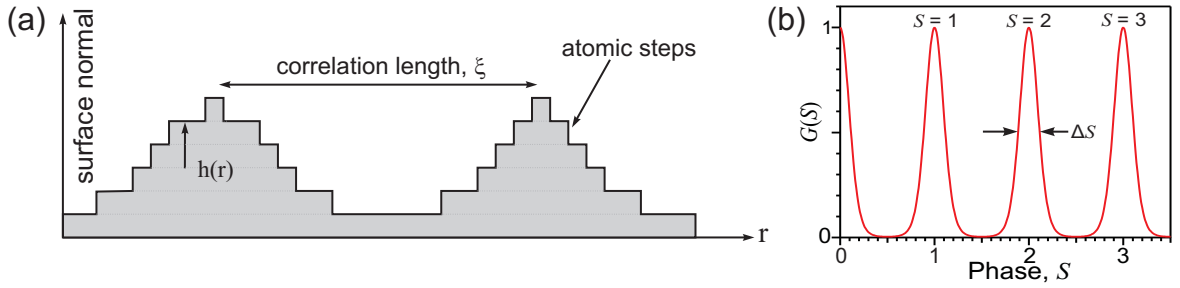

Figure 2.5: (a) Schematic cross-sectional view of a rough surface, which occurs generally in a statistical growth mode (multilayer growth). (b) $G(S)$ curve of the (00)-spot as a function of scattering phase S for the multilevel rough surface, as shown in (a). At the in-phase condition, i.e., $S = n$, all the intensity is confined to the central spike and exhibits the maximum and at the out-of-phase condition, i.e., $S = n + \frac{1}{2}$, the central spike almost vanishes due to destructive interference, showing the minimum intensity.

roughness, i.e., the asperity height $\triangle$, which can be defined by

$$\triangle^2 \equiv d^2 \left[\left\langle h^2(r) \right\rangle - \langle h(r) \rangle^2 \right] = \sum_{h>0} C_h h^2. \tag{2.27}$$

The behavior of $G(k_{\|} = 0, S)$ is connected with the asperity height $\triangle$ as [5]:

$$G(k_{\|} = 0, k_{\perp}) = exp\left[-2\triangle'^2 (1 - \cos(2\pi S) \right]. \tag{2.28}$$

with $\triangle = \frac{\triangle'}{d}$. Assuming the $G(k_{\|} = 0, S)$ has a Gaussian shape close to the in-phase condition [45, 46],

$$G(k_{\|} = 0, S) = G(S) \approx e^{-\triangle^2 (2\pi\delta S)^2} \tag{2.29}$$

where δS is the deviation of the scattering phase S from the next integer value, the asperity height $\triangle$ can be easily estimated via the full width at the half maximum of the $G(S)$-curve.

Geometric distribution

The broadening of the spot profile $\Phi_{diff}(k_{\perp}, k_{\|})$ contains the information about the terrace length distribution $P(L)$. The often used terrace length distribution is a geometric distribution and gives a Lorentzian shape profile of the broadening at the out-of-phase condition [47, 44]:

$$\Phi_{diff}(k_{\perp}, k_{\|}) \propto \frac{1}{\kappa^2 + \left(a k_{\|}\right)^2} \tag{2.30}$$

with $\kappa = \frac{2}{\langle \Gamma \rangle}$, $\langle \Gamma \rangle$: the average terrace length. The average terrace length can be derived from the full width at the half maximum (FWHM) of the broadening via FWHM $= 2\kappa = \frac{4}{\langle \Gamma \rangle}$. For isotropically distributed atomic steps, which is generally the case in the experiment, the

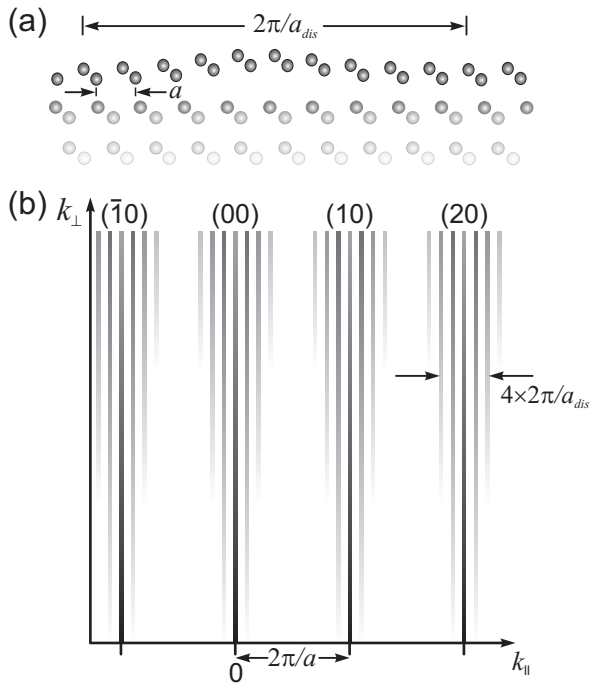

Figure 2.6: (a) Periodic displacement (vertical as well as lateral) of atoms or unit cells from their mean position due to elastic lattice distortion, originated from the interaction between adjacent strain fields surrounding each misfit dislocation at the interface in the lattice mismatched heterosystem. (b) Spot splitting of all fundamental and superstructure spots in an array of satellite spots, due to the surface height undulation caused by an array of dislocation network, which acts as a 2D phase grating for electrons. An average distance between the dislocations can be determined by the separation between the satellite peaks. Up to higher order satellites can be observed at large electron energies, since low energetic electrons are insensitive to the weak height undulation.

geometric terrace length distribution is given by:

$$\Phi_{diff}(k_\perp, k_\parallel) \propto \frac{1}{\left[\kappa^2 + \left(ak_\parallel\right)^2\right]^{\frac{3}{2}}} \tag{2.31}$$

with $\kappa = \frac{[1-\cos(2\pi S)]}{\langle\Gamma\rangle}$. The FWHM at the out-of-phase condition directly provides the average terrace length $\langle\Gamma\rangle$ and the correlation length ξ via $\kappa = \frac{2}{\langle\Gamma\rangle}$ with $\langle\Gamma\rangle = \frac{\xi}{2\triangle^2}$.

2.1.5 Weak height undulation of the surface

In the lattice-mismatched heteroepitaxial growth, it is most likely the case that defects like dislocations are generated at the interface or above the interface to relax the lattice strain. Initially, at a very low coverage regime, the strain fields at each dislocation are isolated locally, giving rise to disordered surface deformation. With increasing coverage and after relaxing the film, more dislocations are generated, which causes a strong interaction between adjacent strain fields. This phenomenon results in the elastic distortion of the lattice plane, which appears as a long range wave-like periodic surface height undulation. Such a surface is compared to a phase grid in optics, producing a spot splitting of the fundamental spots into satellite spots. The separation between the satellite spots is inversely proportional to the average distance between the dislocations [48, 49, 50] (see Fig. 2.6). The intensity of the satellite spots is determined by the geometry and the magnitude of the surface height undulation [51].

Since the (00)-spot is only sensitive to the perpendicular component of the momentum transfer $k_\perp$ (i.e., $k_\parallel = 0$), it is possible to study the configuration of the dislocation network by analyzing the intensity of the (00)-spot satellites spots at different scattering phases S.

For low scattering phases, i.e., for low electron energy, the satellites are hardly visible. With increasing scattering phase S, more satellite spots are visible, since they are more sensitive to the weak height undulation.

Considering small displacements of atoms and small scattering phase S, the resulting phase information of the electrons after diffraction at the surface undulation can be expanded by a Taylor series:

$$\begin{aligned} A(S, k_{\parallel}) &= \int dr\, e^{ik_{\parallel} r}\, e^{i2\pi S\, h(x)} \\ &= \int dr\, e^{ik_{\parallel} r} \left(1 + 2\pi i S\, h(x) - 2\pi^2 S^2\, h^2(x)\right) \end{aligned} \tag{2.32}$$

where $h(x)$ is the vertical component of the one-dimensional surface height undulation. For the simplest case, the height function $h(x)$, with a period of $\langle a_{dis} \rangle$, can be described by a Fourier series with coefficients D_j [51, 52]:

$$h(x) = \sum_{j=0}^{N-1} D_j\, \cos\left(2\pi \frac{x}{\langle a_{dis} \rangle}\, j\right);\; N = \frac{\langle a_{dis} \rangle}{a}. \tag{2.33}$$

Exploiting Eq. (2.32) and (2.33) under the condition of $2\pi S \triangle h < 1$, i.e., for small values of a scattering phase S, the satellite spot intensities can be approximated by a parabolic behavior with S,

$$I_j = 4\pi^2 S^2 D_j^2. \tag{2.34}$$

The total intensity of the (00)-spot is always conserved at the expense of the central spike:

$$I_{00} = 1 - \sum_j 4\pi^2 S^2 D_j^2. \tag{2.35}$$

The absolute values $|D_j|$ can be derived from the slope of the square root of the satellite intensity I_j for the very low scattering phases S.

2.2 Scanning tunneling microscopy

Scanning tunneling microscopy (STM) is a direct imaging technique, which works by scanning an atomically sharp metallic tip over the sample surface with the help of the piezo element. The piezo element can position the tip exactly in the range of sub-Å. The working principle of the STM is summarized schematically in Fig. 2.7. As the tip approaches few Å distance from the sample, some current appears to flow, if some voltage V_{bias} between the sample and the tip (in the range of meV to few eV) is applied. Such a small current (in the range of few pA to few nA), known as the tunneling current I_t, results from the classically forbidden, tunneling of sample electrons near the Fermi edge ε_F to unoccupied states of the tip (or vice versa, depending on the polarity of the applied voltage U_{bias}). The tunneling current I_t decays

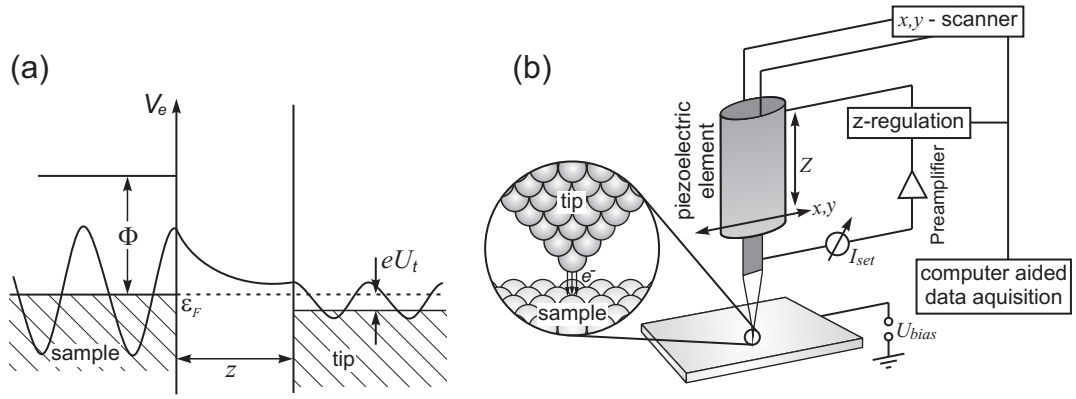

Figure 2.7: (a) Schematic diagram of the tunneling process between the metallic sample and the tip applying a negative voltage. The wave function decays exponentially across the barrier and depends strongly on the tip-sample separation z. (b) Schematic view of the principle of the STM operation. A sharp conductive tip, mounted on top of a piezoelectric element, is scanned line by line across a small region of the sample surface via the piezoelectric element. As the tip is a few Å far from the sample, the tunneling of electrons occurs by applying a bias voltage U_{bias} between the tip and the sample. Hereby, the tunnel current serves as feedback control parameter for the positioning of the tip and the tip follows the contour of the surface at a constant distance.

exponentially with the distance z between the tip and the sample:

$$I_t \propto e^{-2\kappa z} \tag{2.36}$$

where $\kappa = \frac{\sqrt{2m\Phi}}{\hbar}$ is the decay constant, with Φ the average local barrier height between the two electrodes, i.e., the tip and the sample, which depends on the work functions of the electrode materials. In the case of a metallic surface the barrier height Φ is on the order of some eV.

From Eq. 2.36 two main characteristics of the STM can be deduced. An increase of the barrier height by 1 Å will lead to a decrease of the tunnel current by approximately one order of magnitude and hence the STM is highly sensitive to the variation of the distance between tip and sample. Additionally, the tunnel current is laterally confined. In the ideal case the main current is carried by a single atom at the tip apex only.

There are mainly two modes of operation in STM: a constant current mode and a constant height mode. In this work only the constant current mode is used. Typical tunnel currents are on the order of a few nA. In the constant current mode of operation the tip is scanned line by line in the x-y plane across the sample surface. Simultaneously, during scanning, the vertical z-displacement is regulated via the piezoelectric element with the help of a feedback loop. The voltage variations, which are applied to the piezoelectric element by the feedback loop, are recorded for each point. Because of the well-known characteristics of piezoelectric devices, the voltage can be converted into distance changes leading to a 3D image $z(x, y)$ of the scanned area. If the measured area shows monatomic steps, islands, or other features, they are recorded as topography.

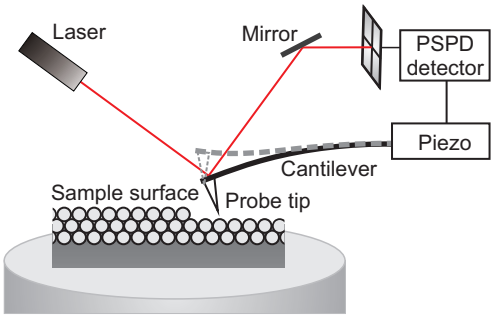

Figure 2.8: Schematic view of the common setup of AFM. The AFM probe has a very sharp tip (diameter < 10 nm) at the end of a small cantilever, which is attached to a piezoelectric scanner tube. The piezo scans the probe across the sample surface. Interatomic forces between the probe and the sample cause the cantilever to deflect as the surface topography. A laser light reflected from the back of the cantilever measures the deflection of the cantilever. This information is fed back to a computer, which generates a map of topography.

2.3 Atomic force microscopy

The topographic information of a grown film has been additionally obtained by *ex-situ* atomic force microscopy (AFM) under ambient conditions. For this, the AFM probes the surface with a sharp tip ($\sim$ few nm diameter), which is located at the free end of a cantilever ($\sim$ few µm long). If the tip approaches the surface, the force between the tip atoms and the surface atoms cause the cantilever to bend or deflect. A position-sensitive photodetector (PSPD-detector) measures the cantilever deflection as the tip is scanned over the sample (by the means of a piezoresistive material - a PZT-scanner). The measured cantilever deflections allow a computer to generate a map of the surface topography.

There are mainly two forces contributing to the deflection of an AFM cantilever: the attractive or van der Waals force and the repulsive or electrostatic force. As the atoms of both the tip and the surface are gradually approached, they start to weakly attract each other due to the van der Waals force. This attraction increases until the atoms of both ends are so close together that their electron clouds begin to repel each other electrostatically. This repulsion progressively weakens the attractive force as the atomic separation continues to decrease. The interatomic force goes to zero when the distance between the atoms reaches a couple of Å (about the length of a chemical bond). When the total of the van der Waals and the electrostatic repulsive force becomes positive, the atoms are in contact. Hence, there are two regimes: the contact regime and the non-contact regime. Depending on these two regimes and the forces acting on the atoms, two scanning modes can be performed: contact mode AFM and non-contact mode AFM. In contact mode AFM the tip makes soft physical contact with the sample. As the piezo scanner gently traces the tip across the sample the contact force causes the cantilever to bend and accommodate changes in the topography of the sample surface. In non-contact mode the tip is kept in a distance of a few nm, which allows the measurement of the topography without any contact between the tip and the sample. For this mode the cantilever is vibrated near the surface of the sample. The spacing between the tip and the sample for this mode is on the order of 10 - 100 Å. This technique avoids a contamination of the sample through contact with the tip and greatly reduces abrasion of the tip.

Except these two modes, there is another mode of operation, the so-called tapping mode

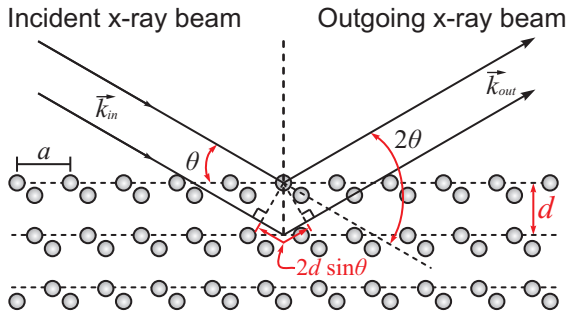

Figure 2.9: Schematic view of the x-ray geometry, where the incident wave $\vec{k}_{in}$ of x-ray beam undergoes a path difference of $2d\sin\theta$ after scattering at the adjacent layers (layer separation = d) of the crystal surface. The scattered wave $\vec{k}_{out}$ are detected in an angle of 2θ (the angle between the diffracted wave and the incident wave).

(Intermittent Contact Mode imaging), which is implemented in ambient air by oscillating the cantilever assembly at or near the cantilever's resonant frequency using a piezoelectric crystal. The piezo motion causes the cantilever to oscillate with a high amplitude when the tip is not in contact with the surface. The oscillating tip is then moved toward the surface until it begins to lightly touch, or tap the surface. During scanning, the vertically oscillating tip alternately contacts the surface and lifts off, generally at a frequency of 50 - 500 kHz. As the oscillating cantilever begins to intermittently contact the surface, the cantilever oscillation is necessarily reduced due to energy loss caused by the tip contacting the surface. The reduction in oscillation amplitude is used to identify and measure surface features. Its short-time interactions with minimal shear are less destructive than the tip-sample forces in contact mode.

Most of the presented AFM images were produced using the non-contact and tapping mode of scanning.

2.4 X-ray diffraction

X-ray diffraction (XRD) is a very powerful and at the same time non-destructive tool for the structural determination of the samples. In this work, bismuth films were studied via laboratory-based XRD in a $\theta - 2\theta$ geometry, schematically shown in Fig. 2.9. Additionally, the film was also examined by a synchrotron-based XRD and reflectometry measurements. Fig. 2.9 illustrates the principle of the $\theta - 2\theta$ geometry, where the incoming x-ray waves $\vec{k}_{in}$ incident on the crystal surface with an angle θ and scattered from the surface with an angle of 2θ. According to the Bragg's law [53, 54], the intensity maxima results if both incoming and outgoing waves interfere constructively. For the case of destructive interference, both waves cancel out each other and intensity minima are observed. Mathematically, it can be formulated as follows: if the path difference $2d\sin\theta$, where d is the layer distance, between both waves is equal to the integer multiple of the x-ray wave length, constructive interference (intensity maxima) occurs,

$$n \cdot \lambda = 2d\sin\theta. \tag{2.37}$$

From Eq. 2.37, it is clear that the intensity maxima are positioned uniquely in the $\theta - 2\theta$ curve for a particular crystal and for a given wavelength of the x-ray source. The peak positions define the layer separation d of the corresponding lattice.

Equivalently, to satisfy the condition of intensity maxima, also the integer multiple of the moment transfer $\triangle\overrightarrow{k}$ of the scattered wave, i.e., the vector difference between the incoming $\overrightarrow{k}_{in}$ and the outgoing $\overrightarrow{k}_{out}$ waves, must be equal to the reciprocal lattice vector $\overrightarrow{G}$ as:

$$n \cdot \triangle\overrightarrow{k} = \overrightarrow{G}. \tag{2.38}$$

Since the wavelength of the x-ray photon is comparable to the lattice parameter of the solid crystal, together with the concept of the reciprocal lattice vector, quantitative information about the geometrical position of the atoms in the solid is obtained.

Beyond the lattice parameter, also the thin film surface and interface morphology can be studied using X-rays in a different geometry. Since a typical energy of x-ray photons ranges from 20-30 kV, it can penetrate the solid crystal up to some µm below the surface. As a result of this, a fraction of the signal originating from the thin film compared to the thick substrate is extremely low. To enhance the signal by reducing the penetration depth, a grazing incident geometry is applied, where the x-ray waves are incident on the surface with an extremely low angle θ_{in} ($\theta_{total} < \theta_{in} < 0.5°$). Analogous to the total reflection of light, x-ray waves are reflected from the defined thickness of the film.

Practically, the intensity is recorded along the crystal truncation rod (CTR), which is the superposition of discrete Bragg diffraction peaks along the surface normal of infinite crystal and the diffraction rod from the ideal surface [55]. The intensity variation $I(\overrightarrow{q})$, where $\overrightarrow{q}$ is the momentum transfer and has the components parallel $q_{\|}$ and perpendicular $q_{\perp}$ to the surface, along the CTR in reciprocal lattice is modified by various factors such as the film thickness Θ, surface roughness σ_s and interface roughness σ_{in} as [55, 56, 57, 58]:

$$\begin{aligned} I(\overrightarrow{q}) &\propto A^2(\overrightarrow{q}) \\ A(\overrightarrow{q}) &\propto \frac{e^{-\sigma_{in}^2\{1-\cos(\overrightarrow{q}\,\overrightarrow{c})\}} - e^{\overrightarrow{q}\,\overrightarrow{c}\Theta}\, e^{-\sigma_s^2\{1-\cos(\overrightarrow{q}\,\overrightarrow{c})\}}}{1 - e^{i\,\overrightarrow{q}\,\overrightarrow{c}}}, \end{aligned} \tag{2.39}$$

where $A(\overrightarrow{q})$ is the amplitude and $\overrightarrow{c}$ is one of the basis vectors of the crystal. Using this technique, the so-called grazing incidence x-ray diffraction (GIXRD), those morphological parameters Θ, σ_{in} and σ_s of the film are determined.

Additionally, the vertical layer distribution of the film is studied by recording the specularly reflected x-ray wave, where the condition $\theta_{in} = \theta_{out}$ makes the variation of the penetration depth inside the film. Using this technique, the so-called x-ray reflectivity (XRR), the thickness variation of the film can be determined precisely [56, 58].

In this work, morphology of the thin Bi(111) films prepared on Si(001) substrate is studied using synchrotron XRR and GIXRD measurements at the beamlines W1 and BW2 of the Hamburger Synchrotronstrahlungslabor at Deutsches Elektronen-Synchrotron (HASYLAB at DESY, Germany).

2.5 Electrical resistivity

It is well known that the electrical conduction in any material (films or wire) is defined by the Ohm's law

$$I = \frac{V}{R}, \tag{2.40}$$

where I is the current, V is the potential difference, and R the resistance of the film or wire. To make the case more general, Eq. 2.40 can be expressed independent of the dimension. Suppose that L and A are, respectively, the length and cross-section of the film or wire; with

$$j = \frac{I}{A}, \qquad \varepsilon = \frac{V}{L}, \quad \text{and} \quad R = \frac{L\,\rho}{A}, \tag{2.41}$$

where j is the current density (current per unit area), E the electric field, and ρ the electric resistivity. $\sigma = 1/\rho$ is the inverse of electrical resistivity, called electrical conductivity. Substituting Eq. 2.41 in Eq. 2.40, we get

$$j = \sigma\,\varepsilon, \quad \sigma = \frac{1}{\rho} = \frac{j}{\varepsilon}, \tag{2.42}$$

which gives a macroscopic view of conduction. This can be further extended in terms of the microscopic properties of the conduction electrons.

Since the flow of the electric current inside the conductor is due to the influence of the electric field, a net force between the electric force $-e\varepsilon$ and a friction force due to the collision of the electrons with the rest of the medium defines the net flow of electrons. The friction force can be expressed as $-m^*\,\vartheta/\tau$, with m* the effective mass of the electron, ϑ the velocity of the electron and τ the electron collision time. Applying Newton's law, the steady state velocity or the drift velocity of the electrons is given by

$$\vartheta_d = -\frac{e\,\tau}{m^*}\,\varepsilon. \tag{2.43}$$

The current density j can be calculated by multiplying the drift velocity from Eq. 2.43 with the charge concentration or the charge per unit volume, i.e., $-n\,e$.

$$j = (-ne)\;\vartheta_d = (-ne)\left(-\frac{e\tau}{m^*}\varepsilon\right) = \frac{ne^2\tau}{m^*}\varepsilon \tag{2.44}$$

Comparing Eq. 2.44 with Ohm's law in Eq. 2.42, the following expression is obtained for the conductivity:

$$\sigma = \frac{ne^2\tau}{m^*}. \tag{2.45}$$

The relaxation time τ in Eq. 2.45 is defined by the exponentially decaying form of the drift velocity ϑ_d with time in the relaxation process. So, the ϑ_d is far lower than the random velocity ϑ_r caused by the random motion of the electrons. In this context, the time τ between

two successive collisions may be expressed as

$$\tau = \frac{l}{\vartheta_r} \tag{2.46}$$

where l is the distance between two successive collisions. Using Eq. 2.45 and Eq. 2.46, the conductivity σ or the resistivity ρ can be written as:

$$\sigma = \frac{1}{\rho} = \frac{ne^2 l}{m^* \vartheta_r}. \tag{2.47}$$

Generally, the resistivity ρ and the effective mass m^* can be considered as scalars; however, the electron density n and the relaxation time τ change according to the various factors such as film geometry, film quality, measurement conditions, etc. Ideally there is no resistivity of a perfect crystal lattice, since an electron can move freely through a perfect rigid crystal without any scattering events. However, a finite relaxation time exists at a temperature $T > 0$ due to the thermal vibrations of the lattice, which causes electron-phonon scattering. Moreover, the relaxation time of electrons also changes significantly due to other scattering processes such as electron-defect scattering, electron-electron scattering, etc. *Matthiessen's rule* provides a good approximation treating such scattering mechanisms as independent, and is expressed as:

$$\frac{1}{\tau} = \frac{1}{\tau_{ph}} + \frac{1}{\tau_i} \tag{2.48}$$

where the first term on the right is due to phonons and the second is due to defects or impurities. The electron-electron scattering can be neglected due to the small effect as compared to other effects. From Eq. 2.46, 2.47 and 2.46, we find

$$\rho = \rho_i + \rho_{ph}(T) = \frac{m^*}{ne^2}\frac{1}{\tau_i} + \frac{m^*}{ne^2}\frac{1}{\tau_{ph}}. \tag{2.49}$$

The resistivity ρ can be split into two terms: a term ρ_i due to scattering by impurities, which is independent of T, and which is known as residual resistivity measurements. The second term is $\rho_{ph}(T)$ due to scattering by phonons; hence, it is temperature dependent, and called the ideal resistivity. In general, the resistivity ρ at room temperature is dominated by electron-phonon scattering and at low temperatures, i.e., close to helium temperatures, is dominated by electron-impurity scattering. For the temperature higher than the Debye temperature Θ_D, the resistivity is proportional to temperature, since the phonon concentration increases with temperature [59]. The overall behavior can be further simplified as

$$\rho(T) = \rho_i + \rho_{ph}(T) = \rho_0 + A \cdot T, \tag{2.50}$$

where A is the temperature coefficient of resistance (TCR), a material constant, and T is the temperature.

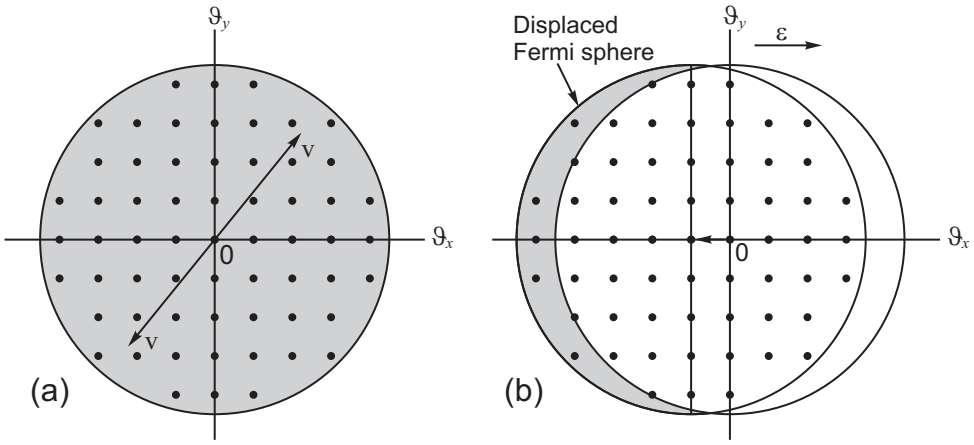

Figure 2.10: (a) Schematic diagram of the Fermi sphere at equilibrium. (b) Displacement of the Fermi sphere due to an electric field.

2.5.1 Concept of 2D conductivity

The classical expression of conductivity in Eq. 2.45 can be further modified in the framework of Fermi-surface (FS). In the absence of an electric field, the Fermi sphere is centered at the origin, since the total velocity of all the electrons is canceled in pairs. Such a pairwise cancellation of the velocities results the total current zero (Fig. 2.10(a)). However, the situation will be changed when an electric field is applied. As shown in Fig. 2.10(b), the Fermi sphere is displaced opposite to the direction of the applied electric field. This causes the change of electron concentration, which is $n = n\,(\vartheta_d/\vartheta_F)$. Now, the current density becomes [60]:

$$J = -e\,n\,(\vartheta_d/\vartheta_F)\;(-\vartheta_F) = ne\vartheta_d \tag{2.51}$$

where ϑ_F is the velocity of the electrons at the Fermi level. On substitution the value of ϑ_d from Eq. 2.44, yields

$$J = \frac{ne^2\tau_F}{m^*}\varepsilon, \tag{2.52}$$

where τ_F is the collision time of an electron at the Fermi level. The resulting conductivity is therefore

$$\sigma = \frac{ne^2\tau_F}{m^*} = \frac{ne^2 l_F}{m^*\vartheta_F}, \tag{2.53}$$

where l_F is the electron mean free path at the Fermi level. l_F is proportional to the T at high temperatures and again Eq. 2.53 is consistent with the previous expression for $\rho = (1/\sigma) \sim T$ (Eq. 2.49).

The same expression in 2.53 can also be applied in connection with band theory, where the quantity n is the concentration of conduction or valence electrons and τ_F is the collision time for an electron at the Fermi level. Similar to the previous case, as shown in Fig. 2.10, every electron in state k, whose velocity is $v(k)$, cancels with another electron in state $-k$, whose velocity is $-v(k)$, resulting in a zero net current [60]. Under application of electric field, the

Fermi level is displaced through k-space at a uniform rate, that is

$$\delta k_x = -\frac{e\varepsilon}{\hbar}\delta t \tag{2.54}$$

where δk_x is the displacement in x-direction at a time interval δt. The average displacement can be described as:

$$\delta k_x = -\frac{e\varepsilon}{\hbar}\tau_F \tag{2.55}$$

Under displacement, some electrons are not canceled, which then contribute to the net current. The current density can be written as [60]:

$$\begin{aligned} J_x &= -e\bar{\vartheta}_{F,x}\, n_u \\ &= -e\bar{\vartheta}_{F,x}\, g\left(E_F\right)\delta E \\ &= -e\bar{\vartheta}_{F,x}\, g\left(E_F\right)\left(\frac{\partial E}{\partial k_x}\right)_{E_F}\delta k_x, \end{aligned} \tag{2.56}$$

where $\bar{\vartheta}_{F,x}$ is the component of the average Fermi velocity in the x-direction, $g\left(E_F\right)$ is the density of states at the Fermi level and δE the energy absorbed by the electron from the field. The product of $g\left(E_F\right)\delta k$ gives the concentration of uncompensated electrons under the action of the electric field. Substituting $\partial E/\partial k_F = \hbar\bar{\vartheta}_{F,x}$ and for δk_x from Eq. 2.55 in Eq. 2.56, Eq. 2.56 turns out to be

$$J_x = e^2\,\bar{\vartheta}^2_{F,x}\,\tau_F\, g\left(E_F\right)\,\varepsilon, \tag{2.57}$$

For a spherical Fermi surface, there is a spherical symmetry and the Fermi velocity can be changed into $\bar{\vartheta}^2_{F,x} = \frac{1}{3}\vartheta^2_F$ for the case of the 3D Fermi surface. Now, after substituting it in Eq. 2.57, this leads finally to the following expression for the electrical conductivity [60]:

$$\sigma = \frac{1}{3}\,e^2\,\vartheta^2_F\,\tau_F\, g\left(E_F\right). \tag{2.58}$$

For a 2D surface, Eq. 2.58 changes into

$$\sigma_{2D} = \frac{1}{2}\,e^2\,\vartheta^2_F\,\tau_F\, g\left(E_F\right). \tag{2.59}$$

Eqn. 2.58 and 2.59 are exactly the solutions of the of the Boltzmann equation [61, 62]. It is an important consequence of the Boltzmann equation that σ_{2D} is proportional to relaxation time τ_F, Fermi velocity ϑ_F, density of states at Fermi level $g(E_F)$, and the mean free path l_{el} $(= \tau_F\,\vartheta_F)$.

The electron concentration n in Eq. 2.53 is generally given in terms of the density of states (DOS), $g(E_F)$;

$$n = \int_0^\infty f\left(E\right)\, g\left(E_F\right) dE \tag{2.60}$$

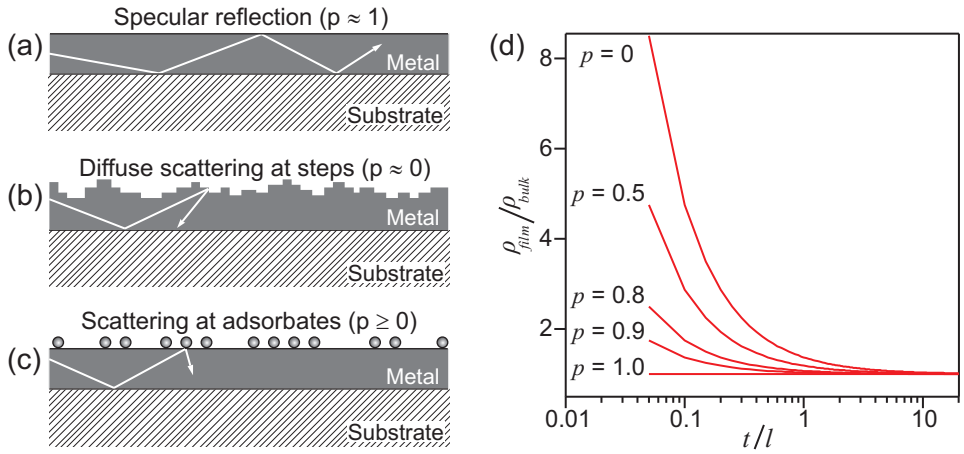

Figure 2.11: Scattering processes at different surfaces: (a) flat surface, (b) stepped surface, and (c) surface with adsorbates. p is a fraction of electrons, which are specularly reflected from the film boundaries (surface and interface). At the flat surface, the charge carriers are specularly reflected ($p = 1$) from the surface and the interface, resulting in no contribution to the film resistivity. However, at the rough surface and the surface with adsorbates, the carriers are scattered diffusely ($p < 1$), which enhances the resistivity of the film. (d) Thickness dependent resistivity curve of metallic films using the Fuchs-Sondheimer model (Eq. 2.65). Decreasing the specularity parameter p from 1 to its minimum 0, i.e., increasing the surface roughness from its ideal flat surface, the film resistivity increases significantly due to the increase of the diffuse scattering at the film boundaries [2].

where the Fermi-Dirac distribution function $f(E)$ is approximated by the step function

$$f\left(E\right) = \frac{1}{exp\left[\left(E - E_F\right)/k_{\mathrm{B}}T\right] + 1} \simeq \begin{cases} 1 & \left(E \leqslant E_F\right) \\ 0 & \left(E > E_F\right) \end{cases}. \tag{2.61}$$

$g(E_F)$ for 3D and 2D free-electron systems are given by

$$g\left(E_F\right) = \frac{1}{2\pi^2}\left(\frac{2m^*}{\hbar^2}\right)^{3/2} E^{1/2}, \ (3D) \tag{2.62}$$

and

$$g\left(E_F\right) = \frac{m^*}{\pi\hbar^2}, \ (2D) \tag{2.63}$$

respectively. The effective mass m^* is estimated from the curvature of the energy dispersion curves $E(k)$ of the conduction or valence band by

$$m^* = \hbar^2\left(\partial^2 E/\partial k^2\right)^{-1}. \tag{2.64}$$

2.5.2 Thin film resistivity and size effect

Except those scattering mechanisms as mentioned earlier, scattering at the film boundaries, i.e., surface and interface is even more important if the film thickness of metals is comparable to or smaller than the mean free path l. Various scattering mechanisms in the thin films are summarized in Fig. 2.11. When the surface of the thin film is changed from its ideal flat

surface to the rough surface, electrons are scattered additionally at the steps, increasing the scattering events, i.e., reducing the relaxation time τ. This phenomena causes a significant contribution in the film resistivity.

2.5.2.1 The Fuchs-Sondheimer theory

Calculation of the resistivity behavior of thin metal films considering those contributions was done with the help of the size-effect theory of Fuchs and Sondheimer [1, 2]. Using Boltzmann's transport theory, the authors concluded that the resistivity of a thin film with thickness t is given by the following forms:

$$\frac{\rho_{film}}{\rho_{bulk}} = 1 + \frac{3}{8t} l_\infty (1-p), \quad t \gg l \tag{2.65}$$

$$\frac{\rho_{film}}{\rho_{bulk}} = \frac{4}{3} \frac{(1-p)}{1+p} \frac{l_\infty}{t\, log\left(\frac{l_\infty}{t}\right)}, \quad t \ll l \tag{2.66}$$

where ρ_∞, l_∞ are the bulk values of the resistivity and mean free path. The phenomenological specularity parameter p describes the strength of diffuse scattering of conduction electrons at the film boundaries, i.e., at the surface and at the interface. Its value extends from 0, extremely rough, to 1, for the ideal flat surface and smooth interface (see Fig. 2.11(a)-(c)). The resistivity is extremely high for rough surfaces since p is close to zero due to the diffuse scattering at surfaces. With decreasing the roughness, the resistivity is also reduced, as long as the interface is smooth and abrupt. For a smooth surface and interface, the resistivity approaches close to bulk value because all the electrons are reflected specularly at the film boundaries and $p \sim 1$. In this case, the parallel momentum of the electrons will be conserved and the surfaces and interface will not contribute to the film resistivity.
The thickness dependent behavior of resistivity of metallic films has been summarized in Fig. 2.11(d). Resistivity is always higher for thin films, i.e., for $t < l_\infty$ because of finite roughness. With increasing film thickness, the resistivity decreases and approaches to bulk value as thickness exceeds the electron mean free path l_∞.

3 The Experimental Construction

In the following sections, the experimental setup of the UHV system, including some devices which have been used during this work, will be introduced. Special emphasis will be given to SPA-LEED, since it is the main experimental tool.

In the first section, the general UHV system will be discussed and the measurement principle of the SPA-LEED will be explained. The second section deals with the evaporators, which are used for growing solid films based on molecular beam epitaxy (MBE). In the third section, short notes about the sample preparation will be reported, especially about the preparation of Si(001) sample. An exclusive analysis about the fabrication of electric contacts will be presented in the fourth section.

3.1 The UHV system and SPA-LEED

A cross-section view of the standard UHV apparatus (made of stainless steel) is shown in Fig. 3.1, which includes a SPA-LEED system, a quadrupole mass-spectrometer, metal evaporators, and a low-temperature cryostat with special sample holder. After a long baking processes of the apparatus, a residual pressure of $\sim 2 \times 10^{-10}$ mbar is achieved. The partial pressure of various gases are examined by the mass spectrometer after each baking process and an average pressure is measured by an ion gauge, which helps to control the vacuum inside the apparatus during the experiment.

A prototype of the SPA-LEED device was developed by Prof. Dr. M. Henzler's group in the Institute of Solid state Physics, University of Hannover [**?**]. It can be operated in two different geometries in reciprocal space: a normal incidence geometry and a grazing incidence geometry. Besides that, a real space mode can also be operated, a so-called low resolution scanning electron microscopy (LRSEM) mode. In the following sub-sections, all three operational modes of the SPA-LEED system are discussed.

3.1.1 Normal incidence geometry

The major parts in this geometry include a fine focus electron gun, an entrance lens close to the sample, an electrostatic or magnetic deflection unit, and an aperture in front of a single electron channeltron detector. The system has also a phosphorous screen at a distance of 24 cm, which gives a quick overview of the diffraction pattern.

The resolution is given by spot size and the entrance slit in front of the channeltron. Small spot size can be obtained via a fine focus electron gun at low electron beam current conditions. Typical current settings range from 50 pA for high-resolution images up to 500 nA for visual

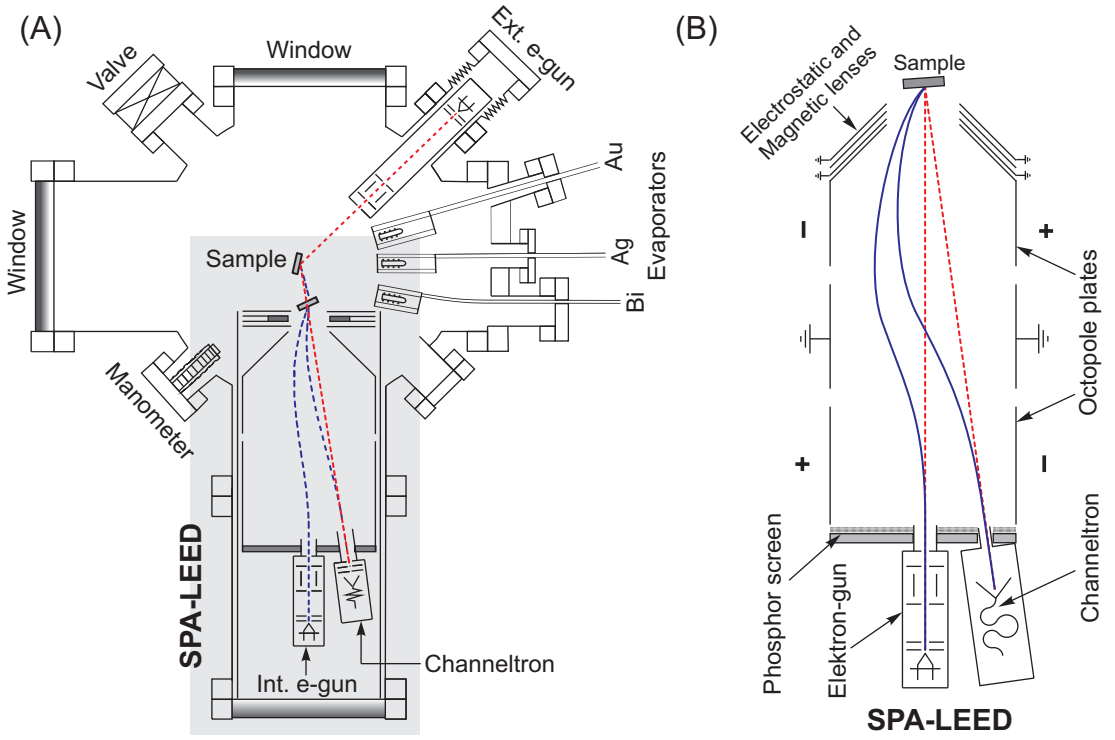

Figure 3.1: Cross-section view of the UHV system, including the SPA-LEED and MBE devices: (A) Experimental setup for the *in situ in vivo* experiments during deposition using an external electron gun in a RHEED-like geometry. All evaporators are directed towards the sample for deposition. (B) SPA-LEED system, where various parts such as the electron gun, the channeltron detector, the electrostatic deflection unit, the entrance lens and the sample are indicated. The electron beam path is shown with blue solid lines.

inspection with lower resolution. The electron energy can be varied from 5-500 eV during the operation. Either electron counts or the intensity can be adjusted via the filament current, the repeller, and the extractor, respectively. The electron beam is focused onto the channeltron aperture. The beam is deflected by applying the voltages via the octopole plates and finally collecting the beam onto the sample by using entrance lens (see Fig. 3.1(B) [42]. The reflected beam is again deflected and finally focused on the detector. The octopole plates are adjusted in such a way that no voltage is applied in the center. Such a way of deflecting the incoming beam and reflected beam changes the incident angle on the sample during the scan, keeping the angle between the incoming and outgoing beam constant $\sim 7°$. This provides a 1:1 imaging of the electron gun's crossover onto the detector, and causes a very small focus of 200-300 µm in the detector plane.

The reduction of spherical aberrations of the entrance lens could be obtained with a magnetic lens, which is integrated into the electrostatic entrance lens. Further reductions could be realized with a magnetic lens, which is integrated into the electrostatic entrance lens. The focus properties depend on the lateral sample position and the rotational orientation of the sample holder. Due to the insensitivity to the sample shape, the magnetic lens allows any sample position and sample holder. Additionally, the potentials of the electrostatic lens are affected due to the punch-through effect of the electrostatic field. This can be avoided by

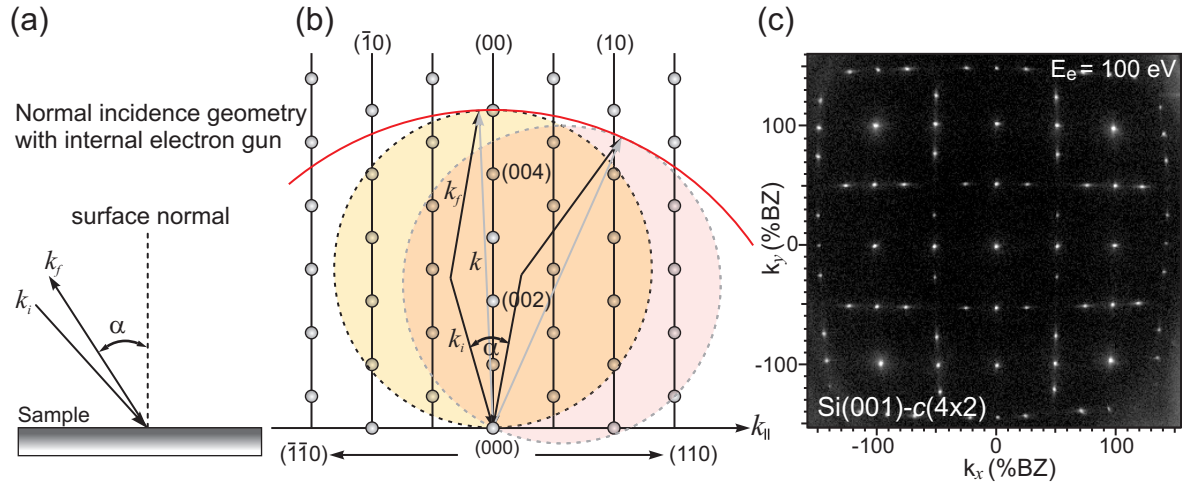

Figure 3.2: (a) Diffraction geometry in reciprocal space for the SPA-LEED in the internal electron geometry. Both the angle of the incident electron beam and of the diffraction pattern are varied continuously in order to record the LEED pattern. The relative angle between incident and final scattering vector stays constant. (b) The resulting diffraction pattern is described by the envelope of the rocking Ewald sphere, which is the sphere centered at the origin of the reciprocal space and a diameter twice the size of the Ewald sphere. (c) A LEED pattern of Si(001)-$c(4\times2)$ surface is shown, which is recorded in this geometry using an electron energy of 100 eV.

using magnetic lens.

As we have discussed earlier, the width of the focused electron beam in the detector plane defines the transfer width of the instrument

$$T = \frac{k_{01}}{\triangle k}\, a_0 \tag{3.1}$$

with $\triangle k$ the width of the beam, k_{01} the distance between fundamental spots and a_0 the atomic row distance at the surface. A larger transfer width results in a more intense but sharper peak, since the integral intensity stays constant. This has an advantage of getting better statistics in the data analysis and resolution.

There are two possibilities to record the data in a scanning mode: one is to record 2D LEED patterns and another is to record 1D profiles at a defined region in the reciprocal space. In the first mode, a set of electrostatic deflection voltages are used to continuously vary the angle of incidence of the electron beam in all directions at the sample position. A second set of plates keep the beam position on the sample constant, independent with the angle of incidence. Those deflection plates are arranged as a set of two octopoles in order to minimize field inhomogeneities in x and y directions (see Ref. [63] for details).

During scanning the incident angle of the electron beam simultaneously varies with the angle under which diffracted electrons from the surface are recorded. The angle between the incident k_i and final scattering vector k_f stays constant, i.e., 7°. In this case the incident angle is changed all the time, which makes the Ewald sphere rotate around the origin of reciprocal space. As a result, the diffraction pattern follows exactly the sphere with the origin at (000) and twice the diameter of the Ewald sphere. The schematic view of the geometry is shown

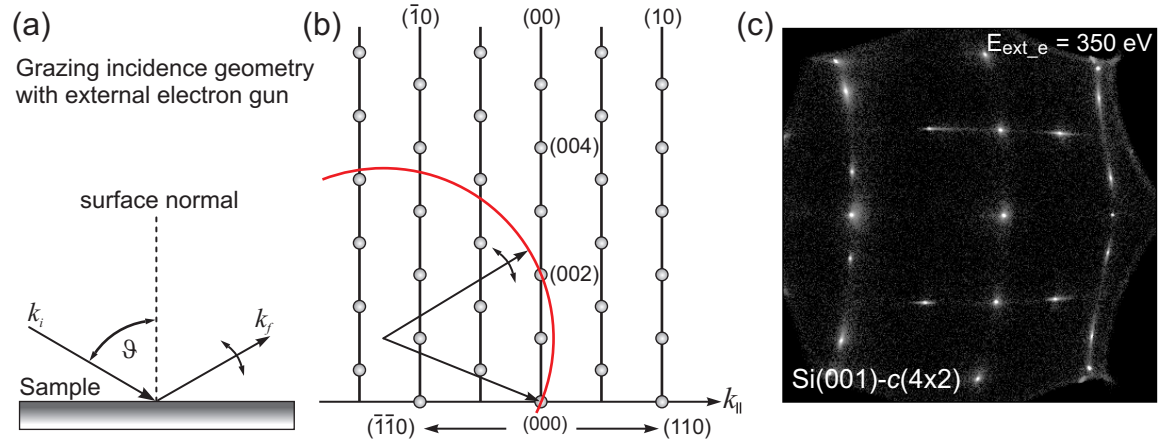

Figure 3.3: (a) Diffraction geometry in reciprocal space with the external electron gun in a RHEED-like geometry. (b) The diffraction pattern is scanned via following the Ewald sphere. (c) A LEED pattern of Si(001)-$c(4\times2)$ is shown, which is recorded in this geometry using an electron energy of 350 eV. The pattern is distorted due to the grazing incidence of $\sim 25°$.

in Fig. 3.2. The angle between the incident and final scattering vector stays constant and is determined by the geometric angle between gun and detector ($\alpha \sim 7°$ in this construction). The angle α is approximated by positioning the sample parallel to the lens via the deflection voltage U/E (deflection voltages U at the rear octopole normalized to the electron energy E):

$$\sin\alpha = a\left(\frac{U}{E}\right) + b\left(\frac{U}{E}\right)^2 + \mathcal{O}\left(\left(\frac{U}{E}\right)^3\right) \tag{3.2}$$

From the modified construction of the Ewald sphere, one can take the following relation:

$$k_{\parallel} = 2\,k_i \sin\alpha \tag{3.3}$$

with $E = \frac{\hbar^2 k_i^2}{2m_e}$. Assuming only the first term in Eq. 3.2, a further simplification can be achieved

$$k_{\parallel} = S_s \frac{U}{\sqrt{E}}. \tag{3.4}$$

The parameter S_s is known as *sensitivity*. For the constant electron energy, $k_{\parallel} \propto U$. This indicates the first order approximation of $\sin\alpha$ which works nicely at the center of the scan region, for small α. However, for large scan regions, i.e., when α is large, some distortions at the boundary are observed due to the non-linearity of U. Nevertheless, since the most interesting region is ±100 %BZ, the distortion is quite small and can be neglected.

In conclusion, SPA-LEED has a great advantage over the conventional 4-grid LEED, since a large area of reciprocal space is accessible to the measurement and largely increased the resolution. However, small barrel distortions of the pattern at the outer regions for a large scan area are caused by small non-linearity of the deflection unit, which could be corrected by remapping the recorded pattern.

3.1.2 Grazing incidence geometry

This mode of operation is often used to perform *in situ in vivo* measurements during adsorption or crystal growth experiments. Unlike in the first described mode, the normal incidence geometry, an external electron gun is used in a RHEED-like geometry with a larger grazing incident angle $(90 - \vartheta) \sim 20 - 30°$ as shown in Fig. 3.1. Despite a larger grazing incident angle, there is still enough space in front of the sample for evaporators. This kind of geometry produces diffraction spots, which are distorted due to the grazing projection of the diffraction rods on to the Ewald sphere (see Fig. 3.3). However, the k-space resolution $\frac{\triangle k_x}{k_{01}}$ along the grazing incidence direction is increased considerably as compared to the resolution $\frac{\triangle k_y}{k_{01}}$ in the y-direction [42]:

$$\frac{\triangle k_x}{k_{01}} = \frac{1}{\cos\vartheta}\frac{\triangle k_y}{k_{01}}, \tag{3.5}$$

Transfer widths of more than 200 nm can be achieved for Si surfaces.

One of the largest advantages of this mode of operation is the possibility to follow the (00)-spot or record the profile during the growth. The intensity curve and the recorded profiles provide information about the surface morphology during growth, which has been successfully applied in this work. However, due to the change of incident angle of the electron beam, the scattering phase also changes and has to be corrected to the following:

$$E_{ext}(\vartheta, S) = \frac{E_{int}(S)}{\cos^2\vartheta} \tag{3.6}$$

where ϑ is the angle between the incident electron beam and the surface normal.

3.1.3 Real space mode

It is possible in SPA-LEED that the direct image of the sample and the surrounding regions can be obtained via elastic and secondary electrons recorded with the channeltron detector. The voltages of the deflection plates are synchronized during the scanning of the electron beam over the sample. However, due to the large working distance ($\sim$ 30 mm) and beam cross-section ($\sim$ 0.5 mm), the image resolution is reduced. That's why it is also recognized as long distance low resolution SEM (LDLRSEM).

Despite the limited resolution, it has a great advantage to optimize the beam position on the sample and the best possible diameter of the beam, which are the important characteristics to enhance the resolution of the SPA-LEED. A typical real space image of the sample recorded in this mode is shown in Fig. 3.4. The Si(001) sample contacted with the molybdenum (Mo) clamps and the surroundings of the sample holder are clearly visible. The beam is focused on the sample by adjusting the (00)-spot in the middle of the sample.

3.2 Evaporators

Two kinds of evaporators were used for the evaporation of materials onto a substrate: thermal and electron beam evaporators. Since Bi has a low melting point ($\sim$ 545 K), direct heating

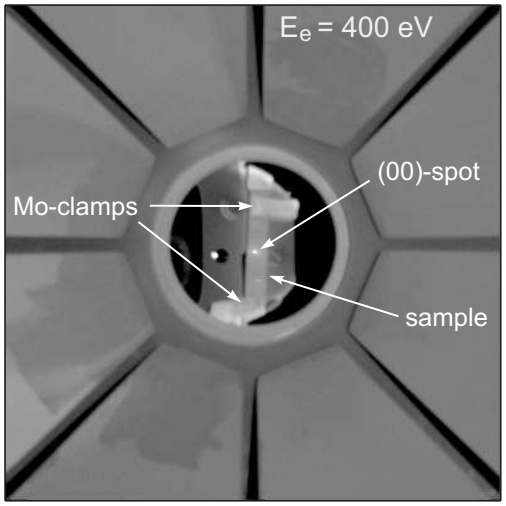

Figure 3.4: Real space image of the sample, sample holder and inner parts of the entrance lens obtained with the low resolution long distance SEM mode. The image is recorded by scanning the internal electron beam over the sample. The (00)-spot in the center of the Si sample is also visible in the image, which helps to optimize the beam position on the sample to find the best focus.

of the source via an electric current is sufficient to evaporate it. This is why a home built thermal evaporator was used to vaporize Bi. Materials such as silver and gold need more heat energy to evaporate them, due to their high melting points, and electron beam evaporators were used. A cross-sectional view of both types of evaporators are sketched in Fig. 3.5(a) and (b).

For Bi evaporation, a ceramic crucible was heated directly by passing the electric current via a thin tungsten filament ($\approx$ 0.15 mm diameter), which was wound around the crucible. The current through the filament was adjusted by monitoring the frequency change in the quartz microbalance, which was attached on the top of the evaporator.

For Ag and Au deposition, tantalum (Ta) and graphite crucibles were used, because of their very high melting points. Both source materials were evaporated by heating the crucible via an electron beam originating from the tungsten filament. Since high positive voltages (typically $\sim$ 1 kV) are applied to the crucible, electrons are accelerated from the filament to the positive pole, i.e., the crucible, and hit on the crucible surface. This process effectively heats the material. During evaporation, it is possible that ions are created along with neutral atoms, which may damage the substrate surface. To avoid the evaporation of ions, a metal plate is mounted between the crucible and the opening of the evaporator as shown in Fig. 3.5(b). Applying high voltage in the plate ($\sim$ 1 kV), the ions are deflected.

The sources in both evaporators were kept heated all the time to avoid adsorption or contamination with the materials. A small current ($\sim$ 1.2 A) (a little below the melting point) was continuously supplied in the filament for the Bi evaporator. For beam evaporators, small power ($\sim$ 3 Watt) was constantly applied. For both cases, crucibles were mounted in water-cooled copper shrouds, which allows to cool the evaporators. This also prevents possible contamination by the desorption of gases from the evaporators during the deposition process. It also prevents the melting of metallic joints of evaporators, which are used to join the capillaries for the construction of the evaporator. On top of the evaporator a shutter is attached, which allows to control the amounts of deposited material.

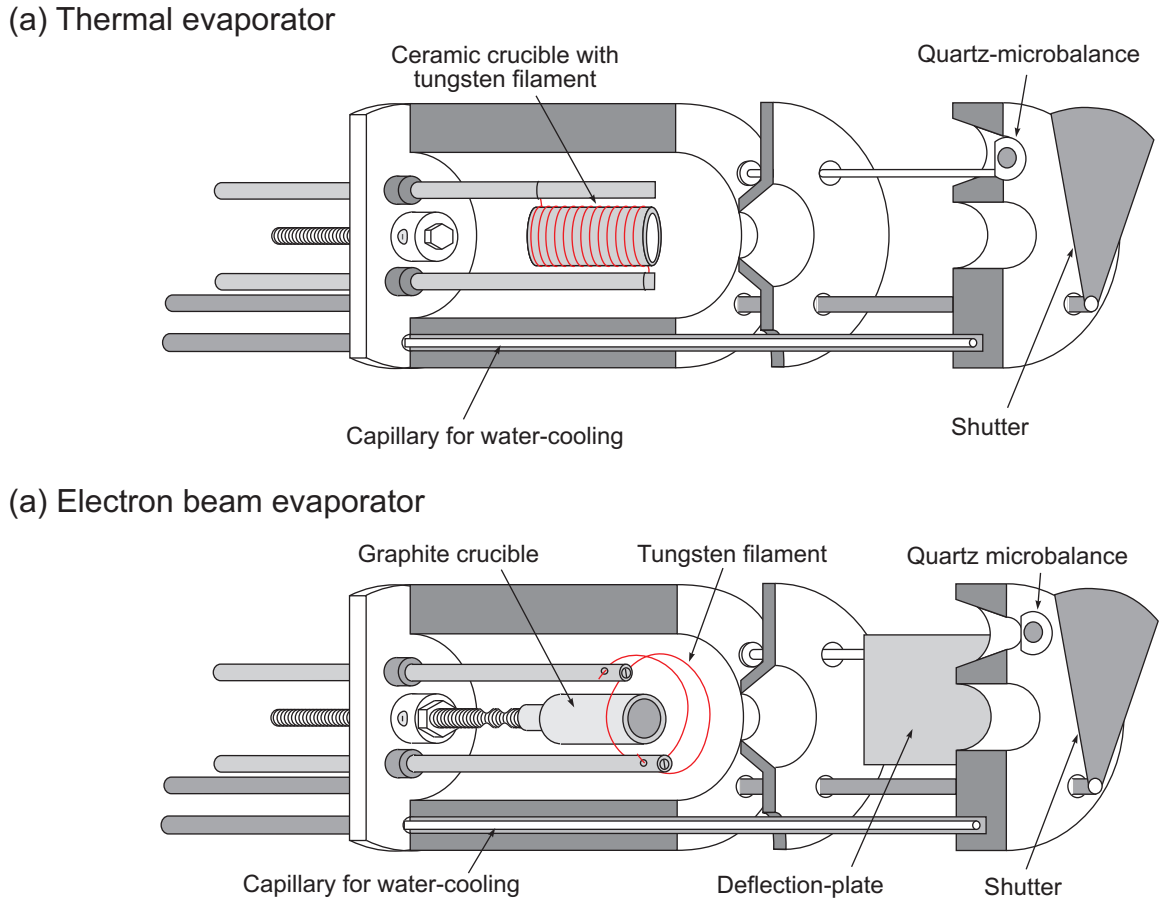

Figure 3.5: (a) Construction principle of a water-cooling thermal evaporator for Bi deposition. Bi is evaporated by passing the electric current via tungsten filament, which is wound around the ceramic crucible. A quartz microbalance is attached on the top of the evaporator for the thickness measurement. (b) Construction principle of a water-cooling electron-beam evaporator for Ag and Au deposition. These materials are evaporated by heating the crucible via electron beam bombardment. Electrons from the tungsten filament are accelerated towards the crucible due to the high positive voltage applied on it.

3.3 Sample holder and 4-point probe setup

A simple construction of the sample holder is schematically shown in Fig. 3.6. One end of the Si sample (dimension: $l = 3.5$ cm, $w = 0.4$ cm, $t = 500$ µm) is fixed with molybdenum (Mo) clamps, which is attached with Sapphire plate for electric isolation with copper block. The other end is suspended freely, and also contacted by a small Mo clamp. A free suspension of the sample has big advantage in getting rid of sample bending via stress caused by high temperature flash annealing. The other two small Mo clamps are also contacted at two positions of the sample at the middle. Silicide contacts (WSi_2) have been fabricated at those four positions for electrical contacts with Si surface or metals/semimetals deposited on it. Details of the silicide contacts will be described exclusively in chapter 6. In this way, those four contacts are used for electrical resistance measurements in a four point probe (4PP) setup: the outer two contacts are used for passing the very small constant currents ($I_{const} = 1^{-4} - 1^{-6}$ A) and the inner two contacts are used for measuring the change of voltage

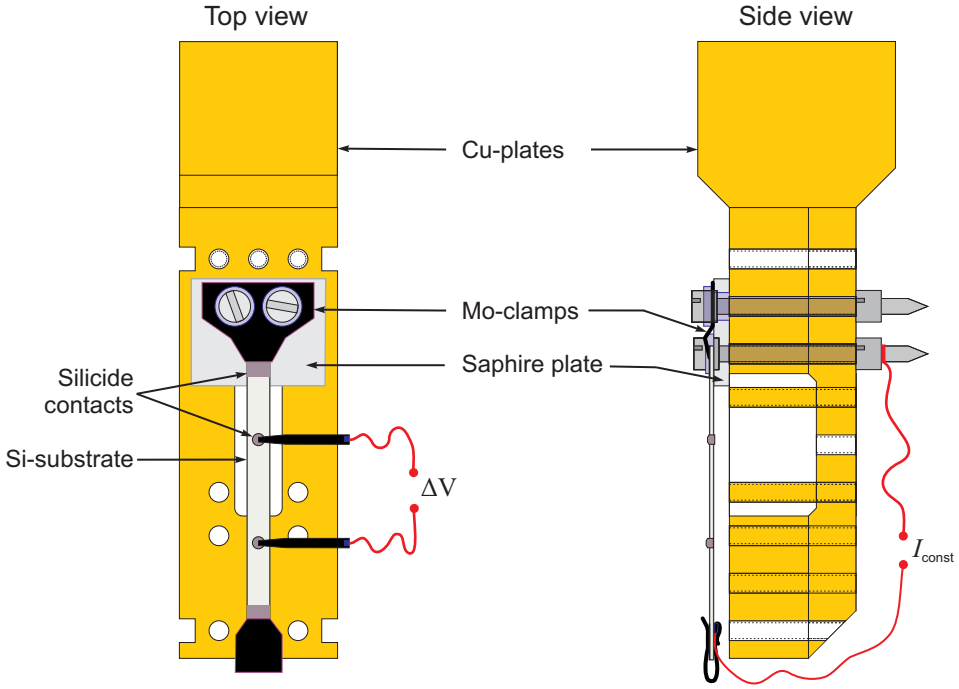

Figure 3.6: A simple schematic view of the sample holder with a Si substrate. The Si sample is contacted by silicide structures (WSi_2) at 4 different regions, which serve as electrical contacts in a 4PP setup. The outer two contacts are used to supply very small constant currents I_{const} and the inner two contacts are used to measure the potential difference $\triangle V$. The sample is attached on Cu plates for good thermal contacts.

V. Now, the resistance R will be converted from potential difference via $R = V/I_{const}$. During deposition or adsorption metallic/semimetallic/molecules on Si surface, the change of voltage between the inner contacts $\triangle V$ will be measured, and accordingly, the resistance change via $\triangle R = \triangle V/I_{const}$. This way of measuring the electrical resistance has a negligible contribution from contact resistance. Additionally, the silicide contacts, which are high quality and ohmic in nature, directly touch the grown film, so that makes it even more surface sensitive as compared to the two point resistance measurement method.

The outer Cu block is attached with cryostat, which is capable of cooling down to a few tens of kelvin via a continuous flow of helium or liquid nitrogen in a controlled manner. Since the sample is fixed with a sapphire plate, which is properly contacted with the Cu block, there is a very good thermal contact between the sample and the Cu block. A type-K thermocouple is connected nearby the sample on the Cu block. Thus, the actual temperature of the sample is believed to be within the error of ± 10 K. The accuracy of the sample temperature was also confirmed via studying the reversible order-disorder phase transition of the Si(001) sample from $c(4\times2)$ at a low temperature to (2×1) at high temperature. The transition temperature was determined to be $\sim$200 K, which is consistent with the previous works (see section 4.1.2.1 for details).

4 The Material System

This chapter gives a brief overview of the substrate material and the material used for the experimental investigation. Special emphasis is put on the atomic structure of clean Si(001) surface, which is used as a substrate to grow metallic/semimetallic overlayers. Since Bi is a central material of investigation, a short introduction about the crystallographic orientation of Bi crystal will also be given.

4.1 The Si(001) substrate

Si (atomic number 14) is a group IV element in the periodic system and has the electronic configuration $[Ne]3s^2 3p^2$. It crystallizes in a diamond lattice structure, which belongs to the face-centered cubic (fcc) space lattice. It can be constructed as two interpenetrating fcc sublattices with one sublattice displaced from the other by one quarter of the distance along the diagonal of the cube (i.e., a displacement of $\sqrt{3}/4$ along [111]) (see Fig. 4.1). In the lattice each atom is surrounded by four equidistant nearest neighbors that lie at the corners of a tetrahedron. Just like other group IV elements, each Si atom shares its four valence electrons with its four nearest neighbors, exhibiting the so-called sp^3-hybridization in a tetrahedral configuration with strong covalent bonds (angle between the bonds = 109° 28', bond length = 2.35 Å). Some relevant properties of Si are summarized in Table 4.1.

Clean Si is a semiconductor with an indirect energy band gap of $E_G = 1.12$ eV at room temperature and the band gap decreases with increasing temperature [64, 65, 66].

4.1.1 Si(001): surface reconstruction

Si(001) can be prepared by cleaving the Si crystal parallel to the {001} plane, which causes reduction of one bond per atom. Such unsaturated bonds are known as *dangling bonds*, which make the surface unstable and are responsible for an increase in the surface free energy. A

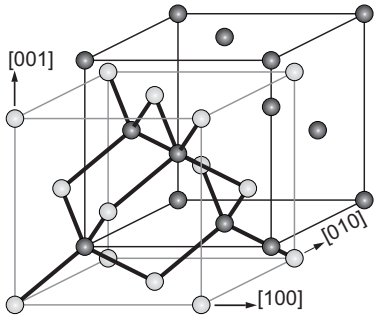

Figure 4.1: The schematic view of the diamond structure. The unit cell is composed of two fcc-lattices (shown with dark and light gray colors), which are shifted by $\frac{a}{4}$ along the cube diagonal [111]. Each atom is bonded by 4 neighboring atoms in a tetrahedral arrangement, which are shown by thick dark gray color lines within the unit cell. The structure resembles with the zincblende structure, if two of the fcc lattices are considered to be of different atoms.

Parameter	Symbol	Value
Lattice parameter	a_{bulk}	5.431 Å
Binding length	$r_0 = a_{bulk}\frac{\sqrt{3}}{4}$	2.35 Å
Row distance	$d_{(001)} = \frac{a}{\sqrt{2}}$	3.84 Å
(2×1) unit cell	$2d_{(001)} \times d_{(001)}$	7.68×3.84 Å
Step height (single)	$d_{001} = \frac{a}{4}$	1.36 Å
Step height (double)	$2d_{001} = \frac{a}{2}$	2.72 Å

Table 4.1: Frequently used structural parameters of Si(001) surface.

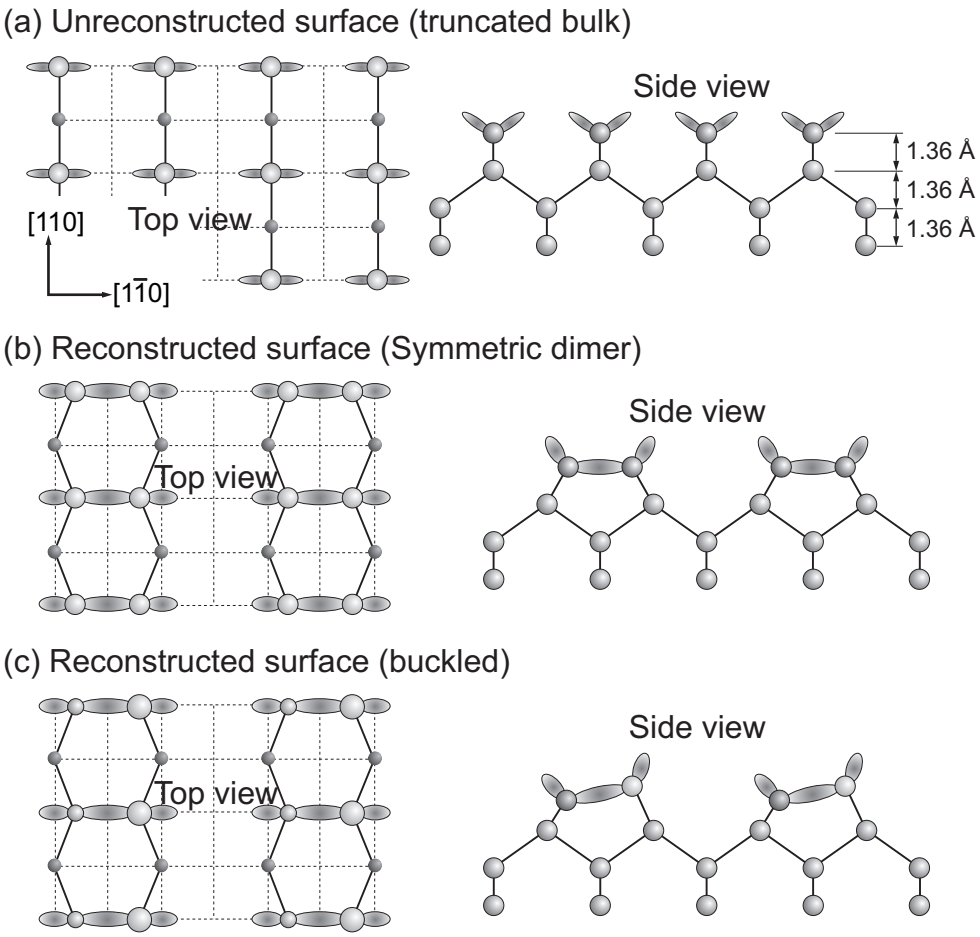

Figure 4.2: Truncated bulk of Si(001) surface: (a) unreconstructed surface, (b) reconstructed surface with symmetric dimers, and (c) reconstructed surface with buckled dimers.

reduction in the number of dangling bonds minimizes this energy and is the driving force behind the surface relaxation and reconstruction. The surface relaxation and reconstruction occurs via the displacement of atoms from their bulk positions. The surface relaxation does not change the surface periodicity or symmetry; however, the surface reconstruction does change via changing the surface unit cell parameter.

Figure 4.2(a) displays the crystal unit-cell with an unreconstructed (001) surface. As a result of energy minimization, two adjacent surface atoms form a dimer, which is the combination

Reconstruction	$\triangle E$/dimer
Si(001)-(1×1) ideal	
⇕	2 eV
Si(001)-p(2×1) Sym.	
⇕	0.2 eV
Si(001)-p(2×1) Asym.	
⇕	0.02 eV
Si(001)-p(2×2)	
⇕	0.002 eV
Si(001)-c(4×2)	

Table 4.2: A schematic representation of the energy differences between different reconstructions of the Si(001) surface [69].

of strong and weak bonds, labeled as σ and π bonds. The direction of the dimerization is predetermined by the orientation of the dangling bonds. Dimerization reduces the density of dangling bonds compared to a bulk terminated surface by a factor of 2, subsequently the surface unit cell is doubled in the direction of the dimer axis forming a (2×1) reconstruction [67, 68].

Due to the symmetry of the diamond lattice, the geometry of the surface of the truncated bulk structure towards the (001) direction is rotated by 90° with the surface of just one atomic layer below. This creates two 90° rotated domains from each preceding atomic layers, which are (2×1) and (1×2) reconstructions.

Details of the reconstructions are schematically shown in Fig. 4.3 and the energy difference per dimer for each reconstructed surface compared to the unreconstructed bulk truncated surface, i.e., (1×1) surface are summarized in Table 4.2. The (2×1) reconstructed surface has 2 eV less energy per dimer compared to the (1×1) surface; however, the energy difference between the (2×1) surface with symmetric configuration and the asymmetric configuration is only 0.2 eV. Chadi [70] has first proposed the asymmetric dimer model of the Si(001) surface. This is the most stable and widely supported by various experimental techniques such as LEED [71], XRD [72], low-energy ion scattering [73], STM [74], etc. However, some authors have also reported symmetric dimers in Si(001) surface [75]. Apart from an energy gain, the buckling of the dimer is accompanied with the formation of a semiconducting electronic band structure [70].

4.1.2 Si(001): structural phase transition

As discussed earlier, Si(001) surface undergoes a (2×1) reconstruction by the dimerization of outermost layer atoms and the energy gain involved in this primary reconstruction is quite strong, i.e., 2 eV. Further energy reduction is achieved via buckling of dimers (up and down). Ihm *et al.* [76] first predicted an order-disorder structural phase transition of the Si(001)

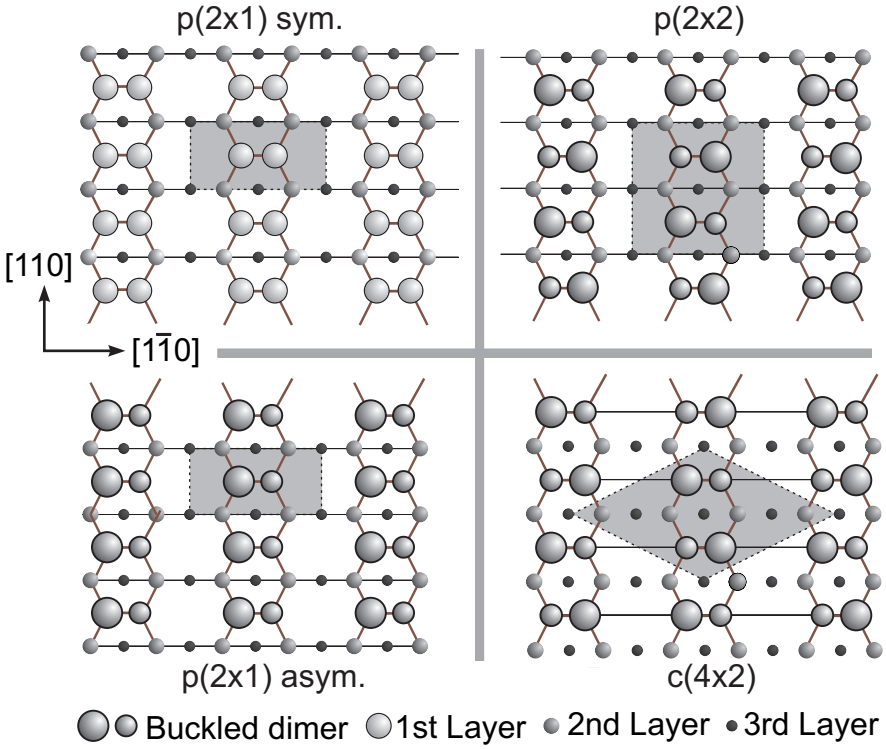

Figure 4.3: Reconstruction of clean Si(001) surface. Unit cells are shown with gray regions. $p(2\times1)$ is the high temperature ($>$ 200 K) reconstruction and the $p(2\times2)$ and $c(4\times2)$ are the low temperature ($<$ 200 K) reconstructions.

surface dependent with temperature and proposed low temperature phase $c(4\times2)$ or $p(2\times2)$ is the ground state of the system. The predicted phase transition has its origin in the disorder produced by a thermal flipping motion between the two possible tilted positions. According to the phase transition simulated by Saxena *et al.* [77] using an asymmetric dimer model representing the Ising system, the low temperature phase of $c(4x2)$ and $p(2x2)$ are the anti-ferromagnetic and layered antiferromagnetic phases, because the nearest neighbor dimers are oriented oppositely, and the $p(2x1)$ is the ferromagnetic phase, since the dimers are aligned. An overview of the dimer orientation at different phases of Si(001) are summarized in Fig. 4.3.

Over a wide temperature range a reversible order-disorder phase, i.e., $(2\times1)\leftrightarrow(4\times2)$ of the Si(001) surface was first observed by LEED via the measurement of spot intensity as a function of temperature [78]. Unlike the order-disorder transition in Ge(001), where the transition occurs at two stages 220 K and 260 K, the transition on Si(001) proceeds by a single step at 200 K without an intermediate phase. However, the transition temperature is strongly dependent on surface quality [79].

4.1.2.1 LEED analysis

The Si samples were cut into the specified dimension (35×3 mm^2) from the Si(001) wafers using a diamond cutter. The samples were cleaned by using isopropanol before transference

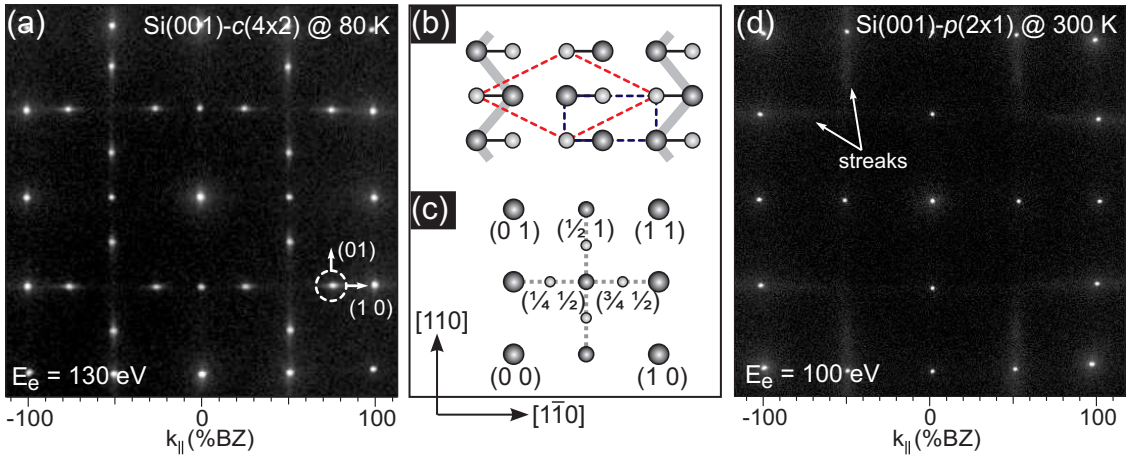

Figure 4.4: LEED patterns of Si(001)-$c(4\times2)$ and -$p(2\times1)$ reconstructions according to the buckled dimer model. (a) Si(001)-$c(4\times2)$ LEED pattern at 80 K. (b) Top view of the buckled-dimer model for Si(00l)-$c(4\times2)$. Paired large and small circles represent buckled dimers in the first atomic layer. A large circle indicates an atom slightly projected out of the surface. The dotted red color lines indicate a unit mesh of the $c(4\times2)$ structure. (c) Schematic LEED pattern from a two-domain Si(00l)-$c(4\times2)$ surface at low temperature. (d) LEED pattern of Si(001)-$p(2\times1)$ reconstruction at 300 K. Diffuse streak features, as indicated by the light Gray dotted lines in (c), were observed instead of the quarter-order spots.

into the UHV chamber.

The LEED measurement was performed at a base pressure of 2×10^{-10} mbar. The temperature dependence of the diffraction spots were obtained at constant incident electron energies of 110 eV. Before starting the measurement at 80 K, the sample was flash annealed to 1480 K. The spot profiles of the quarter order spot and the (00)-spot were recorded during the annealing process. It took about 30 minutes to anneal the sample from 80 K to 400 K. The measurement time was chosen to be short enough to ignore the electron beam irradiation effect on the surface [80]. This was checked by performing an experiment of the time-dependent change of the $c(4\times2)$ spot profile and there was found no significant difference in the shape and the intensity in the period of the 40 minutes of electron beam irradiation.

A typical LEED pattern measured at 80 K is shown in Fig. 4.4(a). The schematic view of the buckled dimer model for a $c(4\times2)$ structure and the corresponding LEED pattern are shown in Fig. 4.4(b) and (c), respectively. At 80 K, sharp and in one direction spots can be seen around the quarter order spots. As the sample is annealed, the intensities and the shape of the quarter order spots change. At temperatures above 200 K, the quarter order spots become weak and streaky, and become even weaker at 300 K. Since the width of a spot represents the degree of order of the corresponding structure, an analysis of the spot profile can yield information about the nature of the phase transition. Due to the asymmetric shape of the quarter order spots, the spot profile was analyzed along the two directions, along the streak, i.e., along (10) and across the streak, i.e., along (01) as indicated by arrows in Fig. 4.4(a). The width along the streak of a spot represents the ordering between the dimer rows and the width perpendicular to the streak represents the ordering in a dimer row, respectively. The larger spot width along the streak shows the ordering between the dimer rows is worse

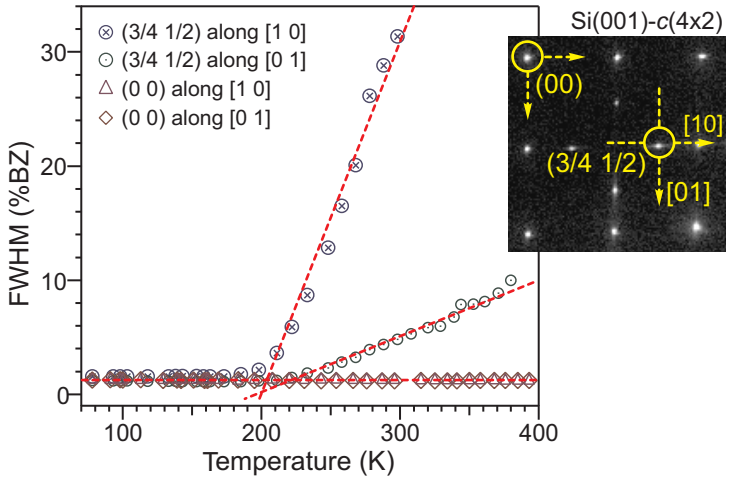

Figure 4.5: Temperature dependent FWHM of the quarter order spots and the (00)-spot of the Si(001)-$c(4\times2)$ surface. The widths are calculated along the [10] and [01] directions, i.e., along the streak and perpendicular to the streak, as shown by dotted lines in the inset. The dotted red lines are just a guide to eyes.

than the ordering in a dimer row. The spot profiles were fitted to a Lorentzian curve, and the full width at half maximum (FWHM) of a spot was determined from the fitting parameter. The temperature dependence of the FWHM for both spots, i.e., the quarter order spot and the (00)-spot, along both directions are plotted in the temperature range from 80 to 400 K (see Fig. 4.5). As the plot shows both widths of the quarter order spot increase abruptly above 200 K, however, the (00)-spot width remains unchanged, indicating an order-disorder $c(4\times2)\leftrightarrow p(2\times1)$ structural phase transition. The non-vanishing width of the quarter order spot suggests that the short range order exists even at 400 K. At room temperature, the LEED pattern of Si(001) shows a two-domain (2×1) reconstruction with noticeable streaks (Fig. 4.4(d)).

4.2 Bismuth

Bismuth (Bi) is a Group V semimetal and exhibits unusual electronic properties [6]. Fermi surface of Bi is highly anisotropic, which causes also the anisotropic effective mass. In particular, due to low Fermi energy (~25 meV) and small effective mass (~$0.001m_e$), it has a very long electron de Broglie wavelength ($\lambda_{el} \sim 30$ nm). These electronic characters make Bi a favorable material to study quantum size effect (QSE), which appears as an oscillatory behavior with film thickness in both resistivity and the Hall coefficient due to electron confinement phenomena as the film dimension becomes comparable to the electron wave length λ_{el}. Ogrin *et al.* [9] in their study of the magnetotransport of the bismuth thin films in 1966 produced the first clear experimental evidence for QSE in any solids. This was attributed due to the quasi-2D sub-bands passing across the Fermi level.

One important consequence of the QSE is the so-called semimetal-to-semiconductor (SMSC) transition [10]. The SMSC transition happens when the energy shift due to the quantum

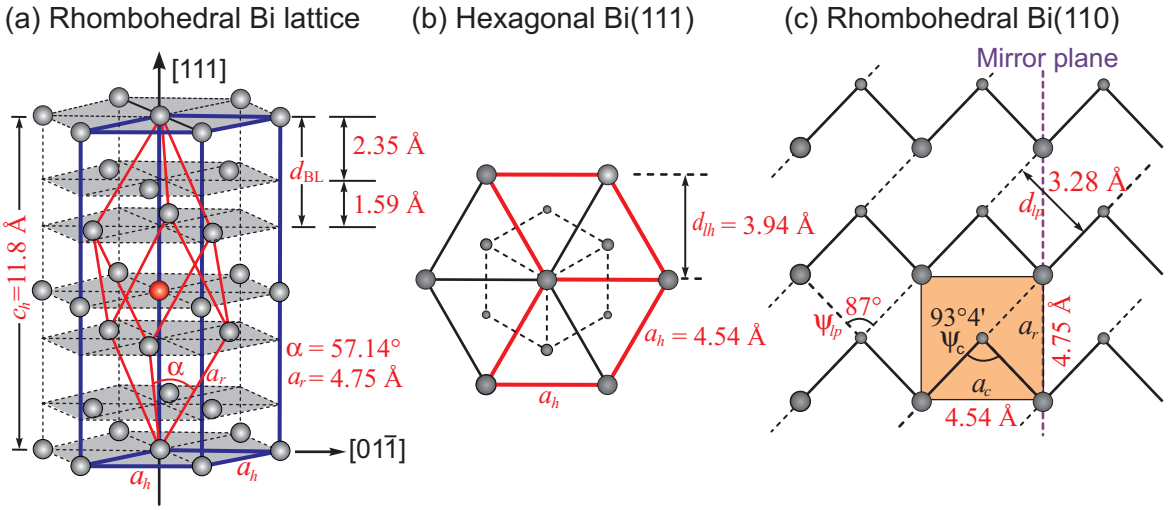

Figure 4.6: Crystal structure of Bi: (a) A 3D view of the rhombohedral unit cell (solid red lines) with rhombohedral axes a_r and the angle α together with the hexagonal unit cell (solid blue lines). The structure shows pairs of planes stacked in the c direction, i.e., along the [111] direction, as shown by gray colored hexagonal planes. The red solid lines show the distorted primitive cube as a rhombohedral unit cell. The gray and the red spheres mark the two atoms in the unit cell. (b) The Bi(111) surface: the red color solid lines indicate the hexagonal surface unit cell with a lattice parameter of a_h. Large and small spheres represent the atoms of first and second atomic layers. (c) The Bi(110) surface: the rectangle filled with the light orange color indicates the unit cell in a rhombohedral Bi(110) surface. The first two atomic layers are represented by large and small spheres, respectively.

confinement becomes large enough so that the lowest electron sub-band rises above the top of the highest hole sub-band, due to their different band masses. The critical thickness of the thin film for the transition to happen, given by most of the theoretical calculation, is between $\sim$ 230-340 Å (see Ref. [81] and other Refs. therein). However, no any clear evidence of sharp SMSC transition has been measured so far, so the existence of the SMSC transition still remains ambiguous. As pointed out by Hoffman *et al.* [81], the main reason for the absence of the sharp transition in the previous works is that people failed to take into account the effect of the surface carrier and surface conductivity, which may be important and even dominating when the Bi films are very thin. A recent study of spin-orbit coupling in Bi by Hirahara *et al.* [17] has also concluded that the highly metallic surface states in Bi(111) surface hinders the SMSC transition to be observed.

Nevertheless, all those intriguing properties of Bi are related to its peculiar crystal structure. Therefore, a detailed understanding of electronic properties requires a full knowledge of its geometrical structure. Additionally, the knowledge about the crystal structure of a solid is very important to understand the growth behavior in a heteroepitaxial system, since the apparent lattice mismatch at the hetero-interface affects the film quality via defect formation. In the case of Bi, which has an unusual crystal structure, an understanding of the crystallographic aspect is even more important and necessary. Therefore, a brief introduction of the real and reciprocal space structure of Bi in general, and the (111) surface in particular, will be discussed in the following section.

Rhombohedral	Hexagonal	Pseudo-cubic	Symmetry	LEED	Ref.
(110)	$(01\bar{1}2)$	(100)	m	1×1	[84]
(111)	(0001)	(111)	$3m$	1×1	[84]

Table 4.3: Indexing symmetry elements of the Bi crystal and the LEED patterns to be observed.

4.2.1 Structure

The crystal structure of bismuth (Fig. 4.6) has a rhombohedral symmetry (space group R$\bar{3}$m, A7-structure) with two atoms per unit cell, which is typical of the group V elements (As, Sb and Bi). This structure may also be considered as a slightly distorted cubic one. Such a Peierls-like distortion of a simple cubic structure results in the small overlap between the conduction and valence bands in the band structure of A7 structure materials such as Bi, Sb, and As [82]. Bi crystallize in this structure under common conditions and it can also be obtained in black phosphorus under pressure [83]. Each atom in the crystal forms three equidistant pyramidal bonds to its nearest-neighbors and three equidistant next-nearest neighbors slightly further away. The bonding between each atom and three nearest neighbors is strong and quasi-covalent and the bonding with the next-nearest neighbors is relatively weaker. This results in puckered bilayers of atoms perpendicular to the rhombohedral [111] direction, as shown in Fig. 4.6, where the intra-bilayer bonding is stronger than the inter-bilayer bonding. This explains why Bi crystals easily cleave along the (111) plane [84] and also grows in a (111) orientation in a bilayer fashion [35]. The bonding angles are close to 90°, suggesting that they are predominantly of p-bonding orbitals [84, 85]. The angle between the vectors spanning the rhombohedral unit cell is $\alpha = 57.14°$ and the ratio between the distance d_1 (distance from the topmost atom of the rhombohedral unit cell to the atom in the middle, as indicated by the red sphere in Fig. 4.6) to the distance d_2 is $d_1/d_2 = 0.88$. If $\alpha = 60°$ and $d_1/d_2 = 1$, the rhombohedral structure would be simple cubic [84]. The A7 structure has two atoms per bulk unit cell, corresponding to the two atoms in the bilayers. Alternatively, the structure can be described as a hexagon with six atoms per unit cell (Fig. 4.6(b)) or as a pseudo-cubic structure with one atom per unit cell [86].

For the surface structural analysis, it is always convenient to characterize the crystal structure as a hexagonal unit cell with unit vectors a_h, as shown by blue solid lines in Fig. 4.6(b). From the surface lattice parameter $a_h = 4.54$ Å, a row distance d_{lh} between each atomic row in a hexagonal plane can be deduced to be $d_{lh} = a_h \times \sin 60° = 3.93$ Å. A detailed description of the relation between those different unit cells can be found elsewhere [84, 86].

4.2.2 Indexing and symmetry

There are various recommendations about indexing the Bi crystal and each uses its own way of indexing to avoid confusion. Most often, in the literature, the indices are referring to either the rhombohedral unit cell, the hexagonal unit cell, or the pseudo-cubic unit cell (the face centered rhombohedral unit cell) [83]. Table 4.3 summarizes the indexing related to the

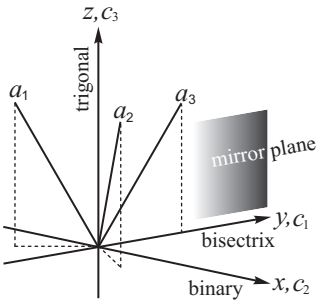

Figure 4.7: The rhombohedral lattice vectors and symmetry elements with respect to a cartesian coordinate system.

different lattices, the symmetry of the surface and the experimentally known LEED patterns. For simplicity, throughout this work, a rhombohedral indexing (hkl) is used to indicate the crystal orientation and referred to the hexagonal surface structure analogous to the fcc metals, which have hexagonal crystal structures, e.g., Ag(111) and Au(111).

Figure 4.7 illustrates the rhombohedral lattice together with the symmetry axes. In the rhombohedral indexing, the lattice is generated by three primitive vectors $(\vec{a}_1, \vec{a}_2, \vec{a}_3)$ of equal lengths a_r and angle α between any pair of the primitive vectors [87]. The two basis contains two atoms that are located at $\pm u(\vec{a}_1 + \vec{a}_2 + \vec{a}_3)$. In contrast, the hexagonal lattice is generated by three primitive vectors $(\vec{a}_{h1}, \vec{a}_{h2}, \vec{c})$, where $\vec{a}_{h1}$ and $\vec{a}_{h2}$ have an equal lengths a_h, and a 6 basis atoms are located at the positions: $(0, 0, u)$, $(0, 0, -u)$, $(\frac{1}{3}, \frac{2}{3}, \frac{2}{3} + u)$, $(\frac{1}{3}, \frac{2}{3}, \frac{2}{3} - u)$, $(\frac{2}{3}, \frac{1}{3}, \frac{12}{3} + u)$, and $(\frac{2}{3}, \frac{1}{3}, \frac{12}{3} - u)$. Both rhombohedral and hexagonal parameters are summarized in Appendix 10.2.

There are some electronic properties of Bi, which are directly related to the symmetry of its crystal structure. The basic symmetry elements of the Bi crystal is briefly described by the sketch shown in Fig. 4.7.

- The trigonal axis: the axis between the rhombohedral vectors, which has three-fold symmetry along the [111] direction.
- The binary axis: the axis is perpendicular to (c_3).
- The bisectrix axis: the axis is perpendicular to (c_3) and (c_2).
- The mirror plane: the plane is suspended by the trigonal and the bisectrix axes is a mirror plane.
- Inversion symmetry.

One of the most important consequence of the symmetry elements in the Bi crystal is that the inversion symmetry is broken at the surface because the trigonal axis has three-fold symmetry, and the binary and bisectrix axes will exist three times. This consequence leads to the spin–orbit splitting effects in Bi surface states [86].

5 The Model of Epitaxial Growth

This chapter deals with some fundamental aspects of the epitaxial growth, which are important in understanding the results obtained during homo- and heteroepitaxial growth of thin metal films. A well-known thermodynamic model of crystal growth will be discussed in the beginning and the atomistic description will be given in the preceding section. A derivation of the surface diffusion barrier will be presented applying the nucleation theory in the homoepitaxial system.

5.1 The thermodynamic model

In this model, epitaxial growth is considered to occur in thermodynamic equilibrium. Suppose a film f grows epitaxially on a substrate s, the form of the film crystal is defined via the minimization of the surface free energy of the crystal. The total change of the surface free energy $\triangle\gamma$ in the system is given by the contribution of three surface free energies, i.e., film γ_f, substrate γ_s, and the interface γ_i as

$$\triangle\gamma = (\gamma_f + \gamma_i) - \gamma_s \tag{5.1}$$

Considering that there is no chemical reaction or alloying at the film substrate interface, or other changes, which could be due to electron bombardment or dissociation during the film growth, three different basic growth modes are categorized in the epitaxial system [88, 89]:

- **Volmer-Weber (VW) or 3D/island growth mode**

If $\triangle\gamma > 0$ or the surface free energy of the film γ_f is large compared with that of the substrate γ_s, the adatom-adatom interaction is stronger than those of the adatom with the substrate

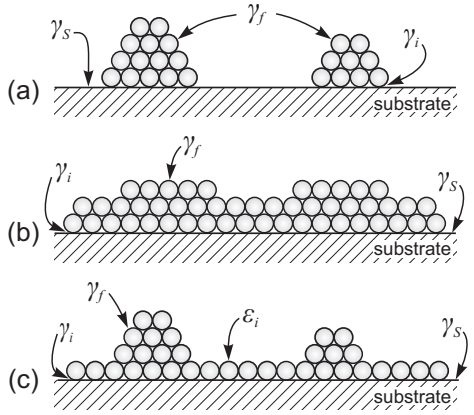

Figure 5.1: Cross-section views of three primary growth modes in epitaxial system: (a) Volmer-Weber or 3D/island growth, (b) Frank-Van der Merwe or layer-by-layer growth, and (c) Stranski-Krastanov or island plus layer growth. Surface free energies of three different contributions, i.e., film, interface, and substrate are indicated by the symbols γ_f, γ_i, and γ_s, respectively. An additional component due to the strain is symbolized by ε_i.

surface. In this case, the system favors growing 3D islands on the substrate, eventually causing multilevel roughness on the surface (see Fig. 5.1(a)). Most heteroepitaxial systems at high temperature follow this kind of mode.

- **Frank-van der Merve (FM) or layer-by-layer growth mode**

If $\triangle\gamma < 0$ or the surface free energy of the substrate γ_s is large compared with that of the film γ_f, the interaction of adatoms with the substrate surface will be stronger than the interaction among themselves. This situation helps adatoms to attach preferentially to surface sites resulting in atomically smooth and continuous layers (see Fig. 5.1(b)). The next layer starts after completing the first layer, following a 2D growth or layer-by-layer growth. This mode mostly occurs in the homoepitaxial systems.

- **Stranski-Krastanov growth mode**

This is an intermediate growth process characterized by both 2D layer and 3D island growth. In the lattice mismatched heteroepitaxial system, there is always a possibility of formation of strain fields at the interface. This causes an additional energy term in Eq. 5.1

$$\triangle\gamma = (\gamma_f + \gamma_i) - \gamma_s + n\varepsilon_i \tag{5.2}$$

where ε_i is the free energy per layer of the strained layers and n is the number of layers. Until some layers, i.e., critical coverage, which depends on both the surface free energy and the lattice mismatch, the condition $\triangle\gamma < 0$ favors the layer-by-layer growth on the substrate surface. Beyond the critical coverage, as the film relaxes towards the bulk lattice parameter, the condition $\triangle\gamma > 0$ favors the 3D island growth on the strained film (see Fig. 5.1(c)).

5.2 Atomistic processes

Although primary growth modes, as discussed in the previous section, have been defined considering the system at thermodynamic equilibrium, kinetic properties also play an important role in epitaxial growth. Considering the kinetic properties, atomistic processes of epitaxial growth have been explained by various authors [90, 91, 92, 93, 94]. Some relevant processes and the entities are summarized in Fig. 5.2.

Once atoms are deposited onto a perfect substrate surface, the evolution of growth front starts via these entities. These deposited atoms (adatoms) gain kinetic energy E_{kin} as they approach the surface due to the cohesive energy of the substrate atoms. The excess energy is dissipated once adatoms collide on the surface atoms, to balance themselves below the adsorption energy E_a. However, the kinetic energy gained during adsorption is sufficient for an adatom to diffuse over the terrace or along the step edge. The rate of diffusion or the jump rate of diffusion of an adatom across the terrace is defined by the activation barrier E_d for surface diffusion, which depends on the substrate temperature being a thermally activated process [95]. If the diffusion length is sufficient to meet the steps or existing large islands,

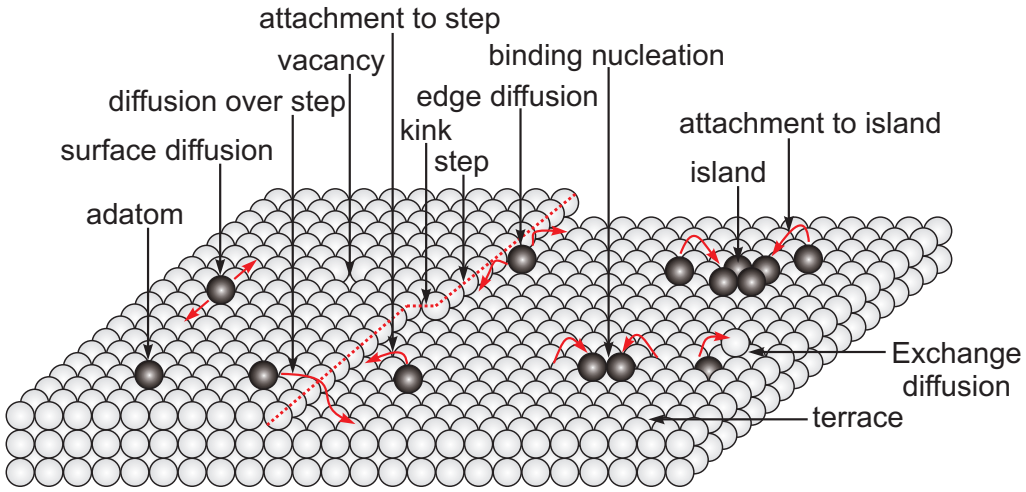

Figure 5.2: Several elemental entities and typical atomistic processes during epitaxial growth. The gray spheres represent atoms of the substrate. The red line shows the location of a step separating the upper and the lower terraces, with the kink along the step. The dark spheres are the atoms adsorbed on the terraces, which run from the left to the right.

they can attach to them; this is the so-called heterogeneous nucleation. However, to reach the steps or large islands, they need to cross large distances. In this case, before reaching to the steps or existing islands, they can nucleate with other adatoms and form a new island on the terrace, either so-called binding nucleation or homogeneous nucleation, characterized by the binding energy of E_b. Similarly, an adatom can also diffuse over the step, if it has sufficient energy to overcome the step edge barrier (*Ehrlich-Schwoebel* step edge barrier). There is also the possibility that small islands are not stable and can dissociate or coalesce to form a stable island. The island which has been initially formed, at defect sites, such as steps, or on the perfect terrace, are not necessarily in their most stable configuration and can re-arrange in different ways such as a mixing of species (alloying), shape changes caused by (surface) diffusion and/or coalescence, annealing of defects, etc. For example, in Pt/Pt(110) [96] and W/Ir(110) [97], adatoms show exchange diffusion with the substrate atoms.

The origin of the terrace diffusion barrier E_d and *Ehrlich-Schwoebel* step edge barrier E_{es} depend not only on the materials of the substrate and the adsorbate but also on the local structure, e.g., an adatom at the kink position attaches more strongly than at the terrace. Sometimes, the barriers can be reduced via various methods such as hindering diffusion along island edges by impurities, increasing island density during growth, increasing the adatom mobility on growing islands, etc. [93]. These methods can be applied through the appropriate manipulation of growth parameters. One particular example of appealing approach is the deliberate introduction of the right type of impurity—a surfactant. So, in all aspects, diffusion barriers are the basic parameters for overall growth processes.

5.2.1 The adatom diffusion and the diffusion barrier

The surface diffusion defines the migration of an adatom as a 2D random walker on the lattice of preferential adsorption sites. For 2D diffusion (for the case of hexagonal lattice), it can be

described by the diffusion coefficient D ((in unit cells per second) as:

$$D = \frac{1}{6}a^2\nu \tag{5.3}$$

where ν is the number of random hops made in unit time and a is a length of hop (normally equal to the surface lattice parameter). During the process of random walk the adatom passes over a saddle point in configuration space separated by the energy barrier E_d. This situation considers a random hop to follow the Arrhenius law for thermally activated processes [55],

$$\nu = \nu_0\, exp\left(\frac{-E_d}{k_\mathrm{B}T}\right) \tag{5.4}$$

where ν_0 is the pre-exponential factor, often referred to the attempt frequency, k_B denotes the Boltzmann constant. The attempt frequency ν_0 is the temperature independent quantity (to a very good approximation), and relates for surface diffusion with the vibrational frequency (surface phonon frequency) of the adatom in its binding site, being of the order of 10^{12} s^{-1}. This is why the attempt frequency ν_0 is a measure for the time scale of the dynamics within an adsorption well. Combining Eq. 5.3 and Eq. 5.4, the diffusion coefficient D can be expressed by E_d and ν_0 as [98]:

$$D = \frac{1}{6}a^2\nu_0\, exp\left(\frac{-E_d}{k_\mathrm{B}T}\right) = D_0\, exp\left(\frac{-E_d}{k_\mathrm{B}T}\right) \tag{5.5}$$

where $D_0 = \frac{1}{6}a^2\nu_0 a^2$, is known as the prefactor of the diffusion coefficient D.

The intra-terrace diffusion barrier is estimated by rate equations, developed by J. Venebles [91]. For the derivation of these rate equations, the growth process is divided into three kinetic regimes as a function of coverage Θ: nucleation, island growth, and island coalescence, respectively.

At the very beginning of the growth, the adatom density increases with the coverage Θ. It continues until either the stable nuclei are formed or the adatom separation becomes comparable to the adatom diffusion length. This regime is known as the nucleation regime, where the adatom density attains its maximum. Then, it suddenly drops after further increasing the coverage, because the adatoms are trapped by existing islands, which behave like a sink. In this aggregation regime (island growth regime), the system is in a quasi steady-state, which continues up to the coalescence regime, where islands touch each other and merge. Upon further deposition, the island density n_x ultimately reduces to zero as the first layer is completed.

Under the assumption of complete condensation (i.e., re-evaporation is negligible) for 2D islands and homogeneous nucleation, the classical nucleation theory based on a rate-equation approach predicts a power law relationship of island density n_x, depending on the deposition rate (flux) r and the deposition temperature T, in the aggregation regime as [90, 91, 92]:

$$n_x(r,\, T) \propto r^p\, \exp\left(\frac{E_n}{k_B T}\right), \tag{5.6}$$

where E_n is the characteristic energy and k_B is the Boltzmann constant. The parameter p is

a scaling parameter, which is determined by the number i of adatoms required for the stable nuclei. The parameters p and E_n are given by:

$$p = \frac{i}{i+2}, \; E_n = \frac{E_i + iE_d}{i+2}, \tag{5.7}$$

Here, E_i is the binding energy of an atom within the critical nucleus, and E_d is the intra-terrace diffusion barrier. Assuming that the size of the critical nucleus is one, i.e., $i = 1$, which corresponds $E_i = 0$, Eq. 5.6 can be simplified to

$$n_x(r, T) \propto r^{\frac{1}{3}} \exp\left(\frac{E_d}{3k_BT}\right). \tag{5.8}$$

For the submonolayer quasi steady-state regime, where the island size grows with coverage [99], the average island separation depends directly on the island density via $\langle L \rangle \sim n_x^{-\frac{1}{2}}$ [100], For a constant deposition rate for each deposition temperature, the rate-equation in Eq. 5.8 can be rearranged as:

$$\langle L \rangle \propto \exp\left(-\frac{E_d}{6k_BT}\right). \tag{5.9}$$

From the Arrhenius plot of Eq. 5.9, the intra-terrace diffusion barrier E_d can be determined.

6 Contacts for Electrical Conductivity Measurements

This chapter will report a method of fabricating thermally stable tungsten disilicide (WSi_2) contacts, which are used to measure the surface and the film resistance in a 4PP setup. Fabrication procedure, morphology characterization, and the electrical measurements will be presented. Finally, the experimental results are discussed exclusively.

6.1 WSi_2 contacts

Metal silicides on silicon have been widely studied because of low resistivity and process compatibility for fabricating semiconductor devices [101, 102]. Among them, the refractory metal (e.g., vanadium, molybdenum, and tungsten) silicides have drawn special attraction to engineers and researchers because of their high-temperature stability and low resistivity in comparison with doped polycrystalline silicon [103]. In particular, tungsten silicides (WSi_2) have become increasingly useful for contacts and gate electrodes, because they also solve the problem of the gate-depletion phenomena in metal-oxide-semiconductor field-effect transistors (MOSFETs) [104].

Besides these technological aspects, high-quality contacts are equally useful for basic research purposes such as the *in situ* measurement of surface or ultra-thin-film resistivity. However, such measurements demand stable contact areas that are compatible with the specific requirements of surface science. In general, the contacts must be ultra-high-vacuum (UHV) compatible, form an ohmic contact with the surface layer, exhibit a low resistance and withstand various preparation procedures. In the case of Si as a substrate, the contact must be thermally and mechanically stable up to flash-annealing temperatures, i.e., 1500 K, without contaminating the remaining Si surface. There has been a concern in the surface science community that silicide contacts are not stable after repeated flash-annealing cycles of the silicon samples. Most of the metals diffuse across the surface due to their high diffusivity (such as Co, Mn, Fe, Cr) and most of them generate defects on the surface (e.g., Ni causes ordered missing dimer defects on the Si surface) [105]. Titanium silicide exhibits very good electrical conductivity, but still has the disadvantages of high-temperature processing limitations [106, 107]. To overcome these problems, tungsten offers an alternative.

There have been several techniques proposed so far to fabricate WSi_2 films on Si. These include: sputter deposition of WSi_2 on silicon [103], reacting tungsten with silicon at high temperatures [108, 109], ion-beam synthesis [110], low-pressure chemical vapor deposition

(LPCVD) [111], and co-deposition from separate sources for metal and Si [112]. However, all these processes have some complexity to achieve low-resistivity contacts that are stable up to 1500 K. Therefore, a simple technique of fabricating contacts, which are stable up to such high temperatures, would be extremely helpful to basic research and the technological aspects, as well.

In the following, a simple recipe for fabricating thermally stable WSi_2 contacts on Si(001) substrates are reported. Those contacts are compatible with classic surface-science sample preparation, i.e., high temperature flash annealing under UHV-conditions without W diffusion or contamination of the area surrounding the contacts. Additionally, the contacts do not affect the surface structure and surface physics. The surface morphology of the WSi_2 contacts and the Si(001) surface are analyzed by *in situ* spot-profile-analyzing low-energy electron diffraction (SPA-LEED) and *ex situ* scanning electron microscopy (SEM), respectively. Additionally, the change of surface morphology of the silicide structure and the surrounding regions of Si are studied by *in situ* low-energy electron microscopy and photo-emission electron microscopy (LEEM/PEEM). The reliability and the quality of the contacts are tested by the resistance measurements of a clean Si(001) substrate under UHV conditions by using a four-point probe (4PP) setup.

6.1.1 Fabrication procedure

The WSi_2 contacts were fabricated in a two-step process (see Fig. 6.1(i)−(iii)): the deposition of W on a native oxide of a Si(001) substrate (boron-doped, resistivity=8−12 Ω-cm, miscut $< 0.2°$, and dimension: l = 3.5 cm, w = 0.4 cm, t = 500 µm) under high-vacuum conditions (base pressure below 1×10^{-7} mbar), followed by subsequent annealing up to 1500 K under UHV conditions (base pressure below $2{\times}10^{-10}$ mbar). A shadow mask was used to define contact regions on the sample for the resistance measurements. For the deposition, a tungsten wire (with a material purity of 99.98 % and dimensions: length = 6 cm, diameter = 0.015 cm) was placed at a distance of 6 cm from the sample and a current of 4 A was supplied until the wire burned out due to the sublimation of W. A homogeneous film of W as shown in Fig. 6.2(a) resulted from the deposition. *Ex situ* atomic force microscopy (AFM) measurements show that under these deposition conditions, the film is 30 nm thick. The actual overall shape of the sample with contact regions is shown in Fig. 6.2(c).

After the deposition process, the sample was transferred into the UHV chamber and annealed at 1000 K for 5 hours, as a first and very important step. The native oxide of the Si surface was then removed by flash annealing to 1500 K for only 3 seconds. This preparation results in a clear (2×1) LEED pattern at room temperature (only at the area where no tungsten was deposited). After cooling to 80 K, the (2×1) reconstruction undergoes the structural phase transition into a $c(4{\times}2)$ reconstruction [70, 78, 113]. It is well known that the $c(4{\times}2)$ reconstruction is extremely sensitive to the surface defects or contamination since the correlated buckling of Si dimers is destroyed by defects [114, **?**, **?**, **?**]. Small traces of metal, especially in the case of W, with a density as low as $6{\times}10^{12}$ atoms/cm^2, transform the

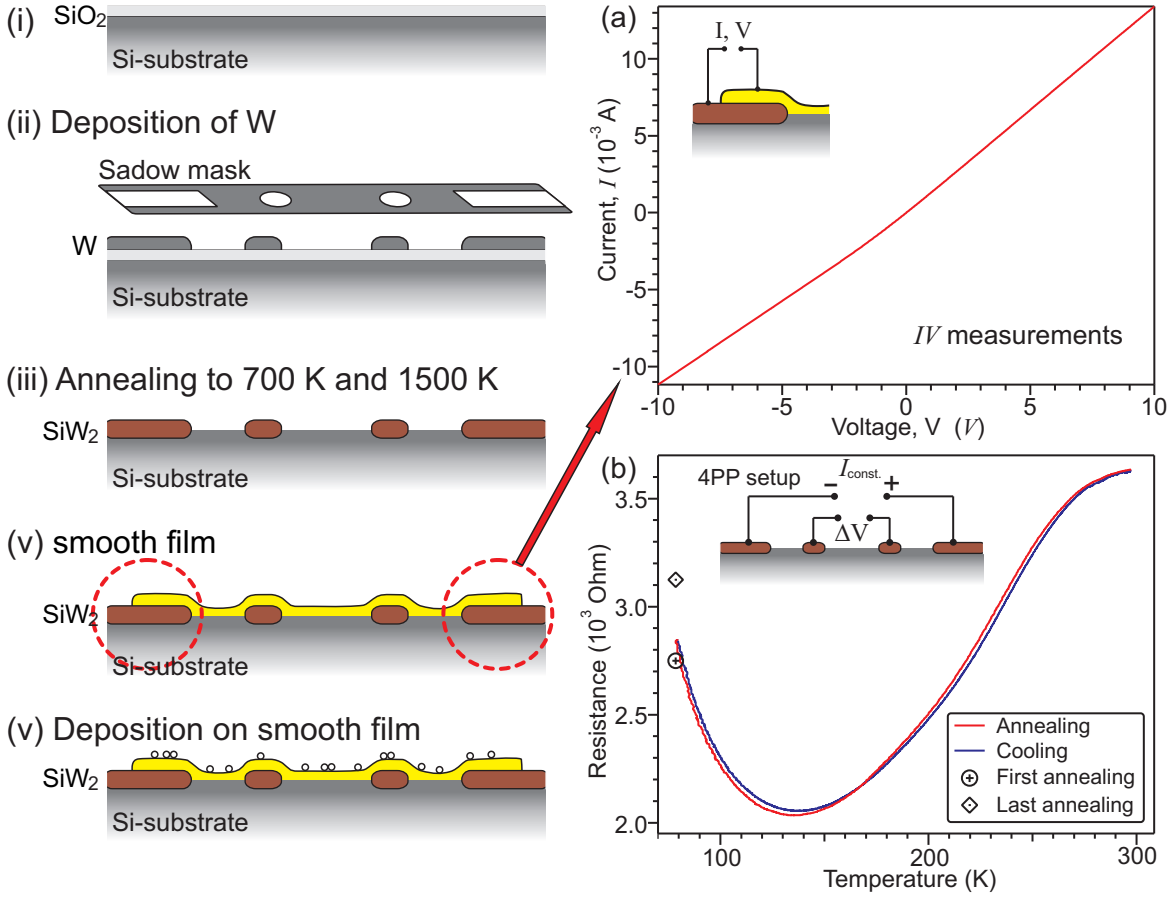

Figure 6.1: Fabrication processes and electrical characterization of WSi_2 contacts: (i) Si(001) sample with native oxide, (ii) deposition of W on the defined regions on the sample using a shadow mask, (iii) sample after annealing to 1500 K, (iv) material deposition on top of the silicide and clean Si(001) surface, (v) additional deposition of materials (low coverage) at low temperatures, (a) current-voltage (IV) measurements between the contacts and the metal layer at RT, and (b) Resistance of the Si(001) sample measured by using the contacts in a 4PP setup.

surface from (4×2) reconstruction to a (2×n) phase, where n is the periodicity length of the missing Si dimers [**?**]. This fact clearly suggests that the bare part of Si(001) surface is free of contamination, at least beyond the upper limit given by Ref. [**?**].

To verify that the contacts are stable at high temperatures, the sample was repeatedly flash annealed to 1500 K. *In situ* SPA-LEED [**?**, 42] measurements were performed to study the surface morphology after the annealing processes. *Ex situ* SEM measurements were performed to study the morphology after several flash-annealing cycles. Furthermore, the long-term reliability of the contacts was verified by measuring the resistance of the Si substrate, using the WSi_2 contacts in a 4PP technique.

The change of morphology during the silicide formation was studied under UHV conditions by IBM's first-generation LEEM/PEEM prototype [115]. A sample (dimension: 6×6 mm^2) with an array of W structures (Fig. 6.3(a)) was prepared by following the same procedure as before and inserted into the microscope. To fabricate an array of microscopic W patches (Fig. 6.3(a)) on the sample, a silicon nitride (Si_3N_4) shadow mask with dimensions below 100

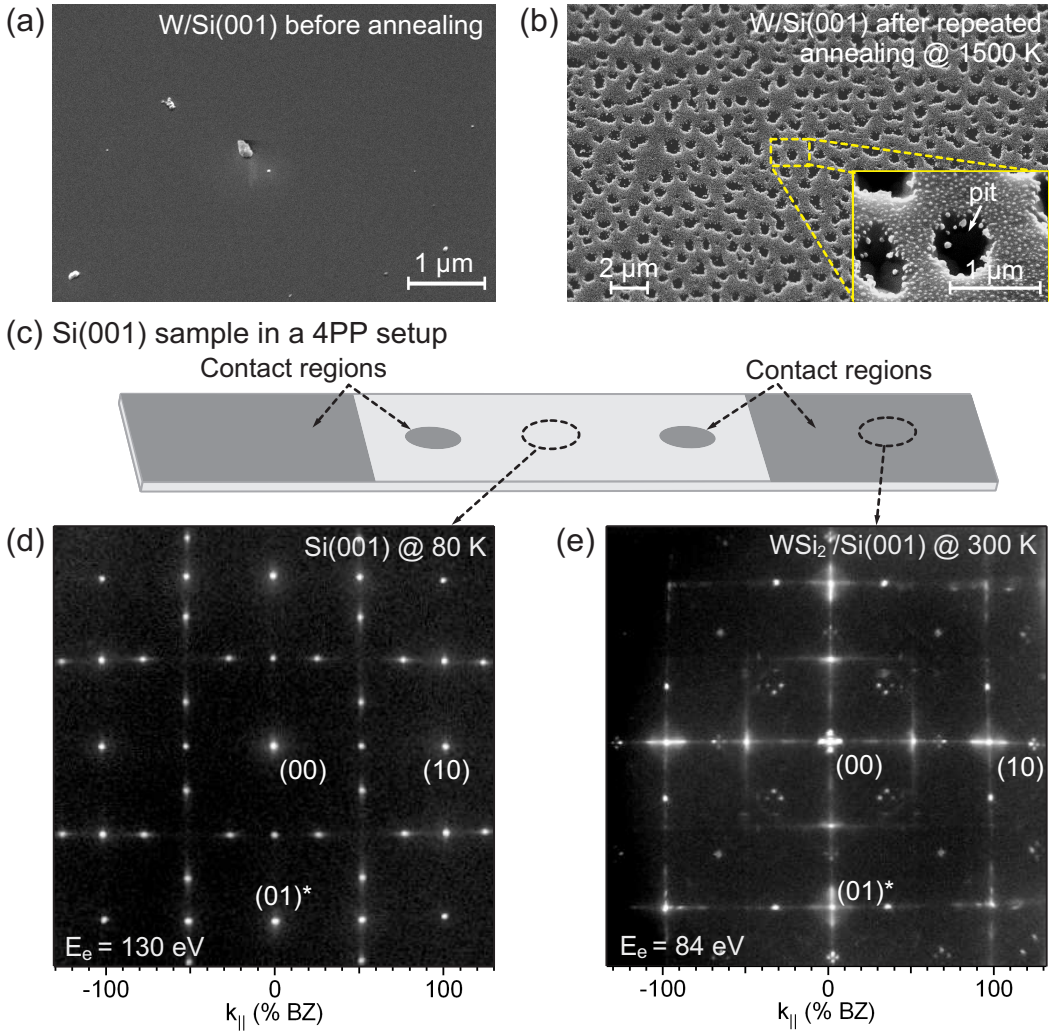

Figure 6.2: The surface structure and the morphology on the sample: (a) SEM images of a vacuum-deposited (at ambient temperature) continuous tungsten film, (b) the surface topography after the annealing processes, with an inset of the magnified image at a particular region showing a pit. (c) A sketch of the Si(001) sample with contact regions in a 4PP setup. (d) LEED pattern taken in the center area of the sample, which shows a clear c(4×2) reconstruction of Si(001) surface at 80 K. (e) LEED pattern taken in the contact regions at both sides of the sample, where W is deposited, shows additional spots on (2×1) reconstructed Si(001) surface, which appear due to the facets surrounding the pit formed by the silicidation process.

µm was used during W deposition. The sample was annealed by following the same recipe as described earlier, and the alloying of the W with the Si was monitored by real-time PEEM.

6.1.2 Results of the experimental observation

LEED measurements were performed in two different regions: the contact regions of the sample, where W was deposited, and in the center of the sample. A sketch of the sample with these different regions and the respective LEED patterns are shown in Fig. 6.2(c). The LEED pattern of the large area of the sample, where no W was deposited, exhibits the sharp spots of a clean Si(001) surface at 80 K (see Fig. 6.2(d)). The surface shows a c(4×2) reconstruction

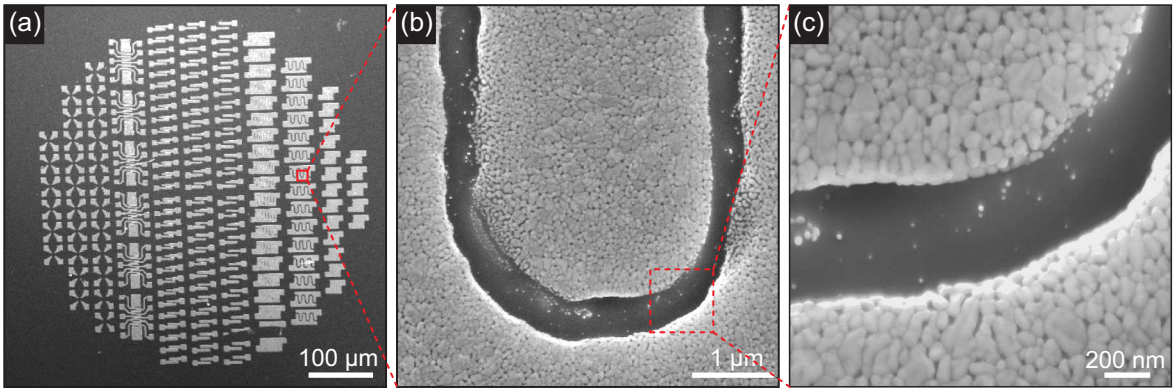

Figure 6.3: SEM images of tungsten (W) structures: (a) W structures deposited using a silicon nitride (Si_3N_4) shadow mask with dimensions below 100 µm, (b) and (c) close-up images near one of the structures.

in two rotational domains. The LEED pattern of the WSi_2 contact regions exhibit additional spots near the spots of Si-(2×1), as shown in Fig. 6.2(e). These spots move in reciprocal space upon changes of the electron energy and reflect the presence of (111) facets. These facets are attributed to the Si substrate. The polycrystalline WSi_2 does not form sharp diffraction spots with sufficient intensity to show up in the LEED pattern.

For the topographic information, the sample was investigated by *ex situ* SEM. The continuous W film as shown in Fig. 6.2(a) was transformed into a WSi_2 film with a high number of micropits (Fig. 6.2(b)). These pits start at the top of the silicide and go deep into the Si bulk. The micropits are also responsible for the additional LEED spots that are observed in the contact area of the sample. The facet spots originate from the side walls of the pits, which consist of Si. The pits are not connected to each other, which suggests that there is a continuous path for the electric current on the WSi_2 contact area.

The silicidation process of W pads, as shown in Fig. 6.3, was also studied with *in situ* LEEM and PEEM. During flash annealing, the size and shape of the patches remained constant, even after many heating cycles (see Fig. 6.4(a)). No spreading out of the patch over the surface was observed. The brightness of the patches and their surrounding, however, changed to reflect the structural change of the W patches and the desorption of SiO_2 in the vicinity of the patches during the initial flash. Figure 6.4 summarizes the LEEM/PEEM results. Fig. 6.4(a) shows the close view of the W patch on the Si(001) surface after the annealing process. Fig. 6.4(c) shows a dark-field LEEM image of a part of a WSi_2 patch with the surrounding Si. Under dark-field imaging conditions in LEEM, one domain of the (2×1) reconstructed Si(001) terraces is imaged in bright, whereas the other domain appears dark. Thus, in the lower part of the image (c), the alternating sequence of bright and dark stripes indicates an undisturbed sequence of clean and reconstructed Si(001) terraces, separated by single steps. It is not surprising that microdiffraction patterns from this area on the surface (one example reproduced in Fig. 6.4(d)) shows a Si(001)-(2×1) diffraction pattern without any indication of W contamination. Closer to the WSi_2 patch, the featureless gray area indicates that the step density is higher in the vicinity of the WSi_2 patch. Microdiffraction patterns of the WSi_2

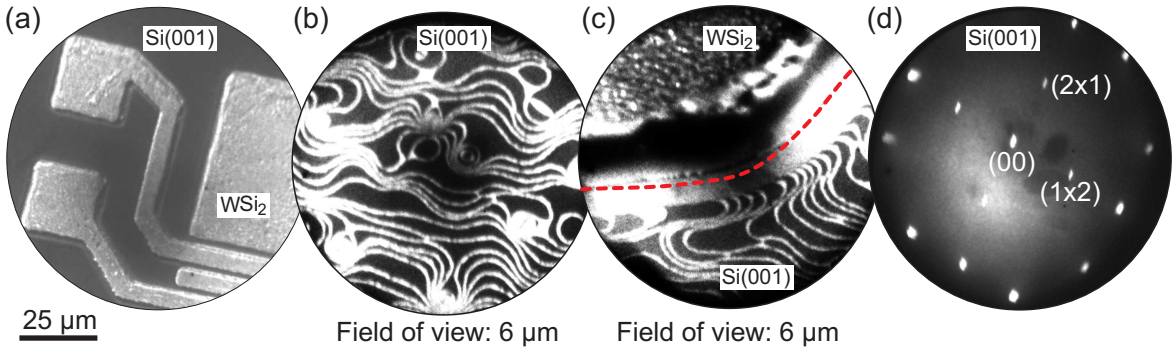

Figure 6.4: (a) PEEM image of the WSi_2 patch on Si(001) substrate, (b) LEEM-DF image taken at a distance of a few µm from the structure, (c) LEEM-DF image taken around the edge of the WSi_2 patch, and (d) microdiffraction pattern of a clean Si(001) surface taken in between the patches at room temperature. Si terraces of both (2×1) and (1×2) reconstructed surfaces appear as bright and dark in (b) and (c). The dotted red line in (c) roughly indicates the boundary between the WSi_2 patch and the Si(001) surface.

patch reveal a polycrystalline composition. Everywhere near the silicide structure (about 1 µm far from the silicide), a regular step train of (2×1) and (1×2) terraces of Si(001) surface was recorded (see the dark-field LEEM image in Fig. 6.4(b)).

It is believed that the grooves around the microscopic patches that were observed in the LEEM/PEEM system fulfill the same purpose as the micropits in the larger patches that were used in the SPA-LEED system, i.e., they provide the material for the silicidation. If the contacts are small enough, as in the LEEM/PEEM case, the material is transported from the sides of the contact patches, leaving the patch surrounded by grooves. Larger contact areas do not have that option, because their dimensions are bigger than the Si diffusion length for diffusion of Si on WSi_2. As a result, Si is transported through cracks in the oxide and leaves micropits. This interpretation is supported by the fact that we do not observe micropits in the small contact areas in the LEEM.

Although the contacts between the WSi_2 and the Si exhibit Schottky-diode behaviors, the characteristics of the individual contact can be bypassed by using a 4PP setup for surface resistivity measurements. In these experiments, where temperatures are changed and films are grown, it is more crucial that the contacts do not peel off and exhibit long-term stability and reproducibility. Moreover, the contacts show an ohmic behavior with the grown film (Bi films), as confirmed by current-voltage (IV) measurements in Fig. 6.1(a). The reliability of the contacts was checked via resistance measurements of the Si(001) sample using a 4PP setup during the annealing and cooling of the sample from 80−300 K and vice versa. The curves in Fig. 6.1(b) show the expected resistance behavior of low-doped silicon [**?**]. Initially, the resistivity decreases due to the ionization of dopants. Around 150 K, the ionization process saturates completely, whereas the carrier density remains unaltered. Above 150 K, the carrier mobility changes with temperature by the carrier-carrier and the carrier-lattice scattering processes, causing an increase of resistance. A small deviation of the cooling curve with respect to the annealing curve was observed due to a small hysteresis during the cooling and annealing cycle. This resistance curve of the silicon substrate was reproduced even after

many flash-annealing cycles of the sample. However, the resistance increases slightly after 30 flash-annealing cycles in several days of experiments (see Fig. 6.1(b)).

6.1.3 Discussion of experimental results

The solid-phase reaction between W and Si starts during the first annealing step at 1000 K [116]. The oxide layer that separates the Si surface from the W pads, however, prevents a direct reaction between the two. Because there are no thermodynamically favorable reaction products found between W and SiO_2 at any temperature [117], another mechanism is necessary to enable silicide formation. Oxide films often exhibit defects such as microchannels or pinholes [118, 119, 117] that are initially present in the native SiO_2 layer, and these are the most likely candidates for the beginning of necessary atomic transport through the oxide. At such intrinsic oxide defects, W atoms or Si atoms might be able to migrate through the oxide to the Si/SiO_2 interface or to the W/SiO_2 interface, respectively. The bulk diffusion of W through SiO_2, however, is too low for effective W mass transport. In contrast, the migration of Si atoms through defects in the oxide to the surface already occurs at 850 K [120]. During flash annealing at 1500 K, the Si reacts with SiO_2 and forms a volatile silicon monoxide (SiO) that already desorbs at 1250 K.

Once the SiO_2 is desorbed, the silicidation of Si from the bulk with the W patches leaves the surface covered with WSi_2 structures, as shown in the SEM image of Fig. 6.2(b). The Si necessary for the alloying process is removed either from the surroundings of the W patches, or, if the contacts are too large to effectively transport Si from the sides to the center of the patch, from the Si below the W patch. In the first case, the patch will be surrounded by grooves with (111) side facets; in the second case, the patches will exhibit micropits with (111) side facets. Nevertheless, once formed, the contacts remain stable and unchanged, even after at least 50 flash-annealing cycles to 1500 K. Identical LEED patterns were obtained after each cycle of flash annealing (Fig. 6.2(d) and (e)), and PEEM did not show any evidence of morphological changes of the contacts during the repeated annealing cycles. The dark-field image in Fig. 6.4(c) confirms that the Si surface only a few micrometers away from the contact is clean and free of contamination, and the surface remains clean even after many flash-annealing cycles.

One important point that should be emphasized is the annealing at 1000 K for 5 hours before the first flash annealing to 1500 K, which seems essential to achieve stable WSi_2 in the contact regions and a clean Si(001) surface in the regions where no W was deposited. We believe that the silicide formation during the first annealing step at 1000 K may have prevented the diffusion of W across the oxide or Si surface at higher temperatures. In contrast, a W-contaminated Si(001) surface was observed when the sample was flash annealed directly to 1500 K, without performing the first annealing step. This is in agreement with a previous study of the formation of epitaxial WSi_2 films on Si(111) [121].

The reproducible resistance curves (Fig. 6.1(b)) during annealing and cooling confirm that the high-temperature annealing step provides stable and metallic silicide contacts. Previous

studies have reported that WSi_2 undergoes a phase transition from a low-temperature hexagonal crystal to a high-temperature tetragonal crystal [**?**, **?**, 121, **?**, 112]. Moreover, they have concluded that the low temperature phase is semiconducting and the high temperature phase is metallic and stable [121, 112]. Obviously, we observe the stable high-temperature phase of WSi_2.

7 Results on Heteroepitaxy

This chapter deals with growth processes, film characterization and some insights into physical phenomena observed during heteroepitaxial growth of Bi on Si(001) and Ag on Si(001). Much of the focus will be concentrated on the system of Bi/Si(001).

Initially, a recipe of preparing Bi films on Si(001) will be described. The morphology and the strain state of the film will be characterized via various techniques. Finally, a closer look at initial stages of growth will be given. The second section will provide a brief description of preparing smooth Ag(111) films on Si(001).

7.1 Bi(111)/Si(001)

This section begins with the growth of Bi(111) films on Si(001) at different temperatures. The morphology of the film will be studied exclusively using SPA-LEED. The lattice accommodation, the strain state and the surface/interface structures of the Bi films will be discussed. To confirm the results from SPA-LEED and gain additional information about the surface/interface and the bulk quality of the films, additional techniques such as the STM and XRD are used and the results from all of those techniques are compared with respect to each other.

7.1.1 Growth at different temperatures

To understand the growth behavior and to find the best possible growth condition, deposition was performed at various temperatures, i.e., 80 - 300 K. During deposition (00)-spot intensity was followed using SPA-LEED in a RHEED-like geometry (see chapter 3). The scattering condition ($S \sim 4.5$) and the deposition rate (0.4 BL/min) were kept constant for each measurement. Before starting each deposition process at respective temperatures, the Si(001) substrate was flash annealed to 1200°C and thermalized at the desired value until the temperature became stable.

Figure 7.1(a) shows the intensity curve recorded at different deposition temperatures. After opening the shutter of the evaporator, the intensity drops due to the scattering at adatoms and small adatom islands. As the adatom density saturates and the island growth starts dominantly during further deposition, the scattering event reduces. This effect causes increase of intensity, which approaches to the maximum at the coverage of 0.6 BL. The maximum for each deposition temperature is consistently constant, indicating a so-called wetting layer of Bi. However, the intensity maximum increases with increasing deposition temperature. This can be understood in a sense that Bi atoms are ordered at higher temperatures due to the

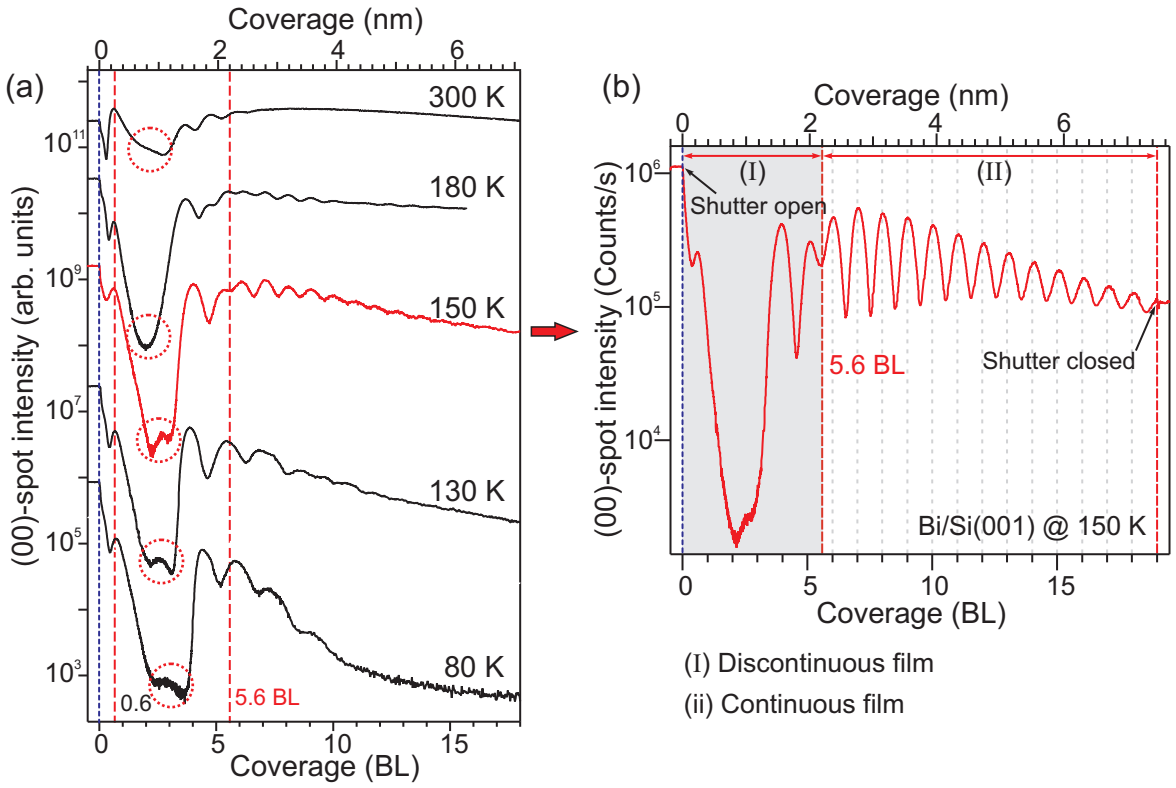

Figure 7.1: (a) LEED (00)-spot intensity during the deposition of Bi on Si(001) at different temperatures. The intensity was recorded at close to the out-of-phase scattering condition, i.e., $S \sim 4.5$. (b) Pronounced oscillation of the out-of-phase ($S \sim 4.5$) (00)-spot intensity recorded during deposition of Bi on Si(001) at 150 K, where two regions (regions (I) and (II)) are separated at 5.6 BL coverage according to the morphology of the film, i.e., (I) discontinuous film and (II) continuous film.

higher mobility of adatoms than at lower deposition temperatures. Beyond the wetting layer, the intensity drops further and almost vanishes at ~ 3 BL coverage. Such a minimum holds until 4 BL coverage. Interestingly, the intensity minimum is split into two sharp minima and the distance between them opens up at lower deposition temperatures or closes together at higher deposition temperatures, as indicated by red dotted circles in Fig. 7.1(a). Above 180 K only one minimum occurs. After 4 BL the intensity recovers as with the intensity of the wetting layer. Until the coverage of 5.6 BL the Bi-film is discontinuous and exhibits various reconstructions. Details of the structural information of initial phases of growth will be reported later in the section 7.1.8. After the initial phases of growth at 5.6 BL the intensity oscillates with the coverage in a bilayer fashion. Such oscillations are indicative for a bilayer-by-bilayer growth. Precise calculation of the layer height will be shown in the later sections. From the variation of the oscillation amplitude and the number of cycles with the coverage at different growth temperatures, the evolution of the growth mode can be easily estimated. At 80 K the oscillation amplitudes the intensity decay faster as compared to the higher deposition temperatures. Since the diffusion of Bi atoms is kinetically limited at lower temperatures, it significantly reduces the inter/intra-terrace mobility. This causes an increase of surface roughness and reduces the intensity and the amplitude of the oscillation. However,

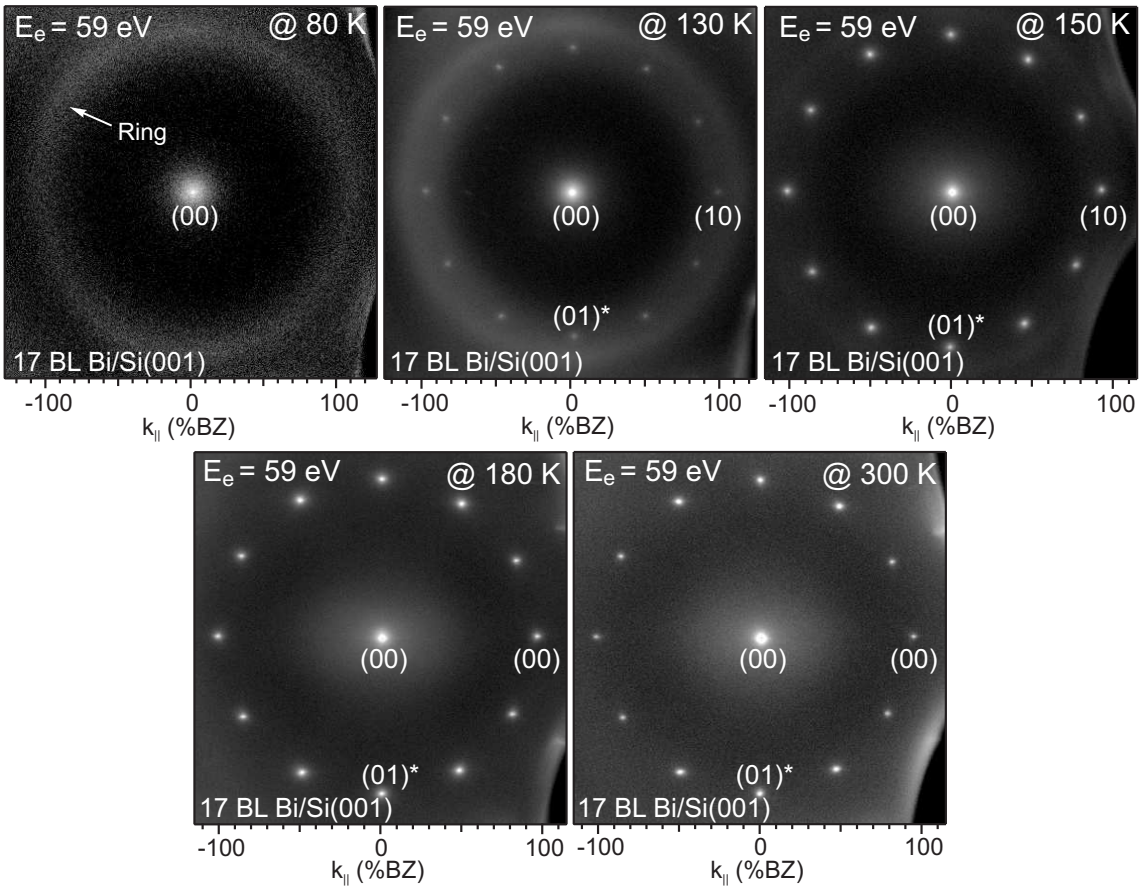

Figure 7.2: Series of LEED patterns of 17 BL Bi films recorded after deposition at different temperatures (80 - 300 K). All patterns are presented in a logarithmic intensity scale.

as the growth temperature is increased, atomic mobility also increases. This process helps to reduce the surface roughness, resulting in long-lasting oscillations. After deposition at temperatures above 150 K, the number of oscillation reduces drastically and almost vanishes at 300 K. The higher mobility of adatoms at higher temperatures enhances the probability of 3D-island formation.

To study the crystallographic orientation of the grown film, 17 BL Bi-films were deposited on Si(001) at different temperatures and 2D LEED patters were recorded after each deposition. In-phase scattering conditions ($S \sim 5$, $E_e = 59$ eV) were chosen for each pattern, since the in-phase condition is sensitive to the bulk defects. Bright 12-fold symmetry spots surrounding the (00)-spot were observed at temperatures higher than 130 K (see Fig. 7.2). Such a rotational symmetry exists, if two 6-fold symmetry (hexagonal) patterns are incoherently superposed and rotated by 90° with respect to each other. Such an azimuthal rotation of Bi(111) crystallites is determined by the two fold orientation of the underlying Si(001) surface, i.e., (2×1) and (1×2) reconstructed domains. This suggests that Bi grows in a (111) orientation along the surface normal and has two equally existing crystallites of same azimuthal orientation but rotated by 90° with respect to each other. With decreasing deposition temperature to 80 K, first order 12-fold symmetry spots disappear remaining only the diffuse ring (see Fig. 7.2). The

radius of the ring, i.e., 113 %BZ, which is equal to the 3.4 Å in real space, matches with the the separation of $d_{lp} = 3.28$ Å (see section 4.2), remaining only 3.6 % strain. This indicates the formation of the ring is in accordance with the formation of rotationally disordered (110)-oriented Bi crystallites. Additionally, as was discussed earlier, the atomic diffusion is limited at low temperatures, causing an increase of surface roughness. As a result of increased roughness, the (111) oriented spots become extremely diffuse and weak. Surrounding the ring, they turn invisible. Further details of the structure will be discussed again in section 7.1.8.

7.1.2 Bi on Si(001) at 150 K: the template

Initially, the Si(001) sample was carefully cleaned following the standard preparation procedure described in section 4.1. A Bi film of 17 BL ($\sim$ 6 nm) coverage was prepared adopting a kinetic pathway: a deposition at low temperatures and subsequent annealing to high temperatures. The growth temperature of 150 K was chosen based on the fact that pronounced long-lasting LEED specular intensity oscillations were observed at 150 K (see Fig. 7.1(b)).

Figure 7.3(b) shows a quasi 12-fold symmetry of LEED pattern recorded right after deposition at 150 K. The distance between the first order spots and the (00)-spot was calculated to be 99 %BZ, which corresponds to a real space row distance of $a_{row} = 3.88 \pm 0.02$ Å. The in-plane lattice parameter $a_{Bi(111)}$ derived from the row distance via $a_{Bi(111)} = a_{row}/\sin 60° = 4.48$ Å. Compared with the Bulk lattice parameter of Bi ($a_{Bi,bulk} = 4.54$ Å) [86, 122] the film is compressively strained by 1.3 %. The initial Si(001) surface consists of both $c(4 \times 2)$ and $c(2 \times 4)$ domains, which rotate by 90° on neighboring terraces (7.3(a)). The alternate buckling of the $c(4 \times 2)$ reconstruction is destroyed by submonolayer amounts of Bi. Then the Bi(111) film obviously grows in crystallites aligned along the dimer orientation and in registry with the Si(001) surface atomic row distance $a_{Si(001)} = 3.84$ Å. The (00)-spot is slightly broadened with a FWHM of 1.3 %BZ indicating a well-ordered continuous epitaxial Bi film with a rough surface. A similar pattern has also been observed for the Ag(111)/Si(001) system [52].

The film was then slowly annealed to 450 K by heating the sample holder with a resistively heated filament. A moderate annealing rate ($\sim$1 K/min) was applied and carefully monitored with a temperature controller system. The sample was kept for 10 minutes at 450 K. LEED patterns were recorded after cooling the sample down to 300 K. As shown in Fig. 7.4(a), spots are changed drastically: each of the twelve (10) spots is alternately elongated in the [110] or [1$\bar{1}$0] direction of the Si(001) substrate. Due to the superposition of both patterns, the (00)-spot becomes elongated in both directions and appears as a plus sign. The subset of (10)-spots from one of the two Bi(111) domains, however, are elongated all in the same direction. When single elongated spots are magnified (see insets of Fig. **??**(a) and (b)), the nature of the elongation becomes apparent, i.e., each of the integer order spots is split into a linear chain of satellite spots with an equal separation of $k_{dis} = 1.9$ %BZ$_{Si(001)}$, i.e., a periodicity length $\langle a_{dis} \rangle = 2\pi/k_{dis} = 200$ Å (Fig. 7.4(c)). Each of the two hexagonal Bi(111) sublattices must therefore exhibit a grating-like periodic variation of its surface properties. Such a phenomenon of periodic modulation of surface height profile, i.e., surface height undulation, arises due to

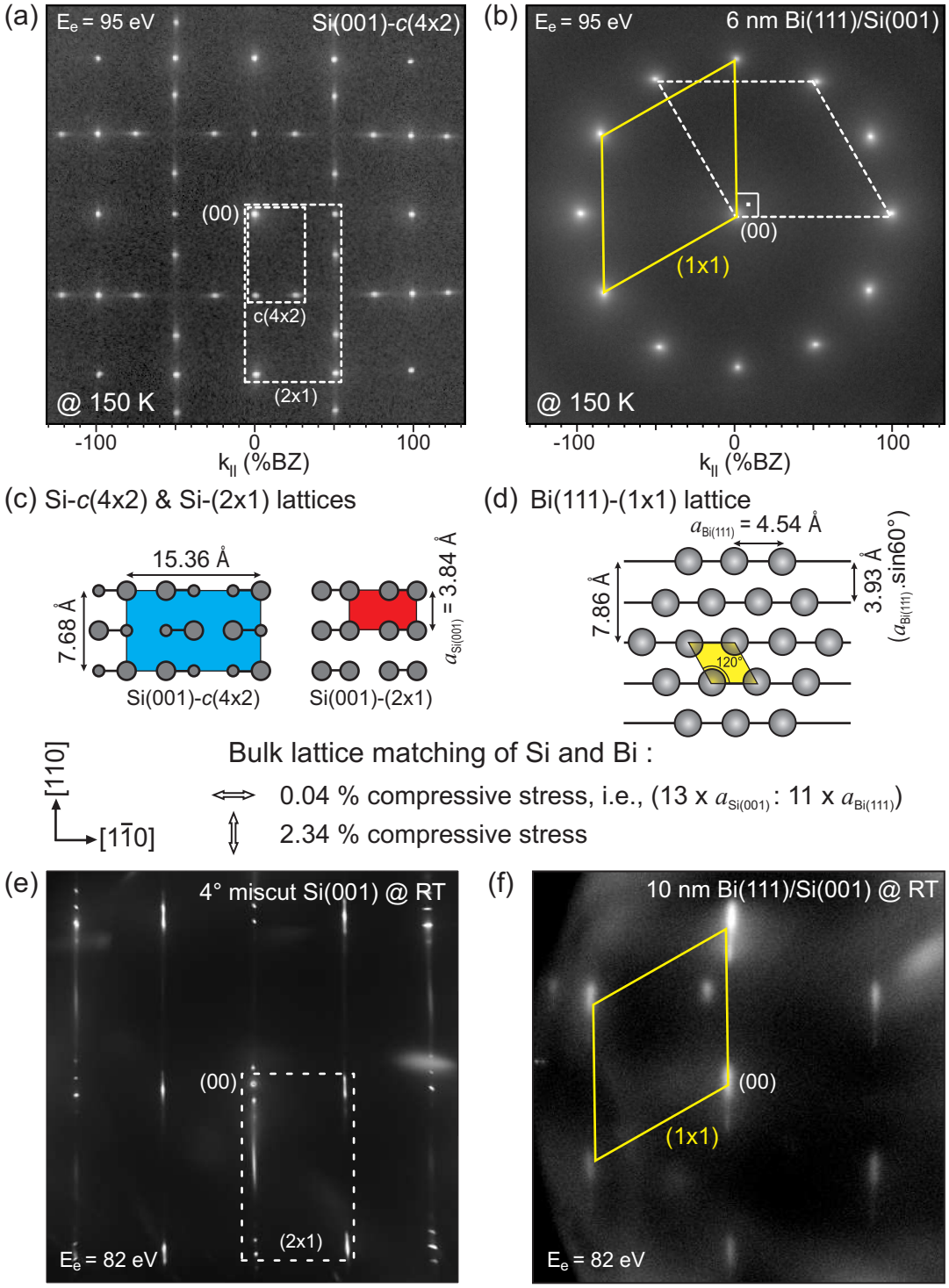

Figure 7.3: A model of lattice accommodation between Bi(111) and Si(001) lattices. (a) LEED pattern of Si(001)-$c(4\times2)$ surface at 150 K. (b) LEED pattern of hexagonal Bi(111) surface after 6 nm Bi deposition on Si(001) at 150 K. The quasi-12-fold symmetry pattern is explained by the superposition of two hexagonal LEED patterns of Bi(111) rotated by 90° with respect to each other. The two corresponding reciprocal 1×1 unit cells are indicated by solid and dashed lines. (c) Top view sketches of the $c(4\times2)$ and (2×1) unit cells of the Si(001) surface. The anti-phase dimer buckling of the $c(4\times2)$ is indicated by small and large Si atoms. (d) A sketch of the Bi(111) surface lattice for one of the rotational domains. Below, the bulk lattice matching of Si and Bi is described. (e) LEED pattern of a 4° miscut Si(001) surface, which shows a single domain Si-(2×1) pattern. (f) LEED pattern of a 10 nm Bi film deposited on the substrate shown in (a) at 300 K. Six-fold symmetry results due to the single domain substrate.

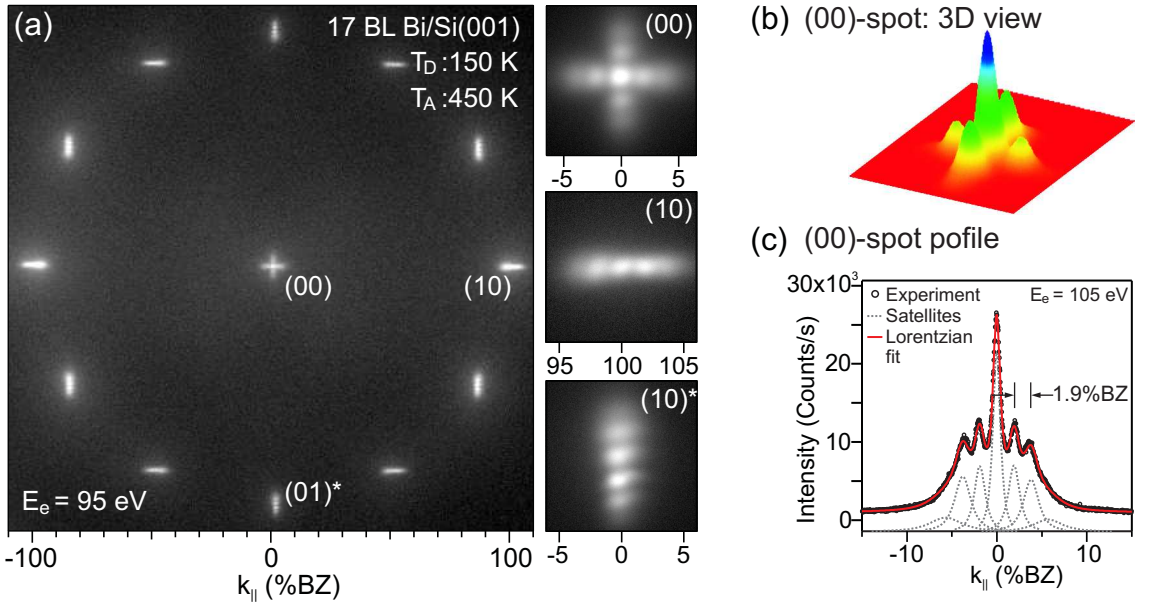

Figure 7.4: (a) LEED pattern of 17 BL Bi film (template) deposited on Si(001) at 150 K and annealed to 450 K. The pattern was recorded after cooling the sample to RT and represented in logarithmic intensity scale. Insets show central (00)-spot and each of the hexagonal domain spots symbolized by (10) and (10)*, respectively. A linear chain of satellite spots is caused by the periodic surface height undulation, which is explained in the text. (b) Colored 3D representation of the (00)-spot, showing an artistic view of the spot splitting. (c) (00)-spot profile measured at $E_e = 105$ eV. A best fit with Lorentzian function resolves up to third order satellite spots with average separation of $k_{dis} = 1.9$ $\%\mathrm{BZ}_{Si(001)}$.

the long range strain fields originating from a periodic interfacial dislocation array, which accommodates the lattice mismatch between Bi and Si lattices (see Fig. 7.5(a)). During the relaxation process, repulsive interaction between the adjacent dislocations causes a long range ordering of the dislocation array, resulting in a periodic nature of the surface height undulation. This kind of lattice accommodation by a periodic array of interfacial dislocations has already been observed for other heterosystems such as Ge on Si(111) [48, 123], EuTe(111)/PbTe(111) [124], Ag(111)/Pt(111) [125], Ag/Si(001) [52], etc.

The driving force for the formation of such a dislocation array is the strain in the Bi film due to the lattice mismatch between Bi(111) and Si(001). Surprisingly, both lattices could be matched commensurably without a buildup of a large amount of strain: in the [110] direction the atomic row distance $a_{row} = a_{Bi(111)} \times \sin 60° = 3.93$ Å of the bulk Bi(111) interface plane almost fits well with the Si dimer distance $a_{Si(001)} = 3.84$ Å. The remaining mismatch of only 2.3 % (the compressive stress in the Bi film) is almost accommodated by the formation of the dislocation array. In the perpendicular $[1\bar{1}0]$ direction both lattices are commensurate with a ratio of 13 × 3.84 Å (Si(001) surface lattice parameter) to 11 × 4.54 Å (the atomic distance of the Bi(111) crystal along the $[1\bar{1}0]$-direction). Figure 7.3 summarizes the simple model of lattice accommodation in the Bi(111)/Si(001) heterointerface. Unit cells of both lattices in reciprocal and real spaces are shown with different colors. The orientation of the Bi(111) lattice structure was independently verified from the LEED patterns as shown in Fig.

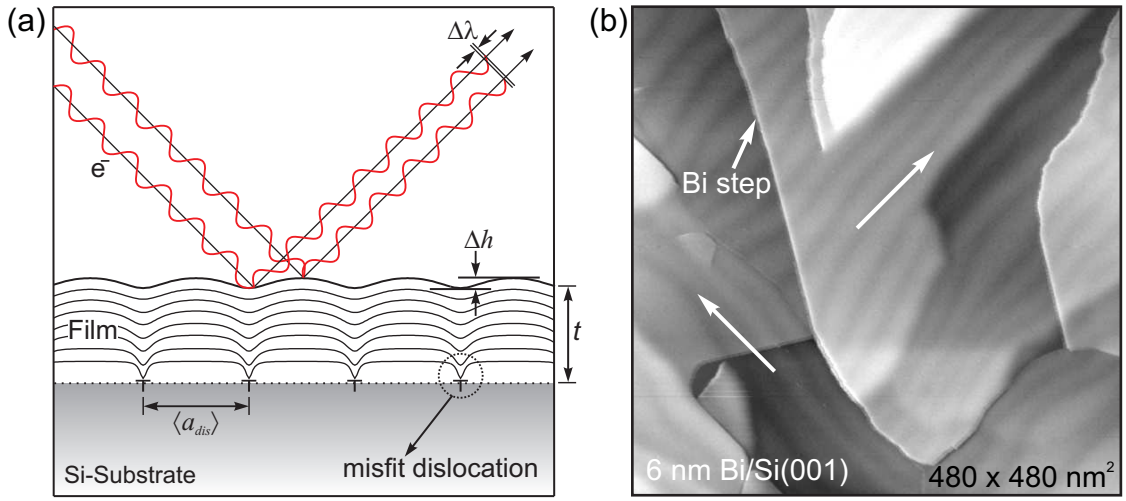

Figure 7.5: (a) Cross-section view of the periodic height undulation via elastic lattice distortion in the lattice mismatched heteroepitaxial system. The distortion is caused by the interaction of adjacent strain fields surrounding each misfit dislocation at the interface. The parameters, such as film thickness t, an average distance between each dislocation $\langle a_{dis} \rangle$, are shown in exaggerated length scale. The symbol of inverted '$\perp$' is indicated for the edge-type dislocation for compressive strain. The upper part of the sketch describes the LEED phenomena, where the electrons undergo a small path change $\triangle\lambda$ after scattering at the wave-like surface of amplitude $\triangle h$, producing spot splitting. (b) STM topography of a 6 nm Bi film prepared by deposition at 150 K and annealing to 450 K. Long running bright and dark stripes represent the height contrast due to vertical height undulation.

7.3(e) and (f), where single domain substrate of 4° miscut Si(001) was used and 10 nm Bi was deposited on it at 300 K. This experiment was performed in another UHV chamber equipped with SPA-LEED. As shown in Fig. 7.3(e), the 4° miscut Si(001) surface shows a double-stepped surface with single (2×1) domain surface. Obviously, Bi grows in a (111) direction, showing a single domain hexagonal pattern (Fig. 7.3(f)). The spot are elongated in a [110] direction, due to the dislocation network caused by 2.3 % strain. Since dislocations are not well-ordered, no spot splitting are observed.

The sharp and individually resolved satellite spots as shown in Fig. 7.4(a) clearly indicate that the film is atomically smooth and continuous, except the long range vertical height corrugation. Three-dimensional (3D) view and 1D profiles along (10)* direction of the (00)-spot are also shown in Fig. 7.4(b) and (c). Each satellite peaks could be fitted by Lorentzian functions, as shown with dotted lines in Fig. 7.4(c). Details of the satellite spots will be discussed in the next sections.

7.1.3 The Bi(111) film using the template

Interestingly, after additional deposition of Bi on the template film at 450 K, the periodic surface height undulation was reduced significantly, without buildup of surface roughness. Evidence of flattening of the surface corrugation can be clearly observed in the LEED pattern (see Fig. 7.6(a)) recorded after additional 19 nm Bi deposition on the template film at 450 K. All the satellite spots, as shown in Fig. 7.4(a), turned into single sharp spots, indicating a smooth surface, free of corrugation. *In situ* observation of the coverage dependent (00)-spot

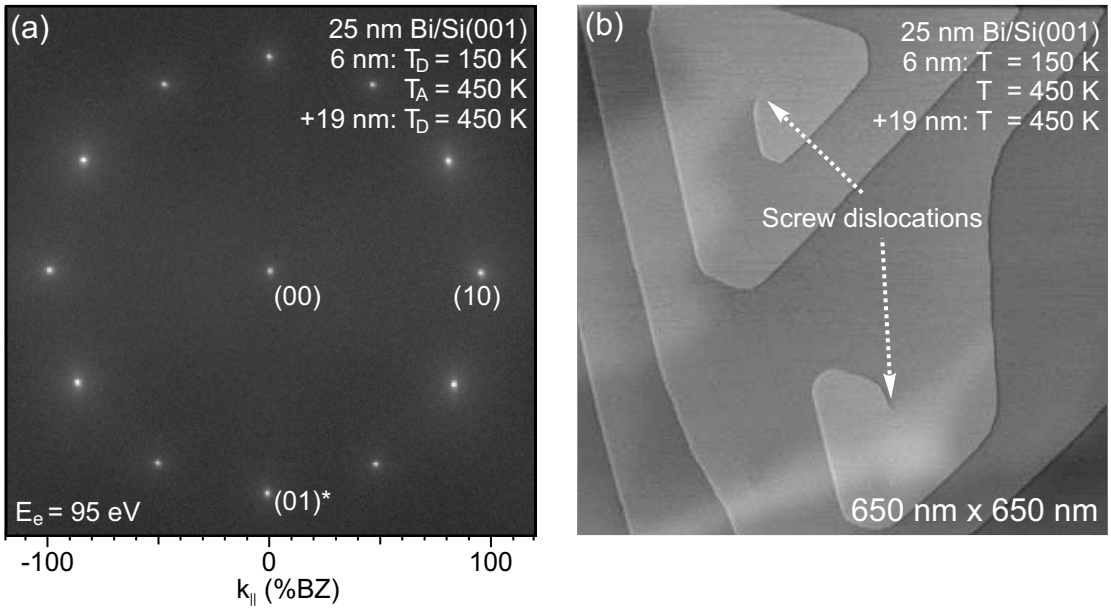

Figure 7.6: (a) LEED pattern of a 25 nm Bi(111) film on Si(001) prepared according to the recipe adopting a kinetic pathway described in the text. (b) STM topography (650×650 nm^2) ($V_{\text{bias}} = 2.1$ V, $I_{\text{tunnel}} = 17$ pA) of a 25 nm Bi film prepared with the same recipe (as in (a)) in other UHV chamber. Arrows indicate the location of screw dislocations.

profile has further confirmed that the intensity of the satellite spots is completely vanished as the total film thickness exceeds the periodic distance between dislocations, i.e., 20 nm. The smoothening mechanism during additional deposition at 450 K will be addressed later in section 7.1.4.3.

7.1.3.1 *Ex situ* morphology and strain state

The morphology and strain state of the thick (thicker than the average dislocation distance, i.e., 20 nm) Bi(111) films were characterized applying various methods such as *in situ* SPA-LEED and STM, *ex situ* NC-AFM and XRD.

An *in situ* recorded in-phase (00)-spot profile is shown with red color solid lines in Fig. 7.9(a). The inset is presented in linear scale. Interestingly, both in-phase and out-of-phase profiles have an equal FWHM, i.e., 0.4 %BZ, which estimates the average terrace width is larger than the instrumental resolution of 100 nm and has extremely low bulk defect density (small angle mosaics, screw dislocations, stacking faults, etc.).

The morphology of the film was analyzed via *ex situ* NC-AFM. Figures 7.7(a) and (b) shows the topography (in a few micrometer length scale) of a 25 nm Bi film prepared in the SPA-LEED chamber using the same recipe as discussed earlier. Various attributes are clearly visible in the AFM images: such as micrometer-sized crystallites separated by grain boundaries, triangular shape (three-fold symmetry) islands (twins and rotated islands), a height contrast of underlying Si domain steps, etc. These attributes are shown in Fig. 7.7(b) with arrows. The three-fold symmetry of the Bi islands is the inherent nature of the hexagonal Bi(111) lattice, which is constructed by three-fold rotational symmetry of Bi planes. The islands are rotated

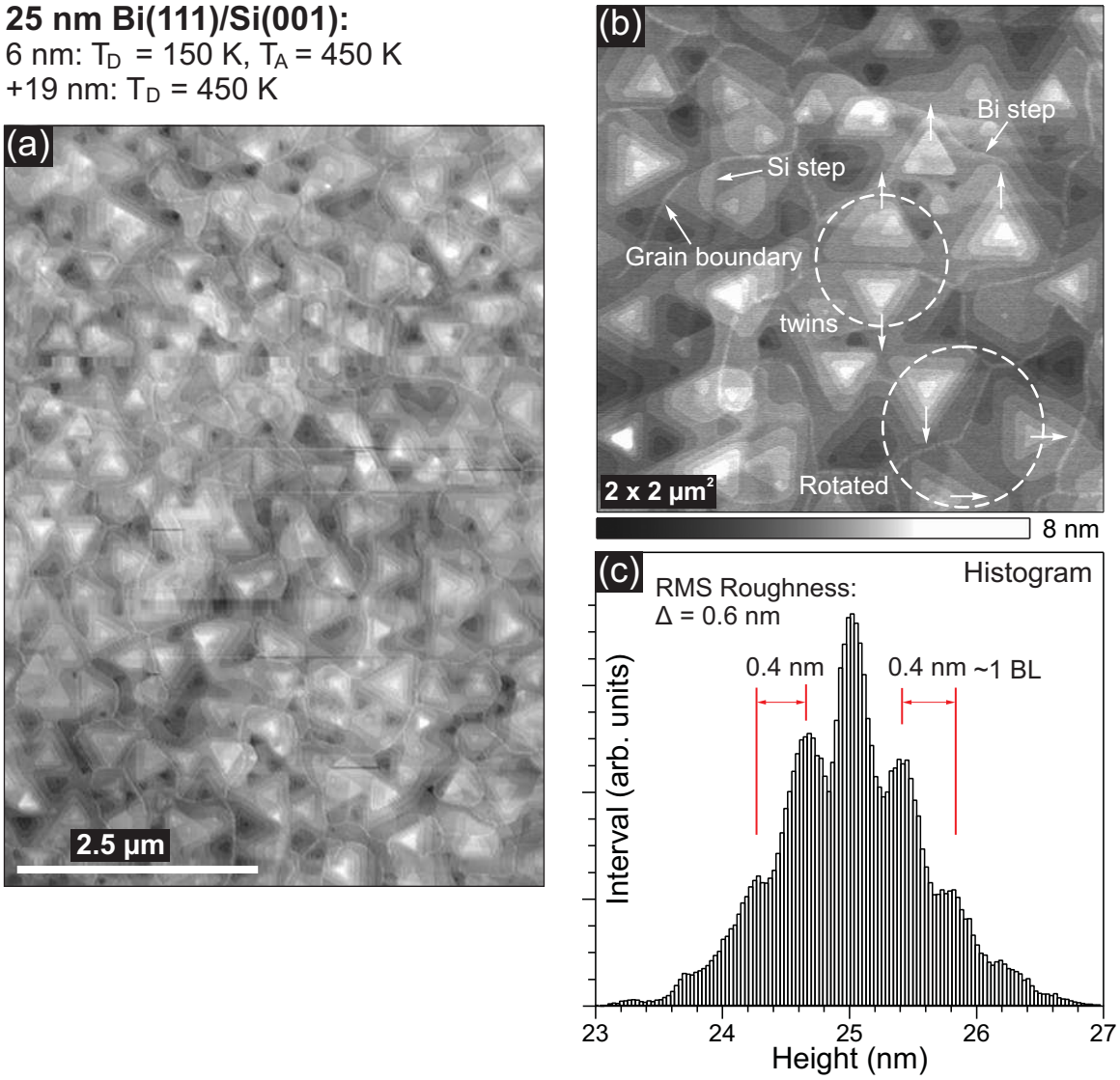

Figure 7.7: NC-AFM topography of a 25 nm Bi(111) film on Si(001) prepared according to the recipe described in the text. (a) Large area overview image of a 25 nm Bi film prepared with the method presented in the text. (b) AFM image (2×2 µm^2) of the same film. Arrows within the dotted circles indicate the azimuthal orientation of neighboring Bi crystallites separated by grain boundaries. Dashed circles highlight 180° rotated (twins) and 90° rotated Bi islands, respectively. (c) Histogram of the film, showing an equally spaced (0.4 nm) height variation. The RMS roughness of $\triangle = 0.6$ nm is calculated from the histogram.

by 90° from one crystallite to another one, which provides a clear indication of the existence of Bi(111) crystallites rotated by 90°. Additionally, twinned areas can also be identified by a 180° rotation of the triangular islands. Twinning of the Bi(111) crystallites occurs because there is no left-right orientation preference with respect to the underlying Si dimer rows. The grain boundaries between those crystallites (both the twinned and the rotated ones) can easily be identified by the decoration (indicated by arrow in Fig. 7.7(b)). Few screw dislocations are also visible, although the density is quite low, i.e., 0.2 μm^{-2}. Interestingly, the step train of Si(001), which has a step height of 1.36 Å, can also be recognized in the topography. It seems that the Bi film overgrows the Si terraces in a so-called "carpet mode" [126, 127].

The quantitative estimation of vertical roughness or the layer distribution of the 25 nm Bi film was performed via determination of overall root mean square (RMS) roughness from the histogram of the AFM topography of Fig. 7.7(b). As shown in Fig. 7.7(c), the histogram shows distinct peaks, which are separated by a nominal height of 0.4 nm ($\sim$ 1 BL height of Bi(111) terrace). This provides a clear indication of a homogeneous distribution of Bi islands, with heights extending multiples of a BL. A RMS roughness of $\triangle = 0.6$ nm suggests that the surface is atomically smooth. Large terraces on a 100 nm scale are observed over the whole surface.

The local structures such as step morphology and point defects of the Bi(111) film were also studied by *in situ* STM. A 25 nm Bi film was prepared using the same recipe as described earlier and the topography was recorded at 150 K (see Fig. 7.6(b)). The surface exhibits atomically smooth terraces in the range of 100 nm to 400 nm. The terraces are separated by bilayer Bi(111) steps, i.e., 3.94±0.08 Å. The film shows no defects such as single adatoms, vacancies or contamination at the atomic level. However, few screw dislocations at a density of 3 μm^{-2} were observed in the STM image. This might act as nucleation centers for growth spirals via step propagation.

The strain state of the film was verified by measuring the lateral and vertical lattice parameters via *in situ* SPA-LEED and *ex situ* XRD measurements. From the distance between the (00)-spot and the first order spots, in the LEED pattern shown in Fig. 7.6(a), a row distance of $a_{row} = 3.93$ Å was calculated for a 25 nm Bi(111) film. This value gives a lateral lattice parameter of $a_{Bi(111)} = 4.54$ Å via $a_{Bi(111)} = a_{row}/\sin 60°$. Comparing with the Bulk lattice parameter of Bi ($a_{Bi-bulk} = 4.54$ Å) [86, 122] the film is relaxed to the bulk lattice parameter.

The vertical layer distance of the film shown in Fig. 7.7, was additionally determined via XRD measurements in a standard $\theta - 2\theta$ geometry setup. Fig. 7.8 shows the $\theta - 2\theta$ scan, which exhibits the (111), (222), (333) Bi(111) peaks and the (002), (004) Si(001) substrate peaks. The Si (002) peak at $\theta = 33.12°$ is normally forbidden; however, it appears due to the double diffraction in the crystal lattice [128]. From the distance between the two consecutive Bi peaks, the layer distance of $d_{Bi(111)} = 3.953 \pm 0.01$ Å is calculated, which matches with the bulk Bi(111) layer distance $d_{bulk} = 3.95$ Å, indicating a complete relaxation. Additionally, thickness dependent Kiessig interference fringes [129] were also observed near the Bi(111) Bragg peak as shown in the inset of Fig. 7.8. Such oscillations are the clear signature of the high crystallanity and the uniformity in the thickness of the film. A nominal thickness of

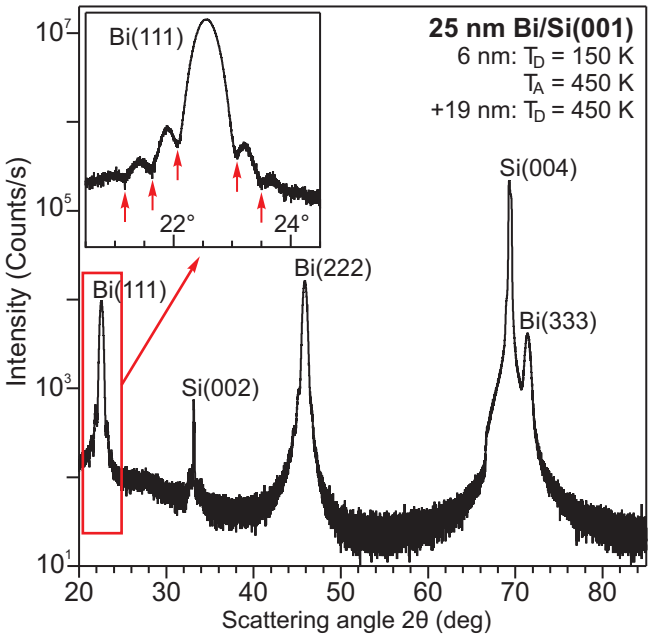

Figure 7.8: X-ray diffraction (XRD) pattern measured by standard $\theta-2\theta$ scan of a 25 nm Bi film prepared with the recipe described in the text. Various orders of Bragg peaks in the Bi film are indicated at each peak position. The inset shows a magnified view of the Bi(111) peak (indicated by red rectangle) and embedded Kiessig interference fringes are indicated by red arrows.

$t = 20.9$ nm was determined by [130]:

$$t = \frac{\lambda}{2 \triangle\theta \cos\theta_n} \tag{7.1}$$

with $2\triangle\theta = 0.43°$, the distance between two successive minima of the fringes, as shown by arrows in the inset of Fig. 7.8, $\lambda = 0.154$ nm the dominant wavelength of Cu-K_α radiation and θ_n the Bragg angle of n^{th} order ($\theta_1 = 22.58°$). The measured thickness is nearly 3 nm less than the originally calibrated thickness of 25 nm by AFM. This might be caused by oxidation of the Bi surface at ambient conditions, which still need to be confirmed. The observed Bi peaks are solely broadened by the finite thickness of Bi films, suggesting the absence of bulk defects like stacking faults, disordered dislocations and small angle mosaics.

7.1.3.2 The comparison with the RT prepared film

The morphology of the above described film was compared with the film, which was prepared in a single step, i.e., deposition at RT and subsequent annealing to 450 K. The substrate, the substrate cleaning procedure, Bi deposition flux, film annealing rate, etc. were kept at the same parameters as previously used. After preparing the 25 nm film the surface morphology was characterized by *in situ* SPA-LEED and *ex situ* NC-AFM.

The difference is clearly visible from the LEED pattern of the film shown in Fig. 7.9(b). As compared to the LEED pattern of the previous film (see LEED pattern in Fig. 7.6(a)), LEED spots in Fig. 7.9(b) are broader and have a higher background, indicating a rough surface. For a one-to-one comparison, the in-phase (00)-spot profiles from both films are shown in Fig. 7.9(a). The FWHM of the RT deposited film is almost 5 times larger than the previous low temperature deposited film. Since the in-phase condition is sensitive to the bulk defects, it is clearly visible that the RT deposited film has higher bulk defects, which cause

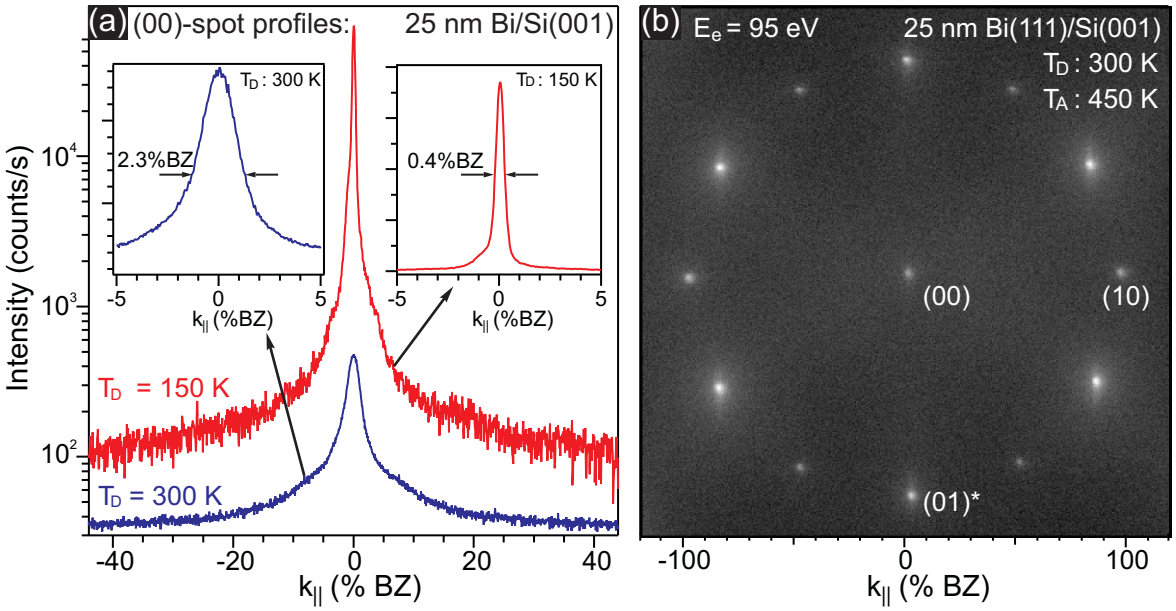

Figure 7.9: (a) LEED (00)-spot profiles in a logarithmic scale of a 25 nm Bi films on Si(001) taken at the in-phase condition: upper curve (the red solid line) prepared with the method described in the text (additional 19 nm deposition of Bi on the template at 450 K), bottom curve deposited at 300 K and annealed to $T_A = 450$ K. Insets show the profiles in a linear intensity scale close-up of the (00)-spot taken at the in-phase condition, which is sensitive to bulk defects (small angle mosaics, screw dislocations, stacking faults, etc. (b) LEED pattern of a 25 nm Bi film on Si(001): deposited at 300 K and annealed to $T_A = 450$ K.

the broadening of the spots. Additionally, the LEED pattern exhibits a clear difference in the intensity between the spots separated by 30°. It is concluded that the relative population between the two 90° rotated Bi(111) domains is in a ratio of 2:1. The preference for one of the (111) azimuthal orientations may be caused by the bare Si(001) substrate during the nucleation of the first Bi islands. For deposition at lower temperatures this effect is not as pronounced because the island density during the initial stage of Bi growth is much higher than at RT.

The large scale morphology of the film is shown in Fig. 7.10. The overview topography clearly shows the scale of surface roughness, which contains a number of clusters with a height up to 30 nm higher than the average surface of the Bi film (the white areas in Fig. 7.10(a), (b) and (c). In addition to the clusters, the surface exhibits multilayer triangular shape islands, which are relatively smooth. Additionally, the long extending tail in the histogram as shown in Fig. 7.10(d) reflects the scale of the height distribution, which is quite broader than the previous one (see Fig. 7.10(c)). The high clusters drastically increases the RMS roughness to $\triangle = 14$ nm, which is much higher than the RMS roughness of the film grown at 450 K on a template.

The cause for the higher surface roughness of the 300 K deposited film might be due to a disordered interfacial dislocation network. To confirm this claim, the 17 BL Bi film was deposited on Si(001) at 300 K with a deposition rate of 0.4 BL/min and subsequently annealed to 450 K (see Fig. 7.11(a)). All the LEED spots appeared to be elongated and diffuse;

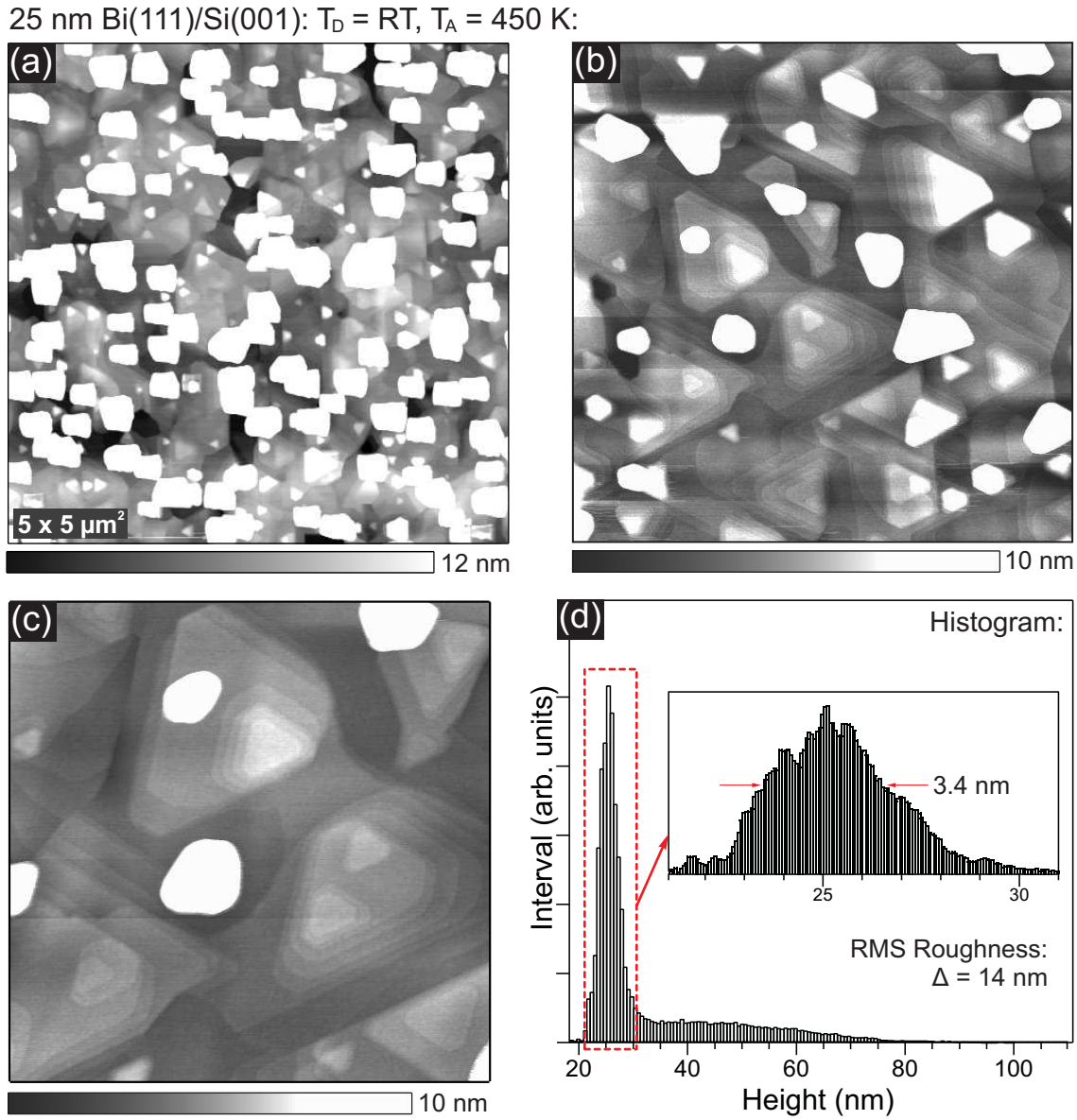

Figure 7.10: (a) Large area AFM topography (5×5 µm^2) of a 25 nm Bi film deposited at 300 K and annealed to 450 K, showing a number of clusters (white area) with average size higher than 14 nm. (b) AFM topography (2×2 µm^2) of the same film, showing multilayer smooth and triangular shape islands along with clusters. (c) Magnified small area AFM image (1×1 µm^2) of the same film, reflecting the presence of a smooth areas (smooth triangular islands) between the high clusters. (d) Histogram of the film taken from the topography (a), showing a long extending tail of height distribution. The RMS-roughness of 14 nm is calculated by its histogram. The inset shows the magnification of the range from 21 nm to 31 nm indicated by red rectangle, which gives a RMS roughness of 3.4 nm. The reduced value of RMS roughness indicates a relatively smooth surface below the very high clusters.

no clear spot splitting was observed. The absence of sharp satellite spots, in comparison with the template film (see Fig. 7.4(a)), indicate the reduced periodicity of the surface height undulation. That means there are no sufficient dislocations generated, which makes a weak interaction between the strain fields surrounding the dislocations. As a result of the weak periodicity of height undulation, atoms are not ordered on the surface, which causes an increase of surface roughness. An AFM topography of a nominal 7 nm Bi(111) film deposited

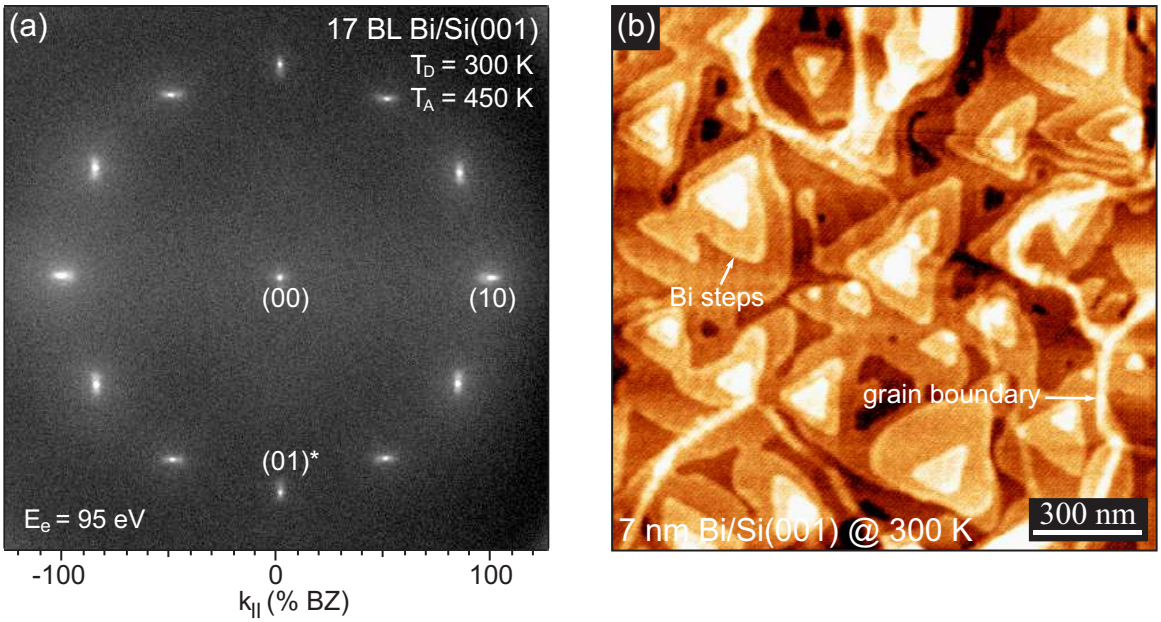

Figure 7.11: (a) LEED pattern of a 17 BL Bi(111) film deposited on Si(001) at 300 K and annealed to 450 K. Spots are elongated by the formation of surface height undulations, which are not sufficiently ordered.(b) NC-AFM topography of a 17 BL Bi(111) film deposited on Si(001) at 300 K.

on Si(001) at 300 K is shown in Fig. 7.11(b), which exhibits three-fold symmetry Bi islands separated by bilayer steps. It is also visible that the islands are rotated by 90° at each crystallite separated by grain boundary. However, the surface morphology does not look as smooth as in the case of the film prepared at 150 K (see Fig. 7.7(a) and (b). Interestingly, no drastic surface roughening via multilayer growth is observed, which contradicts the previous claim of 3D growth at 300 K [25].

7.1.4 The configuration/geometry of the interfacial dislocation network

In the following subsections, the configuration, i.e., the period and the amplitude, of the surface height undulation observed in the 6 nm template Bi(111) film, as shown in section 7.1.2, and the geometry of the dislocation network at the interface, will be estimated quantitatively. The periodicity length, which corresponds also with the average dislocation distance, is calculated directly from the average separation between each satellite peak. The amplitude of the surface height undulation will be evaluated by relating the intensity of satellite peaks with scattering phase S. The intensity of the satellites are also simulated applying the elasticity theory and compared with the measured intensity curves.

The results obtained from the SPA-LEED measurements are independently verified by the STM investigations, where the topography and the height profiles recorded at various coverages can also give a direct quantitative determination of the dislocation geometry.

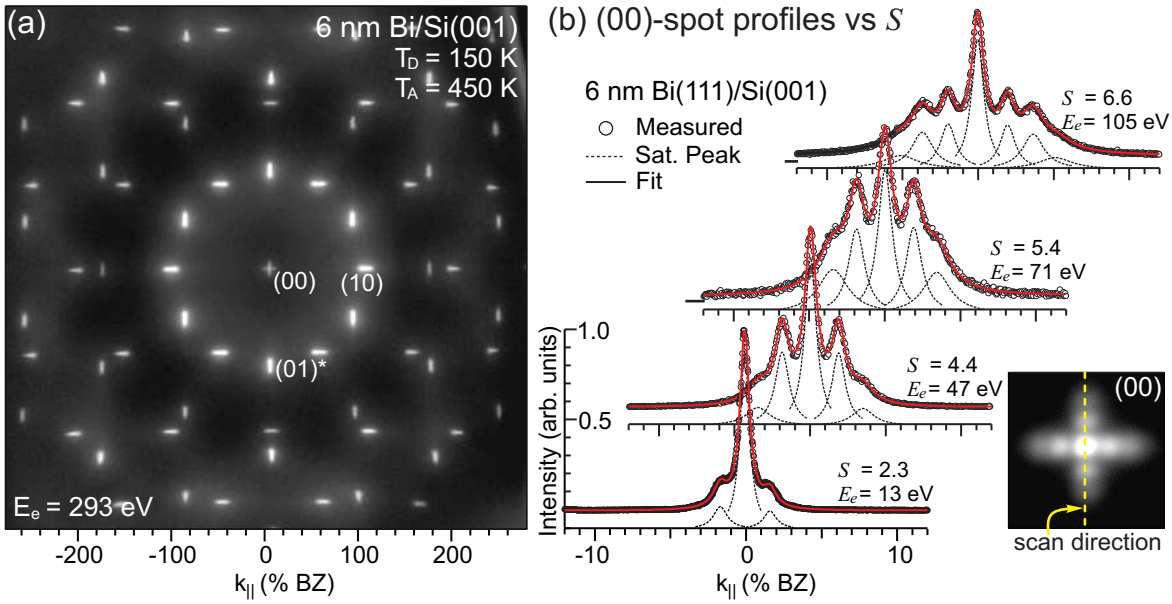

Figure 7.12: (a) LEED pattern (logarithmic scale) of a 6 nm Bi film deposited on Si(001) at 150 K and annealed to 450 K. The quasi 12-fold symmetry is explained by the incoherent superposition of two hexagonal LEED patterns rotated by 90° on a Bi(111) surface. Each spot of the two hexagonal subpatterns seems to be elongated along the [110] or [1$\bar{1}$0] direction. The pattern is recorded at 293 eV to show the higher order spots. (b) Series of (00)-spot profiles recorded at different scattering conditions S. The data are well fitted (solid lines of red color) by a sum of overlapping equidistant satellite peaks with a Lorentzian shape, which are individually shown by dotted lines. The splitting of the spot into a series of equidistant satellites is more pronounced at higher electron energies.

7.1.4.1 A SPA-LEED study of the periodic dislocation network

Fig. 7.12 shows the LEED pattern of the template film and (00)-spot profiles taken at different scattering phases. It is clear from the profiles that with increasing electron energy the satellites become more intense in the expense of the central spike. Since electrons with very low energies (small S) exhibit a very large de Broglie wave length, they are insensitive to the weak height undulation at the surface. Therefore, the splitting is more pronounced with higher energy electrons. Equidistant satellite spots are clearly visible up to the third order at the electron energy of 105 eV.

First, it was started to find the relation between the integral intensity of each satellite peak with the scattering phases S. In order to determine the integral intensity of each satellite peak, the profiles were fitted with a sum of equidistant Lorentzian functions (see subsection 2.1.4) of varying widths, which are symmetric with respect to the central spike. Since the splitting of the (00)-spot is symmetrical for both domains, the data were taken by considering only one domain. All fits (solid red curve in Fig. 7.12(b)) agree well with the measured profiles. To eliminate the influence of the dynamic form factor and to evaluate the data within the framework of kinematic approximation, the integral intensity of the individual peak in the

spot including the central (00)-peak and each satellite peak[1] was normalized[2] by the sum of the integral intensities of the central peak and all satellites. Since the intensity of the central (00)-peak is enhanced by multiple of two, due to the overlapping of two 90° rotated (111) domains, the integral intensity of the (00)-peak is reduced by half accordingly, to consider the splitting only in a single domain.

Fig. 7.13 summarizes the dependence of the normalized integral intensity of the (00)-peak and one of the equivalent pairs of all satellites I_j up to the third order as a function of the scattering phase S, between $S = 1.4$ ($E_e = 5$ eV) to $S = 7$ ($E_e = 118$ eV). Due to the strong Debye-Waller factor in the Bi film [131, 132, 133], the intensity is reduced remarkably at higher energies and higher temperatures. Therefore, the measurement could not be performed at energies higher than 120 eV at 300 K. Nevertheless, it is clear from the measured curve that with increasing the scattering phase, more and more intensity from the central spike is redistributed to the satellites. This dependence on S or $k_\perp$ must originate from a periodic morphological variation of the height of the surface. All the curves show no periodicity with integer values $\Delta S = 1$ of scattering phase S. Thus, the spot splitting could not be explained by any other periodic arrangement of atomic steps. The weak dependence of the satellite intensities on S (with large variations only for large changes $\Delta S > 4$ of S) could only be explained by a periodic height variation of the surface, which is much smaller than the bilayer step height $d_{Bi(111)}$ of Bi(111) surface.

Because the spot splitting occurs only in one direction we have to consider a grating−like periodic surface height undulation as a wave-like height function $h(x)$ with a periodicity length of $\langle a_{dis} \rangle$ (see chapter 2.1.5). For small values of a scattering phase S, spot intensities can be approximated by a parabolic behavior of the integral intensities as a function of scattering phase as given by Eqs. 2.34 and 2.35 in section 2.1.5.

The absolute values $|D_j|$ can be derived from the slope of the square root of the satellite intensity I_j for the very low scattering phase S. The parabolic behavior of the calculated intensities were fitted and shown by dotted blue color lines in Fig. 7.13(a), (b), (c) and (d). The absolute values $|D_j|$ derived from the slopes are $D_1 = 0.042 \pm 0.017$, $D_2 = 0.017 \pm 0.006$ and $D_3 = 0.011 \pm 0.004$ in units of step height of Bi bilayer $d_{Bi(111)}$. Assuming that the surface undulation described by the height function $h(x)$ (Eq. 2.33) is symmetrical, the Fourier coefficients obey the condition $D_j = D_{N-j}$ for $j \neq 0$. The most dominant first order Fourier coefficient produces a cosine-like surface undulation and the surface is equivalent to the periodic arrangement of the Lorentzian functions (Eq. 7.5), as has been sketched in Fig. 7.5(a). The peak to peak amplitude of the undulation can easily be derived from the first order Fourier coefficients as [134]: $\triangle h = 2\{D_1 - (-D_1)\}\, d_{Bi(111)} = 4D_1 \times 3.93\,\text{Å} = 0.66\,\text{Å}$.

The period of the surface height function $h(x)$, which is a measure of the periodic distance

[1] The integral intensity of each satellite peak and the central (00)-peak are calculated via $I_j = c\,(I_{peak,j} \times W_j^2)$ and $I_{00} = c\,(I_{peak,00} \times W_{00}^2)$, respectively, where $I_{peak,j}$ and $I_{peak,00}$ are peak intensities and W_j and W_{00} are widths (FWHM) of j^{th} order satellite peak and the (00)-peak, respectively.

[2] The normalization of the individual satellite peak and the central (00)-peak were carried out via $I_{norm,j} = {}^{I_j}/\left(I_{00}+\sum_j I_j\right)$ and $I_{norm,00} = {}^{I_{00}}/\left(I_{00}+\sum_j I_j\right)$, respectively, where $I_{norm,j}$ is the normalized intensity of each satellite spot of j^{th} order and I_{00} is the integral intensity of the (00)-peak.

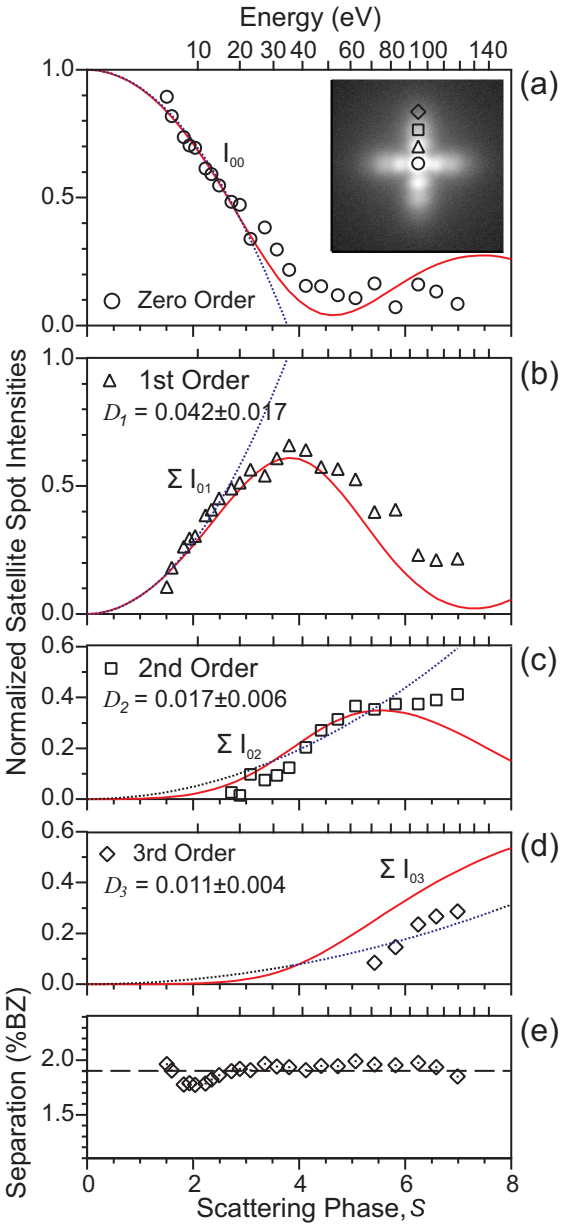

Figure 7.13: Normalized integral intensity of pairs of equivalent satellite spots vs vertical scattering phase S. Each intensity is normalized by the total intensity of the (00)-spot. Dotted lines represent the parabolic behavior (see Eqs. 2.34 and 2.35) for very low electron energies, i.e. large de Broglie wavelength. The corresponding Fourier coefficients D_j are also noted (see section 2.1.5). Solid lines represent simulated satellite spot intensity using the elasticity model described in the text. (a) Normalized intensity of the central peak (open circles). (b) (c) and (d) Normalized intensity of 1st, 2nd and 3rd order satellite peaks. (e) As a test for the consistency of the fit the satellite separation k_{dis} is also shown.

or the separation $\langle a_{dis} \rangle$ between each dislocation, was determined by measuring the distance between the satellite spots at different scattering phases S. The average separation calculated up to the large scattering phases is plotted in Fig. 7.13(e). The data shows a reasonable consistency with an average separation of $k_{dis} = 1.9$ %BZ (the dashed line in Fig. 7.13(e)), which corresponds to 20 nm in a real space. This behavior additionally supports the existence of a periodic height variation on the surface, rather than a vicinal train of a stepped surface, where the satellite peak separation depends on the scattering phase.

The ordering of the dislocation distance can be approximated via a distribution $P(a_{dis})$ of the dislocation distance a_{dis}. The widths of satellite spots give a direct estimation of the distribution $P(a_{dis})$. Fig. 7.14 shows the plot of measured peak width of each satellite including the central peak in the (00)-spot as a function of the satellite order. The order of the satellite peak can also easily be recognized in the insets of Fig. 7.13.

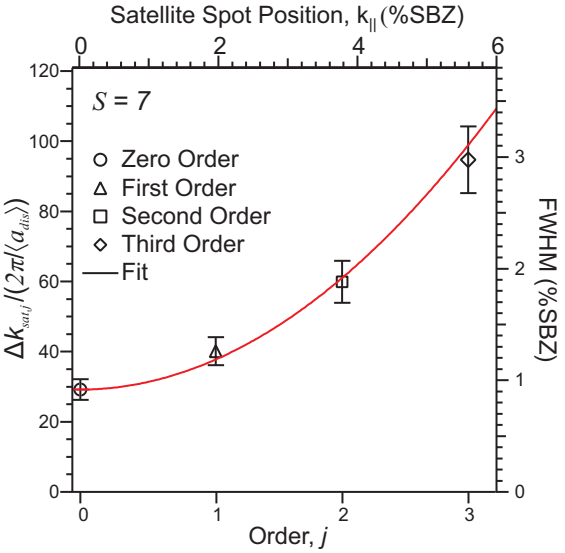

Figure 7.14: FWHM of satellite spots vs. spot positions from the central spike i.e., the (00)-spot of Bi(111). The curve can be fitted with the parabolic function (see Eq. (7.4)) with the slope of $\alpha^2 = 0.04$. To exclude spot broadening by surface roughness, the measurement was done at an in-phase scattering condition with an electron energy $E_e = 118$ eV, i.e., $S = 7$.

Assuming a Gaussian distribution $P(a_{dis})$ of the distances a_{dis} between neighboring dislocation lines, which is independent of the distance of the next neighbor (Markov chain) with a standard deviation σ

$$P(a_{dis}) = e^{-\frac{(a_{dis}-\langle a_{dis}\rangle)^2}{2\sigma^2}} \tag{7.2}$$

the FWHM of the j^{th} satellite spot is given by [135, 136]

$$\Delta k_{sat,j} = \sigma^2 k_{dis,j}^2 / \langle a_{dis}\rangle , \tag{7.3}$$

with $k_{dis,j} = (2\pi/\langle a_{dis}\rangle)j$. After normalizing with the average distance of dislocations $\langle a_{dis}\rangle$ i.e., in reciprocal space $2\pi/\langle a_{dis}\rangle$, we get

$$\frac{\Delta k_{sat,j}}{2\pi/\langle a_{dis}\rangle} = 2\pi\frac{\sigma^2}{\langle a_{dis}\rangle^2}j^2 = \alpha^2 j^2, \tag{7.4}$$

with $\alpha = \sqrt{2\pi}\,\sigma/\langle a_{dis}\rangle$. As expected from Eq. 7.4, the fit (red color solid line) clearly exhibits a parabolic increase of satellite width. From the parabolic fit, i.e., α^2 (see Fig. 7.14) the standard deviation of the occurrence of a_{dis} of j^{th} order satellite spot i.e., $\sigma/\langle a_{dis}\rangle$ is calculated to be 0.08. Thus, the separation between neighboring dislocations varies only by 8 %, i.e., ±16 Å around the mean value $\langle a_{dis}\rangle = 200$ Å. From this sharp distribution we can conclude that the repulsive interaction between the dislocations is high and as a consequence the height undulation on the surface is periodic, giving rise to well-ordered satellite spots.

A comparison of Bi with other systems allows an estimation of how much strain is necessary to induce the ordering of a randomly created set of dislocations. Ordered arrays of dislocations have been observed for a lattice mismatch larger than 2 % as with Ge(111) on Si(111) [51], Ag(111) on Pt(111) [52], or preferentially sputtered $Pt_{25}Ni_{75}$(111) [137]. In contrast to this such ordering is not observed for a lattice mismatch smaller than 2 % as for CaF_2 on Si(111) [138] or a $CoSi_2$ on Si(111) [139], where only a disordered network of interfacial dislocations was observed. This indicates that the formation of an ordered dislocation network is a general

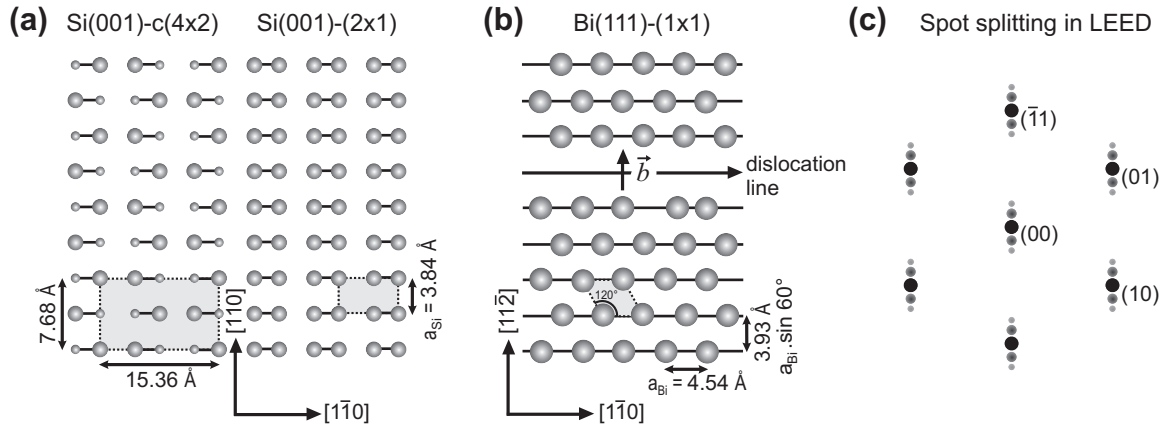

Figure 7.15: Lattice accommodation of the Si(001) substrate and a Bi(111) film lattice: (a) Geometry of the Si(001) surface. At low temperatures $T < 200$ K, a $c(4\times2)$ reconstruction of asymmetric buckled dimers is observed. At higher temperatures $T > 200$ K, a (2×1) dimer reconstruction appears. The unit cells are indicated by gray boxes. (b) Geometric structure of the Bi(111) lattice at the interface with a missing lattice plane indicating an edge-type dislocation. The Burgers vector $\vec{b}$ is oriented perpendicular to the dislocation line and along the direction of the dimer rows of the Si(001) lattice, i.e., along the [110] direction. (c) Resulting spot splitting in LEED due to the periodic height undulation caused by the periodic array of dislocations at the interface.

mechanism for strain relief in metallic, semimetallic and semiconductor heterosystems, as long as the lattice mismatch is large enough to ensure a sufficient overlap of the strain fields.

7.1.4.2 The geometry of interfacial dislocation network

Though both Bi(111) and Si(001) lattices show a completely different geometry, the interfaces match surprisingly well (see Fig. 7.3). The remaining compressive strain of 2.3 % along the Si dimer row is finally accommodated by an array of interfacial misfit dislocations. Figure 7.15(a) and (b) summarizes the interfacial geometry of the Si(001) and Bi(111) lattices at 150 K. The Burgers vector $\vec{b}$, which acts along [110], and the dislocation line, which is perpendicular to the direction of $\vec{b}$, are also shown in Fig. 7.15(b). The resulting spot splitting in LEED (satellite spots) due to periodic height undulation caused by the interfacial dislocations is also schematically shown in Fig. 7.15(c).

The geometry of the underlying dislocation network is further analyzed by comparing the satellite spot intensity with the prediction from a continuum theory of elasticity, applying the expression described by Springholz [124]. For the elastic deformation in an isotropic medium, the vertical surface deformation $u_\perp(x)$ above a single interfacial edge-type dislocation can be described by a Lorentzian function:

$$u_\perp(x) = \frac{b_{\parallel,edge}}{\pi}\left(\frac{t^2}{x^2+t^2}\right), \tag{7.5}$$

with x the lateral distance from the dislocation line, $b_{\parallel,edge}$ the edge component of the Burgers vector parallel to the interface plane [124] and t the layer thickness. The full width at half maximum of this depression at the surface is given by the film thickness t (see Fig. 7.5(a)).

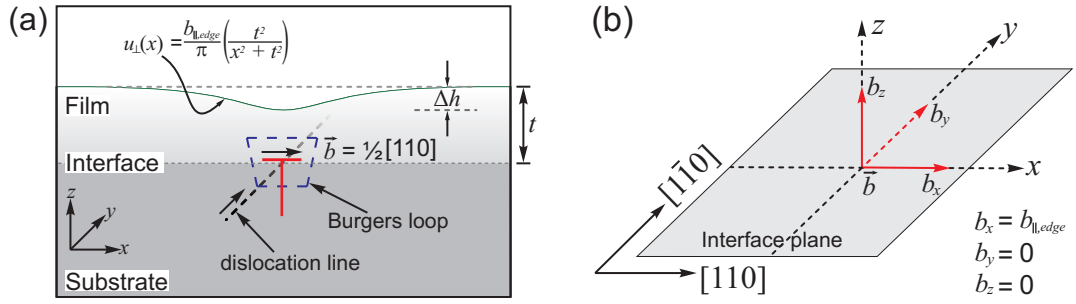

Figure 7.16: Schematic illustration of the misfit dislocation configuration in Bi(111) on Si(001). (a) Cross-section view, showing the substrate, the interface and the surface of the system. A downward depression $\triangle h$ above the dislocation $\overrightarrow{b} = \frac{1}{2}[110]$ and across the dislocation line exhibits a Lorentzian-like surface height profile shown with an arrow. (b) Plane view of the interface plane, showing three perpendicular components b_x, b_y, b_z of the dislocation vector $\overrightarrow{b}$. The only component b_x, which acts along the x-direction, i.e., along [110], exist in this system and symbolized by $b_{\parallel,edge}$.

Figure 7.16(a) illustrates a simple view of the dislocation geometry in the Bi(111) on Si(001) heterosystem. Each interfacial misfit dislocation (indicated by the red color symbol of inverted "⊥"), which causes a pronounced vertical depression $\triangle h$ via elastic distortion of the lattice. To show the direction of the gliding plane across the dislocation line, an interface plane is sketched in Fig. 7.16(b). The Burgers vector $\overrightarrow{b}$, which defines the configuration, i.e., the direction and the absolute value, of each dislocation, acts along three directions, as indicated by three components b_x, b_y, and b_z along x, y, and z directions, respectively. Comparing both figures (Fig. 7.15 and Fig. 7.16) and the grating-like arrangement of the dislocations observed via spot splitting in LEED (Fig. 7.12), it is clear that the existing dislocation acts along the [110] direction. Additionally, a vertical component b_z can also be extracted, since a previous STM study has confirmed no stacking faults at the Bi(111) surface [140]. From all of this information it can be assumed that only a full dislocation along b_x is possible to relieve the compressive strain of the film. A reasonable value for the Burgers vector is equal to the surface lattice spacing of the Si(001) substrate, i.e., $\vec{b} = \frac{1}{2}[110]$ parallel to the interface and with an edge component of $b_{\parallel,edge} = b_x = a_{Si(001)} = 3.84\,\text{Å}$.

Using those parameters, a film of thickness $t = 6$ nm and a separation of the dislocations $\langle a_{dis} \rangle = 200\,\text{Å}$, we therefore constructed the surface undulation by a semi-infinite sum of Lorentzian-like depressions given by Eq. 7.5. Each depression shows an amplitude of $\triangle h = b_{\parallel,edge}/\pi = 1.22\,\text{Å}$, which reduces to $\triangle h = 0.66\,\text{Å}$ (much smaller than the step height $d_{Bi(111)}$) at the thickness of 6 nm. Such a modulated surface and the reduction of the amplitude of the height undulation can also be observed in Fig. 7.5(a). This is analogous to the interaction of adjacent strain fields surrounding each dislocation. The intensity of the satellites was then simulated as a function of scattering phase S and plotted without any fitting parameters, as shown in Fig. 7.13 with solid red lines. The good agreement with the experimental data clearly supports the assumption of full edge-type dislocations with a Burgers vector $\vec{b} = \frac{1}{2}[110]$. The slight disagreement for large scattering phases S may be caused by disorder in the periodic arrangement of the dislocations.

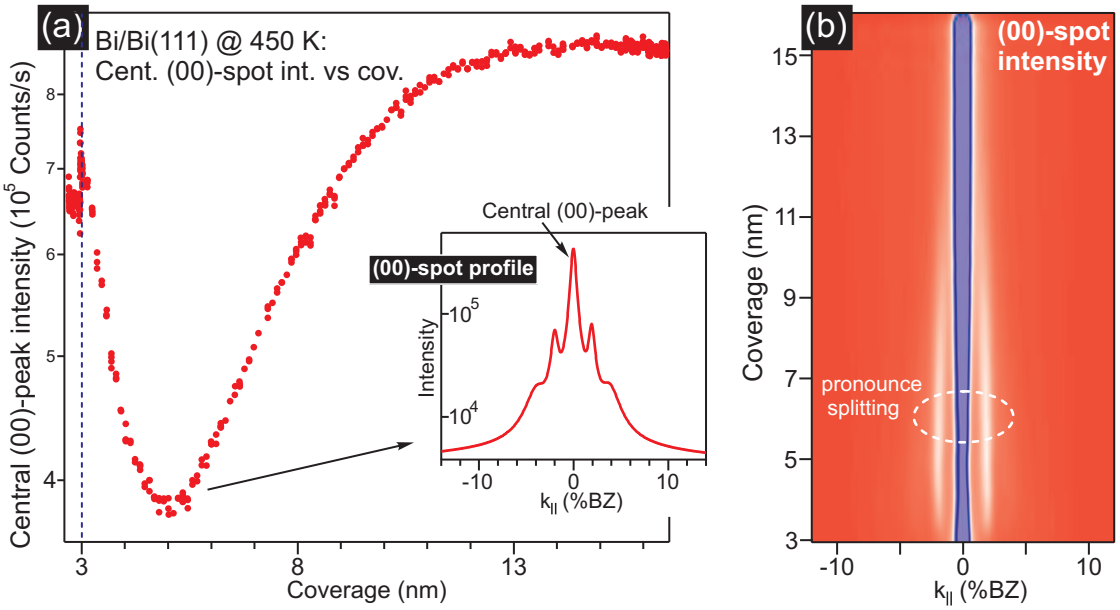

Figure 7.17: (a) Peak intensity of the central (00)-spot recorded during deposition of Bi on a 3 nm Bi(111) film at 450 K. The inset shows the (00)-spot profile recorded at ∼5.5 nm coverage. The satellite spots appear due to the nanoscale periodic dislocation pattern on the surface, which smoothes out with increasing coverage. (b) The intensity distribution of the (00)-spot as a function of coverage. At ∼ 6 nm, pronounced intensity of the satellite peak is observed (as indicated by the dotted line).

7.1.4.3 *In situ* smoothening of dislocation pattern

To study the smoothening behavior of dislocation pattern, (00)-spot profiles were recorded *in situ* during additional deposition of Bi on smooth Bi(111) films. Initially, as a first qualitative study, a 3 nm Bi film was deposited at 150 K and annealed to 450 K. The film is continuous, smooth and strained compressively by 1.3 % with the bulk crystal of Bi(111). Due to a lack of ordering of dislocations at the interface, no periodic height undulation was present at the surface, and as a result no splitting was observed. Additional Bi was deposited on this film at 450 K and the peak intensity of the central (00)-spot was recorded during deposition. As shown in Fig. 7.17, the peak intensity decreases up to 5-6 nm and starts to increase again. As shown by the inset of the corresponding (00)-spot profile at ∼ 6 nm coverage, the cause of changing of central peak intensity is apparent. Up to 6 nm, the intensity of the central peak is distributed to the satellite spots, since the density of the dislocation increases, which causes ordering and forms a dislocation pattern. As discussed in the earlier sections, such a surface causes spot splitting where the intensity of the (00)-spot is distributed to the satellite spots and consequently decreases the central peak. However, the central peak intensity starts to recover again after 6 nm and it continues until all the satellite spots get vanished. At 16 nm, a sharp single (00)-spot was observed with maximum intensity, indicating a surface without a dislocation pattern. The intensity distribution pattern in Fig. 7.17(b) illustrates the whole behavior of appearance and disappearance of the satellite peaks with increasing the coverage. It is evident from Fig. 7.17(a) that at around 6 nm the satellite spots are fully turned, indicating a maximum ordering of the dislocation network.

A similar experiment was performed again in a more systematic way. This time, additional Bi was deposited on a 6 nm well-annealed Bi(111) film. (00)-spot profiles were recorded *in situ* during deposition at 450 K. LEED pattern recorded after an additional deposition of 19 nm Bi film clearly shows sharp LEED spots (see Fig. 7.18(d)), indicating a flat and deformation free surface. To compare the resulting structure with the previous 6 nm film (Fig. 7.12(a)) the LEED pattern was taken under the same scattering conditions.

The development of the dislocation array with increasing film thickness was studied via *in situ* recording of satellite peak intensities during Bi deposition at 450 K. The intensity of individual peaks, i.e., the central spike and the satellites, of (00)-spot, the satellite spot separation and the FWHM of the first order satellites were calculated from the recorded profiles. Figures 7.18(a), (b) and (c) summarizes the data, which is plotted as a function of Bi coverage. With increasing Bi coverage the intensity of the central spike increases at the expense of the satellites. This behavior reflects the smoothening of the surface. This also suggests that the width of each depression in the surface height profile, as shown in Fig. 7.16, becomes so large that they finally cancel each other out [51].

Additionally, the separation of the satellites increases with coverage, reflecting the generation of more dislocations, i.e. further strain relief. The mean separation between the dislocations is reduced from 200 Å to 190 Å after an extra 10 BL coverage and stays almost constant with further deposition. At the same time, the width of the satellites is strongly reduced. These two situations reflect the increase of repulsive interaction between the dislocations with film thickness due to an increase of the overlap between adjacent strain fields [135]. Consequently, an enhancement of the repulsive interaction between the dislocations occurs, resulting in a better ordering of the dislocations.

From the FWHM ($\approx$ 0.7 %BZ) of the (00)-spot, a lower limit of $\sim$100 nm for the size of atomically flat islands can be estimated. In contrast, a film prepared by a single step process (i.e., the deposition of 30 nm Bi film at 150 K and subsequent annealing to 450 K) results in broader LEED spots (see Fig. 7.9(b)).

7.1.4.4 A STM study of the dislocation network

The topography of the Bi(111) films were studied by STM at two different coverage regimes: a low coverage regime, i.e., a 4.5 nm (strained film) and a 7 nm (relaxed film). The films were prepared in the STM equipped UHV chamber applying the same recipe, as discussed in section 7.1.2, and all the topographies were recorded at 130 K.

Figure 7.19(a) shows the STM topography of a 4.5 nm film. The presence of atomically flat and large 2D islands separated by a step height of 0.4 nm confirms the 2D growth mode found in a previous study. Smaller step heights originate from 0.136 nm steps of the underlying Si(001) substrate, which are overgrown by the Bi film in the so-called 'carpet mode' [126, 127]. A grain boundary of two crystallites rotated by 90° is also present. All these observations are indicated by dotted arrows in Fig. 7.19(a).

Additionally, long running, somewhat darker lines appear in the STM image. The surface

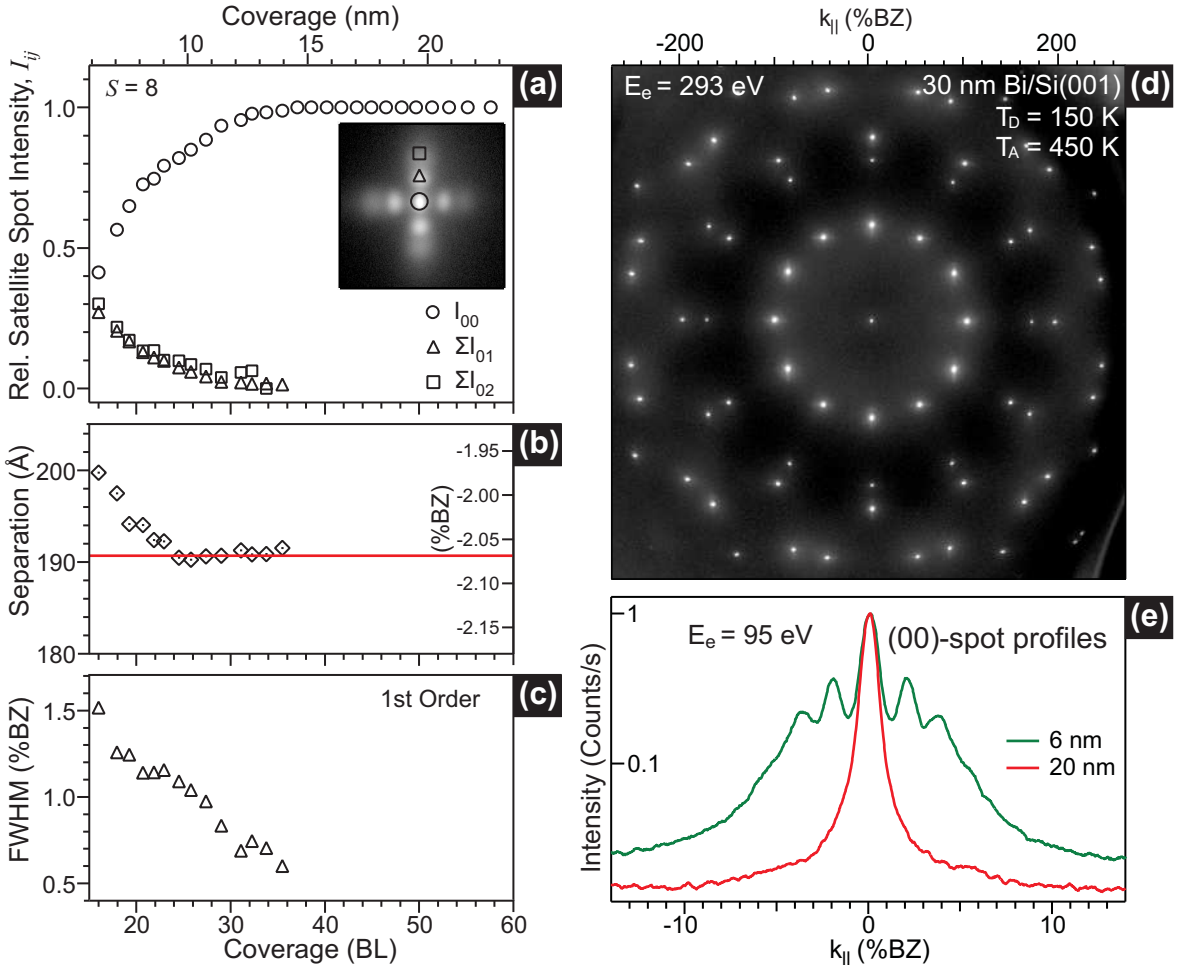

Figure 7.18: (a) The relative satellite spot intensity, (b) spot separation and (c) width of individual peaks of the satellite spots during additional deposition of Bi on a 6 nm Bi(111) film. Spot profiles were recorded in a RHEED-like geometry with an electron energy $E_e = 155$ eV ($S = 8$). (a) The steep increase of the central spike intensity I_{00} compensates for the decreasing intensity of the other satellite spots. (b) From the increase of the spot separation (right axis) a decrease of the mean separation between the dislocations from 200 Å to 190 Å is derived. (c) The FWHM of the first order satellite spot decreases with increasing film thickness. (d) LEED pattern of a 30 nm Bi(111) film (deposition of additional 24 nm Bi on the top of the 6 nm thick Bi film at 450 K) on Si(001). (e) (00)-spot profiles of a 6 nm Bi(111) film (green curve) and after additional 14 nm Bi deposition on the 6 nm film (red curve).

profile measured across each line shows a local surface depression, which is caused by the lattice distortion around each dislocation and indicates the presence of a misfit dislocation beneath the surface. As indicated by solid arrows in Fig. 7.19(a), these dark lines are aligned according to the Bi(111) crystallite orientation. This behavior confirms the 1D nature of the misfit dislocation array (like a grating) and explains the splitting of LEED spots at low coverage. Additionally, the topography clearly shows a large variation in the separation between the dark lines. Due to the large separation of the dislocations the interaction of adjacent strain fields is quite weak. This causes a large standard deviation of the average separation.

One of the isolated dark lines in the topography, which corresponds to a single non-

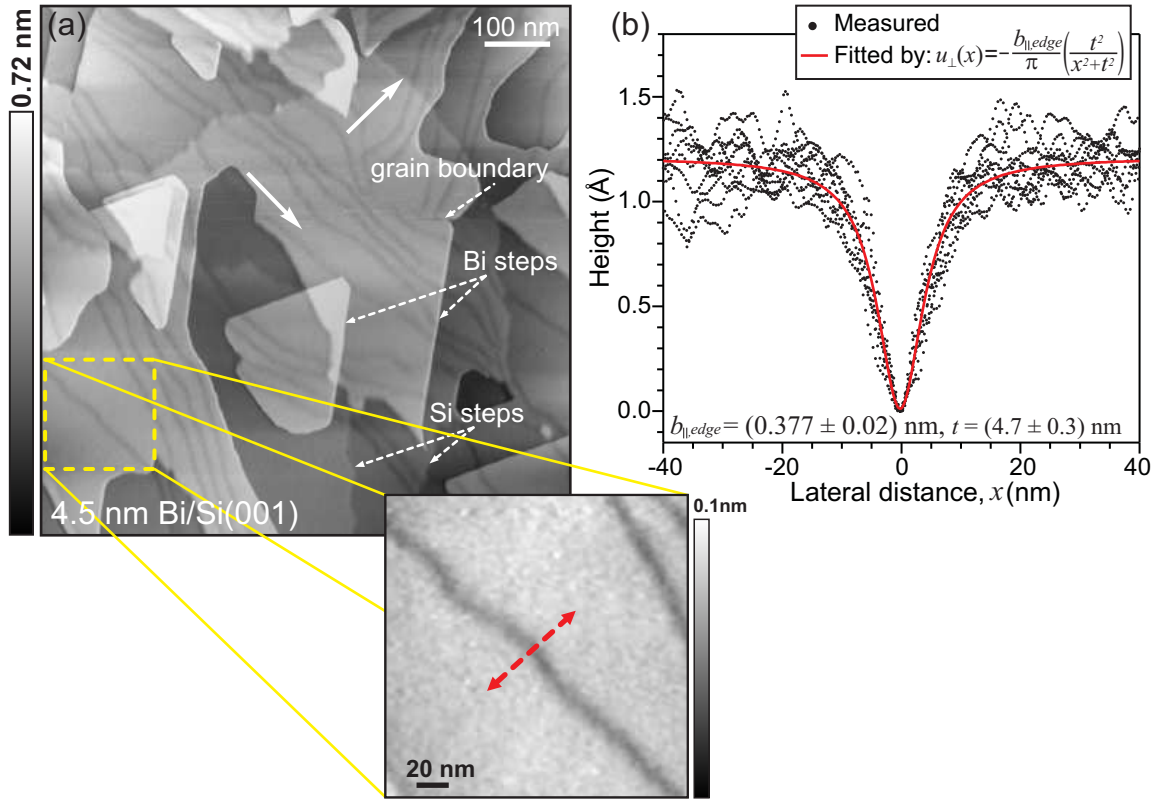

Figure 7.19: STM image (800× 800 nm^2) of a nominal 4.5 nm Bi(111) film on Si(001) taken in a constant current mode with $I_{\text{tunnel}} = 17$ pA at a positive sample bias of $V_{\text{bias}} = 1.8$ V. The surface depressions originating from strain fields at each dislocation are clearly visible as dark lines running across the surface. White arrows indicate the direction of the dislocation lines in two perpendicularly oriented (111) domains. Each Bi terrace terminates with a bilayer step height as indicated by the dotted arrows. The underlying Si-steps overgrown by Bi are also clearly visible in the topography (dotted arrows). To the right, surface height profiles from an isolated dislocation on one single terrace (dark dotted rectangle in the STM image) are shown as gray dots. The best fit with $b_{||,\text{edge}} = 3.77$ Å and $t = 4.7$ nm is shown with a solid line.

interacting dislocation, has been chosen to determine the value of the Burgers vector. The z-piezo was calibrated using the Bi(111) bilayer step height of $d_{\text{Bi(111)}} = 0.394$ nm as a reference. Many parallel height profiles from this particular terrace (indicated by the yellow dotted rectangle in the topography image of Fig. 7.19(a)) were overlapped and fitted with a Lorentzian function (Eq. 7.5), which describes the surface height undulation for an isotropic medium [124, 141]. From Eq. 7.5 it is obvious that the amplitude of the profile is defined by the edge component of the Burgers vector $b_{||,\text{edge}}$ and the shape of the depression is determined by the layer thickness t. The best fit for all parameters is shown by the solid red line in Fig. 7.19(b) with an edge component of the Burgers vector $b_{||,\text{edge}} = 0.377 \pm 0.02$ nm for a thickness of $t = 4.7 \pm 0.1$ nm. The value of $b_{||,\text{edge}}$ matches well with the atomic distance on Si(001) along the dimer row, i.e., $a_{\text{Si(001)}} = 0.384$ nm within the experimental error. This result is strongly supported by previous findings of a full edge type dislocation with a Burgers vector $\vec{b} = \frac{1}{2}[110]$ and a magnitude $b_{||,\text{edge}} = a_{\text{Si(001)}} = 0.384$ nm. From the good agreement between the thickness t from the fit and the deposited coverage of 4.5 nm we conclude that

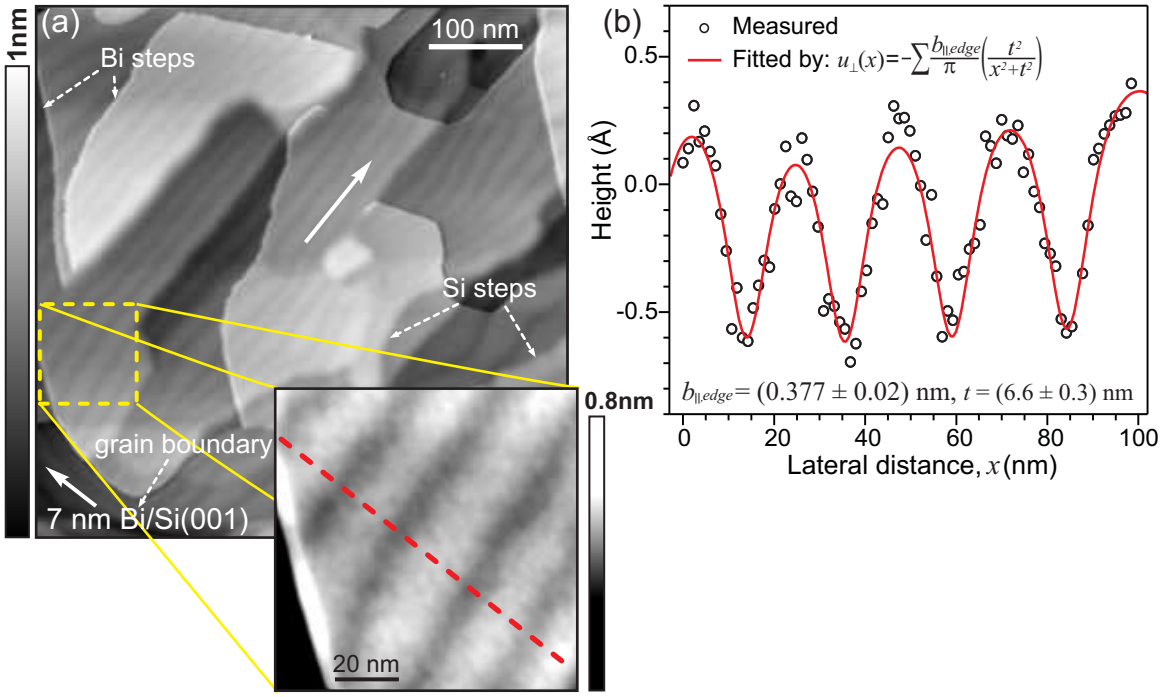

Figure 7.20: STM image (570× 570 nm^2) of a nominal 7 nm Bi(111) film on Si(001) recorded in a constant current mode with $I_{\text{tunnel}} = 17$ pA at positive sample bias of $V_{\text{bias}} = 1.8$ V. The surface corrugation, due to strain fields from the interfacial dislocation array, is clearly visible via dark lines running across the surface. The white arrows indicate the direction of the dislocation lines in two perpendicularly oriented (111) domains. As shown in Fig. 7.19(a), bilayer steps of Bi terraces and a grain boundary between the two domains rotated by 90° are clearly visible. Underlying Si steps are still visible in the topography. To the right, a surface height profile is shown by open circles, which is taken from a single terrace indicated by the dashed line within the dotted rectangle of the topography image. The best fit of the profile is shown as a solid line, yielding a height of $\triangle h = 0.07 \pm 0.01$ nm and an average separation of $\langle a_{dis} \rangle = 24$ nm.

the dislocations are indeed located at the interface between the Si(001) substrate and the Bi(111) film, which is the most effective location to relieve strain.

In the case of a relaxed film of a nominal thickness of 7 nm, as shown in Fig. 7.20(a), the topography changes as expected. The density of the dark lines of surface corrugation was drastically increased as compared to the thinner film. This reflects that more and more dislocations are introduced with increasing film thickness, which enhances the repulsive interaction between the dislocations, causing a much higher homogeneity in the separation between the dislocations. As a consequence, highly ordered parallel corrugation lines appeared at the surface. Figure 7.20(b) shows a surface height profile measured across the parallel corrugation lines. The profile was taken from a small region selected from one of the domains shown in the inset of Fig. 7.20(a). The wave-like periodic surface height undulation pattern is clearly visible. The data was fitted by applying a sum of Lorentzian functions given by Eq. 8.2. We used the Burgers vector of $b_{||,\text{edge}} = 3.77$ Å, which was obtained from the analysis of the thinner film shown in Fig. 7.19(b). We derive an average distance between the dislocations $\langle a_{dis} \rangle = 24$ nm, a corrugation $\triangle h = 0.07 \pm 0.01$ nm. A thickness $t = 6.6$ nm obtained from the fit parameter matches well with the nominal deposited thickness of 7 nm, indicating all

dislocations are located at the interface. Due to the increased overlap of the individual depressions the vertical height corrugation reduces from 0.12 nm to 0.07 nm, as the film thickness increases from 4.7 nm to 6.6 nm, and disappears for $t > a_{\mathrm{dis}}$ [51]. These results agree well with the previous results obtained from high resolution LEED analysis (see section 7.1.4.1). Additional Bi deposition on the 7 nm film results extremely smooth surface with very low defect density as shown previously in Fig. 7.5(b).

7.1.5 The interplay of the strain state, the dislocation and the lattice parameter

The morphology of lattice mismatched heteroepitaxial films is determined by the system's effort to relieve strain and to minimize the free energy [88]. In the case of the Stranski-Krastanov growth mode [142] of pseudomorphic films, strain is relieved by a roughening transition which allows an elastic relaxation towards the bulk lattice parameter of the materials [143, 144, 145, 146, 147]. This mechanism, together with the elastic response of the substrate, is the driving force behind the formation of almost any self-organized strained nanostructure. However, beyond a critical coverage the hetero system relieves strain by the generation of misfit dislocations [148, 149, 150, 151]. Ideally, these dislocations are located at the interface between substrate and heterofilm, accommodating the lattice mismatch, and leaving a relaxed film without threading dislocations as sketched in Fig. 7.21(c). Such ideal and rare situations have been found for Ag(111) on Si(001) [52], Fe(110) on W(110) [152, 153], Ag(111) on Pt(111) [125], EuTe(111) on PbTe(111) [124], and the surfactant mediated growth of Ge(111) on Si(111) [48, 123]. For heterosystems with a lattice mismatch $\triangle a_0 > 2$ % the separation between the misfit dislocations is close enough to ensure ordering into a periodic dislocation network through the elastic interaction of their strain fields [52, 152, 153, 125, 124, 48, 123, 137].

In this section a 6 nm Bi(111) film is used to demonstrate an interplay between strain relief by the formation of an interfacial misfit dislocation array and the change of the lateral lattice parameter. The lateral lattice parameter of the Bi film, together with the observation of misfit relieving dislocations, is measured simultaneously and precisely as a function of annealing temperature.

As discussed in an earlier section 7.1.2, the LEED pattern of a 6 nm thick Bi(111) film annealed at 450 K shows – as a superposition of two hexagonal diffraction patterns rotated by 90° – a quasi twelve-fold symmetry. Each spot of the two hexagonal patterns, however, exhibits a spot splitting into a series of satellites and appears to be elongated either in the [110]- or $[1\bar{1}0]$-directions, respectively. The spot splitting reflects the formation of a 1D periodic array of interfacial dislocations which adjusts the two lattices. The remaining lattice-mismatch of 2.3 % (causing compressive stress in the Bi film) along the Si dimer rows is the driving force for the formation of 1D dislocation array.

The lattice parameter $a_{\mathrm{Bi(111)}}$ is determined from the separation $\triangle k_{first} = 4\pi/(a_{\mathrm{Bi(111)}} \sin 60°)$ between the $(\bar{1}0)$ and (10) spot of the Bi film. The center of mass of these two integer order spots were used to consider spot broadening due to surface roughness and spot splitting due

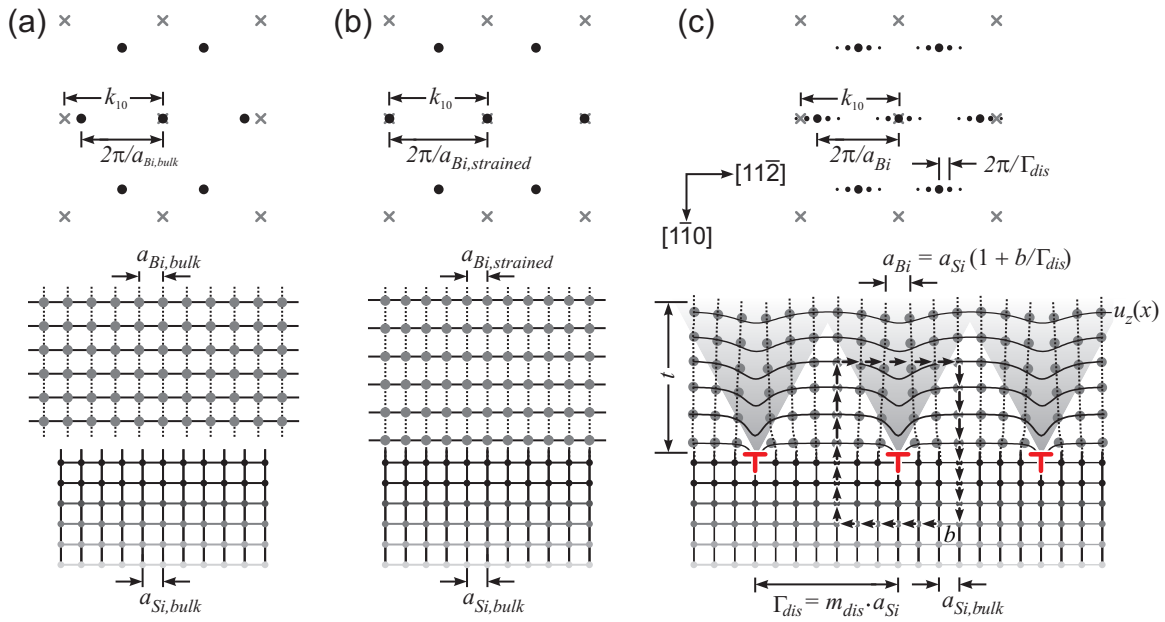

Figure 7.21: Schematic illustration of the strain state of an epitaxially grown Bi film on Si(001): (a) relaxed bulk materials, i.e., Si(001) substrate and bulk Bi(111), (b) pseudomorphically strained Bi(111) film, and (c) relaxed Bi(111) film of thickness t with an interfacial dislocation array (indicated by the symbol of inverted "⊥"'). The strain fields in the Bi film are shown in light gray. The Burgers loop surrounding the dislocation is indicated by a trace of small arrows with the Burgers vector b. On top of the sketches, corresponding LEED patterns are shown. The periodic surface height undulation $u_z(x)$ causes spot splitting into a linear series of satellites. As a reference frame, the square LEED pattern of the Si(001) substrate is plotted in gray '×' marks.

to the interfacial dislocation arrays. This method has independently been calibrated using the first integer order spots of the bare Si(001) substrate with a lattice constant of $a_{Si(001)} = 3.84$ Å at 300 K. This calibration is as precise as ±0.008 Å for the Bi(111) first order spots because the (10)-spots of Si(001) almost coincide with the (10)-spots of Bi(111), which are defined by the distance $a_{\mathrm{Bi}(111)} = (\sin 60° \times 4.533)$ Å = 3.926 Å between atomic rows on the (111) face at 300 K. The variation of $a_{\mathrm{Si}(001)}$ for temperatures between 150 K and 450 K is additionally plotted as open squares in Fig. 3. These data are described well by the small thermal expansion of bulk Si [154, 155]. The weak deviation for $T > 350$ K is considered as an experimental artifact and has been taken into account for the determination of $a_{Bi(111)}$. During annealing from 150 K to 450 K the lattice parameter $a_{\mathrm{Bi}(111)}$ of the 6 nm Bi(111) film (open circles in Fig. 7.23(a)) approaches almost its bulk value (dashed line) at 330 K. The film has relieved 85 % of the lattice mismatch of 2.3 %, i.e. the Bi lattice parameter $a_{\mathrm{Bi}(111)}$ becomes 99.65 % of its bulk value! The thermal expansion of Bi ($\alpha = 17 \times 10^{-6}$ K^{-1}) is almost one order of magnitude larger than that for Si ($\alpha = 2.6 \times 10^{-6}$ K^{-1}) for temperatures between 150 to 450 K. Above 300 K the Bi lattice parameter $a_{\mathrm{Bi}(111)}$ follows this trend and becomes slightly larger. The remaining strain stays constant at 15 %. The film - as deposited at 150 K - is strain relieved already by 30 %. Because the film is continuous and smooth (and therefore is not able to relieve strain by a roughening transition [143], it must already contain disordered misfit dislocations in order to show a larger row distance than the substrate. These defects

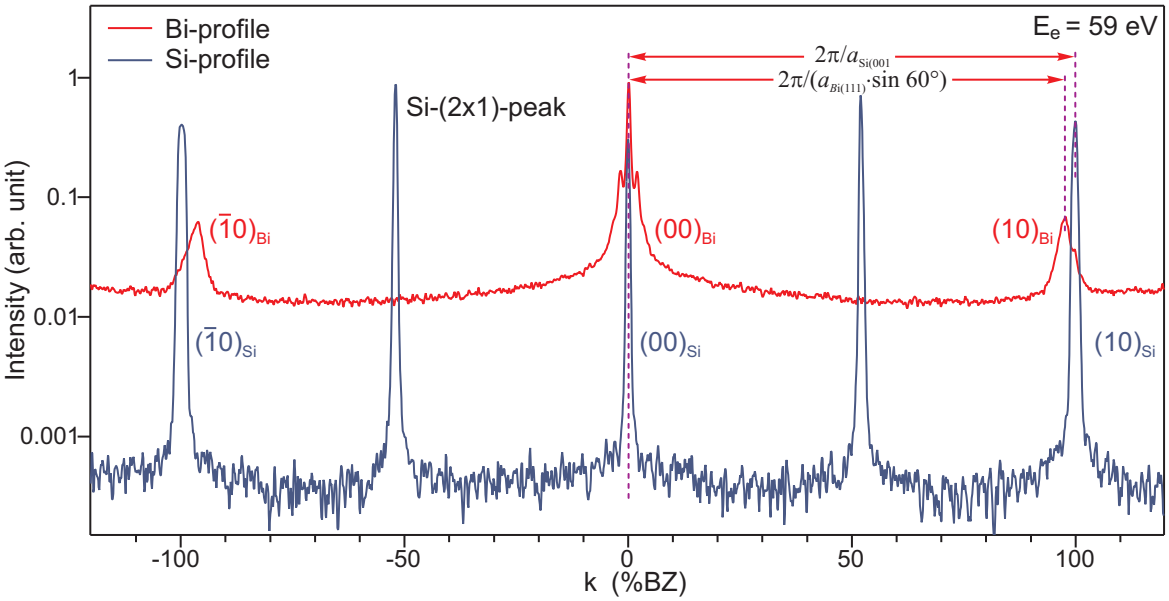

Figure 7.22: LEED spot profiles through the (00)-spot and the first integer order spots of a bare Si(001) surface and a 6 nm thick Bi(111) film at 59 eV (the (555) Bragg condition for Bi) plotted in % of a surface Brillouin zone of the Si(001) substrate (%BZ). The position of the (10)-spots of the bare Si surface has been used as calibration for the distance of the (10)-spots of the strained Bi(111) film. The high dynamic signal to noise ratio allows a precise determination of the spot position.

cause additional broadening of the (00)-spot as seen in Fig. 7.24(b) for 150 K. The broadening could not be caused by surface roughness because the spot profiles have been recorded at normal incidence with an electron energy of 59 eV, i.e., an in-phase or Bragg condition for electron diffraction where the electrons are insensitive to surface roughness [42]. With increasing annealing temperature the spot profile drastically changes its shape and all spots undergo a splitting transition into a linear series of satellites as shown in Fig. 7.24(a). These satellites with a separation of $\triangle k_{dis}$ result from a periodic surface undulation with an amplitude of less than 1 Å and a periodicity of $\Gamma_{dis} = 2\pi/\triangle k_{dis}$. The dislocation array relieves the strained Bi-film: Every $m_{dis} = \Gamma_{dis}/a_{Si(001)}$ atomic rows, a lattice plane of the Bi(111)-film is missing, allowing the expansion of the compressed Bi lattice towards its bulk value as sketched in Fig. 7.21(c).

The lateral lattice parameter $a_{Bi(111)}$ of a pseudomorphic strained Bi film without misfit dislocations is determined by the lattice constant of the substrate, i.e., the dimer separation $a_{Si(001)}$ of the Si(001) surface as shown in Fig. 7.21(b). If strain relieving misfit dislocations are present with a Burgers-vector $b_{\|,edge}$ oriented perpendicular to the dislocation lines (edge type) and an average separation of the dislocations $\Gamma_{dis} = m_{dis} \times a_{Si(001)}$, the lattice parameter $a_{Bi(111)}$ is expanded:

$$\begin{aligned} a_{Bi(111)} &= \left\{ a_{Si(001)} + \left(b_{\|,edge}/m_{dis} \right) \right\} / \sin 60^\circ \\ &= a_{Si(001)} \left[1 + \left\{ b_{\|,edge} / \left(m_{dis} \times a_{Si(001)} \right) \right\} \right] / \sin 60^\circ \end{aligned} \tag{7.6}$$

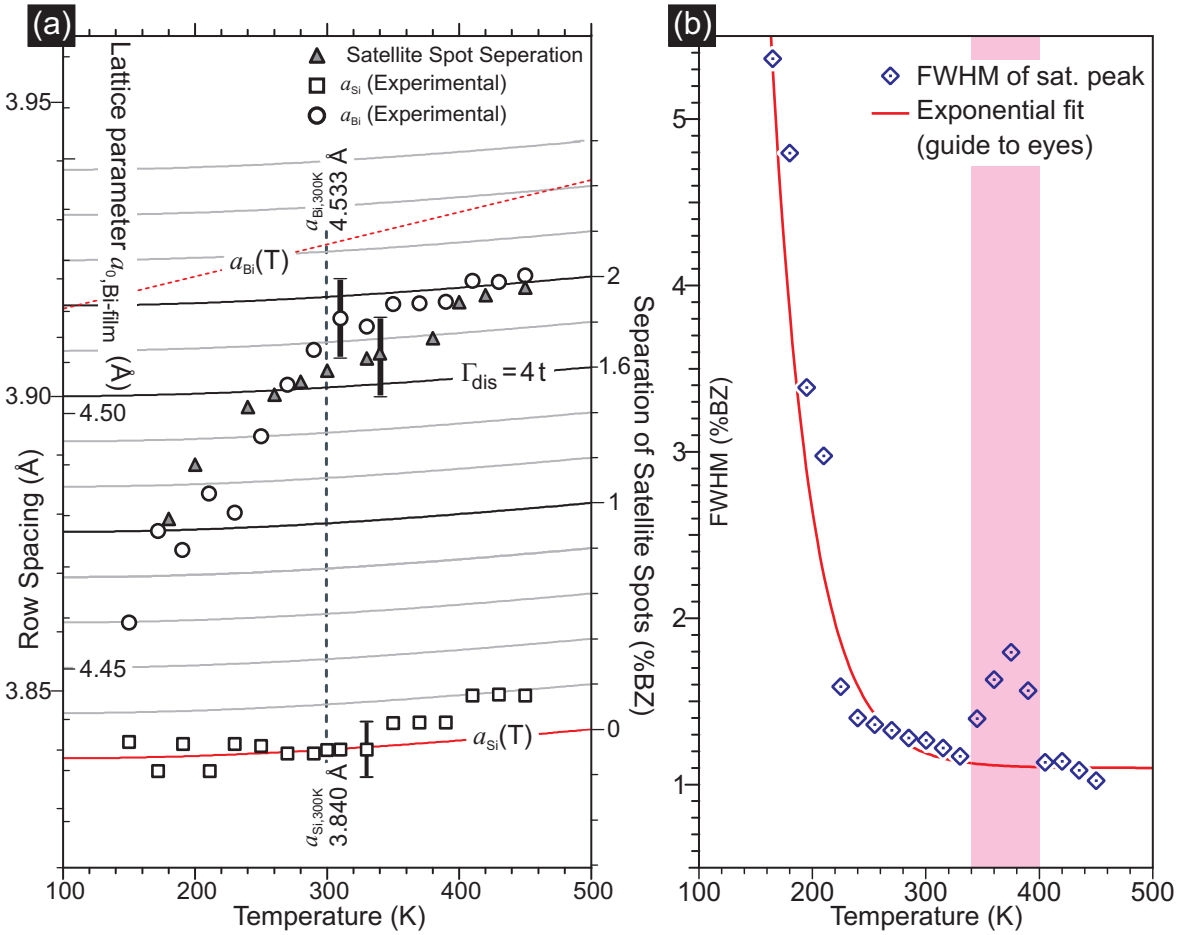

Figure 7.23: (a) Strain state of the 6 nm Bi(111) film during annealing from 150 K to 450 K with respect to the Si(001) substrate. The data is obtained from the distance between first integer order LEED spots and calibrated by the measured lattice parameter of Si(001) as a function of temperature (open squares). Thermal expansion of Si is given by the solid line. The lattice parameter $a_{Bi(111)}$ of the Bi(111) film (open circles) approaches at 300 K almost the Bi bulk value which is given by the dashed line (plotted is the row distance of Bi(111) lattice, i.e., $a_{Bi(111)} \times \sin 60°$. The spot splitting $\triangle k_{dis}$ from the dislocation array is plotted by filled triangles in fractions of the integer order spot separation, which in the case of full dislocations is identical with the change of the strain state of the Bi(111) film. (b) The width of the satellite spots decreases with dislocation density, indicating ordering. Plotted is the half width at half maxima. The red solid line represents the exponential fit for the guide.

Using the separation $\triangle k_{dis} = 2\pi / \left(m_{dis} \times a_{Si(001)} \right)$ of the satellite spot splitting we can express the Bi lattice parameter $a_{Bi(111)}$ directly as a function of the spot splitting $\triangle k_{dis}$ when it is measured in fractions of the integer order distance $k_{10} = 2\pi / a_{Si(001)}$:

$$a_{Bi(111)} = \left\{ a_{Si(001)} + \left(b_{\parallel,edge} \frac{\triangle k_{dis}}{k_{10}} \right) \right\} / \sin 60° \tag{7.7}$$

Because $b_{\parallel,edge}$ is equal to $a_{Si(001)}$ we end up with,

$$a_{Bi(111)} = a_{Si(001)} \left(1 + \frac{\triangle k_{dis}}{k_{10}} \right) / \sin 60° \tag{7.8}$$

i.e., the spot splitting $\triangle k_{dis}$ in fractions of the integer order spot separation ($k_{10} = 100$ %BZ) is a direct measure of the strain, which is relieved by the periodic dislocation array. Ideally, the spot splitting $\triangle k_{dis}$ and the corresponding change of the lattice parameter $\triangle a_{Bi(111)}$ must show the same behavior if $b_{\parallel,edge}$ describes a full dislocation. This spot splitting $\triangle k_{dis}$ is plotted in Fig. 3 with filled triangles as a function of the annealing temperature. For $T =$ 150 K we do not observe satellite spots, i.e., there is no ordered dislocation array formed at the interface yet. For $T > 180$ K an increase of the satellite spot separation from $\triangle k_{dis} = 1.2$ %BZ to 2.0 %BZ is observed, i.e., an increase of the density of dislocations from one each 330 Å to 190 Å. The maximum separation of 2.0 %BZ corresponds to an increase of the lateral lattice parameter of the strained Bi film by 2.0 % to 4.539 Å, which corresponds to a 85 % relaxation of the 2.3 % lattice mismatch at 450 K between Si and Bi (a lattice parameter of bulk Bi, $a_{Bi(111),bulk} = 4.544$ Å at 450 K). With the increasing temperature obviously more and more dislocations are generated in order to relieve the lattice mismatch-induced strain in the Bi(111) film. Because both curves match well we can conclude that for all temperatures the change of the lattice parameter (open circles) can be solely explained by the formation of the ordered interfacial dislocation array (filled triangles). Above 300 K the density of dislocations and the Bi lattice parameter increases parallel to the thermal expansion of the Bi film with a remaining strain of 15 %. This is explained by the necessity of the buildup of sufficient strain for the formation of additional dislocations [150].

7.1.6 Irreversible order-disorder transition of the dislocation network

In the previous section, it was observed that the sharp satellite peaks were suddenly diminished at around 370 K during the first annealing step after the deposition of a 6 nm Bi film on Si(001) at 150 K. The satellite peaks were recovered again at 390 K. To confirm the observed behavior and gain some insights into the underlying physical phenomena we reproduced the same results and additionally recorded (00)-spot profiles during cooling the film from 450 K to RT. Fig. 7.25 summarizes both results, where the recorded (00)-spot profiles are shown with red and blue color solid lines, for annealing and cooling steps, respectively. The peak intensity distribution images are also presented for each case (annealing and cooling), which are quite helpful to distinguish and follow the satellite peak intensity at different temperatures.

In Fig. 7.25(a) it is apparent that the satellite peaks are clearly observable at 340 K. With increasing temperature, however, they are less pronounced and almost overlapped by the central peak at 380 K. Interestingly, the satellites reappear and become sharper with increasing the temperature up to 450 K. Such behavior could be observed more clearly in the intensity distribution image Fig. 7.25(b), where the transition region has been marked by a dotted line. In the region of 370−390 K the intensity line of satellite peaks around the central peak (the white lines) can hardly be distinguished due to an overlapping with the central peak resulting in a shoulder-like profile.

In contrast, the (00)-spot profiles, recorded during the cooling of this annealed film, show no noticeable changes at any temperatures (see Fig. 7.25(c), except the decrease of intensity,

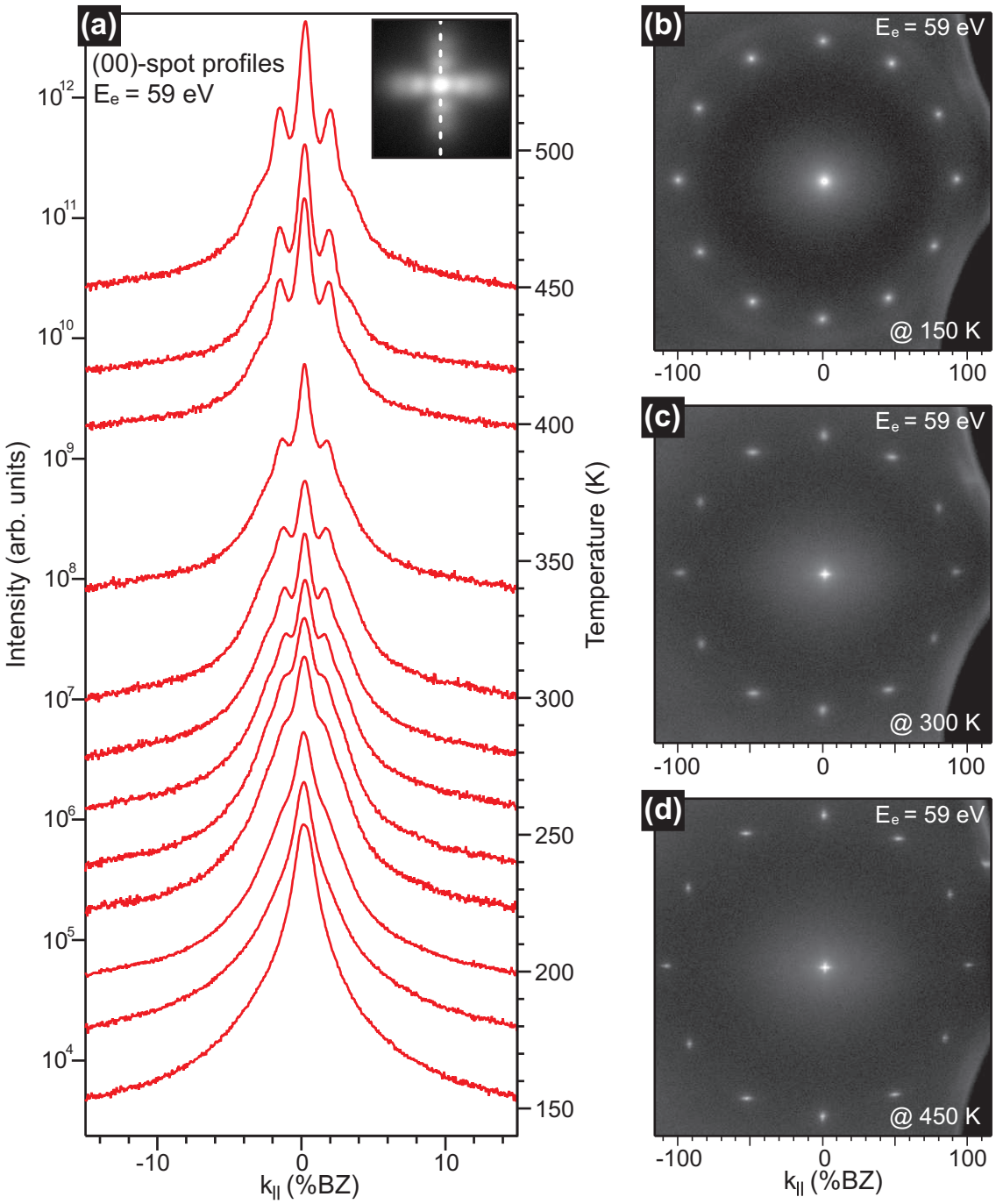

Figure 7.24: LEED (00)-spot profiles from a 6 nm thick Bi(111) film as a function of annealing temperature T. The profile becomes sharper with increasing T. For T >250 K all spots show a splitting into a series of satellites. The spot splitting is most pronounced at an annealing temperature of 450 K. (b), (c), and (d) LEED patterns of the same film recorded at 150 K, 300 K and 450 K, respectively. The first order spots become elongated during annealing and the elongation is directed along the [110] or [1$\bar{1}$0] direction due to having the two 90° rotated Bi(111) domains. The (00)-spot shows the '+' sign due to the overlapping of both domain spots. The spots get split into a series of satellites as apparent from the LEED pattern at 300 K and 450 K. An in-phase scattering condition (E_e = 59 eV, $S \sim 8$) has been used during recording the profiles and patterns because the in-phase condition is insensitive for surface roughness and sensitive to the vertical corrugation.

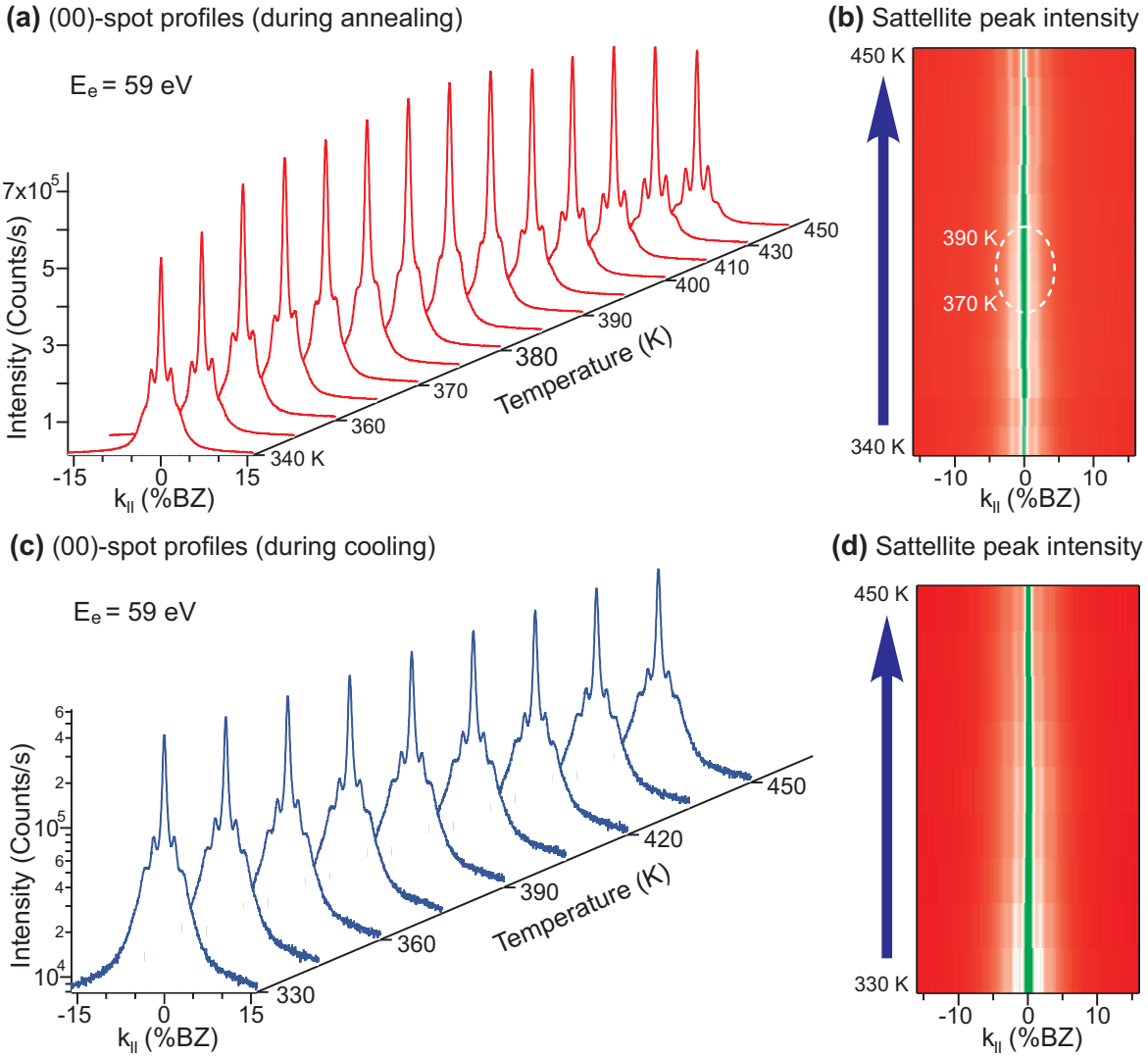

Figure 7.25: *In situ* observation of the ordering of the dislocation network: (a) LEED (00)-spot profiles of a 6 nm Bi film on Si(001) recorded during first annealing after deposition at 150 K. (b) The intensity distribution of the (00)-spot profiles shown in (a). Both (a) and (b) show a vanishing of the satellite peaks at $\sim$ 370 - 390 K. (c) LEED (00)-spot profiles of the same film during cooling down from 450 K to 330 K. (d) The intensity distribution of the profiles shown in (c). Both (c) and (d) images show a gradual change of intensity, without vanishing of the satellite peaks.

which is due to the Debye-Waller effect. Also, in the intensity distribution image to the left (Fig. 7.25(d)), the satellite peak intensity lines (white lines) are clearly visible at each temperature.

Such an observation of the irreversible change of (00)-spot profiles cannot be explained solely by the smoothening effect of the surface during first annealing the film after deposition at a low temperature. In the case of smoothening or morphological transition, the terrace size increases monotonically beyond the transition or critical temperature T_c [45]. There might be other mechanisms, which cause irreversible and continuous transition. Among them, two mechanisms are known to yield increased density of a thermally generated adatom/vacancy gas on the surface. One is a thermal roughening transition and the other one is a surface

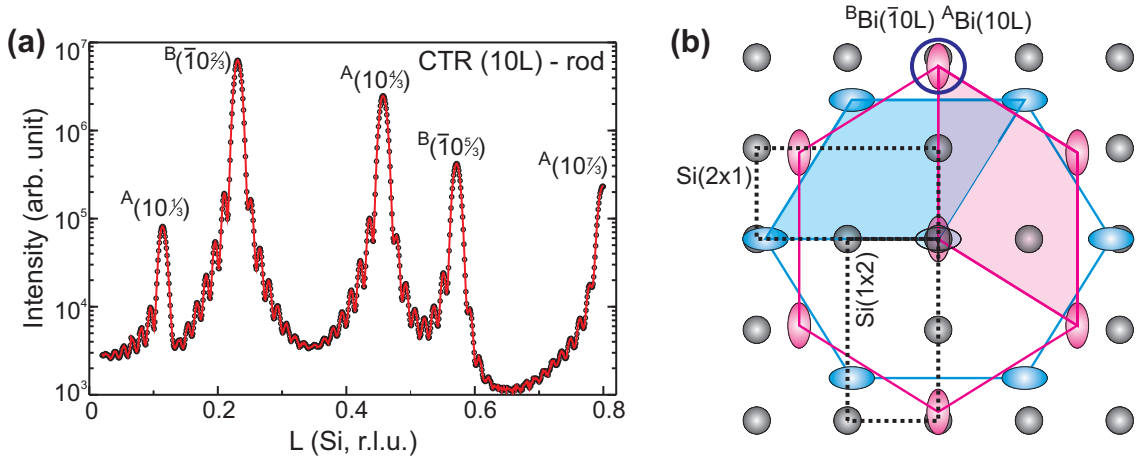

Figure 7.26: (a) Vertical intensity distribution of the (10L) CTR (crystal truncation rod) of the A-type grown Bi(111) on the Si-(1×2) substrate domain, indexed with 'A'. The Bragg conditions of the ($\bar{1}$0L) rod of the B-type grown Bi(111) (rotated by 180° around the surface normal) are also located on this scan and indexed with 'B'. (b) Two dimensional sketch of the inplane location of the CTRs originated by both substrate domains (gray spheres) and the resulting four bismuth species (A-type on Si(1×2), B-type on Si(1×2), A-type on Si(2×1) and B-type on Si(2×1)).

pre-melting transition [156, 157, 158, 159, 45, 160]. Yaginuma *et al.* [161] have observed both irreversible transition (surface morphology change) and reversible transition (surface pre-melting) in epitaxially grown Bi(111) films on Si(111). They found the critical temperature of T_c = 350 K for those transition. Our transition range of temperatures is 370-390 K, which is not far from the 350 K, so we cannot exclude the similar behavior in our Bi films. However, the long range periodicity of the dislocation network could not be destroyed by such a morphological change. Since the (00)-profiles have been recorded at in-phase conditions, the morphological information may be lost in the intensity profiles we have recorded. From the discontinuous change of profiles (Fig. 7.25(a) and (c)), we cannot directly confirm the morphological change, as seen by Yaginuma *et al.* [161]. We can only speculate that there must be some dynamics of the dislocations, which might play a deciding role. All those observations and the evidence of irreversible disordering transition demands more experiments and a theoretical investigation.

7.1.7 Film morphology study by the synchrotron-based GIXRD/XRR

In the previous sections, the surface morphology of the Bi(111) film was exclusively discussed via characterization of various features such as surface roughness, defect structures, and lattice parameters using conventional surface science techniques such as SPA-LEED, AFM, STM and laboratory-based XRD. However, the interfacial quality of the film was unknown. Here, additional important features, such as the interface roughness and the layer thickness variation, will be determined via synchrotron-based x-ray diffraction and x-ray reflectivity (XRD/XRR) measurements.

The measurements were performed at the beamlines BW2 and W1 at HASYLAB, Hamburg. The Bi(111) template film, prepared by following the recipe described earlier in 7.1.2, was

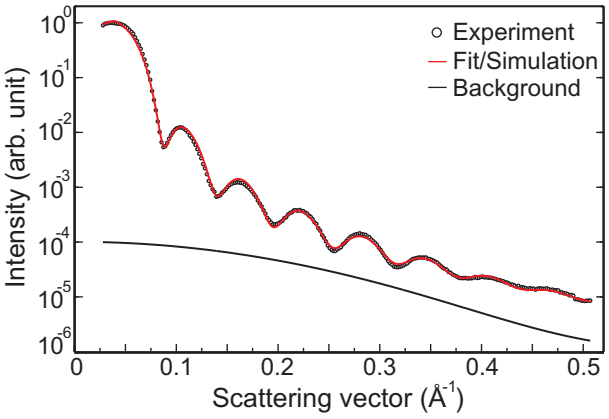

Figure 7.27: Specularly reflected intensity as a function of the scattering vector for a 9 nm Bi(111) film on Si(001) prepared by deposition at 150 K and annealing to 450 K. The closed circle represents the experimental data and the red color solid line is the best fit using the density profile simulation.

examined by two different x-ray techniques: grazing incidence XRD (GIXRD) and x-ray reflectivity (XRR) (Chapter 2.4).

Figure 7.26 shows the intensity along the crystal truncation rod, in (10L)-direction of the Bi(111) film and the schematically represented in-plane location of the CTRs of the corresponding system. The Si(001)-(2×1) spots of the underlying substrate are sketched with gray spheres and the hexagonal Bi(111) spots are denoted with elongated colored symbols. The two 90° rotated domains, caused by the two different substrate domains, are shown with different colors and can be clearly distinguished by the direction of the spot elongation. In each of these rotational domains two different twin domains are present (see AFM study in section 7.1.3.1), which are named 'A' and 'B' (rotated by 180° around the surface normal). The existence of these two twin domains can be verified by their Bragg conditions in the CTR measurements as shown in Fig. 7.26(a). On the (10L) CTR the Bragg condition of both species, A-type and B-type, are present. The intensity shows well-developed film thickness fringes, indicating a very smooth film. From their periodicity we have estimated the thickness of the film $t_{\mathrm{XRD}} = 9.4 \pm 0.5$ nm and an average surface roughness of $\sigma^{\mathrm{surf}}_{\mathrm{rms(XRD)}} = 0.7 \pm 0.03$ nm. From the Bragg-peak positions of the (10L)-rod, a vertical layer distance of $d_{\mathrm{Bi(111)}} = 0.3944 \pm 0.0002$ nm was calculated. This value matches its bulk value, confirming a complete relaxation of the film along the (111) direction.

The template Bi(111) film was also studied by specular reflectivity XRR measurements. Figure 7.27 shows the specularly reflected intensity distribution as a function of the scattering vector. The measured data can be fitted well with the simulation, performed by using a program based on the Parratt algorithm [162]. The best fit confirms that the film has a thickness of $t_{\mathrm{XRD}} = 9.2 \pm 0.5$ nm, an average surface roughness of $\sigma^{\mathrm{surf}}_{\mathrm{rms(XRR)}} = 0.8 \pm 0.04$ nm, and an interface roughness of $\sigma^{\mathrm{interf}}_{\mathrm{rms(XRR)}} = 0.85 \pm 0.04$ nm. From these extremely low roughness values, we can get a signature of an abrupt interface and a smooth surface of the film.

7.1.8 Initial stages of growth

It has been discussed in an earlier section (Sec. 7.1.2) that the (00)-intensity plot as a function of coverage clearly shows two distinct regions of coverages, as symbolized by (I) and (II) in

Fig. **??**(b): (I) discontinuous region of irregular intensity variation, which extends up to the 5.6 BL, (II) continuous region with regular intensity oscillation, which extends beyond that. The irregular intensity variation at the region (I) is caused by the change of the surface reconstructions induced in the sub-monolayer region. In the following such structural changes at the initial stages of growth is explained via LEED images recorded at different coverages.

Fig. 7.28(b)−(i) summarizes various reconstructions via series of LEED patterns recorded at different coverages, as indicated by arrows in the intensity plot in Fig. 7.28(a). At the very beginning, the out-of-phase intensity of the (00)-spot drops sharply until 0.3 BL and increases slightly to 0.6 BL. This behavior attributes the nucleation processes at the early stage of growth, where small Bi adatom islands are randomly distributed on the flat Si terraces. This causes a diffuse background in the (2×1) reconstructed LEED pattern, as seen in Fig. 7.28(b). Additionally, the surface shows a weak (2×2) reconstruction, which lasts until 0.6 BL. However, the diffuse (2×1) pattern still remains (Fig. 7.28(c)), indicating a Bi-induced dimerization, as suggested by previous studies [163, 164, 165, 166]. According to the model suggested by Tang *et al.* [163], Bi adsorption on the Si-dimer (bridge site) favors the (2×2) reconstruction, which occurs below 0.5 BL. Beyond 0.5 BL, Bi starts to adsorb between the dimer rows (cave site), which eventually causes a large relaxation on the surface, leading to the breaking of Si-dimers. This process favors the dimerized Bi-(2×1) structure, the same as Si-(2×1) except for the dimer rows running perpendicular to the Si-dimer rows. Such a process of forming its own dimers at very low coverage leads to a weak phase transition, i.e., (2×2) to (2×1) (Fig. 7.28(b) to 7.28(c)). Additionally, the Bi-(2×2) structure might be distributed only around the local areas on the Si terraces, since any adsorption at the cave site destroys the (2×2) order. This effect has been observed in the LEED image (Fig. 7.28(a)) where diffuse and weak (2×2) spots appears at 0.3 BL.

Further coverage increase up to 2.2 BL leads to a massive increase of disordered crystallites, as evident from the drastic drop of the (00)-spot intensity and extremely high background intensity of the LEED pattern (Fig. 7.28(d)). Shortly at 2.6 BL, 3D crystallites grow in a preferred direction. The LEED pattern shown in Figure 7.28(e) shows sharp 12-fold symmetry first order spots surrounding the (00)-spot. Those 12-fold symmetry spots appear from the incoherent superposition of two hexagonal (1×1) domain spots rotated by 90° with respect to each other. The formation of two 90° domains originates due to the underlying terrace orientation, as discussed in earlier sections. Interestingly, a (7×2) reconstruction is additionally visible. This is similar to the high temperature phase of Bi at sub-monolayer coverages on Si(001), forming a missing dimer reconstruction with a periodicity of $(n \times 2)$ [167, 168]. The n stands for the periodicity length and decreases with the temperature from $n = 13$ at 820 K to $n = 5$ at 530 K [167]. Nevertheless, an appearance of 700 K phase of Bi at 150 K is the first observation of its kind.

After 2.6 BL coverage, the (00)-spot intensity increases rapidly and reaches the same level as 0.6 BL. The LEED image shows a remarkable change in the structural phase (Fig. 7.28(f)). A pronounced ring of diffuse intensity appears surrounding the first order spots and the (7×2) reconstruction disappears. A real-space distance $a_{\mathrm{ring}} = 0.322\,\mathrm{nm}$ is estimated by

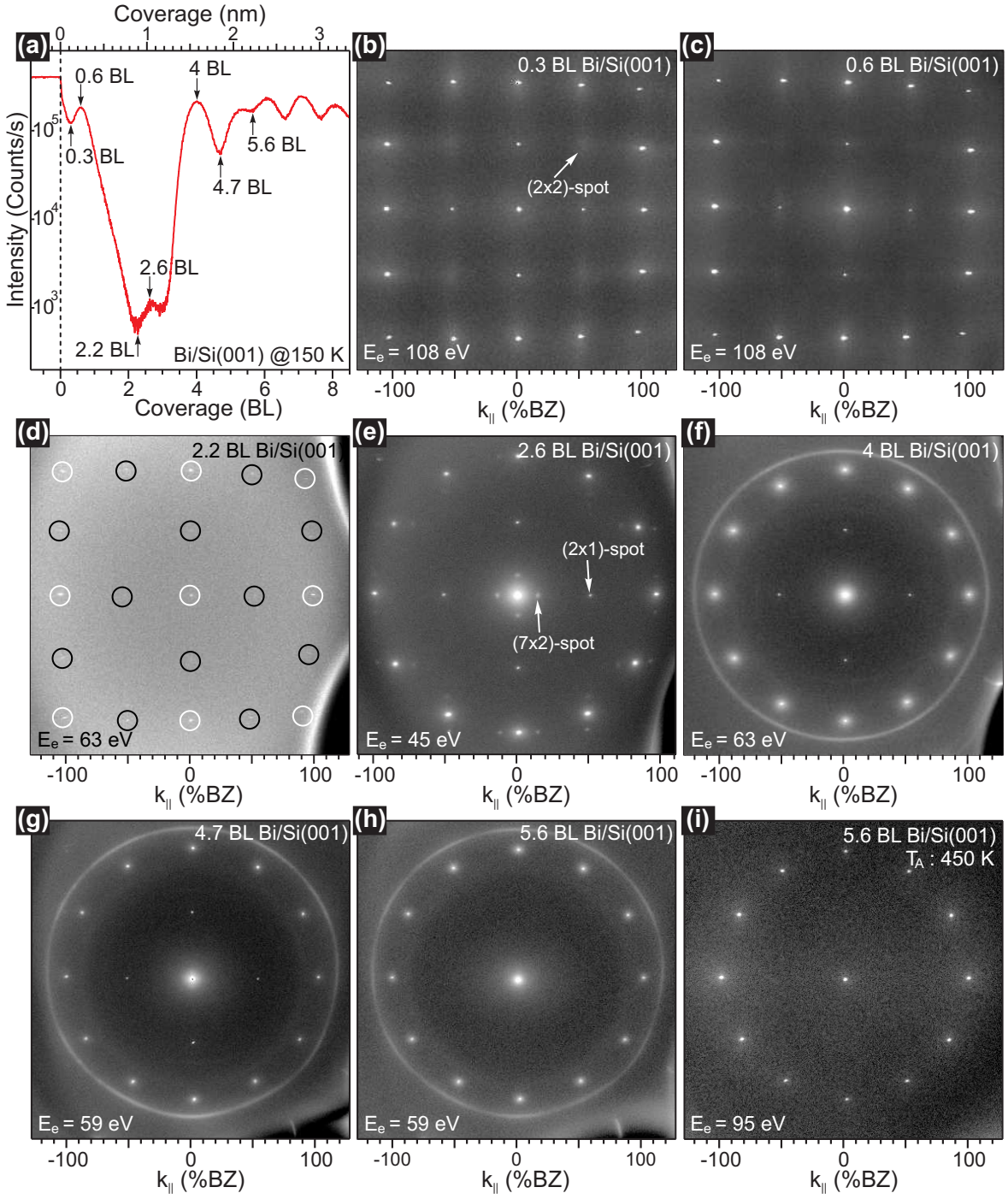

Figure 7.28: (a) The (00)-spot intensity vs. coverage, recorded during deposition of Bi on Si(001)-$c(4\times2)$ at 150 K. The (00)-spot intensity undergoes many maxima and minima due to the structural transformations from sub-bilayer phases, the so-called Bi-induced reconstructions, to the different crystallographic orientations at higher coverages. (b)−(i) Series of LEED patterns recorded at various coverages of Bi. The bottom right pattern is recorded after annealing the thinnest continuous film (5.6 BL) to 450 K. Various structures and the change of morphology have been described in the text.

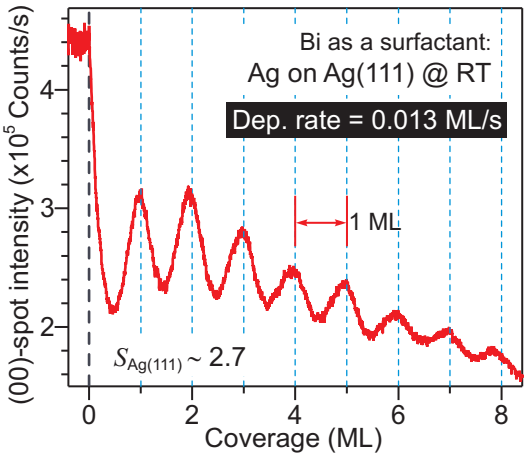

Figure 7.29: LEED specular intensity during surfactant mediated epitaxy of Ag on Ag(111) at RT. The (00)-spot intensity oscillates with the coverage in a layer-by-layer fashion. The amplitude of the oscillation decreases with increasing the coverage, indicating a slow buildup of surface roughness. The scattering condition of $S \sim 2.7$ was used to record the (00)-spot intensity.

$a_{\text{ring}} = 2\pi/k_{\text{ring}}$, which almost matches with the distance of the {011} lattice planes of the Bi(110) surface [24], i.e., $a_{\text{Bi(110)}} = 0.328\,\text{nm}$, with remaining compressive strain of ~ 1.8 % . This estimation shows that rotationally disordered Bi(110) crystallites appear at a coverage of $\sim$ 4 BL. However, the (111) crystallites are dominant and highly ordered as compared to the (110) crystallites. Moreover, the intensity of the ring weakens as the temperature increases during annealing and vanishes completely above 230 K. This behavior suggests that the Bi(110) crystallites may have nucleated at defect sites, such as grain boundaries and vacancies. Such kinds of thermally metastable structure was also reported in a previous publication [140]. An analogous allotropic form was also observed previously in a Bi/Si(111) system at room temperature [20, 24], where Bi(110) orientation undergoes a complete transformation into the Bi(111) orientation after 4.5 ML coverage, showing a coverage dependent structural transformation. We have not, however, observed such a complete structural transformation. The ring exists beyond the 4 BL, as evident from the LEED images Fig. 7.28(g) and (h). At 5.6 BL, LEED image exhibits only (111) and (110) crystallites, the (2×1) spot disappears. This confirms a critical coverage for the continuous Bi(111) film, where the continuity of the film sustains even at 450 K (see Fig. 7.28(i)). From this regime, the (00)-spot intensity starts to oscillate with coverage, which has been shown in the previous sections.

7.2 Ag(111)/Si(001)

It is well known that the heteroepitaxial growth of metal on semiconductor is dominated by many problems, which arise from the difference of lattice parameters, surface and interface free energies and the kinetics of growth. Most of the metals form 3D islands at higher temperatures (> 300 K) due to the high mobility of atoms [169, 170]. Continuous films could be grown at low temperatures, however, high density of defects may incorporate into the film [171]. Additionally, metal layers tends to roughen during growth due to higher inter layer diffusion barrier (*Ehrlich-Schwoebel* step edge barrier), which hinders the 2D growth [172, 173, 174]. Most often the metal/semiconductor systems are lattice mismatched and have different crystallographic structures, which also increases the tendency towards island-

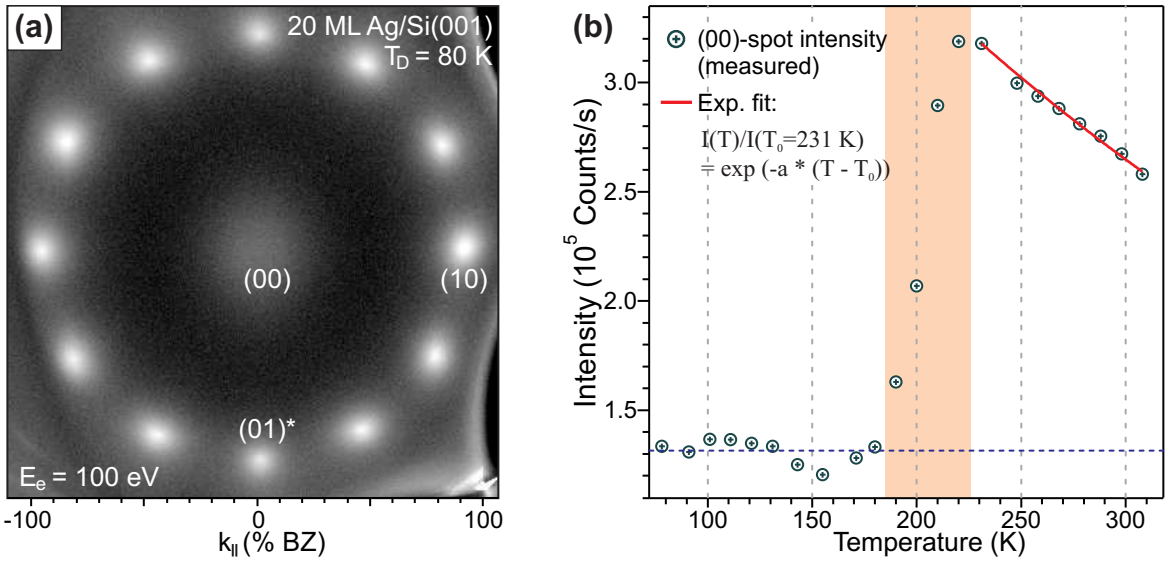

Figure 7.30: (a) LEED pattern recorded after deposition of 20 ML Ag-film on Si(001) at 80 K. Quasi-12-fold symmetry LEED spots arise due to incoherent superposition of 6-fold symmetry hexagonal LEED images. (b) Smoothening behavior of a 20 ML Ag film during annealing from 80 K to 310 K. Plotted is the peak intensity of the (00)-spot at the scattering condition of $S = 3.8$. After 185 K the intensity increases dramatically and it maximizes at 225 K, indicating a significant reduction of surface roughness by increasing the mobility of Ag atoms. After 225 K the intensity decreases due to the Debye-Waller effect.

ing the metal layers, e.g., the room temperature growth of Ag(111) 3D clusters on Si(001) [175]. Despite the complexity and a number of consequences, epitaxial smooth Ag(111) films can be grown on Si(001) by following the kinetic pathways: deposition at low temperature and annealing to high temperature [52]. In this work, the previous recipe [52] was reproduced and additionally a new approach was applied to reduce the surface corrugation on Ag(111) film. Corrugation occurs due to the lattice mismatch of Si(001) and Ag(111) at the interface.

7.2.1 Film preparation: growth and morphology

Ag was deposited on Si(001)-$c(4\times2)$ at 80 K with a deposition rate of approx. 0.7 ML/min (1 ML=13.9×10^{14} cm^{-2}). Fig. 7.30(a) shows a quasi-12-fold symmetry LEED pattern of a 20 ML of Ag film at 80 K. From the LEED pattern it can be concluded that Ag grows in a (111) orientation on Si(001) substrate. The quasi-12-fold symmetry arises due to incoherent superposition of two LEED patterns of Ag(111) surfaces, which are rotated by 90° with respect to each other. Inherently, Si(001) surface has two domains, i.e., (2×1) and (1×2) reconstructions, at each even and odd terraces. Obviously, Ag grows according to the orientation of the surface structure of Si(001) [52]. This behavior seems similar to the growth of Bi(111) on Si(001) (see section 7.1). Each spot at out-of-phase scattering condition exhibits extremely broadened spots, indicating a rough surface. Such a massive roughness may be caused by a kinetic roughening of the Ag film due to the barrier for interlayer diffusion.

Previous studies have confirmed a layer-by-layer growth at low temperatures ($T \sim 130$ K) [176] and multilayer growth (3D growth) at higher temperatures ($T \sim 300$ K) [177, 173].

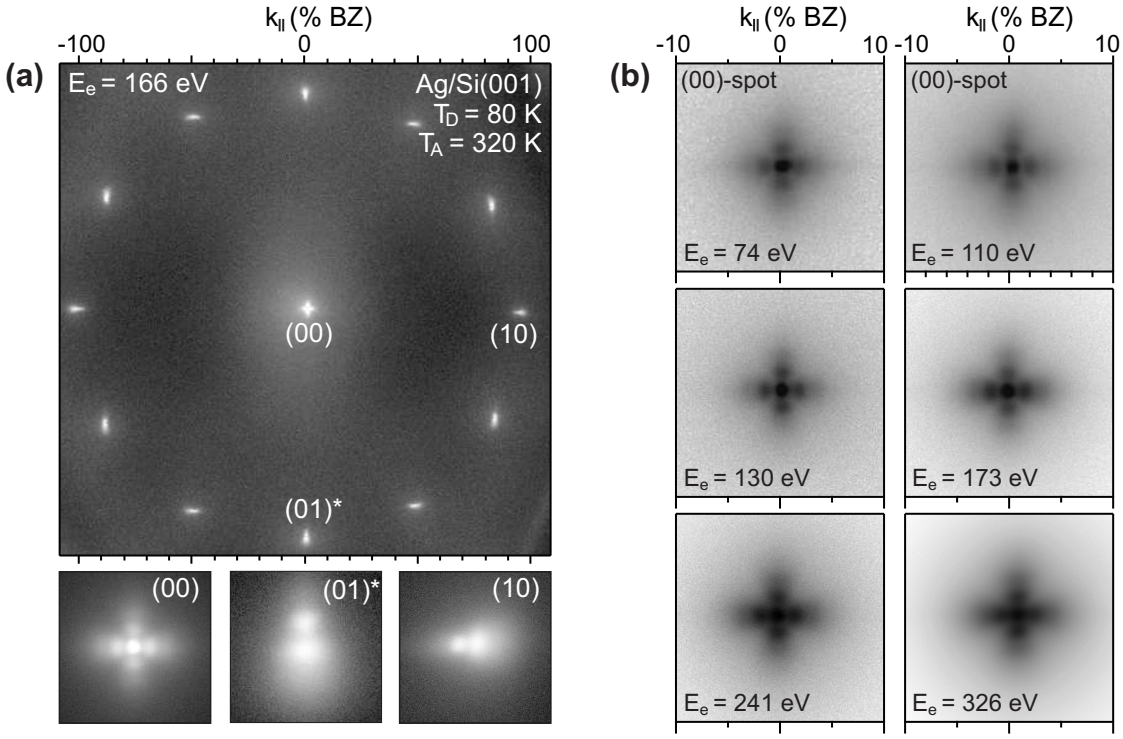

Figure 7.31: (a) LEED pattern of 20 ML Ag film after annealing to 320 K. Insets show central (00)-spot and each of the hexagonal domain spots symbolized by (10) and (10)*, respectively. A linear chain of satellite spots is caused by the periodic surface height undulation, which is explained in the text. (b) LEED pattern of the (00)-spot at different electron energies. The spot splitting becomes more pronounced at higher electron energies, because they are more sensitive to the weak surface height undulations.

Growth mode at high temperatures, however, can be changed by introducing Sb as a surfactant, which increases the density of islands and causes a layer-by-layer growth [173, 178]. Nucleation and growth on the Si(100) surface may also result in an increased island density compared with growth on Ag(111). That might be the reason for the layer-by-layer growth at low temperatures. In this thesis, Sb was replaced by sub-bilayer of Bi, as a surfactant, and Ag was grown on Ag(111) film at 300 K. Similar to the case of Sb [173, 178], Bi has transformed the multilayer growth mode of Ag on Ag(111) to layer-by-layer mode, as shown by the LEED specular intensity oscillations in Fig. 7.29. From the period of the oscillations and the deposition time, precise thickness calibration was performed.

Despite the increased roughness at low temperature growth, the film is continuous 7.30(a). The film was annealed to 320 K and the intensity of the (00)-spot was recorded during annealing (see Fig. 7.30(b)). The intensity increases drastically from 180−230 K and decreases up to the annealing temperature of 320 K. Such a massive increase of the intensity can be attributed as a smoothening of surface roughness. At 230 K, the surface becomes sufficiently smooth and the (00)-spot intensity decreases exponentially due the Debye-Waller effect. *In situ* resistance measurements of the film during annealing has also confirmed the smoothening behavior, which will be addressed in the coming chapters. In addition to the surface smoothening after annealing the film to 320 K, the morphology changes remarkably, which

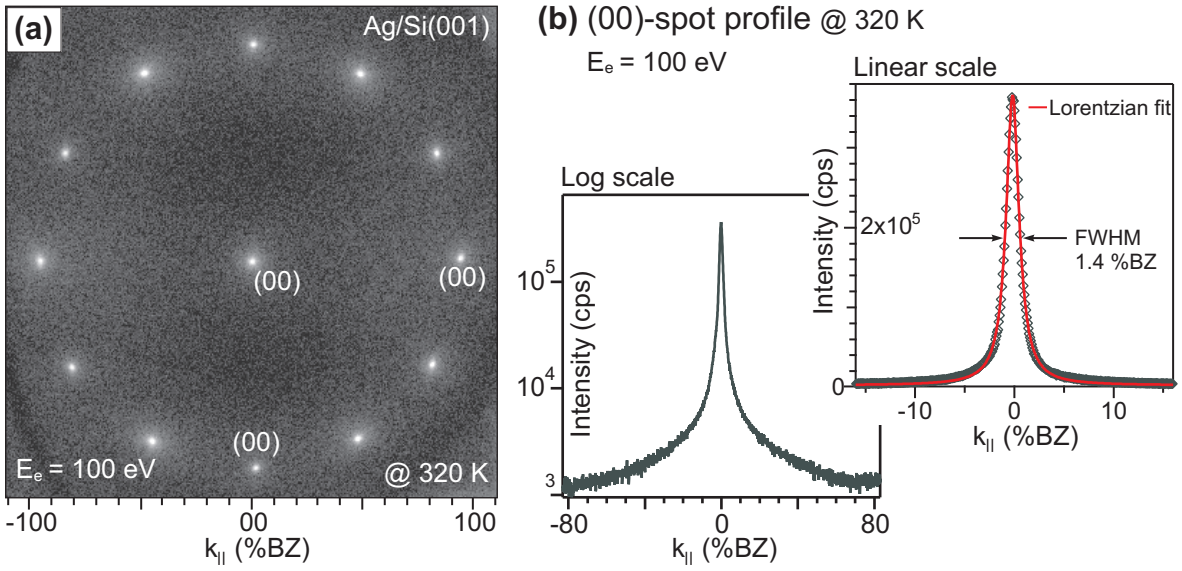

Figure 7.32: (a) LEED pattern recorded after an additional 10 ML Ag deposition on the annealed 20 ML Ag(111) film at 320 K. (b) LEED (00)-spot profile of the corresponding film, which is plotted in logarithmic and linear intensity scales.

can be observed in the extraordinary LEED pattern shown in Fig. 7.31(a). All the integer order spots are elongated in either the [110]- or [1$\bar{1}$0]-directions and the (00)-spot shows the shape of a plus-sign. All spots of each of the two (by 90°) rotated hexagonal patterns are elongated only in one direction. From the close inspection of all integer order spots the nature of the elongated spots becomes apparent: each of the integer order spots is split into short chains of satellite spots with an average distance of $\langle a_{dis} \rangle = 1.4$ %BZ (see insets of Fig. 7.31(a)). The origin of the chains of satellite spots are caused by a weak and periodic height undulation of the surface, resulting from a linear array of interfacial misfit dislocations, as observed in Bi(111)/Si(001) (see section 7.1). The most striking difference between the two systems (Bi(111)/Si(001) and Ag(111)/Si(001)) is the nature of the lattice accommodation. In the case of Ag(111)/Si(001) [52], the distance between three Si atoms (11.52 Å) matches nearly exactly the distance between four Ag atoms (11.56 Å) along the dimer rows. The remaining compressive strain is only 0.36 %. But along the perpendicular to the dimer rows, the separation of the dimer rows of 7.68 Å has to fit with the distance of three dense packed rows of 7.51 Å. This causes a tensile strain of 2.2 %. This anisotropic misfit is relieved (partially) by arrays of parallel dislocations (probably in the interface plane). The strain field of the dislocations give rise to the surface height undulation, which are observed as spot splitting in LEED. The amplitude of the height undulation in Ag(111) surface is relatively small ($\sim$ 0.3 Å) [52] as compared to Bi(111) surface ($\sim$ 0.7 Å).

Fig. 7.31(b) shows the series of LEED patterns of the (00)-spot recorded at different electron energies. Splitting is more pronounced at higher electron energies, since they are sensitive to the large wavelength weak undulations. Except splitting, the (00)-spot is not broadened, which excludes the occurrence of defects such as small angle mosaics as observed for the growth of Ag on Si(111) [179].

A similar approach, as in the case of the recipe which produces thick Bi(111) films on Si(001) (see section 7.1.3), was applied to reduce the surface height undulations without a building up of additional surface roughness. An additional 10 ML Ag was deposited on the 20 ML Ag(111) film at 320 K. The spot profile of the (00)-spot was constantly checked during deposition. As the total coverage exceeded 30 ML, surprisingly, a sharp profile of the (00)-spot was observed. Fig. 7.32(a) and (b) shows the LEED pattern (logarithmic intensity scale) and the (00)-spot profiles (both logarithmic and linear intensity scales) of a 30 ML Ag(111) film.

8 Results on Homoepitaxy

This chapter will focus on the results of Bi(111) homoepitaxy. An exclusive study of growth, morphology and atomic processes will be discussed with the experimental results.

The first section will report a thorough investigation of growth via SPA-LEED analysis. STM is used as a complementary tool, which will access both real space surface analysis and also the reproduction of SPA-LEED data. Our own recipe is used to prepare a base layer of Bi(111) on Si(001), which works as a virtual substrate for growing Bi. In the second section, however, Bi(111)/Si(111) is used as a virtual substrate to study homoepitaxial growth via variable temperature STM. Basically, a compact form of analysis about the nucleation and initial stages of growth of Bi homoepitaxy will be reported.

8.1 Bi on Bi(111)/Si(001)

In this section, homoepitaxial growth of Bi(111) will be investigated in details. Growth modes will be characterized via studying the LEED specular intensity during deposition of Bi on the Bi(111) base film at various temperatures between 80 and 300 K. The surface morphology, island shape/size will be determined by SPA-LEED *in situ* during deposition and afterwards. As a complementary check, STM was used to obtain real-space information of the island shape and the density at 135 K. The intraterrace diffusion energy will be determined from the island density variation as a function of deposition temperature.

8.1.1 Growth mode

Figure 8.1(a) shows the (00)-spot intensity during deposition of Bi on a 9 nm Bi(111) base film at 80 K. An electron energy of 179 eV was chosen as an out-of-phase condition, where electrons interfere destructively after scattering from neighboring terraces. The intensity shows an oscillatory dependence on coverage with BL-periodicity. This behavior clearly reflects a quasi layer-by-layer growth mode. We will show later, that each 2D island exhibits a bilayer height of 0.394 nm: the growth proceeds in a bilayer-by-bilayer mode. At the very beginning of the coverage, we have observed an initial transient in the intensity. Such a transient drop of intensity is caused by the scattering of the electron wave by isolated adatoms [180]. Additionally, the intensity of the periodic maxima is significantly lower than those originating from the initial surface and each maxima of the oscillation exhibits a rounded peak. This can be easily explained with the fact that the nucleation of a new layer occurs before the previous one is completed [109]. Moreover, the amplitude of the oscillation monotonously decreases from layer to layer. Typically, 40 oscillations have been observed at 80 K (Fig.

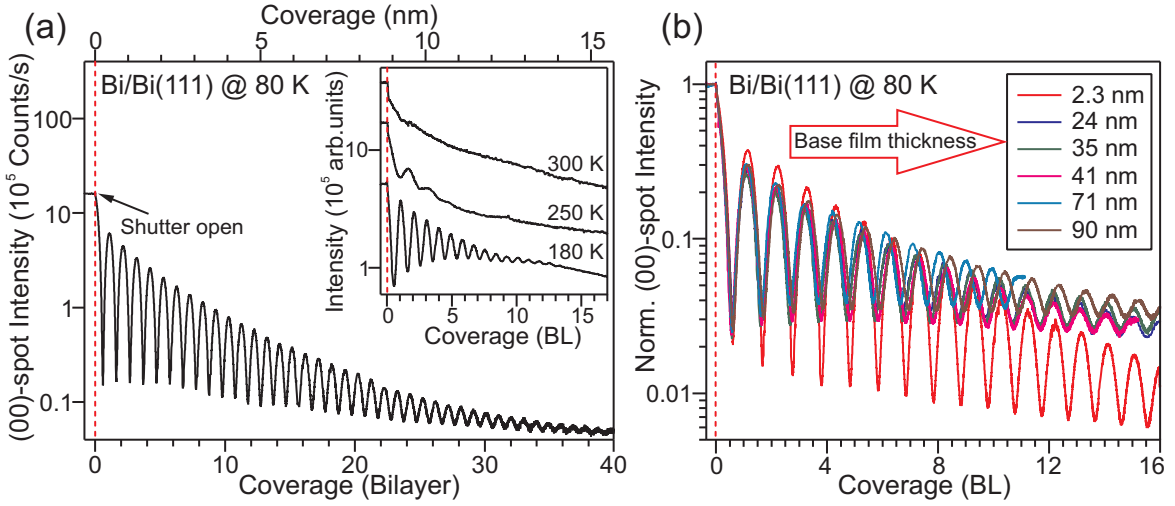

Figure 8.1: (a) LEED (00)-spot intensity oscillations measured at an out-of-phase condition ($S = 3.5$) during deposition of Bi on a 9 nm Bi(111) base film at 80 K. Long-lasting oscillations with a period of bilayer coverage confirm a quasi-bilayer growth mode. The gradual decay of the oscillation amplitude reflects a kinetic roughening of the growth front. The inset shows the intensity oscillations at higher deposition temperatures. (b) LEED (00)-spot intensity oscillations measured at an out-of-phase condition ($S = 3.5$) during deposition of Bi on various coverages of Bi(111) base film at 80 K. Each color line of the oscillation curve represents the respective base film.

8.1(a)), which finally fade out at higher coverages. The oscillations were observed for a wide range of coverages of the Bi(111) base film (see Fig. 8.1(b)). For each base film nearly a constant period of oscillation was obtained, which varies slightly for very high coverages due to a slight increase of vertical roughness. For all base films, the oscillation amplitude decays continuously with increasing coverage, giving an evidence of kinetic roughening of the growth front. We attribute this behavior to the existence of a weak *Ehrlich-Schwoebel* step edge barrier [181, 182], which becomes less effective at higher temperatures, forcing the growth mode towards step-flow propagation. The shift of the growth mode can be clearly observed in the (00)-spot intensity variation at higher temperatures in the inset of Fig. 8.1(a). The oscillation amplitudes are drastically reduced at 250 K and completely turned off at 300 K. Since the (00)-spot intensity at 300 K does not show a constant behavior with the coverage, which is a prerequisite for perfect step-flow propagation, a slight roughening is still present. However, we did not observe a fast drop of intensity at any temperatures. This excludes the situation, where interlayer transport is completely absent (statistical growth).

The origin of the periodic variation of the (00)-spot intensity can be understood from the periodic variation of the (00)-spot profiles recorded during deposition at 80 K. The profiles were recorded by SPA-LEED in a external electron geometry, as sketched in the inset of Fig. 8.2 (see also section 3.1.2). Figure 8.2 shows a series of (00)-spot profiles recorded at an out-of-phase condition ($S = 3.5$) during deposition. The variation of the spot profiles clearly demonstrate the oscillating behavior of the central spike intensity and of the diffuse intensity (which is phase shifted by half a BL) from one bilayer to the next one. The total intensity of the profile is always conserved. The periodic change of the profile reflects the nucleation

and the completion during the course of deposition of one additional BL. For a coverage of half of a complete BL, the central spike almost vanishes in the minima of the intensity oscillations. Only the diffuse shoulder remains, reflecting the morphological uniformity of the film and maximum surface roughness. The diffuse intensity shows a "Henzler Ring" (see also Fig. 8.3(c)), indicating a lateral surface roughness with well-defined terrace width distribution. For a complete BL coverage, the central spike shows its maxima and almost no diffuse shoulder, indicating a flat surface without lateral roughness.

The observation of long lasting oscillations at low temperatures is quite rare in metallic homoepitaxial systems because thermally activated surface diffusion is suppressed and hinders 2D growth. However, as suggested by Egelhoff *et al.* [180] adatoms may use their latent heat of condensation to hop across the surface and finally come to rest at growing island edges. A similar interpretation applied to the reentrant layer-by-layer growth in a Pt/Pt(111) system [172], which is due to the breakdown of the step edge barrier by decreasing the adatom island size, could also be the case for this system. From the out-of-phase (00)-spot profile at 0.5 BL coverage (Fig. 8.2), an average island separation of $\langle L \rangle < 5$ nm can be estimated, which provides a qualitative picture of the extremely small size of Bi islands, i.e., high adatom island number density at a low coverage regime. Additionally, a STM determination of island density with coverage at low temperature and low coverage regime also confirm the high density of adatoms. The detail calculation of the island size and density will be addressed later in the next section (see 8.2). However, unlike the case in a Pt/Pt(111) system [172], the surface undergoes a complete step-flow growth mode[1] at the temperatures higher than 350 K.

8.1.2 Vertical layer distance

In situ recorded (00)-spot profiles during deposition of Bi on Bi(111) at 80 K, as shown in Fig. 8.2, have already indicated that a perfect 2D growth occurring at least up to the first bilayer coverage. Within the regime of single BL, the best regime of 0.5 BL Bi was considered, due to the requirement of better statistics for data evaluation, to determine the vertical layer distance of adatom islands. The exact coverage was achieved by following the (00)-spot intensity during deposition (see Fig. 8.1): the first minima corresponds to 0.5 BL coverage.

The corresponding LEED pattern recorded at an out-of-phase scattering condition for the integer order spots is shown in Fig. 8.3(a) and (b). The initial observation of the quasi 12-fold symmetry spots reminds the symmetry of the base film, which consists of (111) crystallites rotated by 90°. However, a well-defined morphological change can be estimated from the beautiful shape of eye-like spots. Each of the first order spots exhibits a typical "Henzler Ring" of diffuse intensity surrounding a sharp central peak. A representative view of the (00)-spot in a 2D and 3D format, recorded at out-of-phase condition ($S = 5.4$), is also displayed in Fig. 8.3(c) and (d). The diameter of the ring was estimated from the precise measurement of 1D spot profile, as shown in Fig. 8.3(e), which concludes a distance of $k_{\emptyset} = 17$ %BZ,

[1] Step-flow growth proceeds through the attachment of deposited atoms to pre-existing steps, keeping the step density constant [183].

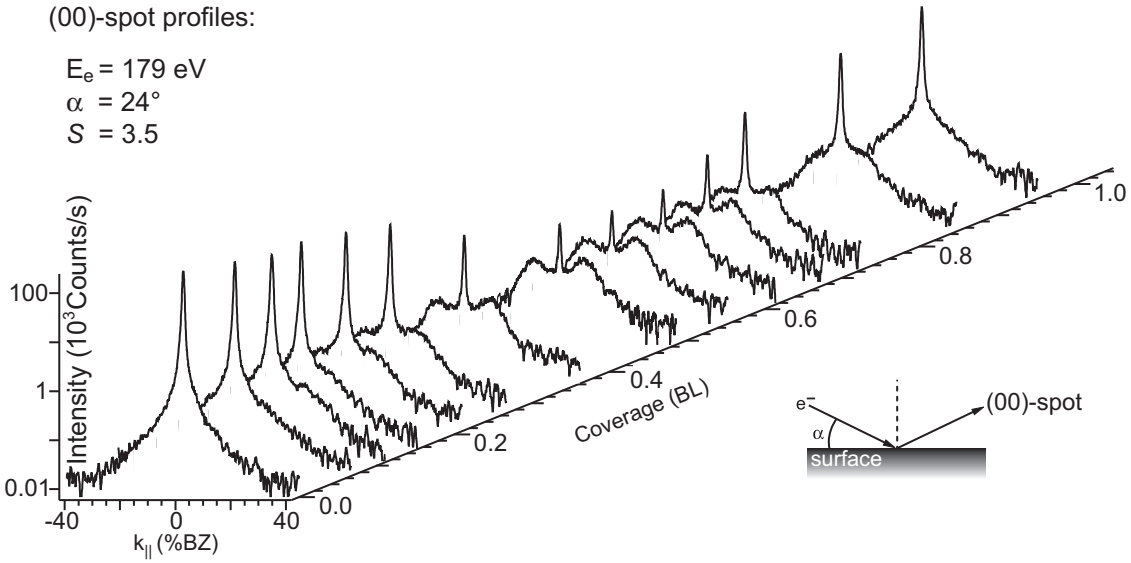

Figure 8.2: LEED (00)-spot profiles recorded at an out-of-phase condition ($S = 3.5$) during the deposition of Bi on a Bi(111) base film at 80 K. The shape of the profile changes periodically with coverage. The sharp central spike $G(S)$ recovers from one complete bilayer to the next complete bilayer, indicating a 2D growth mode. At 0.5 BL coverage, the profile shows a pronounced diffuse shoulder with a sharp central peak, reflecting a surface roughness with a well-defined average terrace separation of $\langle L \rangle = 4.6$ nm. The total intensity of the diffuse shoulder and the central spike is conserved during the morphological changes during deposition. The profiles were measured using an electron beam in a RHEED-like geometry as shown in the sketch (below the profiles).

corresponding an average island separation of $\langle L \rangle = 4.6$ nm.

The island height is determined from the periodic change of spot profiles with a vertical momentum transfer $k_\perp$ or scattering phase S. Therefore, the (00)-spot profiles were recorded over a large range of electron energies - at least from one in-phase condition to the next one. Figure 8.4 clearly shows how the spot profile varies as a function of the electron energy. At the in-phase condition ($E_e = 40$ eV, $S = 4$) the spot shape is narrow and shows only the instrumental broadening. Here the electrons scattered from neighboring terraces interfere constructively, and therefore, only a sharp peak appears. At the out-of-phase condition at 51 eV ($S = 4.5$), where the electrons from the neighboring terraces interfere destructively, the profile shows a diffuse ring of intensity, the so-called "Henzler Ring". The diffuse intensity shows an oscillatory behavior as a function of the electron energy from zero at the in-phase condition to a maximum at the out-of-phase condition and to zero at the next in-phase-condition at 61 eV (Fig. 8.4). The diameter of the "Henzler Ring", however, remains unchanged with the electron energy. This indicates a 2-level system with a well-defined distribution of 2D islands with the same height on the surface [43, 42]. The change of intensity of the diffuse ring proceeds at the expense of the central spike intensity.

In order to eliminate the dynamic form factor of scattering, all spot profiles were normalized by taking the ratio of the integral intensity of the central spike I_{spike} with the total intensity of the spot $I_{total} = I_{spike} + I_{diffuse}$, where $I_{diffuse}$ is the total integral intensity of the diffuse shoulder [184]. To separate the central spike and the shoulder, the profile was fitted with

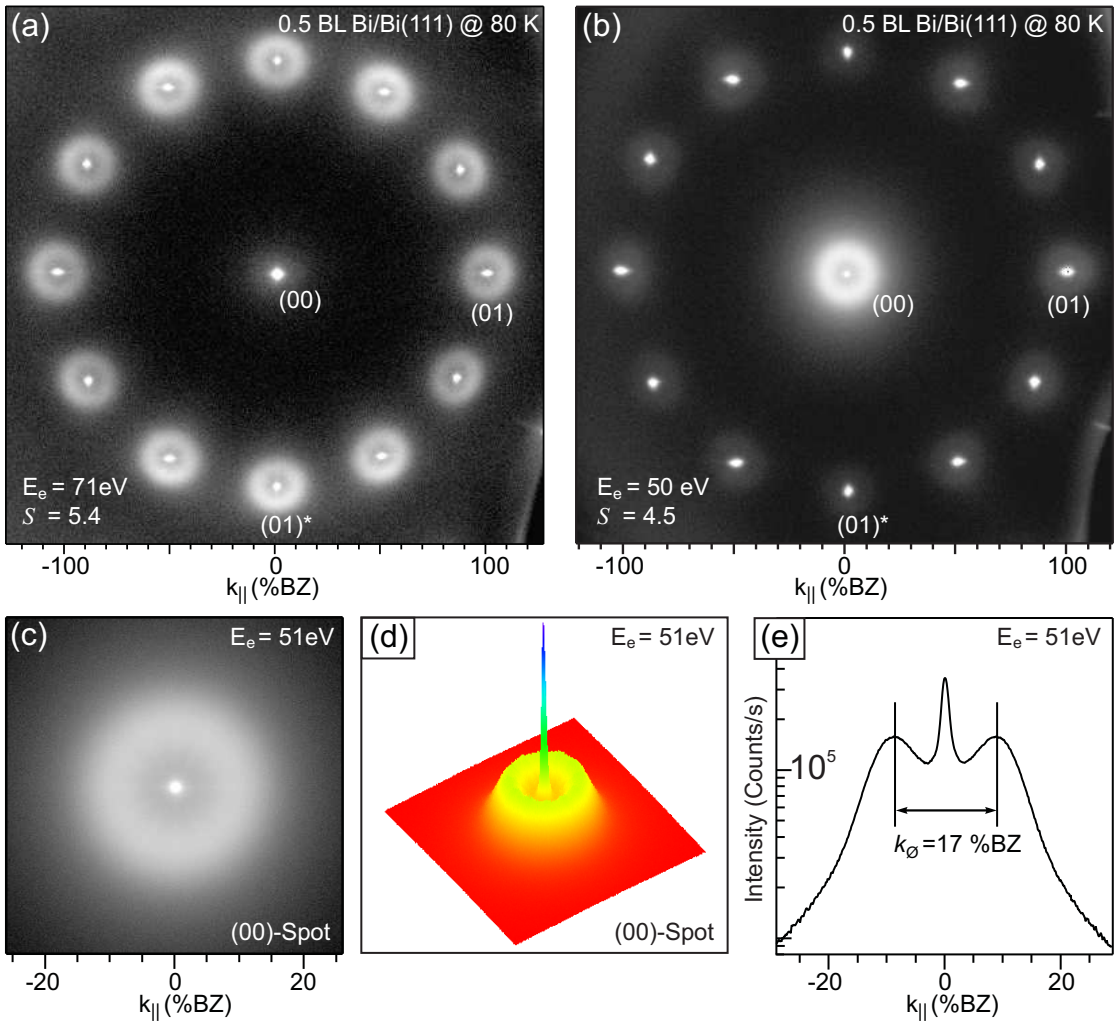

Figure 8.3: 2D LEED pattern of first order spots, (00)-spot and the (00)-spot profile of a base Bi(111) film after deposition of 0.5 BL Bi at 80 K: (a) First order LEED spots close to the out-of-phase condition ($S = 5.4$). (b) First order LEED spots at the out-of-phase condition ($S = 4.5$). (c) LEED pattern of the (00)-spot close to the out-of-phase condition ($S = 4.5$). (d) 3D plot of the (00)-spot at the out-of-phase condition ($S = 4.5$). (e) Corresponding 1D profile of the (00)-spot. Both the (00)-spot and the first order spots exhibit a ring of diffuse intensity surrounding a sharp central peak at the out-of-phase conditions, showing a typical "Henzler Ring".

three Lorentzian functions as shown in Fig. 8.5(c). Then the integral intensity of each profile was calculated as the following (assuming that the profile is symmetrical and isotropic along all directions):

$$\begin{aligned} I_{spike} &\propto w_s^2 \times I_{peak,S} = c\, w_s^2 \times I_{peak,S} \\ I_{L-S} &\propto w_L^2 \times I_{peak,L} = c\, w_L^2 \times I_{peak,L} \\ I_{R-S} &\propto w_R^2 \times I_{peak,R} = c\, w_R^2 \times I_{peak,R} \end{aligned}$$

where $I_{peak,S}$, $I_{peak,L}$ and $I_{peak,R}$ are the peak intensities of the central spike and the left and the right part of the shoulder. w_s, w_L and w_R are the FWHMs of each peak. c is the constant of proportionality. For the total integral intensity of the shoulder we can write $I_{diffuse} =$

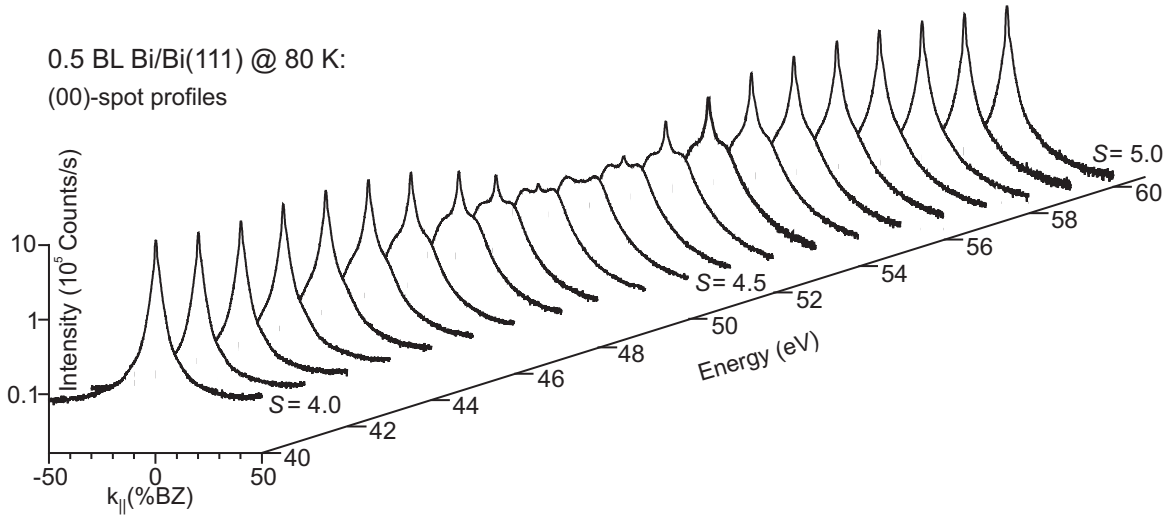

Figure 8.4: Variation of the spot profile of the (00)-spot with the electron energy E or the scattering phase S. The spot profiles are recorded after deposition of 0.5 BL Bi on a 25 nm Bi(111) base film at 80 K. All the profiles are plotted in a logarithmic intensity scale. The profile shows a periodic change from one in-phase scattering condition ($S = 4$) to the next one ($S = 5$). The central spike disappears at the out-of-phase condition ($S = 4.5$) due to the destructive interference of the electrons at the steps of 2D islands. The intensity is redistributed to the diffuse intensity of the "Henzler Ring".

$(I_{L-S} + I_{R-S})$. The normalized central spike intensity $G(S)$ for particular scattering phase S, can be calculated as:

$$G(S) = \frac{I_{spike}}{I_{spike} + I_{L-S} + I_{R-S}} = \frac{w_s^2 \times I_{peak,S}}{w_s^2 + I_{peak,S} + w_L^2 \times I_{peak,L} + w_R^2 \times I_{peak,R}} \tag{8.1}$$

This normalized central spike intensity is plotted in Fig. 8.5(a) as a function of the square root of the electron energies, i.e., as a function of $k_\perp$ or the scattering phase S. The $G(S)$ curve shows an oscillatory behavior with maxima for the in-phase conditions $S = 3$, 4, and 5 and could be well-fitted by a cosine function.

Assuming a perfect 2-level system (the substrate plus islands of the same height) and for the coverage $\theta_1 = 0.5$ (half of a complete bilayer), the observed experimental data can be fitted well using Eq. 2.22 (see also section 2.1.3) [43, 42]. If more than two layers are present, higher Fourier components will contribute to the behavior of the $G(S)$ curve [185, 42].

Additionally, from the knowledge of the electron energies at the in-phase conditions and the corresponding scattering phases S, one can determine the island height d via the Laue condition, as described in section 2.1.2. Substituting the separation $\triangle S$ between two successive maxima or minima of the $G(S)$ and the respective electron energies in Eq. 2.20, the vertical layer distance can be easily calculated [42].

Using all three in-phase conditions, i.e., $S = 3, 4, 5$ an island height of $d_{80K} = 0.389 \pm 0.002$ nm was derived. This value is close to the bulk Bi lattice plane separation of $d_{\text{bulk}} = 0.394$ nm and confirms the previous observation of BL step height on Bi(111) films [186, 20]. However, a contraction of $\sim$1 %, beyond the error margin that could occur during this measurement, is estimated. Such a relaxation of the island height d is probably caused by a smoothening

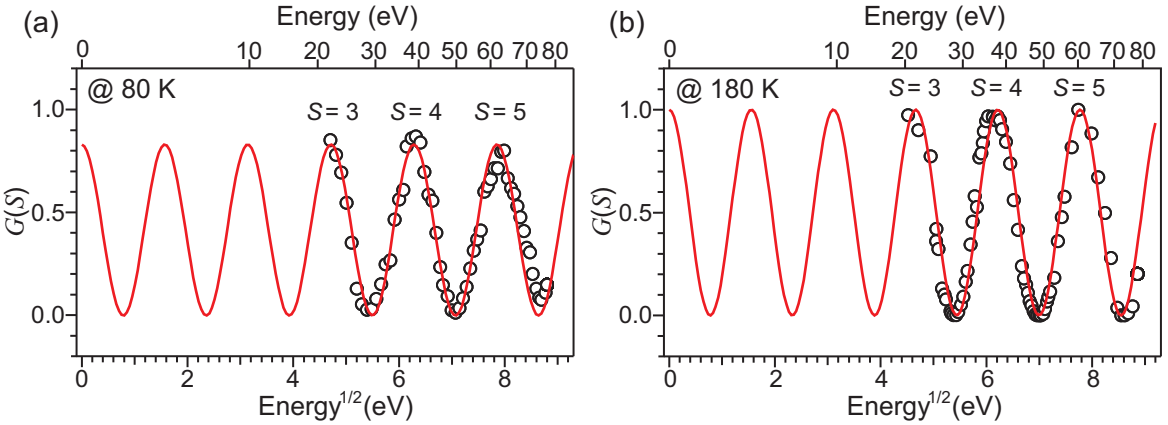

Figure 8.5: Normalized central spike intensity $G(S)$ of the LEED (00)-spot profile as a function of S, i.e., the square root of energy. (a) Deposition at 80 K, (b) Deposition at 180 K. At in-phase conditions, all the intensity is confined to the central spike due to the constructive interference of the electrons and the $G(S)$ curve shows maxima. At out-of-phase conditions, the central spike vanishes due to the destructive interference and the $G(S)$ curve shows minima. The curves were fitted with the cosine function (Eq. 2.22) considering the 2-level system and shown with a solid line. We derive an island height of $d_{80\mathrm{K}} = 0.389$ nm at 80 K and of $d_{180\mathrm{K}} = 0.395$ nm at 180 K.

of the electron density contours at the edges of the small island (the Smoluchowski effect) [187]. A similar effect of inward relaxation of the electron contour of the topmost layer was detected for small Ag islands on Ag(100) by thermal-energy atom scattering (TEAS) analysis [188]. We argue that the effect is more apparent for small islands because the distortion of the electron density at adjacent step edges overlaps, leading to an overall smoothening and inward relaxation of the electron density contour. For large islands, only a negligible contribution of the smoothening effect occurs. In our system, the Bi islands are relatively small (average island width $\langle\Gamma\rangle < 3$ nm) at 80 K, and it therefore has become possible to detect the effect.

The same measurements were performed after depositing 0.5 BL Bi on the Bi(111) base film at 180 K. To avoid any effects of thermal expansion, the data were taken after quenching the film to 80 K. Then the island size is much larger ($\langle\Gamma\rangle > 10$ nm) and the smoothening effect should be smaller. Figure 8.5(b) shows the $G(S)$ curve, which is similar to the 80 K measurement. The cosine behavior of the measured data with scattering phase S, which fits quite well with Eq. 2.20, still reflects a two level system. The location of the maxima, however, is shifted to lower energies, i.e., smaller momentum transfer or larger electron wavelength: the step height is increased to $d_{180K} = 0.395 \pm 0.002$ nm, which matches the bulk value of $d_{\mathrm{bulk}} = 0.394$ nm within the instrumental error. For these larger islands we do not observe a contraction in the layer height of the islands. This result supports the argument of a smaller contribution of the Smoluchowski smoothening effect for larger islands. That might also have been the reason that Bedrossian *et al.* [188] were not able to observe the effect with SPA-LEED, because the investigated Ag islands were rather large ($\langle\Gamma\rangle \sim 7$ nm).

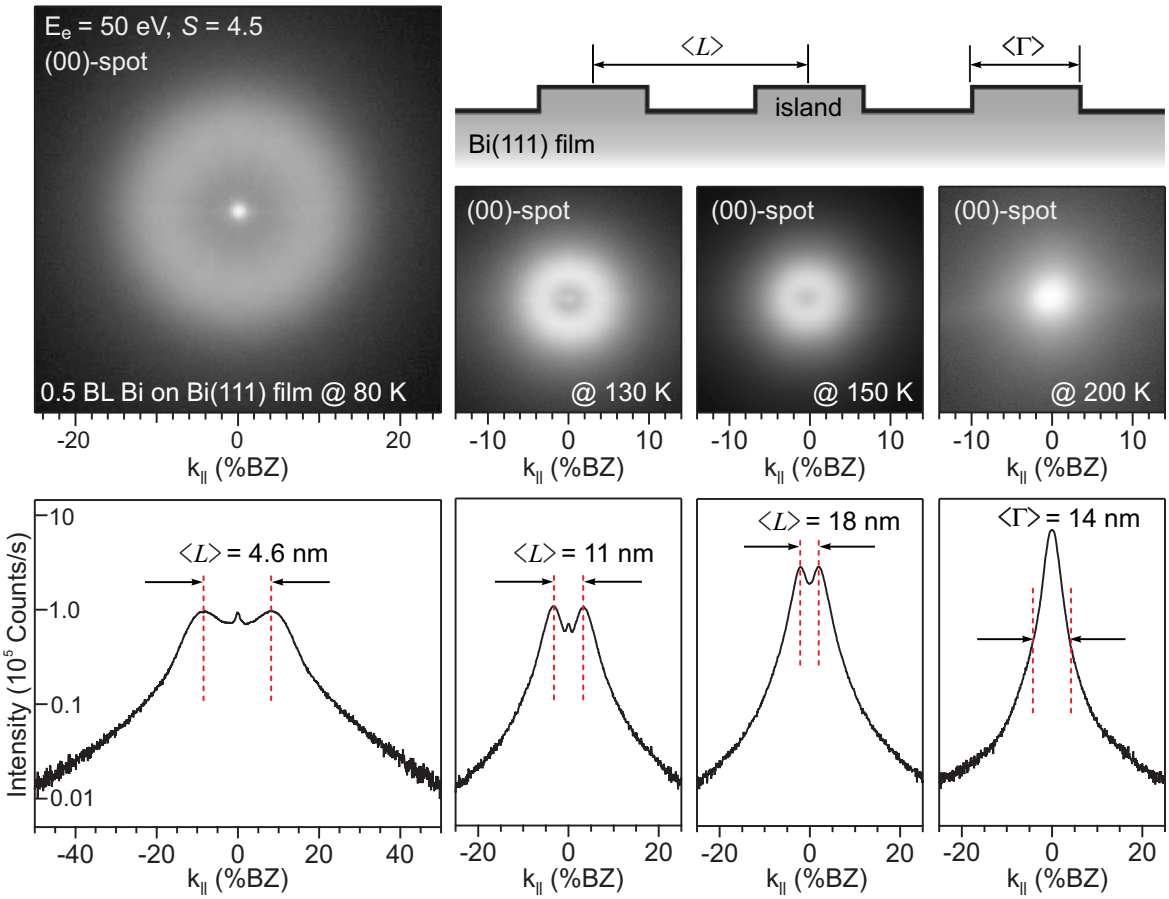

Figure 8.6: LEED patterns of (00)-spot and corresponding profiles after deposition of 0.5 BL Bi on the Bi(111) base film at different deposition temperatures. At 80 K, a distinct ring of diffuse intensity, the so-called "Henzler Ring", appears. The diameter of the ring decreases significantly from 80 K to 150 K. Finally, at 200 K, a single broadened spot appears. The terrace lengths $\langle L \rangle$ at different deposition temperatures (80 −150 K) and the average terrace size $\langle \Gamma \rangle$ at 200 K, as calculated from the 1D spot profile analysis, are shown within the profiles. The cross-section sketch shows Bi islands of average separation $\langle L \rangle$ and average size $\langle \Gamma \rangle$.

8.1.3 Lateral roughness

The average island size $\langle \Gamma \rangle$ or island separation $\langle L \rangle$ was determined from the shape of the diffuse part of the spot profile. The dominant central spike is most effectively suppressed for the out-of-phase condition at half coverage. At 80 K the (00)-spot and the corresponding 1D spot profile exhibit a typical "Henzler Ring" of diffuse intensity surrounding a sharp central peak (Fig. 8.3). The observation of a "Henzler Ring" reflects a well-defined size distribution of regular 2D islands on the surface [99]. The average island separation of $\langle L \rangle = 4.6$ nm is calculated directly from the diameter of the diffuse ring $k_{\emptyset}$ via $\langle L \rangle = 4\pi/k_{\emptyset}$ [99, 189, 190]. This small value for $\langle L \rangle$ indicates a considerable slowdown of mass transport by the existence of an adatom diffusion barrier across the terraces and/or step edges. A higher barrier reduces the adatom diffusion across the terraces, and consequently increases the island density n_x, i.e., decreases the average island separation $\langle L \rangle$.

The temperature dependence of the island separation $\langle L \rangle$ was studied by deposition of 0.5

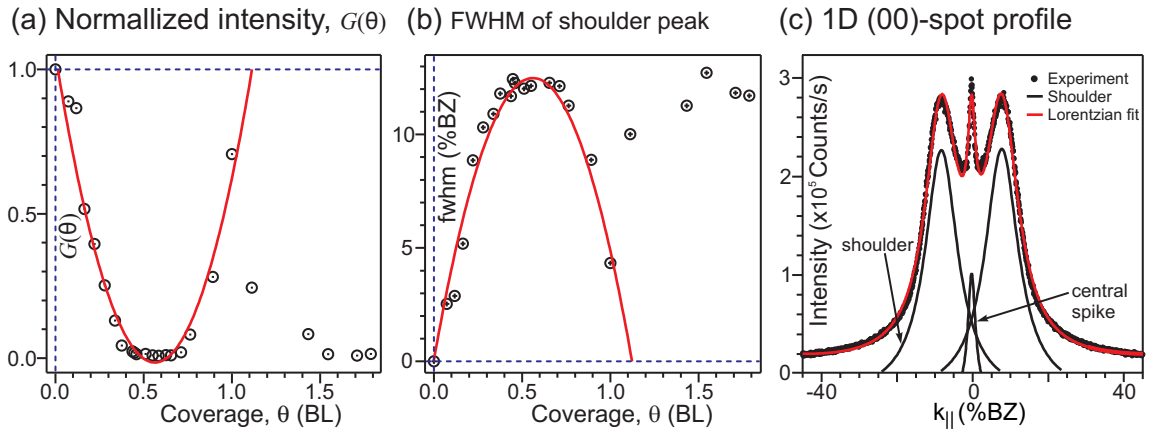

Figure 8.7: (a) Normalized central spike intensity $G(S)$ of the (00)-spot, (b) width of the the shoulder peak, and (c) a typical (00)-spot profile fitted with Lorentzian-functions (see Eq. 2.31). The data is calculated after recording the (00)-spot profiles during deposition of Bi on Bi(111) base film at 80 K.

BL Bi at various temperatures up to 200 K. Immediately after deposition the sample was cooled down to 80 K to inhibit coarsening of the island distribution. LEED patterns of the (00)-spot and the corresponding spot profiles were recorded at an out-of-phase scattering condition ($S = 4.5$) and are shown in Fig. 8.6.

At higher deposition temperatures, the diameter of the diffuse ring decreases significantly and vanishes completely at 200 K. The decreasing diameter $k_{\emptyset}$ of the "Henzler Ring" in reciprocal space reflects the increasing island separation $\langle L \rangle$, which is equivalent to a decrease of the island density n_x. At 200 K, the island size is so large as compared with the instrument response function that the "Henzler Ring" vanishes and a broadened spot remains. Under this condition, the (00)-spot profile gives information about the lateral size of the islands $\langle \Gamma \rangle$ and not the average island separation $\langle L \rangle$. The profile can be fitted well by a Lorentzian function (Eq. 2.31), assuming a geometric distribution of islands. The average island size of $\langle \Gamma \rangle = 14$ nm was directly determined from the FWHM κ of the profile by $\langle \Gamma \rangle = 2/\kappa$ [179].

For deposition between 200 K and 300 K, a slight broadening in the spot profile was still observed due to a buildup of small surface roughness. The intensity during deposition as shown in the inset of Fig. 8.1 clearly exhibits a small decrease even at 300 K. The mobility of the Bi adatoms became so high, that the growth proceeds via almost step propagation of the pre-existing steps of the initial Bi base film. This trend continues up to 450 K, where the spot profile shows only the instrumental broadening, symbolizing a perfect step propagation growth mode.

For comparison, STM micrographs of 0.5 BL Bi deposited at nominally 135 K were additionally recorded. Figure 8.8(a) shows 2D triangular-like islands of almost the same size and separation. All islands exhibit a quasi-dendritic shape as obvious from the higher magnification micrograph in Fig. 8.8(b). The quasi-dendritic shape is caused by the asymmetry in diffusion of adatoms from corners to the steps, which generally occurs on a hexagonal surface [191, 192, 193]. All islands exhibit the same height of $d \cong 0.4$ nm, i.e., a bilayer height. The islands are touching each other. Coalescence and coarsening, however, is not observed. By

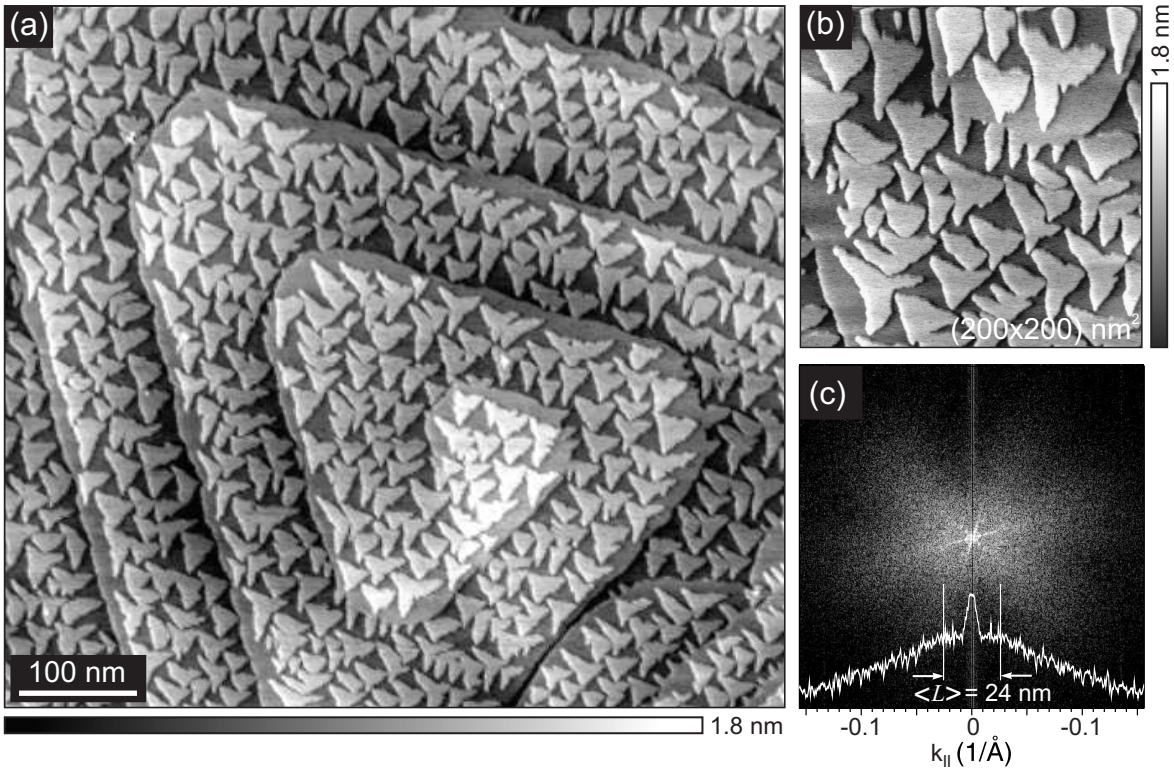

Figure 8.8: STM topography ($V_{\text{bias}} = 1.8$ V, $I_{\text{tunnel}} = 17$ pA) of a 0.5 BL Bi grown on a 25 nm Bi(111) base film at 135 K. (a) The 2D Bi islands of quasi-dendritic shape are distributed on a highly smooth Bi(111) base film, which exhibits regular step trains of 100 nm separation (which form a growth spiral centered at a screw dislocation). (b) Small region at higher magnification clearly reflects the dendritic shape of the 2D Bi islands. Due to piezo creep, the topmost parts of both STM images appear slightly deformed. (c) The power spectrum of the large STM image (a) shows a "Henzler Ring". From its profile we conclude an average island separation of $\langle L \rangle = 24$ nm which is consistent with the island density of $n_x = 2.5 \times 10^{11}$ cm^{-2}.

counting the 2D islands, an island density of $n_x = 2.5 \times 10^{11}$ cm^{-2} was determined. From this, an average island separation of $\langle L \rangle = 20$ nm was estimated.

The power spectrum of the STM micrograph is shown in Fig. 8.8(c). The profile of the power spectrum also shows a "Henzler Ring" with a diameter of $k_{\emptyset} = 0.053\,\text{Å}^{-1}$, which converts to an average island separation of $\langle L \rangle = 24$ nm. This value is is consistent with the island counting analysis and qualitatively supports the spot profile analysis of the LEED patterns.

8.1.4 Surface diffusion barrier

Diffusion is a process which is thermally activated and therefore depends strongly on temperature. Thus, the adatom diffusion parameters can be estimated, based on the nucleation theory [91] (see section 5.2.1), under the assumptions of the absence of adatom-adatom interactions, the absence of contamination effects, etc. To fulfill those critical assumptions, experiment was performed at low temperatures, i.e, 80−200 K. A suitable reference coverage within the range $0.1 \leq \Theta_{max} \leq 0.5$, identified from the STM determination of island number density as a

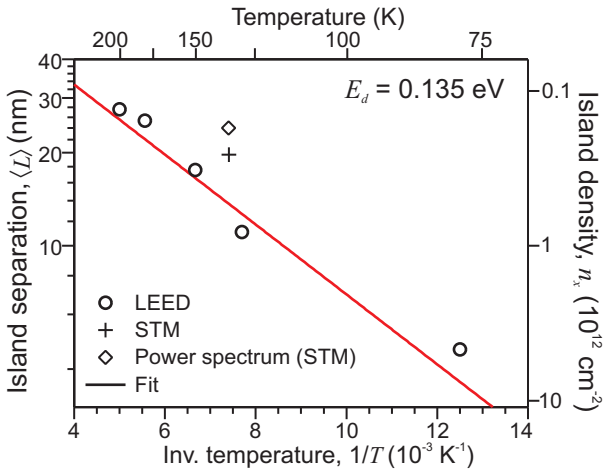

Figure 8.9: Arrhenius plot of the average island separation $\langle L \rangle$ and the island number density n_x for a 0.5 BL Bi on Bi(111) base film deposited at different temperatures T (80−200 K). The measured data are fitted using Eq. 5.8, where the slope of the fit (the red line) gives an intra-terrace diffusion barrier of $E_d = 0.135$ eV.

function of coverage (see section 8.2.2.1), was chosen. To detect the measurable change in the spot profile, a coverage of 0.5 BL was evaporated at a constant flux for each temperature. To avoid the possible thermal effects, all spot profiles were recorded after cooling of the sample down to 80 K (see Fig. 8.6). The (00)-spot profile for the deposition temperature of 180 K was not included in Fig. 8.6.

The average island separations, calculated from the recorded profiles, were plotted as a function of inverse of deposition temperature (Fig. 8.9). The average island density n_x, which depends on the average island separation via $n_x \sim (1/\langle L \rangle)^2$, was also shown in the plot. The data was fitted using the Arrhenius Eq. 5.8 (see section 5.2.1) (the red solid line in Fig. 8.9). From the slope of the fitted line, the intra-terrace diffusion energy of $E_d = 0.135$ eV was determined. The island density and the average island separation obtained from the STM image and the corresponding power spectrum for 135 K (Fig. 8.8) were not considered for the linear fit. However, the values are very close to the fit, within an error of data evaluation, showing a qualitative agreement.

In general, the value $E_d = 0.135$ eV is far lower as compared to metal(100) homoepitaxial systems and fairly comparable with metal(111) systems [194, 195]. However, exceptionally, as in the Pt/Pt(111) system [196, 197], a weak *Ehrlich-Schwoebel* step edge barrier and asymmetric dendritic shaped islands might be the dominant factors associated with the smooth growth of Bi(111), even at low temperatures.

8.1.5 Island shape

As islands continue to grow beyond the saturation regime, specific island morphologies or shapes develop. There are basically two types of islands, considering the growth conditions: one type of islands including compact form of squares, triangles and hexagons with relatively straight island edges, and another type which have fractal-like rough island edges or highly anisotropic shapes. Typically, growth at a low temperatures leads to less compact and anisotropic islands, which transforms to a compact shape as the sample is annealed to higher temperatures. This behavior tells us that the compactness is largely controlled by the extent of adatom diffusion along the island edges and the probability of crossing an adatom

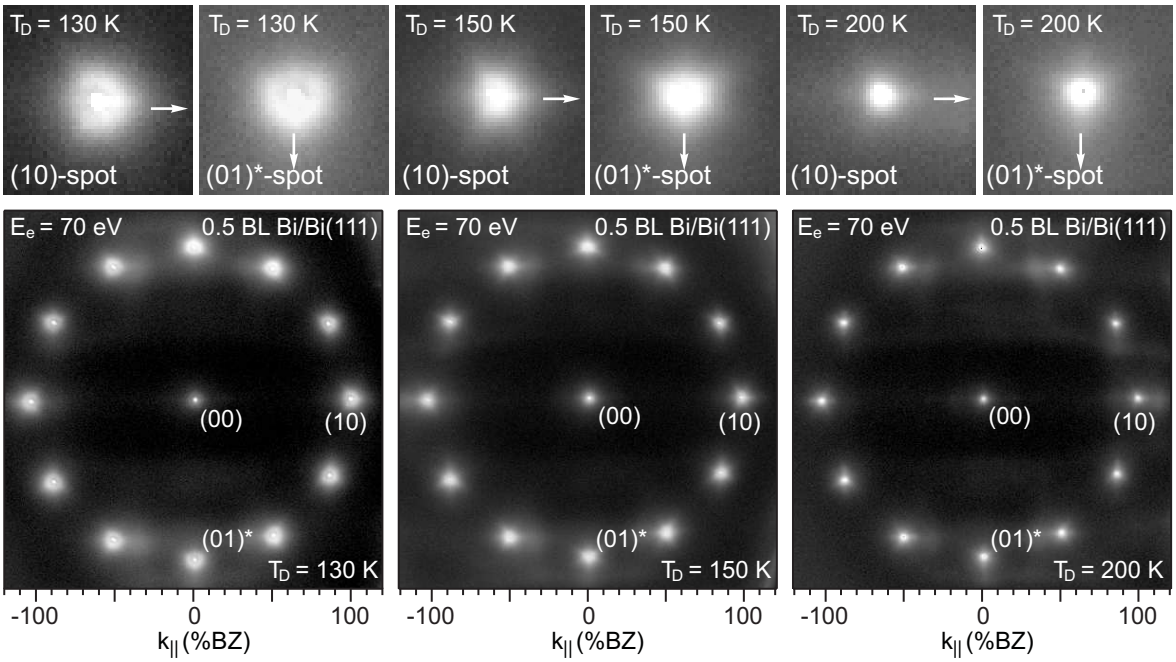

Figure 8.10: LEED patterns recorded after deposition of 0.5 BL Bi on a smooth 25 nm Bi(111) base film at different deposition temperatures (130−200 K). The shape of first order, i.e., (10)-spots changes with increasing the deposition temperature, which is caused by the change of 2D islands. The insets of (10) and $(01)^*$ spots from each LEED pattern are shown on the top.

across the corners where two edges meet. Such an ability of adatom diffusion along the island edges and corners, called the perimeter mobility, depends on the temperature, subsequently assisting to control the island shape via the substrate temperature. Along with the substrate temperature, the island shape is also influenced by the substrate symmetry. As an example, fractal or dendritic two-dimensional adatom islands could be grown at low temperature by homoepitaxial or heteroepitaxial deposition on a fcc (111) or hcp (0001) surfaces. It has been already known that on substrates with trigonal symmetry in general, hexagonally distorted islands evolve [198], while substrates with square or rectangular symmetry (e.g. (100), or (110) surfaces) lead to formation of square or rectangular islands [199, 200]. Obviously, there are also some other attributes, diffusion barriers (the terrace diffusion barrier and the step-edge barrier) [201, 198, 202, 193, 203], the external growth parameters such as the deposition flux, and the strain in the case of heteroepitaxy [94], which can strongly influence the island shape, which are beyond the topics of this thesis. In the following paragraphs and section, the evolution of the island shape at different growth temperatures will be discussed by using SPA-LEED and STM, which seems related to the phenomena expressed earlier.

It is obvious in the LEED pattern that the (00)-spot provides an information on the average surface morphology and does not reflect the individual shape of the islands. Since the Bi(111) base film emerges with two rotational domains and two twin domains, any information about non-isotropic island shapes will be hidden by the incoherent superposition of the individual patterns. That is the reason that (00)-spots recorded at different deposition temperatures (Fig. 8.6) show a circularly ring-shaped spot, while the first order spots exhibit a clear

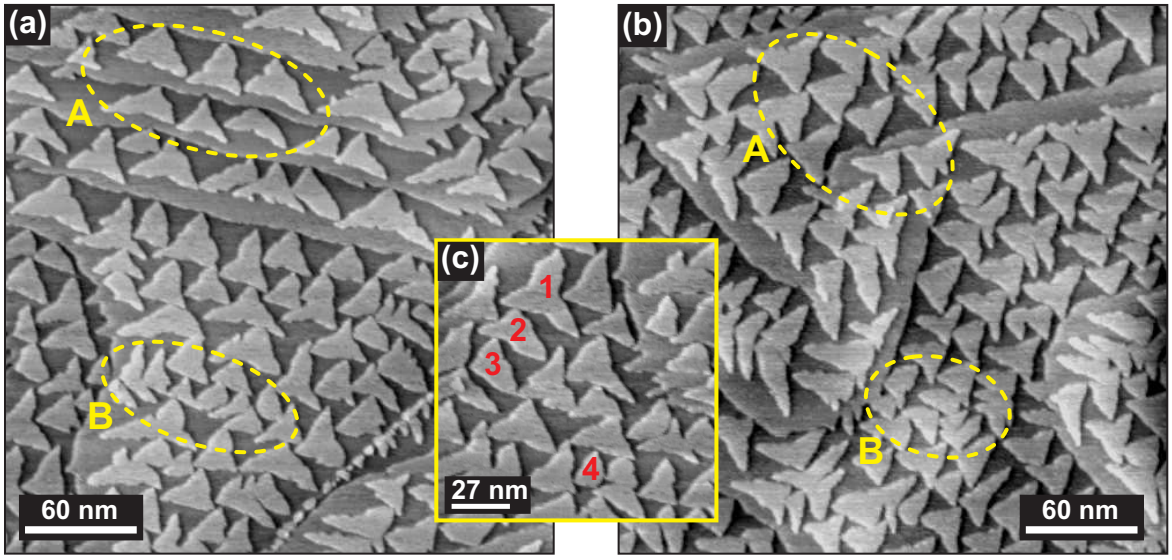

Figure 8.11: Influence of the diffusion fields on the growth of 2D islands after deposition of 0.5 BL Bi on a 25 nm Bi(111) base film at 135 K. The shapes of the islands in the areas indexed by A, B in images (a) and (b) are discussed in the text. Change of individual islands in (c) are symbolized by 1, 2, 3 and 4, are also discussed in the text..

difference in shape between 80−200 K (see Fig. 8.6 and 8.10). Because the islands are rather small at 80 K, which are confirmed by the small island separation, i.e., $\langle L \rangle = 4.6$ nm, the actual shape of the islands cannot be resolved by a LEED pattern. In contrast, at deposition temperatures between 130 −150 K, a three-fold symmetry of the first order LEED spots is observed (see Fig. 8.10). Despite a large diffuse background, the actual shape of the spot can be clearly recognized. A close inspection of each (10)-spots, as shown in the inset of Fig. 8.10, clearly resolves a three-fold rotational symmetry in the vicinity of the triangularly shaped diffuse intensity, which surrounds the central spike. Additionally, the symmetry of each domain spot, i.e., (10) and (01)* spots, are rotated by 90° from one domain to another (as indicated by arrows in the insets of Fig. 8.10). From this kind of characteristic shape of the (10)-spots, actual shape of the islands can be qualitatively estimated. Obviously, the three-fold symmetry of both domain spots suggests triangular shaped islands, which must be rotated by 90° from one domain to another. Large inhomogeneity in the triangularly shape islands may be expected from the diffuse background of the (10)-spots.

For the comparison, STM micrographs were recorded after deposition of 0.5 BL Bi on a smooth Bi(111) base film at 135 K. Figure 8.11(a) and (b) shows pure 2D and triangular-like islands of almost the same size and separation. All islands exhibit a quasi-dendritic shape, a so-called dendritic-skeletal island landscape, as is obvious from the higher magnification micrograph in Fig. 8.11(c). The quasi-dendritic shape is caused by the asymmetry in diffusion of adatoms from corners to the steps, which occurs generally on a hexagonal surface [191, 192, 193].

There are also some cases of island-island interaction, which caused a change in the shape of the islands [198]. Figure 8.11(a) and (b) illustrates some cases particularly in the regions

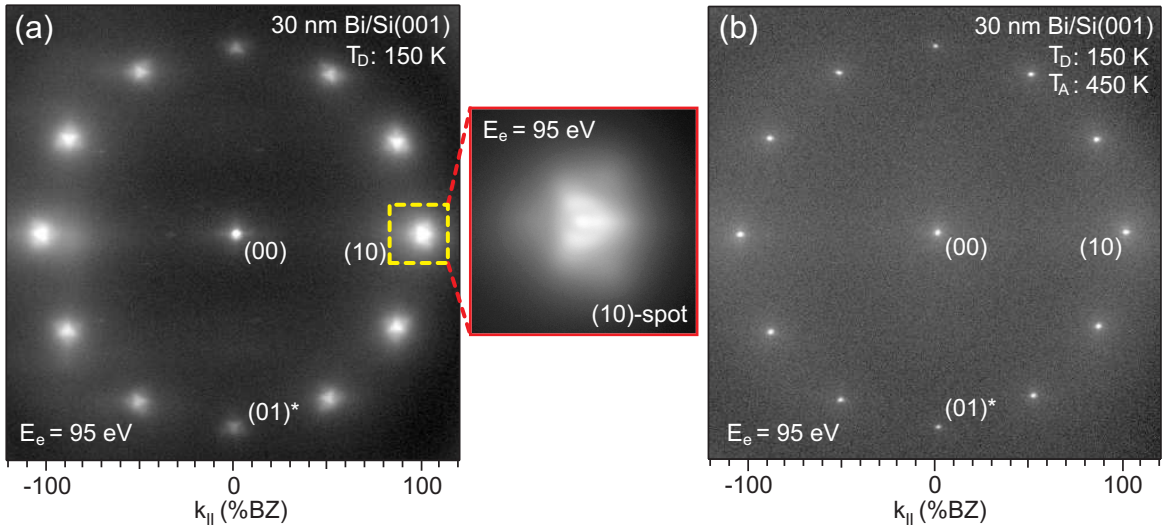

Figure 8.12: (a) LEED patterns recorded after deposition of 30 nm Bi on Si(001) at 150 K. The shape of the first order spots changes into a star-like shape (inset of the (10)-spot of the pattern (a)), reflecting an increase of surface roughness. (b) After annealing the film of (a) to 450 K, the spots become sharp, indicating a significant decrease of surface roughness.

symbolized by A and B. The islands indexed by A are located in regions that are relatively free of other islands. Except for the step edges, there are no other islands nearby. This is why the tips of the islands grow undisturbed due to the large diffusion fields. In contrast, the situation of the islands indexed by 'B' is typical for the islands, which can interact via the diffusion field. Because of interaction, the development of the island shape is screened by other islands, resulting in features of instability. Thus, the triangular-shape island is not sufficient for the onset of instability. Figure 8.11(c) shows four different island shapes (1,2,3 and 4) developed by the extent of interaction between the surrounding islands within the diffusion field. For the case of island-1, it has sufficient space due to surrounded by a large diffusion field. This causes a low interaction with surrounding islands, resulting in a complete shape of the island. In contrast, the interaction is gradually increased for islands 2, 3 and 4, respectively, due to the increase of the surrounding islands. As a result of increasing interaction, the size of the islands are gradually decreased.

8.1.6 Annealing behavior

Initially, a 0.5 BL Bi was deposited on a 25 nm Bi(111) base film at 80 K. The film was annealed slowly (5 K/min) from 80 K to 450 K. (00)-spot profiles were recorded during annealing after each interval of 20 K. The out-of-phase scattering condition (E_e = 49.3 eV, S = 4.5) was chosen for recording 1D (00)-spot profiles, since the profile is most sensitive to the lateral surface roughness. Figures 8.13(a) and (b) show the recorded (00)-spot profiles and the intensity distribution image, respectively.

At 80 K, the profile exhibits a typical ´Henzler Ring'-like profile with a sharp central peak at the center (see also Fig. 8.3). The profile shows a constant shape up to 130 K. Above 130 K, it changes considerably, which can also be observed in the intensity distribution image obtained

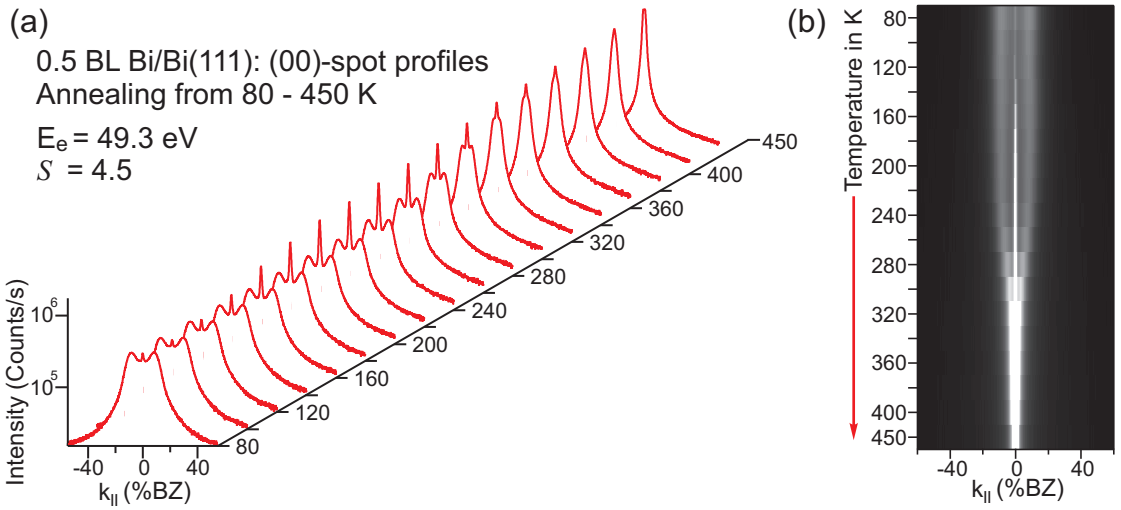

Figure 8.13: (a) LEED (00)-spot profiles recorded during the annealing of a 25 nm Bi(111) base film from 80−450 K after deposition of 0.5 BL Bi at 80 K. The profile exhibits a pronounced shoulder and vanishing central peak at 80 K and changes drastically during the annealing process. (b) Intensity distribution image obtained from the corresponding profiles. The image clearly shows the narrowing of the shoulder peaks, which merge into a single sharp peak at higher temperatures, indicating a smoothening of the surface into flat terraces.

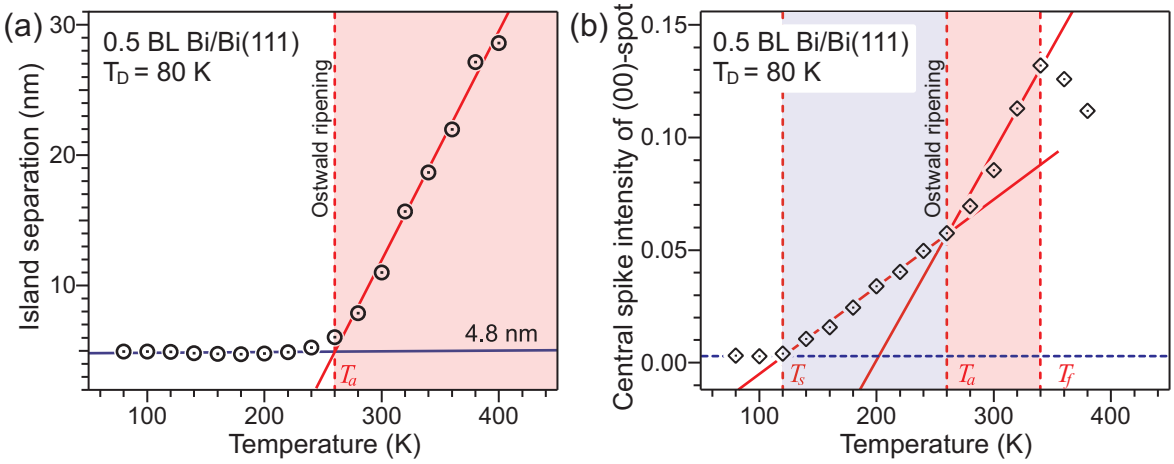

Figure 8.14: *In situ* estimation of island separation during annealing of a 25 nm Bi(111) base film after 0.5 BL Bi deposition at 80 K. The red line represents a linear fit. At 250 K, the separation increases rapidly, giving a rough estimation of the critical annealing temperature of $T_a \approx 260$ K. (b) Annealing behavior of the central spike intensity of the (00)-spot. The red lines represent linear fits with different slopes. The change of the slope at $T_s = 120$ K, $T_a = 260$ K and $T_f = 340$ K is discussed in the text.

from the recorded profiles (see Fig. 8.13(b)). There are mainly two changes observed in the profile: (1) the ring diameter reduces with the annealing temperature and (2) the central peak intensity increases sharply in the expense of shoulder intensity. From those changes observed in Fig. 8.13 (a) and (b), it can be estimated that the surface undergoes a notable transition at certain temperatures.

To understand the transition, profiles were analyzed by fitting with a Lorentzian functions as illustrated in 8.7(c). The ring distance, which corresponds the average island separation,

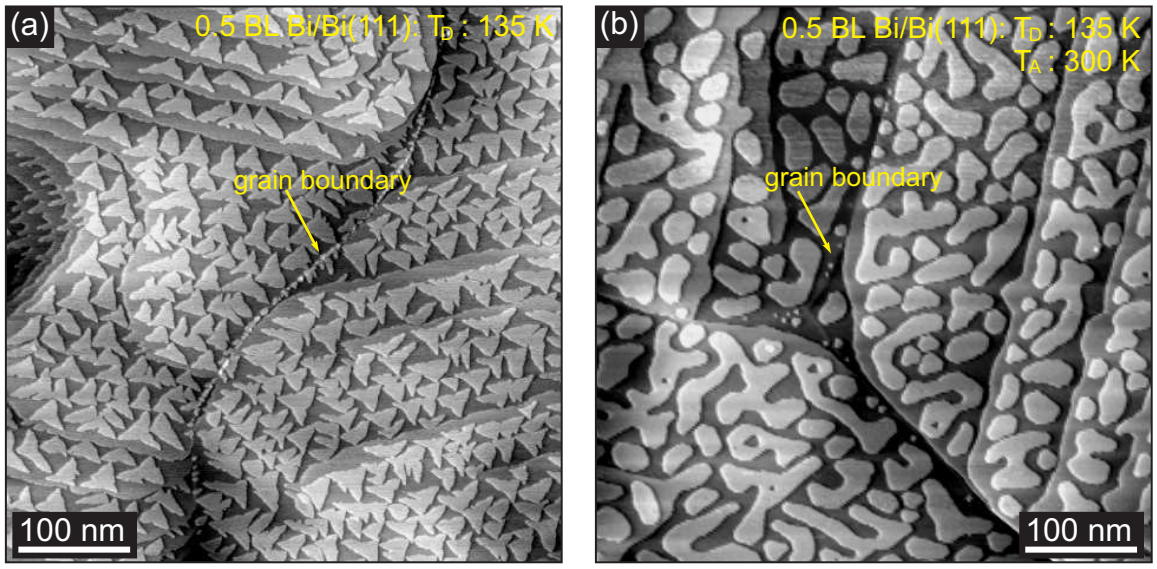

Figure 8.15: STM topography ($U_{\text{bias}} = 1.8$ V, $I_{\text{tunnel}} = 17$ pA) of a 0.5 BL Bi grown on a 25 nm Bi(111) base film at 135 K: (a) before annealing at 135 K and (b) after annealing to 300 K.

was determined directly from the distance between the shoulder peaks. The normalized integral intensity of the central spike was calculated, using the method described in chapter 2.1.1. Figure 8.14(a) and (b) summarizes both results, which are plotted against the annealing temperatures. It is clear from the first curve in Fig. 8.14(a) that there is a sharp increase of the island separation at $T_a = 260$ K, indicating a critical annealing temperature. Above T_a, the average island separation increases almost linearly with temperature, reflecting an increase of island size. Due to the thermally activated diffusion process, smaller islands are diffused to form bigger islands and some even merge into the existing islands, resulting in a rapid growth of size, the so-called Ostwald ripening. In the intensity plot 8.14(b), however, the slope changes at three temperatures, i.e., $T_s = 120$ K, $T_a = 260$ K and $T_f = 340$ K, respectively. The change of slope at $T_a = 260$ K is the similar effect (the Ostwald ripening) as discussed earlier. However, the change of slope at $T_s = 120$ K cannot be caused by surface smoothening effect via island coalescence since the island separation stays constant until 260 K. There are other processes, i.e., some of the adatoms are diffused from the grain boundaries to the existing Bi terrace steps and/or island edges. The interlayer diffusion of adatoms and/or tiny islands before Ostwald ripening, without increasing the island density, also causes an increase of the central spike intensity. The intensity maximum at $T_f = 340$ K indicates that the film morphology smoothes out completely and the intensity decreases afterwards due to the Debye-Waller effect.

The change of the surface morphology with annealing temperature was also studied by STM for two different coverages: 0.5 BL and 1.1 BL Bi on a 25 nm smooth Bi(111) base film. It was already discussed that quasi-compact triangular-like dendritic-skeletal shape Bi islands are formed at 0.5 BL coverage at 135 K (see Fig. 8.15(a)). After annealing to 300 K, the island shape changes drastically and is transformed into irregular 2D structures, which have almost the same width and different lengths, as shown in Fig. 8.15(b). This peculiar image

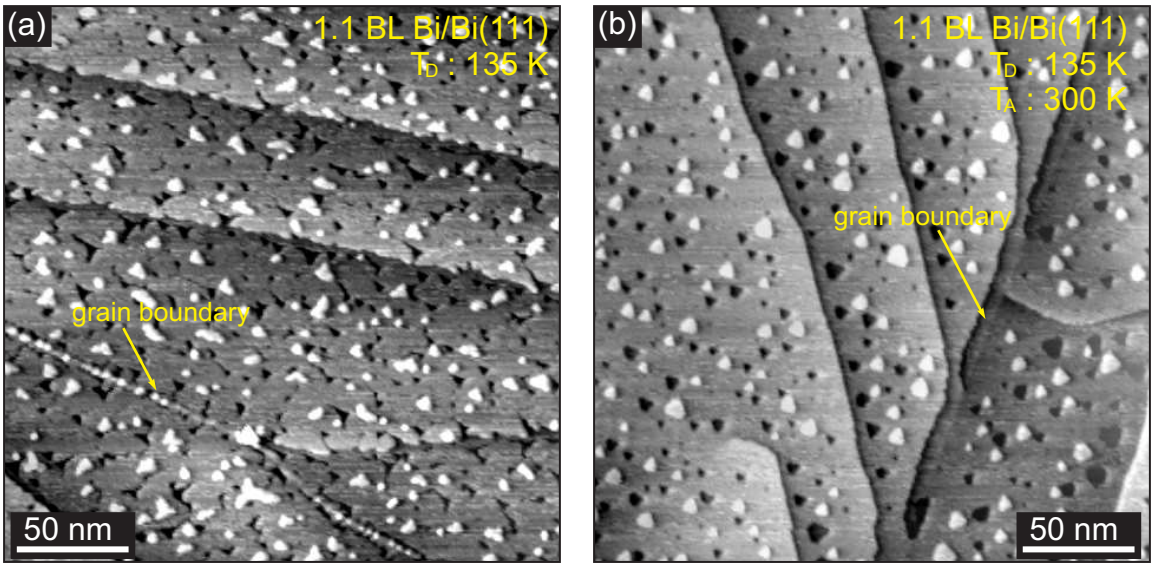

Figure 8.16: STM topography ($U_{\text{bias}} = 1.8$ V, $I_{\text{tunnel}} = 17$ pA) of a 1.1 BL Bi grown on a 30 nm Bi(111) base film at 135 K: (a) before annealing at 135 K and (b) after annealing to 300 K.

in Fig. 8.15(b) indicates that Bi islands avoid touching each other even at 300 K, which may be caused by covalent-like bonding in Bi crystal. Extreme electronic properties of Bi may also have contribution to make almost homogeneous width of 2D islands, which needs to be verified. Particularly, the cluster of atoms gathered in the grain boundary are depleted and almost all of the atoms are diffused to existing islands or step edges, which can be seen by a close inspection of Fig. 8.15(a) and (b). Interestingly, almost all of the atoms within a terrace are still not diffusing to the step edges; rather, they are merging to form bigger islands. This behavior suggests that the diffusion length is still comparable to the average island separation at that temperature, i.e., ~ 10 nm. In the case of 1.1 BL covered film, the annealing behavior of the morphology seems almost the same (see Fig. 8.16). The large number of trenches appearing at 135 K are partially filled up at 300 K. Additionally, mildly ramified small islands are turned into compact triangular islands. Beautifully decorated grain boundary as shown in Fig. 8.16(a) is almost vanished at 300 K (Fig. 8.16(b)). The overall annealing behavior is consistent with the SPA-LEED measurements in Fig. 8.14(a), the adatom diffusion is still limited within the small region at 300 K. Further increasing temperature higher than 350 K, the surface morphology changed dramatically, extremely smooth surface, as in the case of base Bi(111) film (Fig. 7.6(b)), was recovered.

8.2 Bi on Bi(111)/Si(111)

As long as the surface structure and the quality of the base film persists, the substrate orientation does not play a role for homoepitaxy. That is why the Si(111) substrate was chosen to grow a base Bi(111) film at 300 K. The first subsection will report briefly about the base film preparation, although the core of the recipe has already been established from previous works [22, 20, 24].

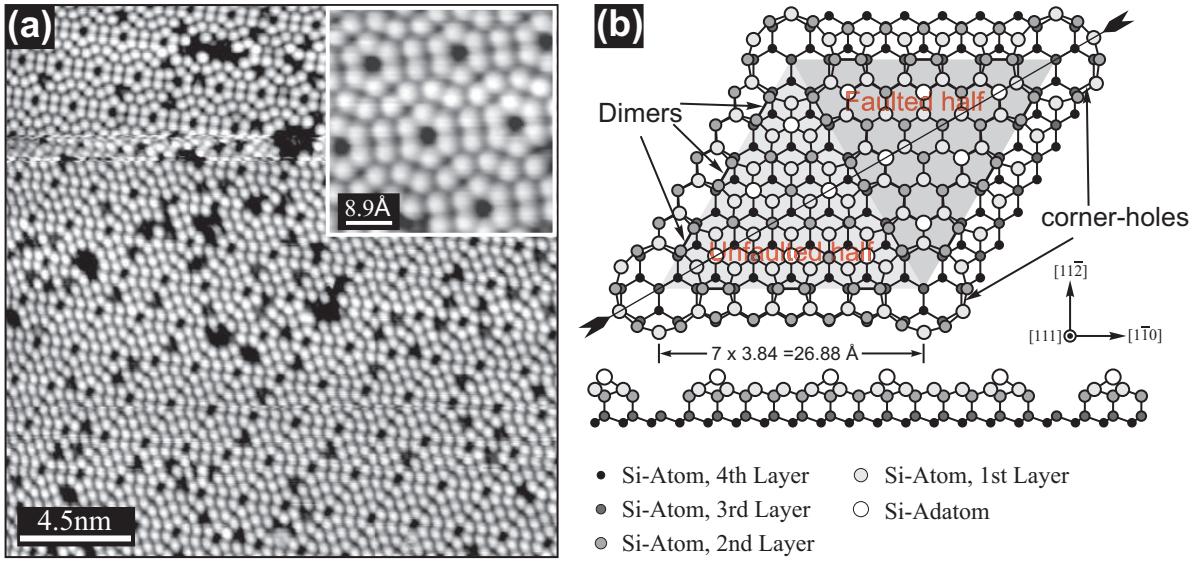

Figure 8.17: (a) STM topography ($U_{\text{bias}} = 1.8$ V, $I_{\text{tunnel}} = 17$ pA) of a Si(111)-7×7 surface, recorded at RT. (b) Atomic structure model (Dimer-Adatom-Stacking, DAS model) of the Si(111)-7×7 surface [204, 205].

The second subsection will explore the nucleation and adatom diffusion in the early stages of growth of Bi on Bi(111). Diffusion parameters will be determined via the estimation of the island density at different coverages.

8.2.1 Growth and morphology

A standard cleaning process was applied to prepare a clean Si(111)-(7×7) surface. Initially, the sample was flash annealed via resistive heating to ∼ 1500 K for a few seconds before following a short annealing at 1100 K and a slow (∼1 K/s) cooling down to room temperature. Such a method of preparation produces the Si(111)-(7×7) surface structure, as shown in Fig. 8.17(a), which is considered to be one of the most complex and widely studied surface of a solid. Since the first study by Schlier/Farnsworth in 1959 [68], an enormous amount of effort has been extended to elucidate the properties of this surface. Based on this work, it is now generally accepted that the geometry of the (7×7) reconstruction is described by a Dimer-Adatom-Stacking fault (DAS-model) as proposed by Takayanagi *et al.* [204, 205]. The schematic view of the model is shown in Fig. 8.17(b). The Si(111)-(7×7) surface is also known as the equilibrium high temperature phase until the temperature 1100 K. Details on the (7×7) structure can be found elsewhere [206, 207].

Bi was deposited from the resistive heated ceramic crucible onto the freshly prepared Si(111)-(7×7) surface at room temperature. Bi flux was calibrated in another high vacuum chamber before introducing the Bi evaporator to the STM chamber. Thickness calibration was performed by monitoring the change of frequency of a quartz microbalance during Bi deposition at room temperature. For the preparation of base Bi-film, higher flux was chosen keeping the residual pressure as low as possible, so that no defects would incorporate the film.

Bi (Purity 99.9999 %) was evaporated at 300 K from a resistively heated ceramic crucible

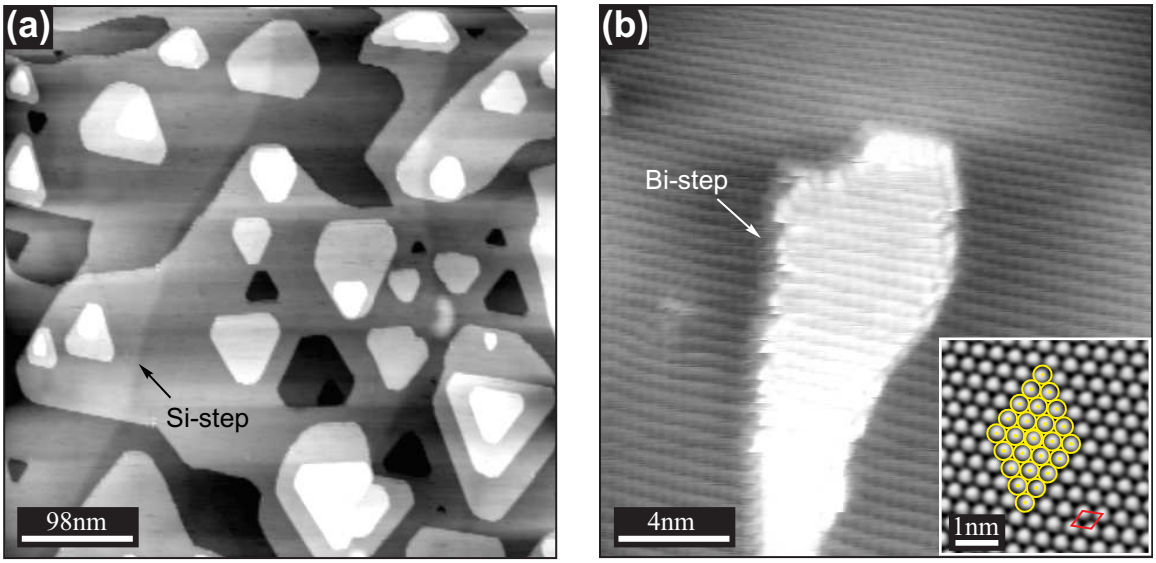

Figure 8.18: (a) STM topography of a 20 nm Bi(111) film grown on Si(111) at RT and annealed to 400 K. (b) STM topography at the different position of the same sample, showing an atomic resolution of a hexagonal surface structure. The hexagonal unit cell is indicated by the red line in the inset. All images were recorded at RT.

mounted in a water cooled copper shroud at a deposition rate of 0.01 BL/s [1 BL (bilayer) corresponds to the Bi(111) atomic density of 1.14×10^{15} atoms/cm^2]. The rate was monitored via a quartz microbalance mounted on the evaporator. The background pressure was better than 1×10^{-9} mbar during deposition. A nominal 20 nm thick Bi film was deposited on Si(111)-(7×7) at room temperature (RT) following a recipe given by Kammler *et al.* [22, 24] or Nagao *et al.* [20, **?**]. Additionally, the film was annealed to 400 K, which increases the average terrace length significantly [208]. Figure 8.18(a) shows the topography recorded at 300 K after annealing the film. The average terrace size is estimated to be larger than 100 nm and the apparent step height shows approximately a BL distance, i.e., ~ 4 Å. In addition, a weak height contrast, which reflects the underlying Si step (as indicated by an arrow in Fig. 8.18), is also visible in the topography. Figure 8.18(b) exhibits a flat surface with a 2D island in an atomic resolution. Surface lattice parameters are indicated by red lines in the inset.

The origin of the atomically flat morphology and single-crystalline nature of Bi(111) film has two reasons: a structural modification and an allotropic transformation from a black phosphorous-like pseudocubic crystal up to the 4 monolayers and the early formation of the lattice-matched hexagonal nuclei beyond 4 ML coverage [20, 209, 210]. The lattice accommodation between Bi(111) and Si(111)-(7×7) in a commensurate relationship, the so-called magic mismatch ($6\times\ a_{Bi(111)} = 7 \times a_{Si(111)}$), is also a strong reason for high crystalline nature of the film [20].

8.2.2 Early stages of growth

In section 8.1, homoepitaxial growth of Bi(111) at temperatures between 80–300 K was studied using SPA-LEED and STM. The surface morphology, island shape/size and the adatom

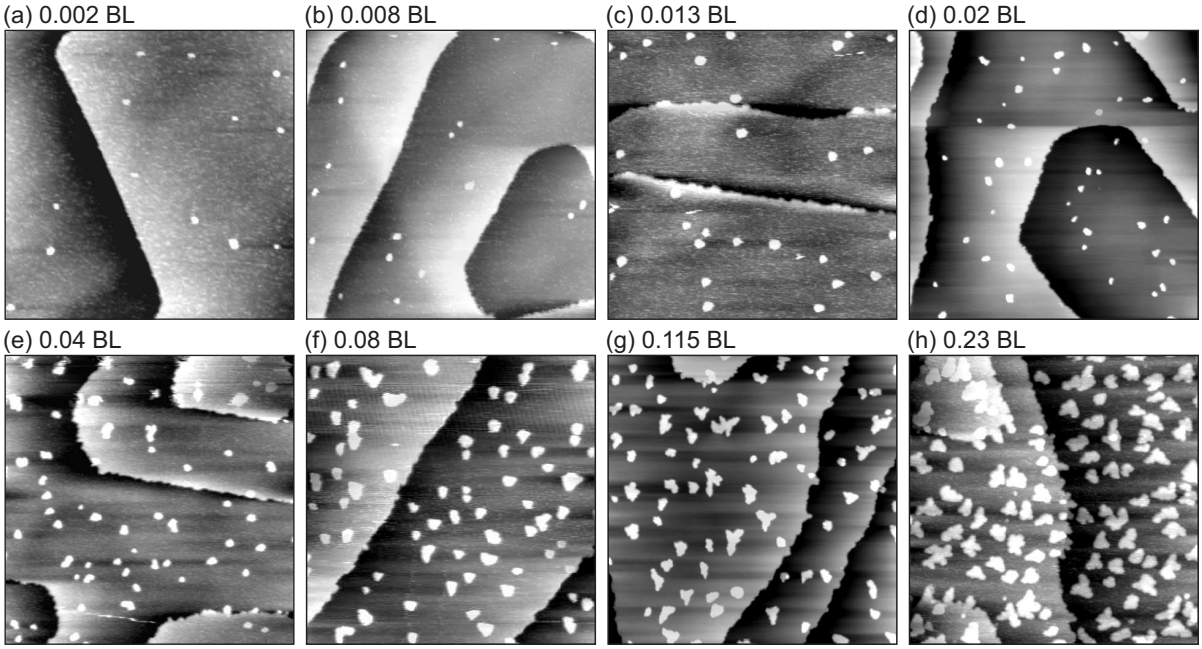

Figure 8.19: STM images (image size = 150×150 nm^2, $I_{\text{tunnel}} = 50$ pA, $U_{\text{bias}} = 1.0$ V) showing the variation of island density and the island shape transition from a compact to a quasi-fractal shape for different coverages of Bi on Bi(111) films at 130 K. The images are recorded from two experimental runs, i.e., Fig. (a), (c), (e), (f) and (h) are from run I and Fig. (b), (d) and (g) are from run II. A flux of $R = 3.7 \times 10^{-4}$ BL/s was used during each deposition for both experimental runs.

diffusion barrier were determined after deposition of 0.5 BL Bi on a Bi(111) base film. However, nucleation and an early stages of growth, which are essential in order to understand the microscopic processes, are missing.

This section will report an important STM investigation of the early stages of growth in Bi(111) homoepitaxy. Relevant diffusion parameters will be determined from the relation of island density with coverage at a constant temperature of 130 K. Finally, A novel shape transition of Bi islands will be discussed.

8.2.2.1 Diffusion parameters

High quality Bi(111) films with a thickness of 20 nm, as discussed earlier, were used as a virtual substrate to grow additional Bi at low temperatures. Since the Bi(111) buffer films are atomically smooth with an average terrace size larger than 100 nm, that does not affect the nucleation behavior during a further sub-monolayer deposition of Bi. These Bi buffer films were transferred to the STM chamber and cooled to 130 K. Further Bi deposition in the sub-monolayer regime were performed inside the STM using a second Bi evaporator at a flux of 3.7×10^{-4} BL/s and a base pressure of 5×10^{-10} mbar. This special experimental setup allows to deposit very small amounts of Bi and subsequently image the topography by STM without major displacements of the sample or changes of sample temperature.

In order to study the island nucleation and growth we have followed the change of the Bi(111) surface morphology as a function of coverage at 130 K. Figure 8.19 shows a series

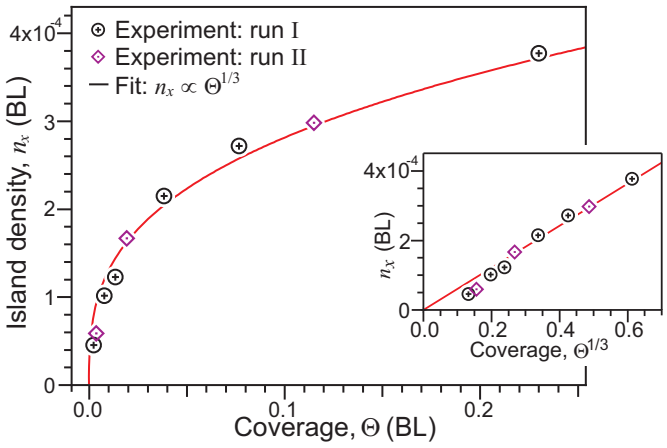

Figure 8.20: Island density versus coverage at 130 K, as estimated from the STM images shown in 8.19. The data are taken from two experimental runs (as indicated by I and II). In the inset, the data are plotted as a function of the cubic root of Bi coverage, showing a small deviation of island density at very low coverage.

of STM micrographs with a size of 50×150 nm^2 for coverages starting as low as 0.002 BL up to 0.23 BL of Bi. The micrographs were recorded from two experimental runs under the same conditions. At a very low coverage, Bi islands are imaged as bright protrusions while at higher coverages irregular shaped islands are apparent. The islands are randomly distributed over the surface, as evident from all images. It is also obvious that the island density and size have increased from Fig. 8.19(a) to (h). Additionally, a shape transition of the Bi islands is observed around 0.1 BL, where the compact shape of islands were transformed into a quasi-fractal form. However, no sharp or abrupt transition has occurred, as evident from the images 8.19(f) to (h), where only few of the compact islands have turned into quasi-fractal shapes at 0.115 BL, before leading to the anisotropic branching at 0.23 BL.

The island density as a function of Bi coverage was determined from the series of STM micrographs shown in Fig. 8.19 and plotted in Fig. 8.20. The island density does not change in the time between the deposition steps as confirmed by a high resolution LEED study where the onset of Ostwald ripening was observed only for temperatures above 200 K. Below 200 K, the island morphology is stable. The quantitative evaluation of the island density for each coverage was performed by island counting in each STM image. The island density was normalized to the atomic density of Bi(111) BL to extract the density in terms of atoms per lattice site, equivalent to BL.

Before we start with the discussion of these results let us briefly recapitulate some basics of nucleation theory. Single atom diffusion is governed by the diffusion barrier E_d and the attempt frequency ν_0. Both parameters define the migration of an adatom as a random walker on the surface lattice. For 2D diffusion, the diffusion coefficient D (in unit cells per second, or simply s^{-1}) could be expressed by E_d and ν_0 as [98]:

$$D = \frac{1}{6}\nu_0 \, exp\left(\frac{-E_d}{k_B T}\right) = D_0 \, exp\left(\frac{-E_d}{k_B T}\right) \tag{8.2}$$

with $D_0 = \frac{1}{6}\nu_0$, known as prefactor of the diffusion coefficient D and T the substrate temperature. In the initial phase of deposition the surface diffusion coefficient D determines the outcome of the competition between nucleation of new islands and the coarsening of existing islands. It therefore defines the stable island density at a given deposition rate R. Thus,

the value of the diffusion coefficient gives an estimation for the probability that a deposited adatom finds an existing island before it meets with another adatom and forms a stable nucleus and subsequently affects the number density of saturated islands.

In the section 8.1.4, the traditional approach, Venables nucleation theory [90, 91], was applied to evaluate an activation barrier for an adatom diffusion in Bi(111) surface. Here another approach is used to relate the island density with coverage, which is explained as follows.

Dimensional arguments, based on the theory of random walk, applied to the random-walk motion of adatoms in the nucleation process provides a simple relation between the surface adatom diffusion coefficient and the island number density as [211, 212]:

$$n_x^3 = \frac{3R\,\Theta}{D}. \tag{8.3}$$

Eq. 8.3 is valid for long hop distances in an isotropic 2D random-walk. Additionally, some important assumptions such as absence of coalescence or coarsening effects must be made before applying Eq. 8.3, which include mainly: (a) a collision of two adatoms forms a stable dimer and (b) there is no coarsening or coalescence of islands during deposition. Since experiments have been performed at 130 K and Bi atoms are covalently bonded within the lattice [20], thus the first assumption is valid for our system. The coverage regime we have studied is far below the coalescence regime, since a previous study exhibited no coalescence at 0.5 BL coverage (see section 8.1.3). That is why the second assumption also safely holds.

According to Eq. 8.3, we concentrate on the evolution of the island density n_x at different coverages at a constant temperature of 130 K and constant deposition rate R. Figure 8.20 shows the island density as a function of coverage. The island density increases rapidly at very low coverage and slows down afterward. However, no saturation or decrease of the density is apparent in the plot, indicating the absence of coalescence, which is consistent with a previous study (see section 8.1.3). The experimental data were fitted by using Eq. 8.3 (see Fig. 8.20), which agrees quite well except for a slight deviation at the very beginning (see inset of Fig. 8.20). This might be due to the fact that, below 0.0038 BL the monomer density slightly exceeds the stable island density, being just above the transition between the nucleation and the growth regime. The STM can hardly detect a single mobile Bi atom. The island size calculated from the ratio of the coverage to the island density at 0.0023 BL is ∼50 atoms; the observation of the pure nucleation regime can be excluded. From the slope of the fit the surface diffusion coefficient was calculated to be $D = 5.1 \times 10^6$ s^{-1}. Substituting the value of D and using the diffusion energy of $E_d = 0.135$ eV from the previous findings (section 8.1.4) in Eq. 8.2, the attempt frequency can be extracted to be $\nu_0 = 5.3 \times 10^{12}$ s^{-1}. This value is quite reasonable in the case of Bi, which has a sufficiently low atomic vibration frequency (bulk phonon frequency of $\nu_0 \simeq 3 \times 10^{12}$ s^{-1} for the optical branch [213]) as compared to other metallic systems.

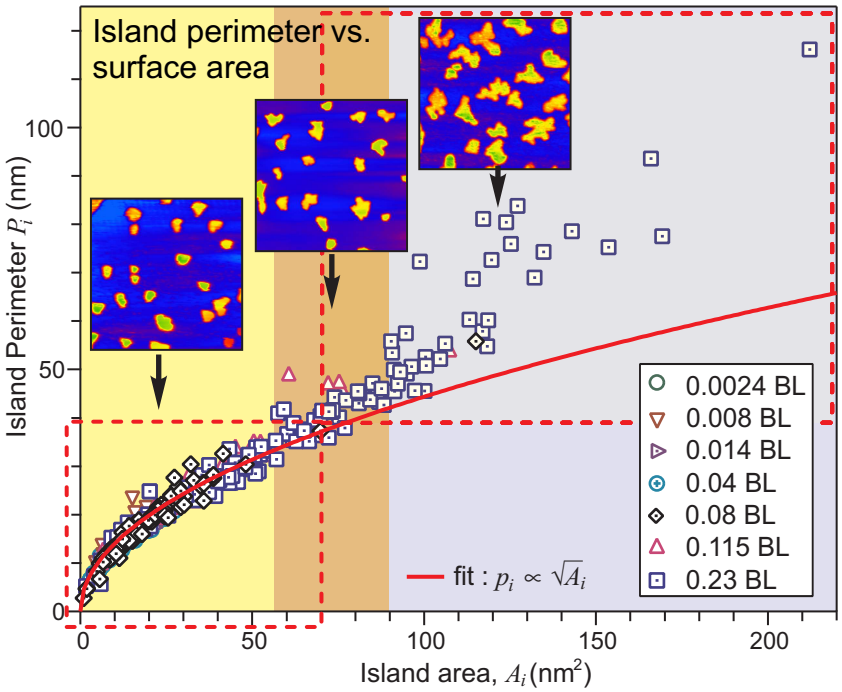

Figure 8.21: Island perimeter p_i versus surface area A_i plotted for different coverages, as indicated by different symbols. The red solid line represents a quadratic fit, i.e., $p_i \propto \sqrt{A_i}$. Dotted rectangles are shown for the guide to eyes to distinguish the regions of island shape transition. Typical islands from Fig. 8.19(f), (g) and (h) are also attached to show the shape transition. All images are shown in the same magnification scale.

8.2.2.2 Island shape transition

In the following we will evaluate the island shape transition as a function of coverage. From the inspection of the STM micrographs shown in Fig. 8.19 it is obvious that there is a notable change in island shape beyond a coverage of 0.076 BL. To quantify this transition in island shape systematically, we determined the perimeter p_i and the area A_i of each individual island for all STM micrographs shown in Fig. 8.20. All these data pairs (island area A_i, perimeter p_i) are plotted in Fig. 8.21 with different symbols for each coverage. Most of the data points overlap on a curve, which is well described by a square root of the coverage. This dependence is easily explained for compact islands of the same shape where the perimeter p_i increases, by definition, with increasing the surface area a_i following the square root behavior (circular: $A_i = p_i^2/4\pi$ or hexagonal: $A_i = \sqrt{3}\,p_i^2/24$). This agrees quite well up to 0.076 BL, as shown by the red solid line fit in Fig. 8.21. At 0.115 BL and even more clearly at 0.23 BL, a deviation from this square root dependence is evident. The deviation is observed for islands larger than $\sim$70 nm^2. Most of the islands from the STM micrograph at 0.23 BL coverage (dotted squares) lie far above the solid line, indicating a higher perimeter islands, i.e., quasi-fractal shapes in our case.

Considering the deposition conditions, regime and the coverage, such a shape transition has rarely been found in other systems. Brune *et al.* [214] have observed anisotropic branching of the islands in Ag/Pt(111) beyond the critical island size of heptamer, leading to an exclusive

island growth. It has been argued as a low perimeter mobility for attaching adatoms [215, 216, 217]. Unlike this case, the critical island size in our system is quite large, i.e., 70 nm^2 ($\sim$ 800 atoms), however, the transformed island shape is quite similar, i.e., branching in the triangular symmetry. This fact obviously reveals that the same argument may also drive the shape transition. However, a slightly lower diffusion barrier may have caused the large critical island size. Additionally, the shape transition observed here is far from the nucleation regime, which is not the case for Ag/Pt(111), where the shape transition has been found just at the transition from nucleation to growth regime.

9 Resistance Measurements

In situ surface resistance measurement is a quite sensitive experiment in a sense that a small perturbation in the condition of measurement may affect the expected value of the result. First of all, the quality of the electrical contacts on the Si(001) substrate is extremely important, since the resistance is measured during deposition of thin films on the substrate. Quality contacts are ohmic and thermally stable up to the annealing temperature of the Si. Additionally, no contamination should occur; the surface should be atomically clean. Those contacts are fabricated on the Si(001) substrate (in a 4PP setup), as described in section 6.1. Using the method described in section 6.1, the resistance of the sample is measured during deposition of the materials on the substrate and the base films.

In this chapter, results from the experimental observation of resistance change during heteroepitaxial and homoepitaxial growth at different conditions are discussed. The underlying physical phenomena such as structural, morphology and the electronic properties, which may have caused the change of resistance, are identified and an attempt is made to address them quantitatively. Initially, the resistance change during heteroepitaxial growth will be explained before the results of the homoepitaxial system are discussed.

9.1 Bi(111)/Si(001)

The study of growth and morphology during deposition of Bi on Si(001) was reported in section 7.1. At different coverages, various structural phases and reconstructions were observed via SPA-LEED measurements, where the resistance of the film was also measured simultaneously. Results of such an *in situ* observation of electrical resistance of the Si(001) substrate during deposition are presented in the following sections.

9.1.1 The influence of surface structural transformation

Fig. 9.1(a) shows the results of simultaneously recorded LEED (00)-spot intensity and the resistance of the sample during deposition of Bi on Si(001) at 150 K. Such an *in situ* measurement allows a direct observation of morphology and its influence on film resistance. For the precise knowledge of surface structural phases, LEED patterns were recorded at various coverages. The relative resistance of the Bi film is derived by subtracting the resistance of the initial clean substrate from the measured total resistance and normalized by initial resistance at zero coverage.

It has been shown in section 7.1.8 that Si(001) surface undergoes various phases under the sub-bilayer deposition of Bi at 150 K. With increasing the coverage different phases of crys-

tallographic orientation appear. Direct evidence of such a surface structural transformation is also obtained from the resistance measurement. As the surface undergoes different surface crystallographic phases, the film resistance changes noticeably. However, due to the consequence of morphological change overlapped with structural transformation, a sharp transition is not observed in the resistance curve (Fig. 9.1(a)). To explain the resistance behavior more systematically, the most significant changes of surface structure are classified into five stages (i)-(v), where the resistance slope changes noticeably. In the stage (i), Bi atoms are adsorbed randomly on the Si(001) surface and build their own dimers at sub-bilayer coverage. Until ∼2 BL coverage there are already Bi islands formed on the wetting layer, which are highly disordered (see Fig. 7.28). Since the islands are still not connected, the resistance change is negligibly small, indicating that neither the wetting layer nor the islands do form a substantial current path. Further increasing the coverage (stage ii) the resistance falls sharply, which indicates the lateral size of the islands increases and islands start to join each other. More significantly, in this stage, the surface morphology changes rapidly; each disordered crystallite is turned into ordered and oriented one. Sharp spots of a 12-fold LEED pattern in Fig. 9.1(b) clearly reflect the ordered nature of Bi islands. However, rotationally disordered Bi(110) crystallites equally appear, as indicated by a ring of diffuse intensity. Additionally, the Bi-induced (7×2) reconstruction also appears at the beginning of this stage. In stage (iii), the islands start to connect faster and the (7×2) structure vanishes, and only two crystallographic orientations remain, i.e., (110) and (111). At 5.6 BL the film becomes continuous. Such a

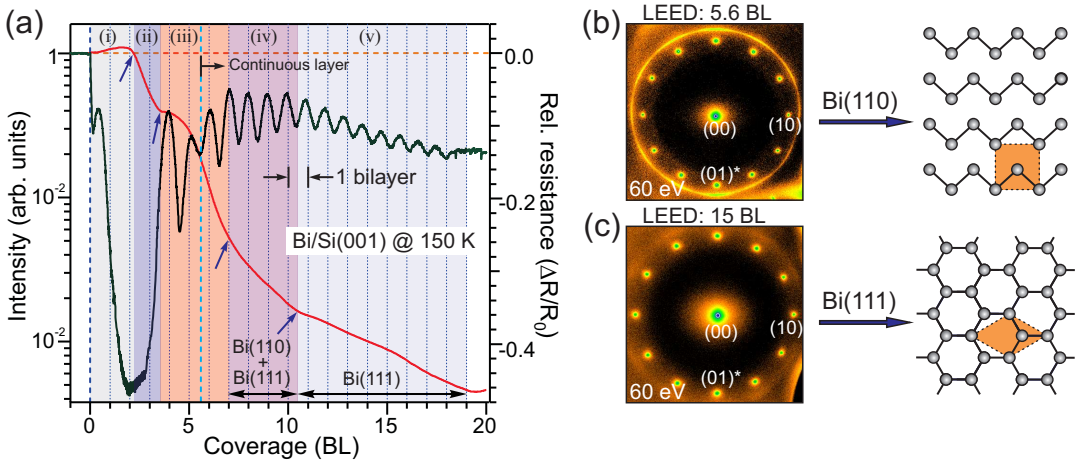

Figure 9.1: *In situ* observation of resistance change due to the change of surface structural phases during deposition of Bi on Si(001) at 150 K: (a) *in situ* recording of LEED (00)-spot intensity at an out-of-phase condition and relative change of resistance during deposition of Bi on Si(001) at 150 K. The slope of the resistance curve changes as the surface undergoes various surface crystallographic phases depending on the coverage. Noticeable changes are marked via directed arrows. (b) Overlapping of two crystallographic phases, i.e., highly oriented (111) and rotationally disordered (110), which have been recorded at 5.6 BL, as the Bi film turns continuous. The (111) orientation can be recognized by the 12-fold symmetry spots surrounding the (00)-spot. The disordered (110) phase can be interpreted due to the ring of intensity. (b) Dominating (111) phase observed as the film gets thicker than 12 BL. The extreme right of both figures (b) and (c) shows the sketches of corresponding crystal structures with unit cells painted.

morphological development on the surface causes a significant reduction of the resistance. However, after formation of the continuous layer at 5.6 BL, the resistance changes relatively fast. But this doesn't last longer; the slope of the resistance changes as the coverage reaches stage (iv). A LEED investigation shows that the (110) crystallites start to fade away slowly at this stage. A decrease of ring intensity with the coverage confirms that Bi grows only in a (111) orientation. At the same time, the surface gets roughened due to the kinetic limitation of adatom diffusion. This can be observed as a decreasing amplitude of the intensity oscillations. The combination of all those effects results in a further decrease of resistance, but at a slower rate than at stage (iii). This indicates the metallic nature of the film. At stage (v), the (110) oriented crystallites are almost completely disappeared, and only (111) oriented structures remain. LEED patterns shown in Fig. 9.1(b) and (c) clearly show the structural transformation as the coverage exceeds the stage (iv). However, the structural transformation is not sharp and abrupt. Until 16 BL coverage the mild intensity of the ring can still be observed (Fig. 9.1(c)). Such an allotropic transformation from stage (iv) to stage (v) again causes the change of resistance slope. After the stage (v) resistance decreases monotonously with the coverage.

Recent studies have shown that Bi undergoes a unique 2D allotropic transformation from puckered layers of (110) orientation to the bulk like (111) orientation at 4 ML coverage during the growth of Bi on Si(111) at RT [24, 20, 218]. It has been shown that the surface conductance increases significantly when the film crystallites transform from (110) to (111). Since no other significant morphological changes have been observed, it has been attributed that highly metallic surface states at the crystal truncation of (111) surface is the only cause, responsible for higher surface conductance. Recent investigations have further confirmed that the Bi(111) surface has nearly 2 orders of magnitude higher carrier density, concluding that the surface state dominates the electrical transport for thin Bi films [219]. Those previous investigations and arguments also support our results of resistance change at stage (iv), where both the (110) and (111) crystallites are present at the beginning and slowly transforms into entirely (111) oriented surface. Since the surface turns metallic in nature due to the crystallographic transformation, the resistance decreases. However, despite the similar results, the situation differs significantly as compared to the previous system. We performed the experiment at 150 K, so the kinetic roughening of the surface might destroy the surface state quite significantly. Moreover, the activation barrier for atomic diffusion is large as compared to the RT, which might hinder a sharp transition, although such a transformation only involves the conversion of the bond orientation and does not require much atom diffusion.

Similar experiments were also performed at different temperatures, i.e., 200 K, 280 K and 300 K. Both the resistance and the LEED (00)-spot intensity were recorded *in situ* during deposition. The curves in Fig. 9.2 exhibit marked differences to the one proposed at 150 K. The curve at 200 K shows that the resistance decreases monotonously as the Bi islands start to coalesce. Interestingly, a mild oscillation can also be observed, which is attributed to the change of morphology dominating the resistance. Since the (110) crystallites are significantly suppressed at 200 K, only (111) orientated crystallites are present. Obviously, the resistance

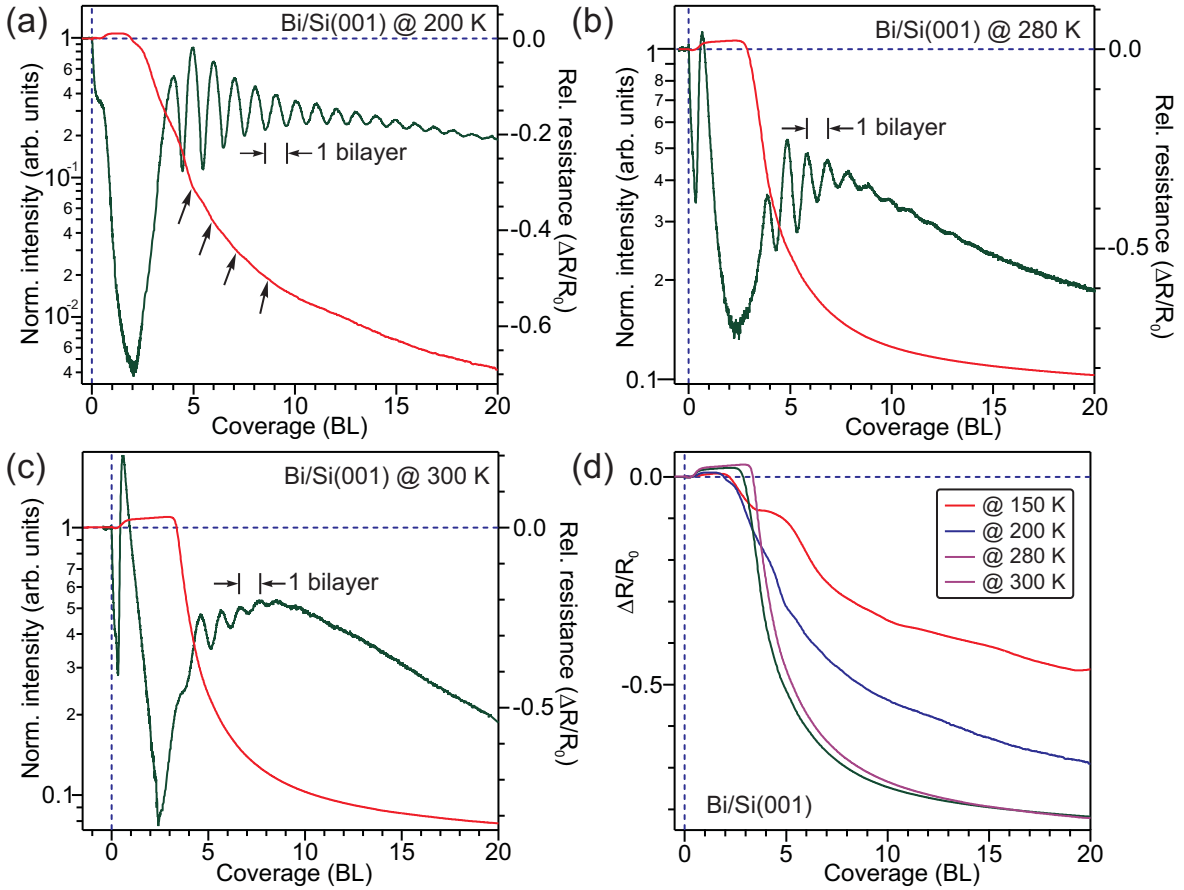

Figure 9.2: *In situ* observation of resistance change (red lines) and the surface morphology via LEED (00)-spot intensity (green lines) recorded during deposition of Bi on Si(001) at (a) at 200 K, (b) at 28 K, and (c) 300 K. (d) All the resistance curves from (a), (b) and (c) are plotted in a single graph.

changes according to the change of morphology. In contrast, the resistance at 300 K shows almost the $1/d$ behavior, where d is the film thickness. This is a typical behavior of resistance, which is mainly caused by scattering at surface roughness and known as classical size effect (see section 2.5.2). As it is clear from the (00)-spot intensity curve at different temperatures, the oscillation amplitude decreases faster when the growth temperature is increased. That means the growth advances towards the Stranski-Krastanov mode (3D mode) as the temperature is increased, which causes an increase of surface roughness via 3D islands. However, the bulk defects are annihilated and the grain size is increased as the deposition temperature is increased. A direct consequence of this effect can easily be observed when those four resistance curves are compared (see Fig. 9.2(d)). At the same coverage (20 BL), the relative change of resistance for a RT deposited film has the highest and for 150 K the lowest.

9.1.2 Temperature and thickness dependent behaviors of the conductance

Electrical properties of those well-annealed Bi(111) films were characterized via *in situ* resistance measurements at different temperatures. Interestingly, as shown in Fig. 9.3, the conductance of the film, i.e., the reciprocal of resistance, increases exponentially with increas-

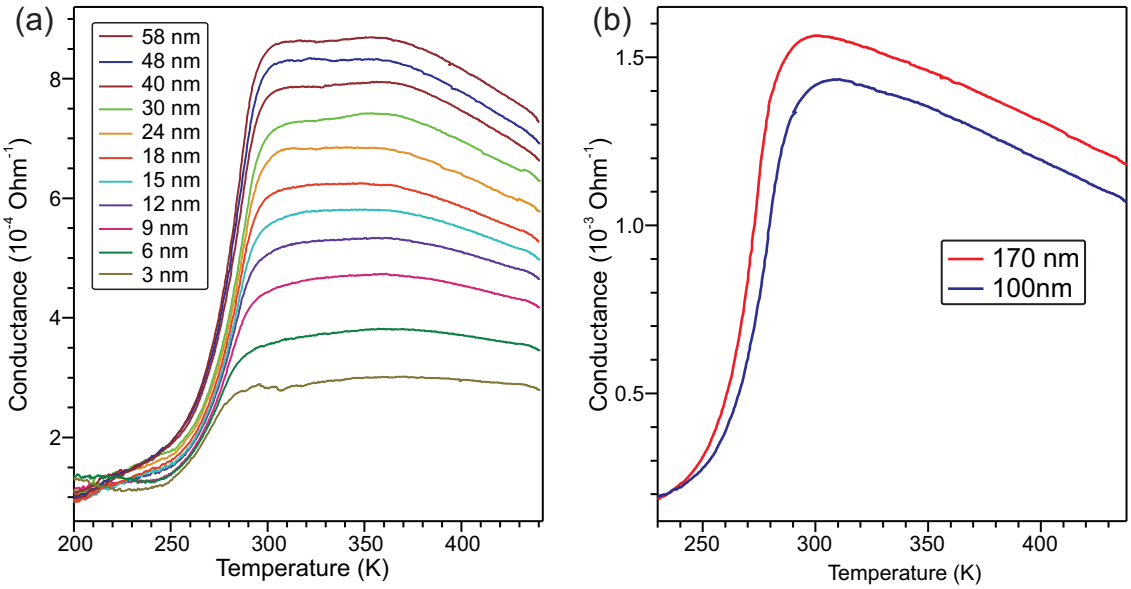

Figure 9.3: Conductance of Bi films as a function of temperature. (a) Conductance measured for various thicknesses (3-58 nm), as indicated by solid lines of different colors. Conductance increases exponentially with temperature from 200 K to RT and levels off up to around 350 K. Beyond 350 K, it begins to decrease. (b) Conductance of 100 nm (the blue line) and 170 nm (the red line) films as a function of temperature. After rapid increase of the conductance up to RT, it decreases immediately; no saturation region appears.

ing temperature in the range from 200 K to RT. After saturation at RT, it starts to decrease at ∼370 K. This behavior is characteristic for a doped semiconductor with a small band gap. Initially at low temperatures, the conduction band is not populated by electrons. After achieving a certain temperature, the conduction band starts to be populated by electrons via ionization of donor atoms. After complete ionization, the conduction band is saturated. Such a drastic change of carriers results in an exponential increase of conductance over a small temperature range. Until 350 K (depending on the thickness), thermal energy is still not sufficient to eject the majority of electrons from the valence band to the conduction band. However, beyond 350 K, carriers are able to cross the band due to the sufficient thermal energy and the conduction band is highly populated by electrons. At such a high temperature, lattice vibration becomes more effective and the electron-phonon scattering reduces the conductance of the film. Additionally, such an exponential increase of the conductance at low temperature and the linear decrease at high temperature becomes more pronounced with increasing film thickness. As shown in Fig. 9.3(a), for a 3 nm film, the conductance increases nearly 130 %, and for a 58 nm film, it increases nearly 800 %. As the film gets thicker and thicker, the conductance increases but at a slower rate. At the same time, the saturation region shrinks down as the film gets thicker and completely vanishes for the films thicker than 100 nm. As shown in Fig. 9.3(b), the conductance decreases immediately after approaching the maximum at around 300 K; no saturation region is observed.

The observation of the unusual electrical character of grown epitaxial Bi films on Si is significantly different from bulk single crystalline Bi and grown epitaxial Bi films on different

substrates. In the case of bulk bismuth, except at an extreme low temperature [220], the resistivity increases almost linearly with temperature [221]. It happens as a consequence of competition between the large increase of carrier density and the decrease of carrier mobility due to increased lattice vibrations [222, 221, 223]. This increase of carrier density results in a lowering of mean free path and as a whole leads to an increase of the resistance. In contrast to bulk, the carrier mobilities as a function of temperature are not so strong in thin films [224]. So, the difference of carrier density and the mobility in thin films may lead to a different resistance behavior as compared to bulk crystal.

Our observation of the doped semiconductor nature of the Bi films absolutely disagrees with the metallic nature of epitaxially grown Bi films [12]. Moreover, no semimetal-to-semiconductor (SMSC) transition, as predicted by Lutskii [10], was observed. The SMSC transition happens when the energy shift due to the quantum confinement becomes large enough so that the lowest electron sub-band rises above the top of the highest hole sub-band, due to their difference band masses. The critical thickness of the thin film for the transition to happen is between ~30 Å [81]. In contrast to the SMSC transition, all films up to 58 nm have shown the same behavior like extrinsic semicondoctors. We can speculate that a highly ordered interfacial dislocation network at the interface may have trapped charge careers and each dislocation becomes like a donor. Since it is a thermally activated process, they release the charge and subsequently increases the carrier density in the film, which increases the film conductance drastically. However, at higher temperatures, the carrier density is sufficiently high and the film shows a metallic behavior. This kind of phenomena is not new for direct semiconductors such as GaAs [225] or GaAs-based heterostructures [226], where dislocation-like defects behave as an electron trapping center at a deep level. Due to a lack of quantitative information about the career density of the film, it is hard to confirm the speculation. Nevertheless, this can provide an important basis for further analysis to draw a significant conclusion.

The conductance of each film at RT and 80 K, extracted from Fig. 9.3(a), was also plotted along with the results from the other two samples. As shown in Fig. 9.4(a), the conductance increases with an increase of the film thickness, indicating that surface and interface scattering of carriers dominates the conductance of the film. However, the increase of conductance is not linear for all films of different thicknesses, suggesting that a thickness dependent change of mobility or mean free path, also play a role. Recent reports have shown that the Bi surface has highly metallic surface states [17] and the carrier density at the surface is two orders of magnitude higher than in the bulk. So, the film conductivity $\sigma(t)$ is the combination of a surface contribution σ_{SS}, which is thickness independent [17], and the carriers inside the film $\sigma_{film}(t)$. From the estimation of mean free path l_{el} in epitaxial Bi films (l_{el}~10 nm), Hirahara *et al.* [219] have argued that the conductivity of very thin Bi films ($t < l_{el}$) is dominated by metallic surface states plus the surface/interface scattering. This situation causes a parabolic dependence of conductivity with thickness $\sigma \sim t^2$, because the film conductivity σ, according to the Drude model, is defined by the carrier concentration n_{2D} and the mobility μ as $\sigma = en_{2D}\mu$. Both the 2D career concentration n_{2D} and the mobility μ increase with thickness t.

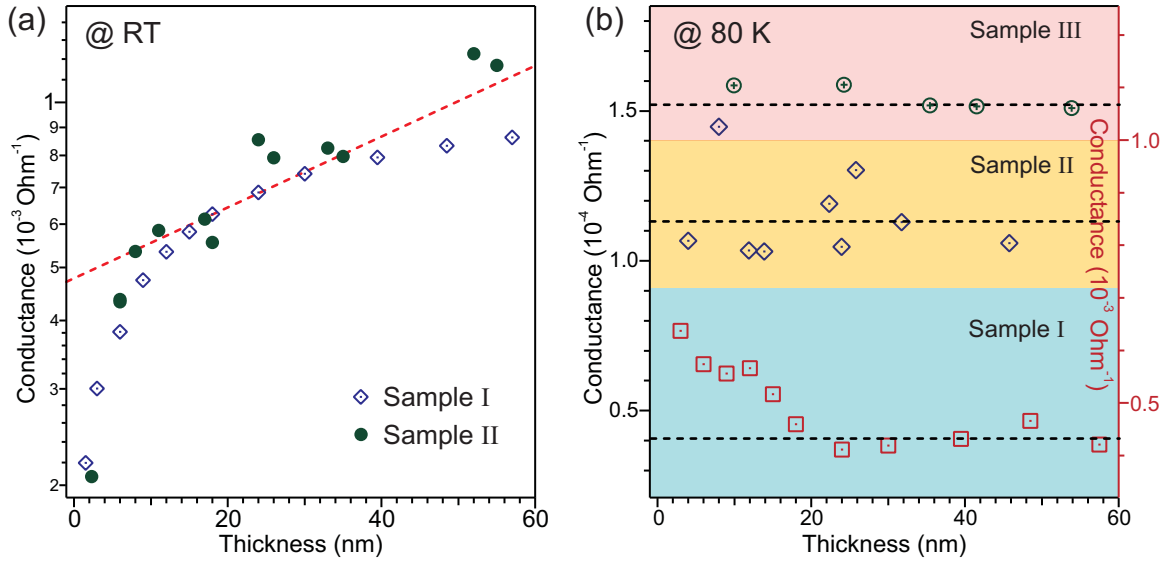

Figure 9.4: Resistance of Bi(111) films as a function of thickness at (a) RT and (b) 80 K. (a) Measurements from two samples (sample I and sample II) are shown with blue and green symbols. The red dotted line is the fit to the data from sample II (green symbol). (b) Bi films prepared from three Si samples are shown with different symbols and colors. Dotted lines are drawn as a guide.

For larger films ($t \geq l_{el}$), the conductivity is the combination of the surface states plus the phonon or impurity scattering, which causes a bulk-like linear dependence with thickness t. Our observation of rapid increase of conductance for thinner films ($t < 12$ nm) can also be argued due to the combination of both the surface/interface scattering proposed by Fuchs-Sondheimer [1] plus the metallic surface states. The conductance deviates at 12 nm and follows the linear behavior, indicating that the thickness becomes larger than mean free path l_{el}.

At 80 K, surprisingly, almost constant conductance was observed up to 60 nm thick films. Results from 3 different samples are plotted in Fig. 9.4(b). Results extracted from Fig. 9.3(a) is indicated by Sample I and results from other two samples are indicated by Sample II and Sample III. Samples II and III are cut from the same wafer and the sample I is cut from the different wafer, which has a slightly different doping level. Sample I shows slightly higher conductance for very thin films, but the other two samples hardly show any changes of conductance. Such a weak dependence of conductance with film thickness clearly suggests a constant carrier density, which is independent of film thickness. This can only be explained if we consider the film conductance is dominated by metallic surface states. This statement is supported by recent results from Hirahara *et al.* [17], where no thickness dependent is found in the band structure. Previous results of scanning tunneling spectroscopy studies of a single-crystal surface revealed the presence of metallic states in a two dimensional layer in Bi(111) [227]. The electron density of states at the Fermi level was found to be that of a typical metal, significantly larger than what is to be expected from semimetallic bulk Bi. Previous angular-resolved photoemission (ARPES) experiments also reported increased emission at the Fermi level region due to surface states and resonances located close to the

Fermi level [228, 229, 230].

9.2 Bi/Bi(111)

In this section, an important investigation, the influence of isolated adatoms on the surface state resistance on Bi films, will be discussed. Following the additional deposition of Bi on smooth Bi films, it will be shown how a simultaneous measurement of resistance (via 4PP setup) and the surface morphology (via LEED (00)-spot profile analysis) allow us to evaluate precisely the behavior of surface resistance change as a function of the change of surface morphology.

The measured resistance change at a very low coverage regime could not be simply explained by considering the electrical transport via thin films, because of the inherent large Fermi wavelength and extremely low carrier density in Bi films. Highly metallic surface states, as confirmed by constant conductance at 80 K (9.4(b)), allow the carrier transport dominantly via Bi surface states. Under those conditions, a simple scattering mechanism combining with the experimental observation of Bi island density vs. coverage, the observed variations of the resistance can be fully interpreted.

9.2.1 Surface resistance and morphology

Measured results of the resistance and the surface morphology (via (00)-spot profiles and the intensity variation) change during additional deposition of Bi on well annealed Bi(111) base film at 80 K are shown in Fig. 9.5(a). The solid red curve shows the relative change of resistance, which has been calculated via $\triangle R/R_0 = (R(t) - R_0)/R_0$, where $R(t)$ is the measured resistance with increasing thickness and R_0 is the resistance of the base film. The solid green lines indicate the peak intensity of the (00)-spot. Blue symbols represent the FWHM of the shoulder profiles of (00)-spots recorded during deposition. The FWHM is measured in the reciprocal unit, i.e., %BZ, where the 100 %BZ is equivalent to the $2\pi/a_{Bi(111)}$. Within a half BL coverage, the resistance increases nearly 17 % and decreases monotonously after undergoing some visible oscillations.

It has already been explained (see section 8.1) that Bi grows in a purely 2D mode at very low coverages and slightly roughens as the thickness increases and finally undergoes a large scale roughness due to the kinetic limitation of adatom diffusion at a sufficiently low temperature. LEED specular intensity oscillation at the interval of each BL coverage at the out-of-phase scattering condition clearly manifests the growth behavior. As expected, the film resistance also exhibits an oscillation in a BL mode, but the peaks of the amplitude are antiphase to the intensity maxima. The oscillation peaks of resistance are indicated by arrows and follow the oscillation matching with the period of a BL (see Fig. 9.5(a)). The short range oscillation with coverage is the result of step density oscillation at surface. If growth occurs in a bilayer-by-bilayer mode, surface roughness or step density oscillates from a minimum at complete layer and a maximum at a half integer order of coverage. At the lowest

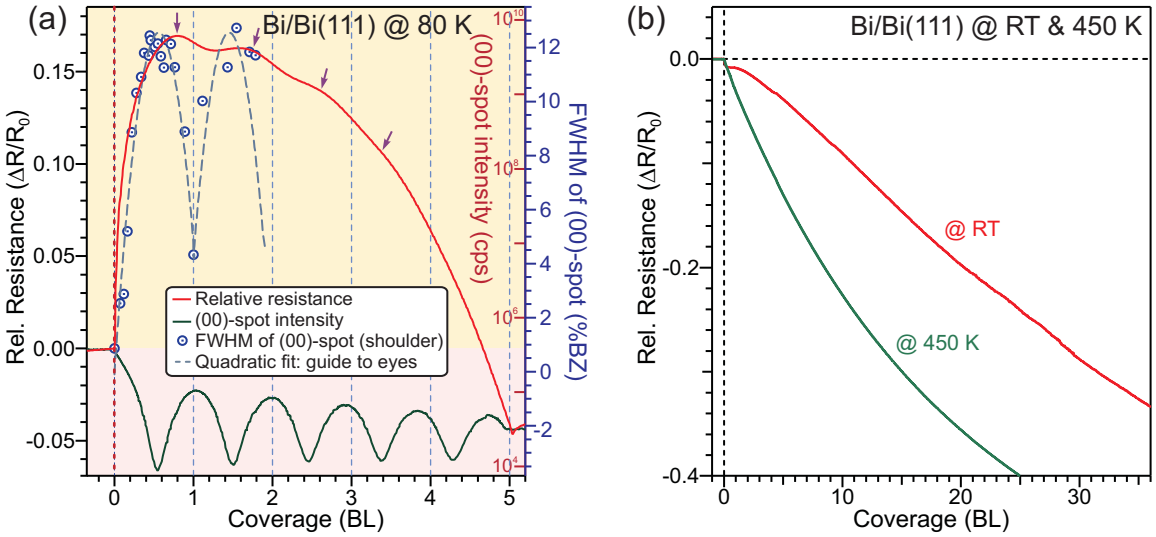

Figure 9.5: Relative change of resistance (red curve) and intensity of (00)-spot (green curve) during additional deposition of Bi on a smooth Bi(111) films (a) at 80 K, (b) at RT. (a) LEED (00)-spot intensity oscillation reflects a 2D bilayer-by-bilayer growth mode. Periodic change of the (00)-spot width (the blue symbol) shows a variation of island density during deposition. Such a periodic change of surface morphology also induces an oscillation of the resistance. Up to four maxima of the oscillation amplitude could be observed (blue arrows). (b) At RT, the resistance immediately decreases and follows a linear dependent with increasing the coverage. The decrease of the LEED (00)-spot intensity indicates a buildup of surface roughness as the coverage increases.

roughness, i.e., the integer layer coverage, the scattering probability is minimum, resulting in the specularity parameter p close to 1 (see section 2.5.2). According to Eqs. 2.65 and 2.66 from the Fuchs-Sondheimer model [1, 231], the resistance is the lowest at this coverage. At the highest roughness, i.e., the half integer layer coverage, the scattering probability is the highest, resulting in the specularity parameter p close to zero. Such a periodic modulation of p is visible as an oscillation.

The change of surface morphology can also be confirmed via the precise roughness analysis during deposition. It is obvious that the smooth surface shows a sharp profile without a shoulder. With increasing roughness via additional deposition, a shoulder appears (see section 8.1). From the FWHM of the shoulder, an estimation of the surface morphology variation is achieved. Blue symbols and the scales to the right side of the graph in Fig. 9.5(a) show the FWHM data, which has the maximum exactly at the minimum of the intensity peak and the minimum at the peak position of the intensity curve, further confirming the periodic variation of the surface morphology with coverage. Despite a constant period (1 BL) of all three oscillations, i.e., resistance, FWHM and the (00)-peak intensity, a slight change of the peak positions of the maximum or the minimum for all oscillations are observed. This behavior reflects the slight variation of the layer distribution during growth. As explained earlier in section 8.1, the second layer starts before completing the first layer as growth proceeds. Such a variation of layer distribution has slightly shifted the peak position towards the higher coverage in the resistance curve. In the course of the deposition, the oscillation amplitudes are strongly damped and finally disappear at higher coverages. The damping of oscillation

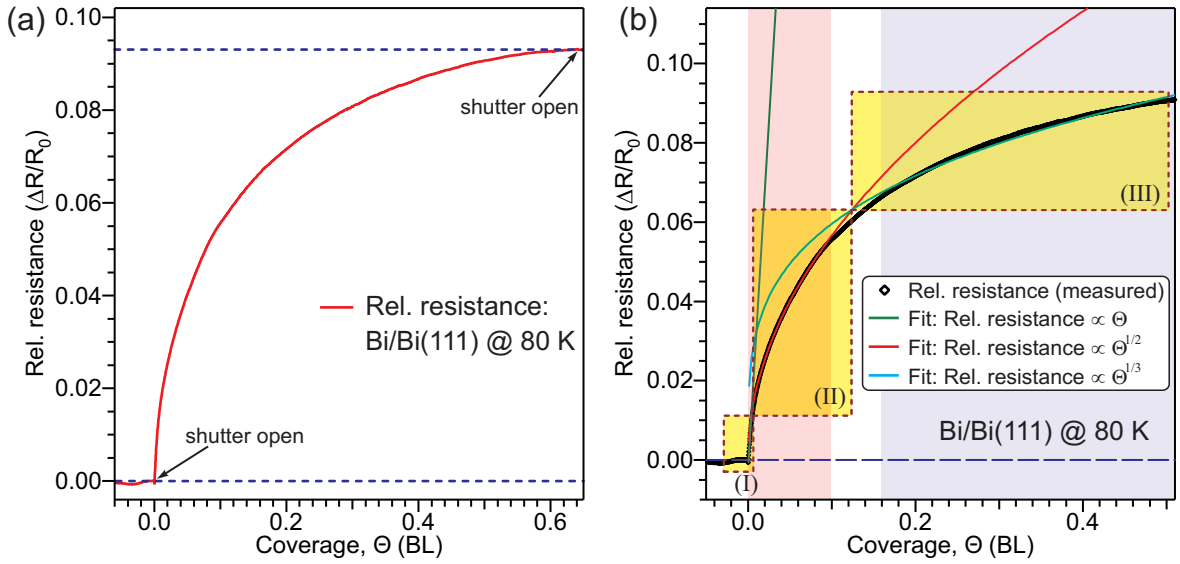

Figure 9.6: (a) Relative change of resistance during deposition of Bi on Bi(111) film at 80 K at low coverage regime. (b) A measured curve (the red curve in (a)) could be divided into three different regimes depending on the coverage, as indicated by three rectangles. Each individual regime could be fitted by three different functions, as shown by the blue line (the linear fit), the red line (the square root fit) and the green line (the cubic root fit), respectively.

occurs along with the decrease of resistance. This has been caused by the slowly increasing surface roughness with coverage, as indicated by the reduced amplitudes of the intensity peaks. Finally, the resistance decreases rapidly and monotonously, showing a typical bulk behavior of film resistance, which decreases with increasing coverage.

In contrast to the previous measurements at 80 K, the resistance decreases immediately after starting the deposition of Bi on smooth Bi films at RT (see Fig. 9.5(b)). Interestingly, the resistance decreases following a linear behavior with the coverage. In the growth front, as discussed in Fig. 8.1, growth of Bi on Bi(111) changes from a bilayer-by-bilayer mode at 80 K to step-flow mode at 450 K. Similarly, the buildup of surface roughness during deposition decreases with increasing the deposition temperature. At RT, growth proceeds already in a quasi step-flow mode; however, a slight buildup of surface roughness is still visible via the slow drop of (00)-spot intensity with increasing the coverage (Fig. 8.1). Such a growth behavior clearly shows that the adatom mobility at RT is sufficiently high and adatoms can diffuse across the surface up to the long distances, i.e., up to the step edges. This process reduces the step density significantly and eventually decreases the probability of additional scattering events. Obviously the resistance decreases monotonously with increasing coverage, as in the case of bulk-like behavior in thin metallic films. The change of resistance is even faster at 450 K (Fig. 9.5(b)), since the growth proceeds in a purely step-flow mode at 450 K.

The consequence of such a drastic change of growth modes can be understood in the context of large scale roughness within the widely accepted model of surface scattering (the Fuchs-Sondheimer model). However, a drastic jump of resistance at the extremely low coverage regime (below 10 % of the 1 BL) cannot be understood in this simple model. To explore the quantitative description of the drastic rise of resistance, we concentrate our calculation

only up to half a bilayer coverage as shown in Fig. 9.6(a). The measured curve resistance could be separated into three different regimes, i.e., 0-5 %, 5-10 %, and 10-50 % of the single bilayer coverage, considering its change of slope as a function of coverage, as indicated by filled yellow color rectangles in Fig. 9.7(b). A close inspection indicates the curve could be fitted well by three different functions, i.e., linear, square root, and cubic root, from the low to the high coverage regime, respectively. If we consider the first two regimes, up to 10 % of a BL coverage, it seems obvious in the context of general nucleation behavior in metals and scattering at adatoms. Since the adatom density increases linearly with coverage during nucleation and each isolated adatom behaves as a single scatterer for conduction electrons, the resistance increases linearly with coverage. After the nucleation phase, the increase of resistance slows down and behaves like the square root behavior, since the island density stays constant which causes the island perimeter proportional to $\Theta^{1/2}$ (i.e., n_x= constant, $A_x n_x = \Theta_{Bi}$, $p_x \sim A_x^{1/2} = (\Theta_{Bi}/n_x)^{1/2} \sim \Theta^{1/2}$, where A_x: average island size, p_x: average perimeter of islands), as shown in Fig. 8.21. However, the initial stages of growth in Bi on Bi(111) studied by STM (see section 8.2) shows that the island density increases with a relation of $n_x = \Theta^{1/3}$, as shown in Fig. 8.20. If we apply this relation with the simple scattering phenomena (the Fuchs-Sondheimer model), we would expect an increase of the resistance as $\Delta R/R_0 \sim \Theta_{Bi}^{2/3}$, at least in the regime II (Fig. 9.7(a)). Due to the large Fermi wavelength ($\lambda_F \sim 30$ nm) of charge careers in Bi, the scattering cross-section increases quadratically with the structural parameter [4]. This modifies the resistance change, as a whole, to be $\Delta R/R_0 \sim \Theta_{Bi}^{4/3}$, which is not the case in our observation that fits well with $\Delta R/R_0 \sim \Theta_{Bi}^{1/2}$ (Fig. 9.7(a)). Such a disparity of the simple scattering model indicates that the scattering of the charge carrier via transport in 2D surface electronic states is the dominant mechanism in the case of Bi thin films. This conclusion allows us to formulate a novel but simple scattering model, which explains the observed square root behavior of resistance, i.e., $\Delta R/R_0 \sim \Theta_{Bi}^{1/2}$.

From the STM study (see section 8.2), it has been shown that the island density varies with coverage as $n_x = \Theta^{1/3}$. With $A_x n_x = \Theta_x$, we get an expression for the average island size A_x and perimeter p_x as:

$$\begin{aligned} A_x &= \Theta_{Bi}^{2/3} \\ p_x &\sim A_x^{1/2} = \Theta_{Bi}^{1/3}. \end{aligned} \tag{9.1}$$

We have conductivity in a 2D-surface state. Let us assume that $\Delta R/R_0$ is proportional to the visible cross section of islands with the "eyes" of an electron in the 2D surface state, i.e., proportional to the perimeter p_x. The more distant an island is, the smaller would be the apparent cross section, i.e., inversely proportional to the island separation $l_x \sim n_x^{-1/2} = \Theta_{Bi}^{-1/6}$. Both contributions add up and provide:

$$\Delta R/R_0 \sim \frac{p_x}{l_x} = \Theta_{Bi}^{1/2}. \tag{9.2}$$

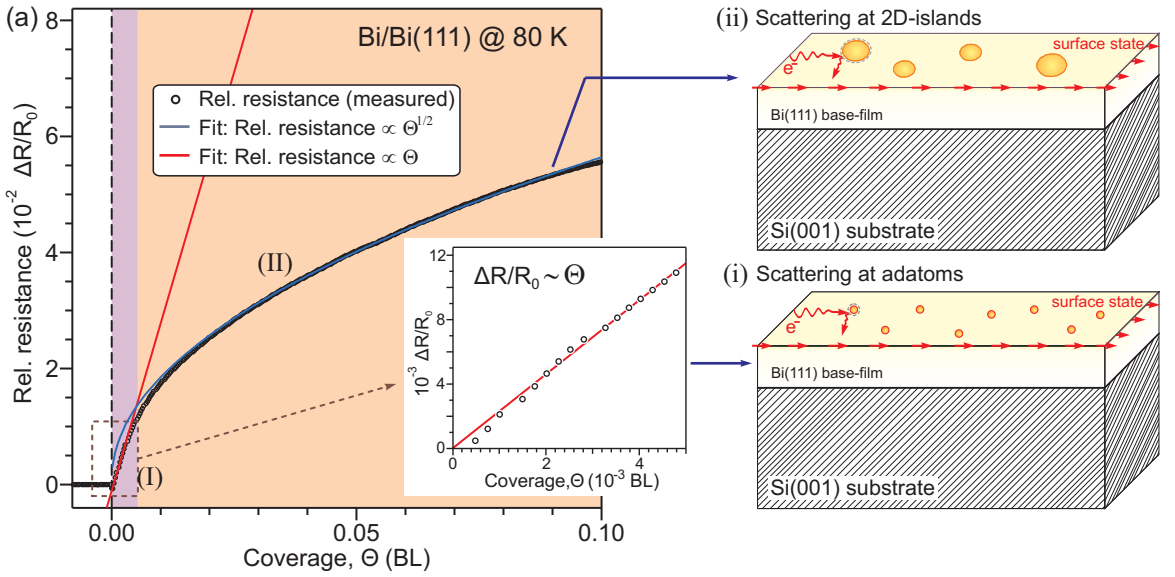

Figure 9.7: (a) Relative change of resistance during deposition of Bi on Bi(111) film at 80 K at low coverage regime. The solid red line shows the linear fit of the measured data up to the 1 % of a BL coverage. The solid blue line is a square root fit of the measured data in the range of 1 - 10 % of a coverage. Inset shows the close-up view of the linear plot up to 1 % of a BL. To the right, sketches of the underlying scattering mechanisms are shown: (i) carrier scattering at adatoms (the red spheres), which causes linear increase of the resistance, and (ii) carrier scattering at 2D islands (cluster of the red spheres), which causes square root behavior of the resistance. Since the carrier density at Bi(111) surface states is higher than the carrier density within the film, the carrier scattering mechanism is dominant at the 2D surface states (as shown with yellow color).

In other words, the mean free path of an electron λ_{el} in the 2D-surface state is defined by the length until it hits another 2D island. The separation between the islands is given by $l_x \sim n_x^{-1/2} = \Theta_{Bi}^{-1/6}$. The probability to hit an island is given by its diameter, i.e., $d_x = (4A_x/\pi)^{1/2} \sim \Theta_{Bi}^{1/3}$. That means bigger islands has higher probability to hit the electron but the mean free path will be reduced because of increased probability of scattering. Combining both contribution for l_x and the d_x as a function of λ_{el} leads to:

$$\lambda_{el} = \frac{l_x}{d_x} = \Theta^{-1/2}. \tag{9.3}$$

With $\Delta R/R_0$ inversely proportional to the mean free path λ_{el}, we obtain the same result as in Eq. 9.2:

$$\Delta R/R_0 \sim \lambda_{el}^{-1} = \Theta_{Bi}^{1/2}. \tag{9.4}$$

In this way, both expressions Eqs. 9.2 and 9.4 agree perfectly with the experimentally observed behavior of the resistance. However, beyond the coverage of 10 % of a BL, the curve slowly deviates from square root behavior (Fig. 9.6(b)). The observed behavior of $\Delta R/R_0 \sim \Theta_{Bi}^{1/3}$, beyond 10 % of a BL, suggests that simultaneously, as a whole, carrier transport via bulk plays a role. That means the increase of resistance slows down significantly via scattering at island steps.

9.2.2 The surface-state conductivity and the carrier mean free path

It was demonstrated that the drastic increase of resistance, during additional deposition of Bi on smooth Bi(111) surface at 80 K, is an important consequence of carrier transport via 2D metallic surface states. However, the surface state is gradually destroyed as the coverage increases because of surface roughening. So, it can be a plausible assumption that the surface state only remains active up to the first maxima of the resistance at half BL coverage. After that, the resistance changes periodically with the coverage, matching with the oscillation of step density on the surface (Fig. 9.5(a)). Under the above assumption, the 2D surface state conductivity is considered to be equivalent to the increase of the resistance up to the half of a BL coverage.

Let us assume that the lower limit of the relative increase of resistance caused by the scattering at the surface states to be 9 %. This value may vary according to the quality of the base film such as the surface morphology of the base film. Observation has shown that the maxima of the relative resistance ranges from 9 % to 17 % of the base film resistance and it is extremely sensitive to the small scale surface roughness. We can assume that the highest measured value of the rise of the resistance, i.e., 17 % is caused by the complete destruction of surface states by adatoms or small islands of Bi. From this assumption, a 2-dimensional surface state conductivity σ_{2D} can be determined as:

$$\sigma_{2D} = \frac{1}{\triangle R} \times \frac{L}{W} \tag{9.5}$$

where $L = 10$ mm is the length and $W = 4$ mm is the width of the Bi film. Using initial rise of the resistance[1] $\triangle R = 1170\ \Omega$ in Eq. 9.5, the 2D conductivity was calculated to be $\sigma_{2D} = 2.1 \times 10^{-3}\ \Omega^{-1}/\square$. This value appears to be slightly higher than the value obtained by Hirahara *et al.* [219] (see table 9.2). Since no significant temperature dependent variation of the surface conductivity has been observed by Hirahara et al. [232], the contribution from the possible error in the geometrical parameters (L and W) of the sample and the quality of the contacts might be the causes for higher conductivity. Obviously, as the surface states are gradually destroyed during deposition, the carrier density is reduced significantly and the bulk-like characteristic of the Bi film plays a role. In this situation, carriers are scattered at the island edges and coupled with the total change of the resistance $\triangle R$. It might be possible that nearly 60 % of the measured resistance $\triangle R$ is caused by the destruction of the surface states and the remaining 40 % is due to the surface roughness. This can only be distinguished if Bi(111) surface is completely destroyed via oxidation [219]. However, that process may irreversibly change the surface morphology of the film. Another option would be via adsorption of gases, which is outside the focus of this thesis.

Despite of the rough estimation of the 2D surface state conductivity, it has an advantage to determine an important parameter, the scattering mean free path in a 2D surface state l_{el}. The scattering mean free path in a 2D surface state can be determined by using the Boltzmann equation (Eq. 2.59) [233]. The essential electronic parameters are the 2D conductivity, the Fermi velocity υ_F and the 2D density of states $g(E_F)$. Since the surface states can be

[1] This particular value of $\triangle R$ has been taken from one of the samples (sample II, base film thickness = 8 nm), which has a resistance of $R_0 = 6909\ \Omega$ before additional Bi deposition (see Fig. 9.4(b)).

System	$\frac{m^*}{m}$	k_F (Å^{-1})	v_F (cm/s)	τ_{el} (s^{-1})	$\sigma_{2D}(\Omega^{-1}/\square)$	l_{el}(nm)
Si(111) $\sqrt{3}\times\sqrt{3}$Ag [233]	0.13	0.1	9×10^7	2.2×10^{-15}	7.5×10^{-5}	1.9
Bi(111)/Si(111)	0.1	0.4[234]	1×10^8	1.1×10^{-14}	1.5×10^{-3}[219]	11
Bi(111)/Si(001) (present work)	0.1	0.4[234]	1×10^8	1.5×10^{-14}	2.1×10^{-3}	15.6

Table 9.2: Conductivity parameters of Bi.

considered as a 2D metal, the density of states has a constant value, i.e., $g(E_F) = \frac{m^*}{\pi\hbar^2}$, assuming the nearly free electron model. The Fermi velocity depends on the Fermi vector k_F at the surface state band as $v_F = \frac{\hbar k_F}{m^*}$. So, both parameters are strongly dependent on the 2D surface state band structure, which is quite critical in the case of Bi because Bi has a highly anisotropic Fermi surface [221, 234]. For bulk Bi, the effective mass for the hole pockets at the T points is not so small, but for the electron pocket (the so-called massive Dirac Fermions) at L, it is about 0.003 times the free electron mass m_0. The surface-state band dispersion along $\overline{M}-\overline{K}$ for the electron pocket at $\overline{M}$ is also quite steep, even comparable to the bulk value [17]. Also, the hole pockets have a quite steep dispersion along the line parallel to $\overline{M}-\overline{K}$, while that along $\overline{\Gamma}-\overline{M}$ is very flat [17]. So, it is a bit ambiguous to take one effective mass for the whole band structure, which has a discrepancy of nearly two orders of magnitude across the surface state band dispersion, i.e., m^* ranges from $0.003m_0$ to $0.5m_0$. A reasonable value of $m^* = 0.4m_0$ has been used to to calculate $g(E_F)$, since previous studies have suggested that the surface state band dispersion has a higher effective mass than bulk effective mass [235]. Similarly, the Fermi velocity v_F also varies strongly along the band dispersion, since both effective mass m^* and Fermi vector k_F depends on the band dispersion; along the $\overline{\Gamma}-\overline{M}$ direction, it ranges from 5×10^7 to 1.5×10^8 cm/s, but along the $\overline{\Gamma}-\overline{k}-\overline{M}$ direction, it is $2\times10^7-6\times10^7$ cm/s. A value of $v_F\sim1\times10^8$ cm/s would be consistent with the chosen values of the Fermi wave vector $k_F\sim0.3$ Å^{-1} and an effective mass $m^*=0.4m_0$. Hirahara *et al.* [17, 234] have observed localized surface states along $\overline{\Gamma}-\overline{M}$ at $k_F\sim0.3$ Å^{-1}, which are slightly thickness dependent. Considering their observation, a value of $k_F\sim0.35$ Å^{-1} might be the reasonable choice. All those parameters are also summarized in Table 9.2. Inserting those parameters, the Fermi velocity, the 2D density of states and the mean scattering time were calculated and inserted in Eq. 2.59. From the calculation, the carrier mean free path l_{el} was determined, which turned out to be $\sim$ 30 nm.

This value seems quite large as compared to the recent investigation by Hirahara *et al.* [219]. Using the 2D surface conductivity of $\sigma_{2D} = 1.5\times10^{-3}$ $\Omega^{-1}/\square$, their estimation, via integrating the Fermi velocity along the surface state dispersion, as described by Matsuda *et al.* [233]), turns out to be 2−5 nm [219]. From this large discrepancy, it is important to emphasize here that the scattering mean free path l_{el} cannot be so precise using a constant

effective mass and a constant Fermi velocity in the case of the anisotropic Fermi surface of Bi(111). A detail calculation of surface state band dispersion is necessary. However, this kind of rough estimation allows us to understand the underlying mechanism of electron scattering at surface states via surface manipulation, which is a new and interesting topic.

9.3 Ag/Si(001)

In the previous section (section 7.2), we have shown that the most effective way of growing smooth, continuous and epitaxial Ag films is to follow the kinetic path way, i.e., deposition at low temperature and annealing to room temperature. It was apparent, via the LEED observation, that surface roughness was increased rapidly with increasing coverage. However, upon annealing the film from 80 to 300 K, the surface turns out to be extremely smooth.

In the following section, it is shown, via the resistance measurements, that the contribution of surface roughness directly influences the resistance of the film.

9.3.1 Resistance change during growth

Figure 9.8(a) exhibits the relative change of resistance during deposition of Ag on Si(001)-$c(4 \times 2)$ surface at 80 K. Since the Si substrate we have used is highly ohmic ($\sim$10 kΩ) and the measurements are performed at low temperatures, the substrate can be assumed as an insulator. So, therefore, the additional resistance change during deposition is mostly caused by the Ag. The overall behavior has been categorized into three different regions (i), (ii) and (iii), where the slope of the relative resistance changes significantly.

In the region (i), as indicated by the yellow color in Fig. 9.8(a), the resistance stays constant, showing only the substrate resistance. Constant resistance indicates that there is no current path due to separated small Ag islands. At 2 ML coverage the resistance starts to decrease, indicating the percolation threshold (i.e., critical coverage Θ_c) for Ag films. At this stage, the film is discontinuous, but it possess a hole- and channel-like structure. So, the resistance is dominated by the tunneling process from island to island. The stage (ii) continues until 12 ML coverage, where the film finally becomes continuous. The first conformation of a continuous film was obtained from the LEED image, which did not show any spots of the underlying Si substrate. Beyond the stage (ii), the resistance decreases with $1/\Theta$ behavior, as indicated by the solid blue line. Such a thickness dependent relative resistance can be explained by the simple model of electron scattering, i.e., the Fuchs-Sondheimer. As explained in section 2.5.2, the fraction p of the specularly reflected conduction electrons are reduced significantly as the coverage increases, because the surface roughness increases with coverage. However, the events of electron scattering cannot be distinguished or separated from other various scattering mechanisms such as grain boundary scattering, scattering at defects, etc. Recrystallization and bulk defect formation due to a rising film thickness causes additional complications. To reduce such complications, it is necessary to have a well-defined film with a smooth surface.

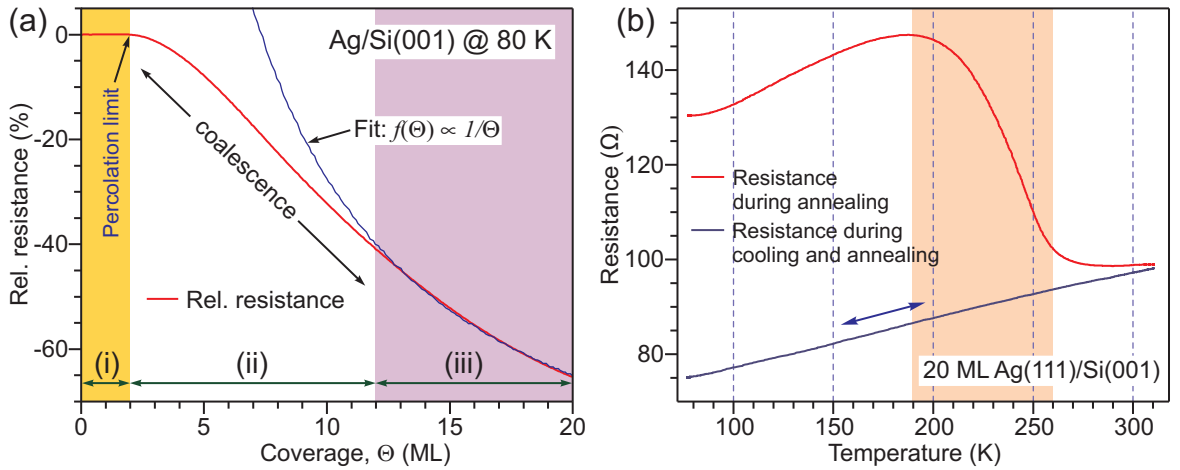

Figure 9.8: (a) Relative change of resistance during deposition of Ag on Si(001) at 80 K. Three regions, i.e., (i), (ii) and (iii), are indicated where the resistance changes differently. At (iii), the resistance change could be fitted via $1/\Theta$ behavior, indicating a bulk-like behavior. (b) Annealing behavior of 20 ML smooth Ag(111) film. The solid red curve shows the change of resistance during first annealing after deposition at 80 K. Resistance increases slowly up to ∼190 K and drastically decreases ∼260 K. However, resistance follows the reversible linear behavior after the annealing step. Surface smoothening effect, together with electron-phonon scattering could be responsible for this behavior of resistance (explained in the text).

9.3.2 Resistance change during annealing

As discussed in section 7.2, a continuous film, prepared at 80 K, is rough and a number of defects are incorporated into the film. However, upon annealing to 320 K, the film quality is remarkably improved and the surface turned out to be extremely smooth. The annealing process via measuring the change of (00)-spot intensity, which indicates the change of surface morphology, was already discussed in section 7.2. It is also well known that the residual resistivity of the film will be reduced significantly if the defect density in the bulk and at the boundaries is reduced. To understand the underlying behavior, the annealing process of the film was also monitored by continuously measuring the resistance of the film.

Figure 9.8(b) summarizes the annealing behavior of the resistance of the 20 ML Ag(111) film. The solid red line indicates the resistance of the film during the first annealing from 80 K to 310 K. In the beginning, from 80 K to 190 K, the resistance slowly increases. However, the surface morphology hardly changes until 190 K (see Fig. 7.30). This behavior is the consequence of electron-phonon scattering, which increases with increasing temperature. After 190 K, the resistance starts to decrease and within the range of 190−250 K, the film resistance reduces quite significantly and slowly meets a minimum at T_A. The dramatic reduction is mostly caused by the smoothening effect of the surface roughness and the reduction of bulk defects. However, the defect annihilation plays a dominant role in the annealing process, since the film resistance reduces more sharply even after the surface gets relatively smooth at 225 K.

9.4 Ag/Ag(111)

Finally, after growth characterization and resistance measurements during thermal treatments, it is identified that the film is ideal to study the contribution of resistance (dominantly) due to surface scattering mechanisms. In the following section, the observation of resistance change caused by surface roughness and the influence of growth condition in the resistance are discussed. The results are explained simply by using the concept of the Fuchs-Sondheimer model of electron scattering at surface [1].

9.4.1 Contribution of large scale roughness

It is extremely necessary to have a continuous, epitaxial and atomically smooth metallic film to observe the contribution of surface roughness to the resistance of the film. Such a well defined Ag(111) film was prepared under UHV conditions, as discussed briefly in section 7.2. Those films were used as a virtual substrate for the additional deposition of Ag at different temperatures. Resistance measurements were performed during deposition and, simultaneously, LEED (00)-spot profiles were recorded at different coverages.

Figure 9.9(a) summarizes the relative change of resistance of a well-annealed 20 ML Ag(111) base film during additional Ag deposition at different temperatures. Different color curves represent different deposition temperatures. At a substrate temperature of 80 K, film resistance increases by ∼3 % of the base film resistance. The maximum is observed at an overlayer thickness of about 1.2 ML. Beyond this thickness, the resistance slowly decreases. An increase of substrate temperature by 40 K causes a significant reduction of the maximum decrease of the initial slope and the shift to smaller film coverage. The maximum of the curve continuously shifts towards the lower coverage with increasing substrate temperature. With a deposition at 240 K and 310 K, however, the film resistance immediately decreases with increasing film thickness.

To discuss these results it is appropriate to divide the measured curve into three parts of different coverages: (a) a submonolayer regime (<1% of ML), (b) a few monolayer regime (1% - 2 ML), and (c) large coverages (>2 ML).

(a) submonolayer regime (<1% of ML): While starting the deposition by opening the shutter of the evaporator, single adatoms impinge on the surface terraces. At sufficiently low temperatures (<80 K) the adatoms can only make a few jumps due to an extremely low mobility. This effect makes each adatom a single scatterer for the conduction electrons. Since the adatom density increases linearly with coverage at this extremely low coverage regime, the probability of specularly reflected part of the conduction electrons decreases proportionally to the number density of the adatoms. As a result, resistance increases linearly at submonolayer coverage (<1 % of the ML). To observe the linear behavior, however, the substrate temperature should be well below so that the adatoms can stick, once they hit the surface. This is not the case for Ag, which still has a small mobility even at 80 K. So, a slight deviation from linear behavior was observed during deposition at 80 K.

(b) few monolayer regime (1% - 2 ML): It is known that the homoepitaxial growth

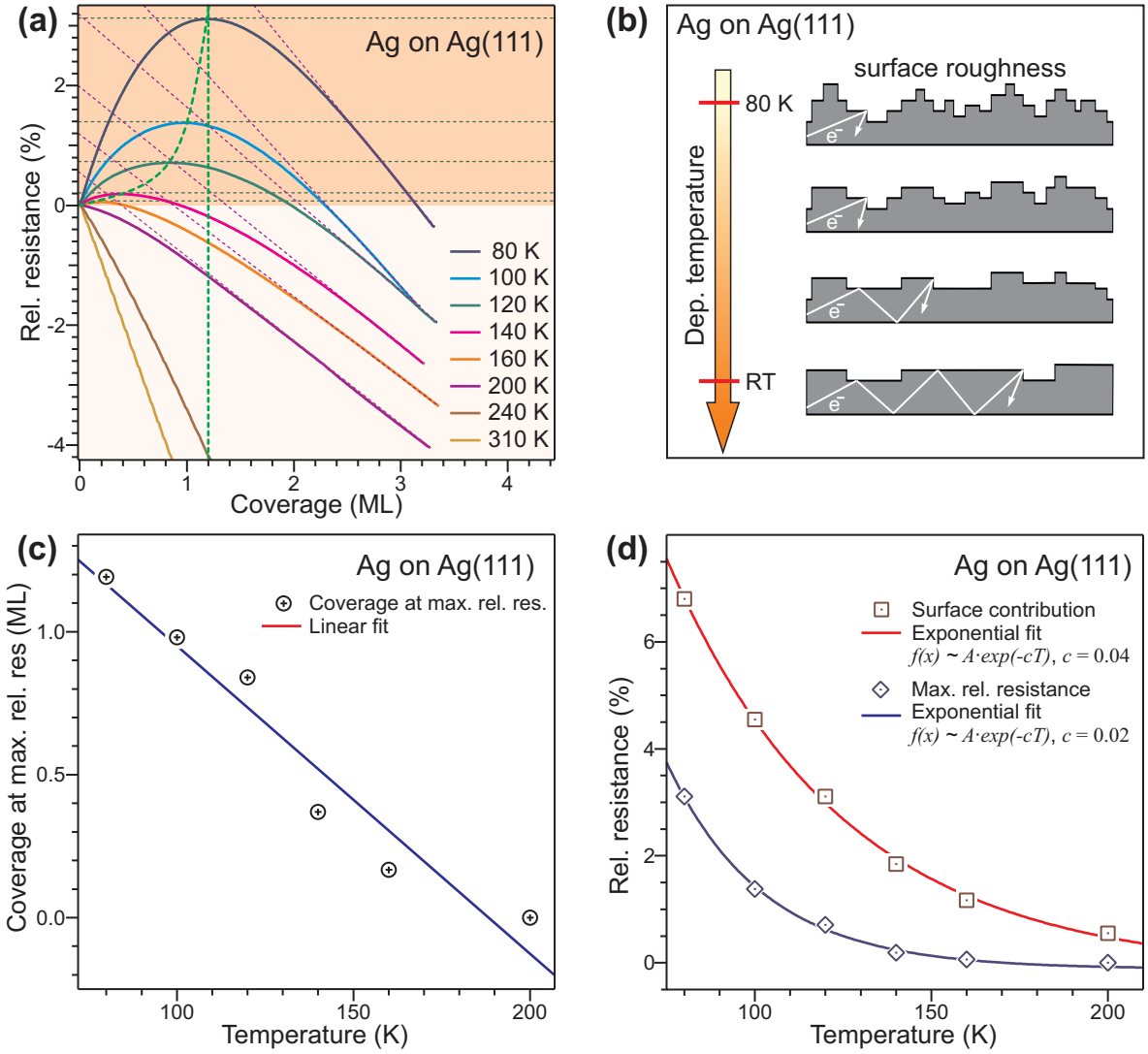

Figure 9.9: Contribution of surface roughness in the resistance of the Ag films. (a) Relative change of resistance of the Ag(111) base films during additional deposition of Ag at different temperatures. The resistance increases due to the scattering at the island edges. The maximum change of resistance, which shifts towards the lower coverage with increasing the deposition temperature. (b) Sketches of the Ag film morphology after additional deposition of Ag on the base films. Surface roughness decreases as the deposition temperature is increased and subsequently the diffuse scattering is reduced significantly. (c) The coverage at each maximum change of resistance plotted with deposition temperature. (d) Surface contribution of film resistance as a function of deposition temperature. The maxima of the resistance change are also plotted with temperatures. Both curves are fitted with exponential functions.

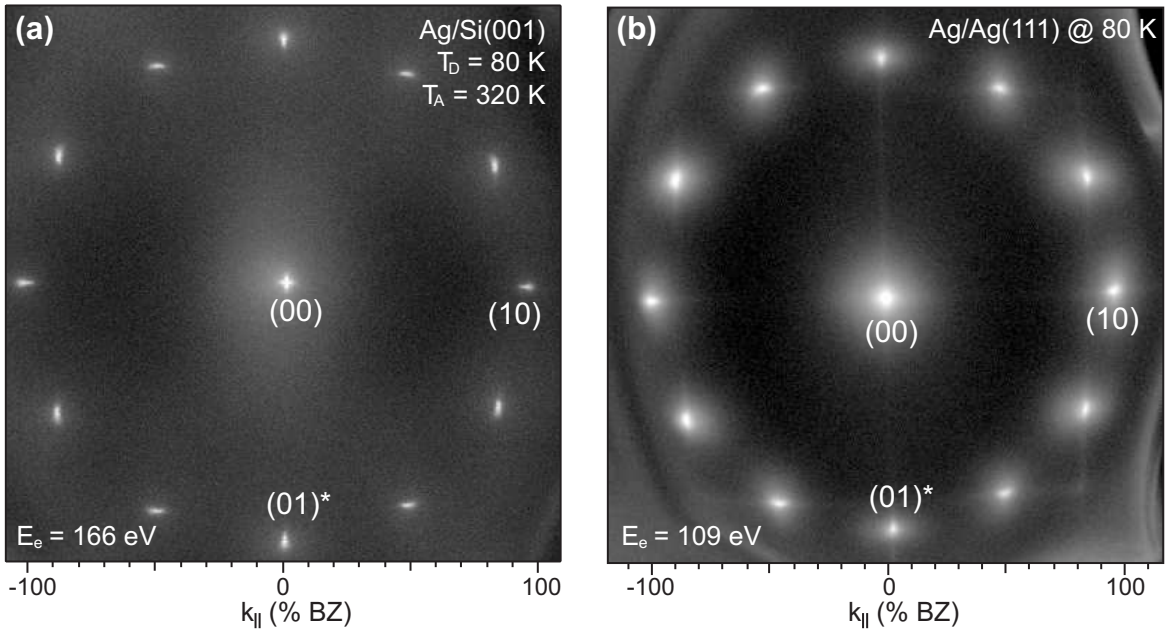

Figure 9.10: LEED patterns of 20 nm Ag(111) films: (a) after annealing to 320 K (b) after additional deposition of 3 ML of Ag at 80 K. The increase of surface roughness is clearly visible from the spot broadening after additional deposition.

of Ag(111) at low temperatures proceeds in a multilayer growth mode, where the surface roughens massively with increasing coverage. Direct evidence of this effect can be observed in Fig. 9.10, where the sharp LEED spots in Fig. 9.10(a) are turned into a diffuse spot by an additional 3 ML Ag deposition on a 20 ML Ag film (Fig. 9.10(b)). However, the growth front could be improved by increasing the deposition temperature. This behavior concludes that the surface morphology changes with increasing the temperature as shown schematically in Fig. 9.9(b). A direct consequence of this behavior was observed in the resistance measurement at different deposition temperatures, where the maximum of the resistance decreases as the deposition temperature increases. Additionally, the maximum also shifts towards lower coverage, showing a linear dependence with deposition temperatures (Fig. 9.9(c)), and finally at higher deposition temperatures (>240 K) the resistance falls immediately right after deposition.

Basically, the conduction electrons are scattered diffusely at the island edges or steps, resulting in a small probability of specularly reflected electrons p. If we compare Eqs. 2.65 and 2.66 in section 2.5.2, it is apparent that the increase of resistance is large for small p. If the surface roughness decreases, the step density also decreases. This causes an increase of the value of p, and subsequently reduces the maximum of the resistance. After 240 K surface effect becomes no more dominant with respect to the increase of thickness, and the bulk properties dominate the thin film resistance.

(c) large coverages (>2 ML): As said earlier, if the coverage exceeds a few more MLs, the bulk-like behavior of resistance dominates the surface scattering phenomena, which is inversely proportional to the thickness. At higher coverages all curves in Fig. 9.9(a) exhibit

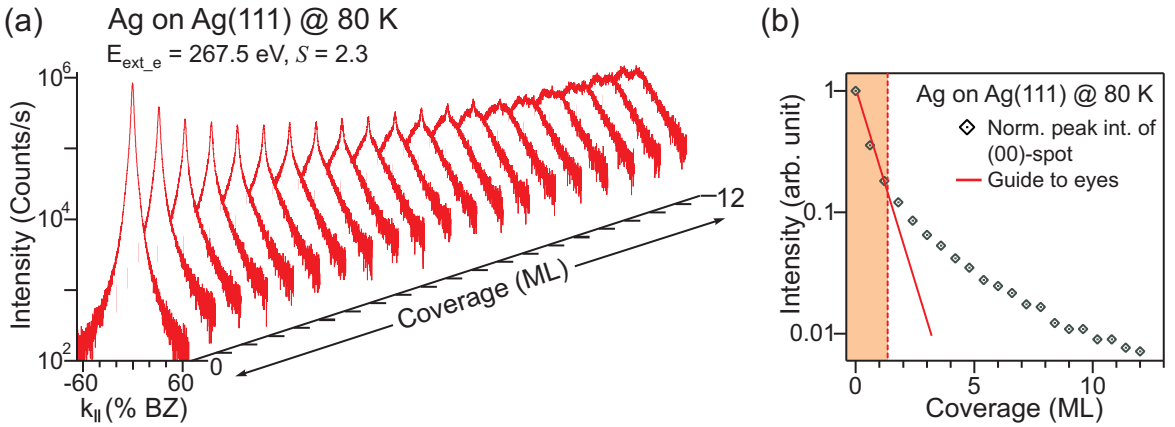

Figure 9.11: (a) *In situ* observation of surface morphology change during deposition of Ag on Ag(111) base film via recording of (00)-spot profiles. (b) Normalized intensity of the (00)-spot profiles from (a). The intensity decreases sharply up to ∼1.2 ML due to the maximum roughness and monotonously decreases with increasing the coverage, indicating a multilayer growth.

almost the same linear slope. The y-intercept (relative resistance) for each linear fit of the relative resistance curves, as shown by dotted lines in Fig. 9.10(a), is plotted in Fig. 9.10(d). This can be attributed as a contribution of the surface scattering on film resistance, which decreases with increasing deposition temperature. Similarly, the maximum also decreases, supporting the similar arguments. Both curves can be fitted with exponential functions as shown in Fig. 9.10(d). However, the theoretical basis for using the exponential fit is not clear yet.

The surface roughening behavior at 80 K was studied by analyzing the recorded (00)-spot profiles during deposition, as shown in Fig. 9.11(a). The spot profile shows a gradual change of shape with increasing the coverage. Each profile was fitted with Lorentzian functions and normalized by the total intensity of the spot (see section 8.1.2 for the calculation of the normalized intensity). The intensity decreases monotonously after a sharp fall to 1.2 ML (see Fig. 9.11(b). This behavior supports the maximum relative resistance obtained at 1.2 ML (Fig, 9.9(a)). Additionally, the gradual decrease of intensity is the clear indication of the multilayer growth, as expected for this system at 80 K.

9.5 Au/Ag(111): contribution of surface alloying

It was shown in section 9.4 that the conduction electrons are diffusely scattered by edges or steps caused by surface roughness, resulting in a large increase of the film resistance. It was verified via the resistance measurements during additional deposition of Ag on a smooth Ag(111) surface at various temperatures. That was the simple case of electron scattering phenomena, where the interface between the growing metal and the base film was coherent due to the homoepitaxial system. The situation could be complicated and interesting too in the case of a heteroepitaxial metallic system, where the interface and the morphology might not be so trivial. So, we have chosen Au to deposit on a well annealed Ag(111) film,

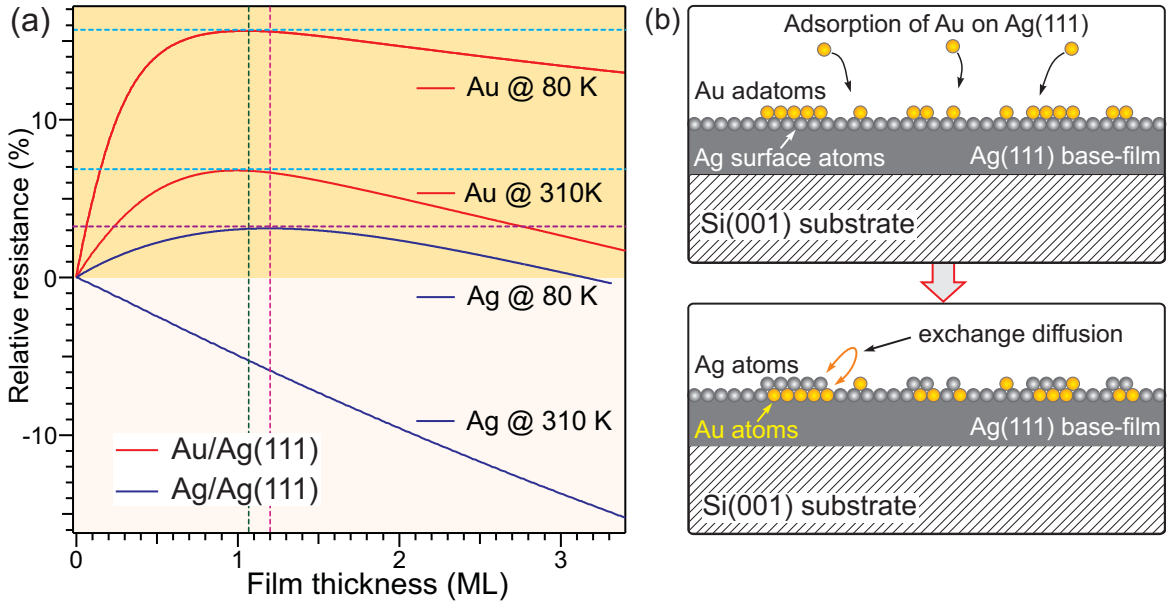

Figure 9.12: (a) Relative resistance during deposition of Au on Ag(111) at 80 K and 310 K (red solid lines). For a one to one comparison, relative resistance data during homoepitaxial growth of Ag(111) are also plotted in the graph (blue solid lines). (b) A simple model of exchange diffusion during submonolayer deposition of Au on Ag(111) surface at RT.

simply because Au grows epitaxially with a same orientation as Ag(111) [236] and both lattices almost match (lattice mismatch < 0.3 %) and both have comparable free-surface energies [237]. Those attributes could reduce additional complexities caused by strain induced phenomena. Resistance measurement was performed *in situ* during deposition at 80 K and 310 K.

Figure 9.12(a) summarizes the results of the relative change of resistance during deposition of Au on Ag(111) film at 80 K and 310 K. To demonstrate the difference to the homoepitaxial system, results on Ag/Ag(111) are also embedded on the plot, as shown by solid blue lines in Fig. 9.12(a). As indicated, the resistance increases by more that 16 % at 80 K. This value is nearly 5 times higher than in the case of Ag homoepitaxy at similar conditions. Such a massive increase of resistance causes a large increase of an initial slope in the case of Au deposition on Ag(111). The maximum of the resistance occurs just above a single layer of coverage and then the resistance decreases monotonically. The coverage at the maximum lies around 1 ML, just below the maximum in the case of Ag, as indicated by different dotted lines in Fig. 9.12. A similar continuous curve was also obtained during deposition of Au on the Ag(111) base film at 310 K. However, the maximum has been reduced to 7 %, which is still more than 2 times higher than the maximum in the case of Ag on Ag(111) at 80 K. Interestingly, in contrast to the case in Ag on Ag(111) at different temperatures (Fig. 9.9(a)), the maximum hardly shifts towards lower coverage. This behavior excludes a similar effect as in the the case of Ag, i.e., a drastic improvement of surface roughness or a smoothening of the surface at 310 K. Some estimation of a change of roughness can be obtained from the LEED pattern and the (00)-spot profiles recorded after deposition of approx. 3 ML of Au on Ag(111) at 80 K (see Fig. 9.13(a) and (b)). The LEED pattern shows the same orientation, without

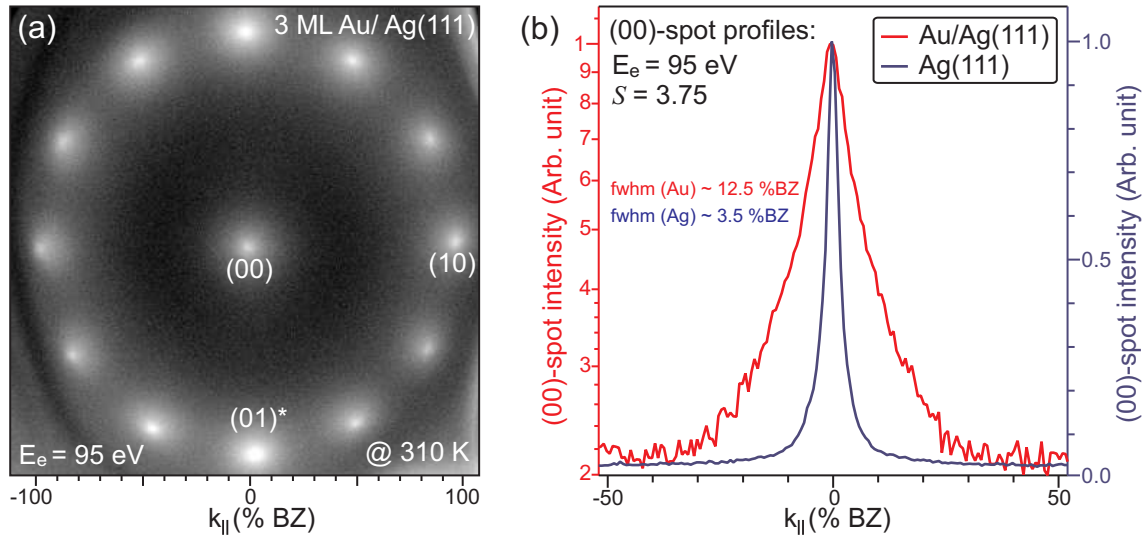

Figure 9.13: Roughness estimation via LEED measurements: (a) 2D LEED pattern after deposition of Au on Ag(111) at 310 K, (b) corresponding (00)-spot profile at the same condition. To compare with Ag deposition at 310 K, both profiles are shown with differently colored solid lines.

changing the spot position, indicating a relaxed epitaxial Au(111) film. However, large spot broadening was observed, which suggests an increase of surface roughness. Full width at half maximum (FWHM) of the (00)-spot increases almost 4 times higher than the roughness in the base Ag(111) surface (see Fig. 9.13(b)).

Although Culbertson *et al.* [238] have reported that Au grows epitaxially on Ag(111) in a layer-by-layer fashion, there have been lots of controversies in confirming the results. There are several reports, which also suggest an abrupt interface in Au/Ag(111) epitaxy [239, 240, 241, 242]. However, other several convincing reports contradict their claims and put forward a strong indication of severe atomic-scale interdiffusion, which results in a nontrivial interface [243, 244, 245, 246]. Rousset *et al.* [243] and Hayoz *et al.* [247] have observed an exchange diffusion mechanism at submonolayer coverage of Au on Ag(110) at room temperature, leading to an intermixed Volmer-Weber growth mode. This kind of mechanism is supported by theoretical investigations [244, 248], which demonstrate that subsurface-alloy formation might be energetically very favorable. In this context, it is also interesting to note that a study of a "diffusion size effect" in thin Au films on Ag(111) [249]. Goldiner *et al.* [249] have observed a surface segregation effect: Ag is enriched in the topmost atomic layer via surface diffusion induced by the near-surface crystal lattice dynamics (vibration amplitudes near the surface are greater than inside the crystal) in an epitaxial system of Au/Ag(111). This observation may also be related to the surface alloying effect as mentioned earlier.

From all those results, the widely accepted model of surface alloying via exchange diffusion between Au and Ag atoms at the interface, as shown schematically in Fig. 9.12(b), is proposed to explain the resistance behavior during deposition of Au on Ag(111) at 310 K. Rough interface caused by subsurface-alloying between the growing Au layer and Ag(111) surface leads to diffuse scattering (the specularity parameter p close to 0) and causes a strong increase (nearly 7 %) of resistance even at 310 K (Fig. Fig. 9.12(a)). This result also indicates that

intermixed subsurface-alloying can have even more scattering efficiency than a homoepitaxial rough surface.

10 Conclusions and Future Outlook

In this chapter, various conclusions are drawn on the basis of experimental results and theoretical support. Some future perspectives, which are related to the results of this thesis, are also highlighted to gain further insights. Some of the preliminary results, which might bring some interesting breakthroughs, will also be outlined in the preceding section.

10.1 Conclusions

This thesis was actually aimed at accomplishing two important tasks: (i) the preparation of high quality metallic (Ag) and/or semimetallic (Bi) overlayers, with well defined morphological parameters, on Si(001), and (ii) an *in situ* study of surface resistance change by surface manipulation via additional deposition or annealing. Concentrating on these two goals, the following conclusions are drawn:

Preparation of high quality films

- A novel recipe consisting of a two step process, employing a kinetic pathway for the growth, was reported, which results in high quality epitaxial films of Bi(111) on Si(001) substrate. The growth of a 6 nm template film at lower temperatures ($\sim$ 150 K) hinders island formation and annealing at higher temperatures ($\sim$ 450 K) enables the formation of an interfacial misfit dislocation array, which accommodates the inherent lattice mismatch between both lattices. A further deposition at elevated temperatures ($\sim$ 450 K) allows the growth to the desired thickness. Due to the two-fold symmetry of the underlying Si(001) substrate both twinned and 90°-rotated Bi(111) crystallites with micrometer size are formed. The surface of a Bi(111) film is surprisingly smooth with atomically flat terraces larger than 100 nm and a roughness of $\triangle \sim 0.6$ nm on a 2.5 μm length scale. X-ray diffraction measurements have confirmed that such films are relaxed to the bulk value and have an abrupt interface.

- Growth of Bi on Si(001) proceeds in a bilayer-by-bilayer mode at lower temperatures ($<$ 200 K) and a 3D mode at higher temperatures ($>$ 200 K). At low coverages ($<$ 10 BL), rotationally disordered Bi(110) crystallites are observed, which thermally unstable. However, a pure (111) orientation dominates at higher coverages ($>$ 17 BL). The experimental observation has suggested that the rectangular (110) crystallites may have nucleated at the defect sites such as grain boundaries and vacancies.

- Below 5.6 BL of Bi on Si(001), the surface undergoes various Bi-induced reconstructions such as (2×1), (1×1), (n×2) etc., where n is an integer. After a continuous layer at 5.6 BL, the growth proceeds in a 2D layer mode. With increasing coverage, the surface roughens slightly due to the kinetic limitation of adatom diffusion at low temperatures.

- Bi grows with a (111) surface orientation in order to minimize its surface free energy. Lattice accommodation between a hexagonal Bi(111) film on a rectangular Si(001) substrate results in a complex interface geometry with a reduced symmetry to the Si(001) substrate. In the [1$\bar{1}$0] direction, the large lattice mismatch of 18 % is adjusted by a commensurable registry of 11 Bi atoms to 13 Si atoms. The small lattice mismatch of 2.3 % in the [110] direction (along the Si dimer rows) is accommodated through a grating-like periodic array of interfacial misfit dislocations with a Burgers vector of $\overrightarrow{b}$ = 1/2[110], i.e., equal to the Si lattice constant in [110]. The highly anisotropic strain of the Bi(111) film with respect to the Si(001) substrate with its four-fold symmetry results in the formation of a 1D dislocation network, which distinguishes the Bi/Si(001) case from most material combinations, where typically a two-dimensional network is observed.

- A periodic dislocation pattern was observed in the heterosystem of Bi(111) on Si(001) via a strain contrast in STM topography. The strain field of an interfacial misfit dislocation line is observed via a vertical depression of $\triangle h = 0.12$ nm. The dislocation configuration, i.e., edge type Burgers vector $\overrightarrow{b}$ = 1/2[110] with a magnitude of $b_{\parallel,edge} = 0.377$ nm was estimated from the Lorentzian shape height profiles of isolated non-interacting dislocations for a 4.7 nm Bi film. As the coverage increases, more dislocations are generated enhancing the periodicity in the dislocation pattern due to increasing interaction between strain fields. An average periodicity of $\langle a_{dis} \rangle = 24$ nm and an amplitude of the corrugation $\triangle h = 0.07$ nm of the dislocation array are estimated for a 6.6 nm Bi film. This was compared to the SPA-LEED results.

- A very first study of nucleation and growth on semimetallic homoepitaxial system of Bi/Bi(111) was performed. Bi grows in a quasi bilayer-by-bilayer mode at low temperatures (< 200 K) and grows at step flow mode at higher temperatures (> 300 K). From the slow kinetic roughening of the growth front, we conclude the existence of a weak $Ehrlich - Schwoebel$ step edge barrier for interlayer diffusion across step edges. Small relaxation of the bilayer island height was observed, which is caused by a smoothening of the electron density contours at the edges of the small island (the Smoluchowski effect). An activation energy for intralayer diffusion was estimated to be $E_d = 0.135$ eV, which is comparable to values typically observed for metallic homoepitaxy. At intermediate temperatures, 2D islands exhibit a threefold dendritic shape due to kinetic limitations of edge diffusion.

- Simultaneous measurements of strain state and the lattice parameter of Bi film were performed, during annealing of a 6 nm Bi film after deposition on Si(001) at 150 K.

For all temperatures the change of the lattice parameter can be solely explained by the formation of the ordered interfacial dislocation array. Above 300 K the density of dislocations and the Bi lattice parameter increases parallel to the thermal expansion of the Bi film with a remaining strain of only 15 % (85 % relaxation of the 2.3 % lattice mismatch is relieved). This is explained by the necessity of buildup of sufficient strain for the formation of additional dislocations.

Resistance of thin films

- A simple and easy-to-use recipe to fabricate metallic WSi_2 contacts for surface conductivity studies on Si surfaces was reported. The contacts are mechanically stable and reliably withstand many flash-annealing cycles up to 1500 K. No contamination of the bare Si surface at distances larger than 2 µm from the contacts via diffusion of W atoms was detected during the course of these experiments. The contacts have shown an ohmic nature with the grown film of Bi, which allows us to measure the resistance of the sample *in situ* during deposition. Using those silicide contacts in a 4PP setup, resistance measurements were performed.

- In the case of Bi deposition on Si(001), the resistance decreases with increasing coverage, however, the slope of the resistance curve changes at different coverages. Those changes of the slope matches with various structural phases of the Bi and gives an indication of the electronic contribution of different structural phases.
  However, resistance decreases monotonously after the percolation limit in the case of Ag deposition on Si(001), which can be attributed as a bulk-like behavior.

- Resistance behavior of Ag films during annealing has shown a linear and positive coefficient of temperature, as expected. However, Bi films have shown an anomalous behavior: an exponential increase of surface conductance from 250 K to 300 K, which hardly changes until 350 K, then decreases linearly for temperatures > 350 K. The maximum of the conductance also increases with increasing film thickness. This behavior resembles the behavior with doped semiconductor. This character of Bi films absolutely disagrees with the metallic nature of epitaxially grown Bi films. We have speculated that the highly ordered interfacial dislocation network at the interface may have trapped charge carriers and each dislocation becomes like a donor, as in the case of semiconductors.

- Bi films have shown different conductance behavior with thicknesses at 300 K and 80 K. At 300 K, the conductance shows a linear dependent on thickness for $t > 10$ nm, but for thinner films $t < 10$ nm the conductance increases more quickly. This behavior indicates the presence of a higher carrier density for thinner films. In contrast, Bi films up to a 60 nm thickness have shown almost a constant conductance. This result can only be explained if carrier transport occurs via surface electronic states.

- In the case of Bi deposition on Bi(111), the resistance behavior above half of a BL can be well understood from the 2D growth nature of Bi, where the step density modulates the

scattering probability, resulting in thickness dependent short range oscillation. However, the resistance curve at sub-BL coverage cannot be explained by the Fuchs-Sondheimer model, since extreme electronic properties of Bi (a large Fermi wavelength, a large mean free path, etc.) does not allow the observed square root behavior with coverage. A novel approach, combining with the experimental results of island density vs. coverage in the low coverage regime, perfectly fits the experimental behavior of resistance, considering transport occurs dominantly via surface states. A linear increase of the resistance, at a coverage of lower than 1 % of a BL, explains the scattering at isolated adatoms, which increases linearly with coverage before starting the steady state growth regime.

- An important estimation of the 2D surface state conductivity of $\sigma_{2D} = 2.1 \times 10^{-3}$ $\Omega^{-1}/\square$ agrees well with the previous work. From this value, the carrier scattering mean free path l_{el} at the 2D surface states was roughly estimated to be $l_{el} \sim 15$ nm. The discrepancy has occurred due to the anisotropic Fermi surface of Bi.

- Influence of surface roughness was successfully measured during the additional deposition of Ag on smooth films of Ag(111) at different temperatures. The maximum of the film resistance decreases with an increasing deposition temperature from 80 K to 300 K. This behavior clearly indicates that the higher density of steps, resulting from the lack of adatom diffusion at lower temperatures, reduces the probability of specularly reflected electrons at surface. At higher temperatures, the resistance decreases immediately after additional deposition of Ag, suggesting a bulk-like behavior of the resistance.

- A characteristic large increase of resistance was observed during deposition of Au on smooth Ag(111) films both at 80 K and RT. A simple model of surface alloying via exchange diffusion qualitatively explains the observed behavior at RT.

10.2 Future Outlook

There are many interesting future directions that can be followed in the study of transport behavior on semimetallic/metallic systems. The thoroughly studied system of Bi/Si(001) has lots of promising aspects, especially, which can open up new physics and new applications. In the following sections, some possible directions, which are related to the experimental results of this thesis, will be outlined.

Bi/Si(001)

Recently, surface states on "cleaved'' semi-infinite Bi surfaces [16] and ultra-thin epitaxial Bi films [17] have been found to show high electron density and large spin-orbit (SO) splitting due to the loss of the inversion symmetry (Rashba effect). Moreover, the highest conductivity for metallic surface states (as compared to the surface state conductivity in metals) has been measured in Bi [219]. Those exciting results suggest that ultrathin Bi films may be promising materials for spintronic device applications.

This work has produced an important breakthrough of growing high quality Bi films on the technologically relevant substrate of Si(001). High-resolution techniques such as SPA-LEED, STM and XRD have confirmed the quality of the film, i.e., an extremely smooth surface, abrupt interface and excellent crystalline quality, via quantitative evaluation of structural parameters of the film. Thus, these films can be potentially applicable for technological purposes.

Despite the technological applications, Bi/Si(001) can be a model system for semimetallic homoepitaxy, since Bi grows on Bi(111) almost perfectly in a 2D mode. A weak *Ehrlich-Schwoebel* step edge barrier and low terrace diffusion energy contributes to quasi-bilayer-by-bilayer growth up to large coverage regimes at low temperatures. The microscopic understanding of atomic processes on this system may help to improve the quality of the films, and eventually increase the device performance.

Moreover, the highly ordered dislocation pattern, i.e., surface height undulation, may be utilized for selective adsorption and growth of self-assembled nanostructures. Additionally, it is interesting to look into how such a dislocation network modulates the electronic properties of the heterofilm on a small length scale.

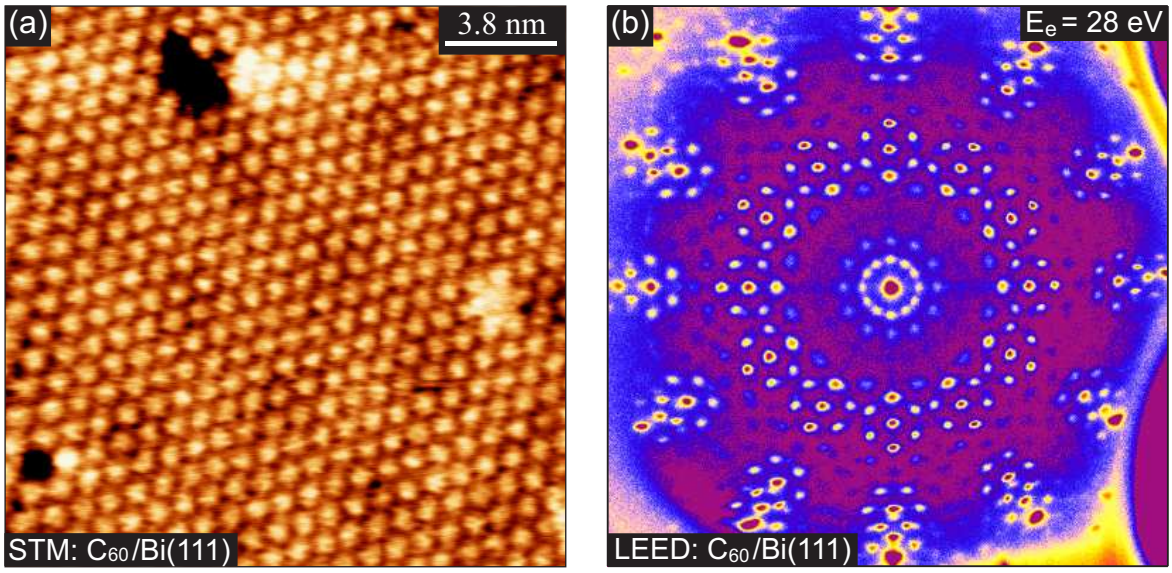

Figure 10.1: (a) STM topography ($V_{\text{bias}} = +0.7$ V, $I_{\text{tunneal}} = 0.1$ pA) and (b) SPA-LEED pattern recorded after sub-monolayer deposition of C_{60} on Bi(111) films. Each protrusion in the STM image corresponds to a single C_{60} molecule and the additional large scale modulation is attributed to a Moiré pattern, originating from the overlapping C_{60} and Bi(111) lattices. Spot splitting in LEED confirms the additional periodicity caused by the Moiré pattern.

C_{60}/Bi(111) and C_{60}/Ag(111)

High quality Bi films, prepared according to the recipe described in this thesis, can also be used to grow epitaxial organic films such as C_{60} or pentacene. Extremely smooth surface of a Bi film and unique lattice matching between fcc(111) C_{60} and Bi(111) drives the formation of highly ordered C_{60} epitaxial thin films [250, 251]. The line-on-line periodic structure is

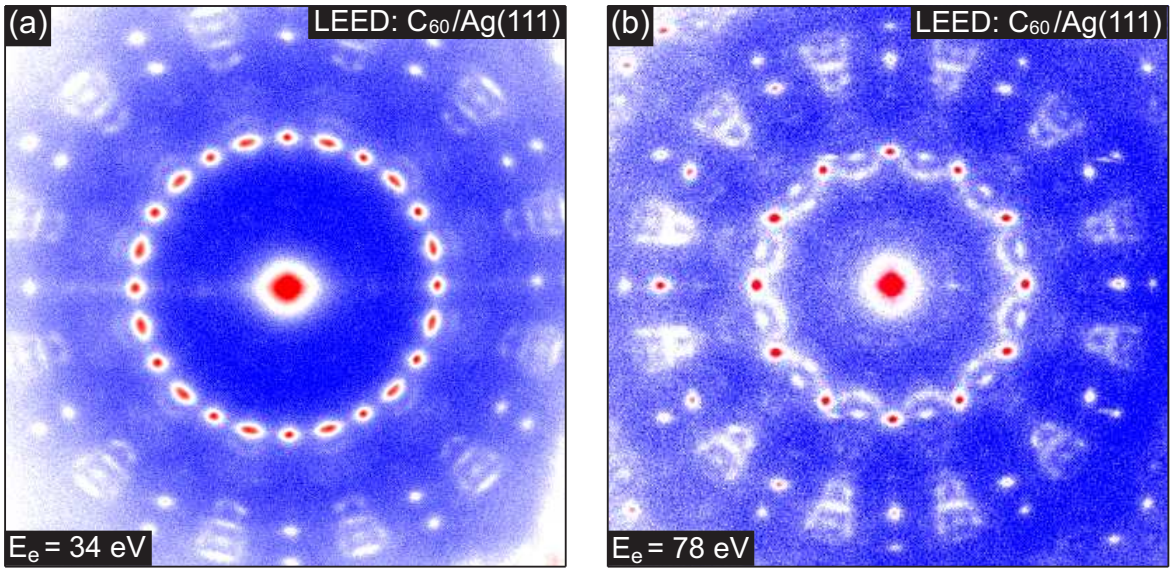

Figure 10.2: SPA-LEED images after few monolayer of C_{60} deposition on a smooth Bi(111) film. Images are recorded at 34 and 78 eV electron energies.

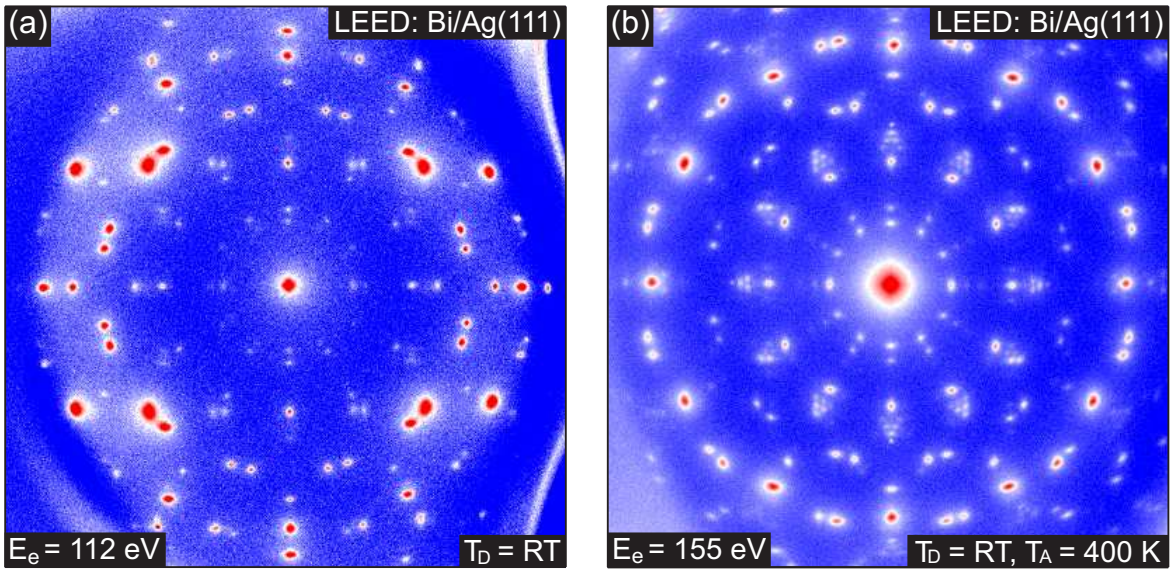

Figure 10.3: SPA-LEED images after sub-monolayer Bi deposition on a smooth Ag(111) film: (a) at RT and (b) after annealing to 400 K.

realized in spite of a weak interaction between C_{60} molecules and the Bi(111) surface [252]. Our initial work of growing C_{60} on Bi(111) has exhibited smooth epitaxial C_{60} films. A high-resolution STM image taken from the C_{60} film is shown in Fig. 10.1(a), where each protrusion corresponds to a single C_{60} molecule. Additional large scale modulation is attributed to a Moiré pattern originating from the overlapping C_{60} and Bi(111) lattices. A high-resolution LEED image clearly confirms the ordered Moiré pattern via spot splitting in a hexagonal symmetry (Fig. 10.1(b)). An exciting work, recently published by Bannani *et al.* [253], has demonstrated a ballistic transport via those epitaxially grown C_{60} film on Bi(111). This has also opened up a further motivation towards high quality Bi films.

Similarly, the preliminary study of C_{60} growth of Ag(111) has shown a complex geometry of surface structure (Fig. 10.2(a) and (b)). Orientation of C_{60} molecule and interaction with Ag surface atoms might play a role to form such complex surface structures. This might be an interesting system to compare the structural and electronic properties with the semimetallic system. Obviously, the lateral electron transport during adsorption of those molecules might be another interesting topic in both systems.

Bi/Ag(111) and Au/Ag(111)

It was shown in section 9.5 that surface alloying via exchange diffusion of Au on Ag(111) film enhances the surface resistance dramatically. That was the case of two lattice matched heteroepitaxial system of Au(111) and Ag(111), where a simple hexagonal structure prevails after Au deposition on the Ag(111) surface. However, under adsorption of Bi at 300 K, a hexagonal symmetry of the Ag(111) surface changes into a complex symmetry as shown in Fig. 10.3(a). Alloying becomes even more effective after annealing the sample at 400 K, which can be observed in the LEED pattern of Fig. 10.3(b). Recently, Ast *et al.* [254] have observed a giant spin splitting at the surface electronic structure of ordered surface alloys of Bi/Ag(111). Now, it would be interesting to investigate further how the structure of alloy or the ordering influences the lateral electrical transport of the film.

Appendix A

1. Structural and physical parameters of Bi

Parameter	Symbol	@ 78 K	@ 298 K		Ref.
Hex. lattice constant	a	4.535	4.546 Å		[255]
Hex. trigonal axis	c_h	11.814	11.863 Å		[255]
Bi(111) layer distance	$d_{Bi(111)}$		3.94 Å		[86]
Thermal expansion coefficient (parallel to (111) plane)				11.4×10^{-6} K^{-1}	[256]
Thermal expansion coefficient (perpendicular to the (111) plane)				16.8×10^{-6} K^{-1}	[256]
Melting point				544.7 K	[131]
Debye Temperature (bulk Bi)				112 K	[257]
Debye Temperature (Bi(111) surface)				42-49 K	[131, 257, 133]

2. Electronic parameters of Bi

Parameter	Symbol	carrier density	Ref.
Electron density (Bi(111) surface)	n_e (cm^{-2})	5.5×10^{12}	[235]
Hole density (Bi(111) surface)	n_h (cm^{-2})	1.1×10^{13}	[235]
Electron density (bulk)	n_e (cm^{-3})	2.75×10^{17}	[258]
Electrical conductivity (Bi(111) surface state) @ RT	ρ ($\Omega^{-1}/\square$)	1.5×10^{-3}	[219]
Electrical resistivity (bulk) @ 77 K	ρ (Ω cm)	0.58×10^{-4}	[259]
Electrical resistivity (bulk) @ 300 K	ρ (Ω cm)	1.14×10^{-4}	[259]
Band overlap	$\triangle E$ (meV)	40	[6]
Effective mass (Bi(111) surface state band)	$\frac{m^*}{m_e}$	0.003−0.5	[235, 232]
Effective mass (bulk band)	$\frac{m^*}{m_e}$	0.001−0.005	[258]
Fermi wave length (bulk)	λ (nm)	30	[8]
Carrier mean free path (Bi(111) surface state)	l_{el} (nm)	2−3	[219]
Carrier mean free path (bulk)	l_{bulk} (µm)	0.59	[259]

Bibliography

[1] K. Fuchs. The conductivity of thin metallic films according to the electron theory of metals. *Proc. Camb. Phil. Soc.* **34**, 100–108 (1938). 2, 26, 131, 133, 141

[2] E. H. Sondheimer. The mean free path of electrons in metals. *Adv. Phys.* **1**, 1–42 (1952). 2, 25, 26

[3] D. Schumacher. *Surface scattering experiments with conduction electrons* (Springer-Verlag Berlin, 1992). 2

[4] A. Kaser, E. Gerlach. Scattering of conduction electrons by surface roughness in thin metal films. *Z. Phys.* **97**, 139–146 (1995). 2, 135

[5] E. Z. Luo, S. Heun, M. Kennedy, J. Wollschläger, and M. Henzler. Surface roughness and conductivity of thin Ag films. *Phys. Rev. B* **49**, 4858–4865 (1994). 2, 14

[6] J. P. Issi. Low temperature transport properties of the group v semimetals. *Aus. J. Phys.* **32**, 585 (1979). 2, 40, 158

[7] V. S. Édel'man. Electrons in bismuth. *Adv. Phys.* **25**, 555–613 (1976). 2

[8] N. Garcia, Y. H. Kao, and M. Strongin. Galvanomagnetic studies of bismuth films in the quantum-size-effect region. *Phys. Rev. B* **5**, 2029–2039 (1972). 2, 158

[9] Yu. F. Ogrin, V. N. Lutskii, and M. I. Elinson. Observation of quantum size effects in thin bismuth films. *JETP Lett.* **3**, 71–73 (1966). 2, 40

[10] V. N. Lutskii. Features of optical absorption of metallic films in the region where the metal turns into a dielectric. *JETP Lett.* **2**, 245–248 (1965). 3, 40, 130

[11] F. Y. Yang, Kai Liu, Kimin Hong, D. H. Reich, P. C. Searson, C. L. Chien, Y. Leprince-Wang, Kui Yu-Zhang, and Ke Han. Shubnikov-de Haas oscillations in electrodeposited single-crystal bismuth films. *Phys. Rev. B* **61**, 6631–6636 (2000). 3

[12] F.Y. Yang, K. Liu, K. Hong, D. H. Reich, P. C. Searson, and C. L. Chien. Large magnetoresistance of electrodeposited single-crystal bismuth thin films. *Science* **284**, 1335–1337 (1999). 3, 130

[13] G. Schmidt, D. Ferrand, L. W. Molenkamp, A. T. Filip, and B. J. van Wees. Fundamental obstacle for electrical spin injection from a ferromagnetic metal into a diffusive semiconductor. *Phys. Rev. B* **62**, R4790–R4793 (2000). 3

[14] S. A. Wolf, D. D. Awschalom, R. A. Buhrman, J. M. Daughton, S. von Molnar, M. L. Roukes, A. Y. Chtchelkanova, and D. M. Treger. Spintronics: A spin-based electronics vision for the future. *Science* **294**, 1488–1495 (2001). 3

[15] K. I. Lee, M. H. Jeun, J. Y. Chang, S. H. Han, J. G. Ha, and W. Y. Lee. Spin transport in an FM/Bi/FM junction. *Phys. Stat. Sol. (b)* **241**, 1510–1513 (2004). 3

[16] Y. M. Koroteev, G. Bihlmayer, J. E. Gayone, E.V. Chulkov, S. Blügel, P. M. Echenique, and Ph. Hofmann. Strong Spin-Orbit Splitting on Bi Surfaces. *Phys. Rev. Lett.* **93**, 046403 (2004). 3, 152

[17] T. Hirahara, T. Nagao, I. Matsuda, G. Bihlmayer, E. V. Chulkov, Yu. M. Koroteev, P. M. Echenique, M. Saito, and S. Hasegawa. Role of Spin-Orbit Coupling and Hybridization Effects in the Electronic Structure of Ultrathin Bi Films. *Phys. Rev. Lett.* **97**, 146803 (2006). 3, 41, 130, 131, 138, 152

[18] H. Iwasaki and T. Kikegawa. Structural Systematics of the High-Pressure Phases of Phosphorus, Arsenic, Antimony and Bismuth. *Acta Cryst. B* **53**, 353–357 (1997). 3

[19] K. Sokolowski-Tinten, Ch. Blome, J. Blums, A. Cavalleri, C. Dietrich, A. Tarasevitch, I. Uschmann, E. Förster, M. Kammler, M. Horn-von-Hoegen, and D. von der Linde. Femtosecond X-ray measurement of coherent lattice vibrations near the Lindemann stability limit. *Nature* **422**, 287–289 (2003). 3

[20] T. Nagao, J. T. Sadowski, M. Saito, S. Yaginuma, Y. Fujikawa, T. Kogure, T. Ohno, Y. Hasegawa, S. Hasegawa, and T. Sakurai. Nanofilm Allotrope and Phase Transformation of Ultrathin Bi Film on Si(111)-7x7. *Phys. Rev. Lett.* **93**, 10 (2004). 3, 95, 106, 117, 119, 122, 127

[21] B. Krenzer, A. Janzen, P. Zhou, D. von der Linde and M. Horn-von Hoegen. Thermal boundary conductance in heterostructures studied by ultrafast electron diffraction. *New J. Phys.* **8**, 190 (2006). 3

[22] M. Kammler. *Heteroepitaxie auf Silizium mit Adsorbaten.* Master's thesis, Universität Hannover (1996). 3, 117, 119

[23] T. Nagao, T. Doi, T. Sekiguchi, and S. Hasegawa. Epitaxial Growth of Single-Crystal Ultrathin Films of Bismuth on Si(111). *Jpn. J. Appl. Phys.* **39**, 4567–4570 (2000). 3

[24] M. Kammler and M. Horn-von Hoegen. Low energy electron diffraction of epitaxial growth of bismuth on Si(111). *Surf. Sci.* **576**, 56–60 (2004). 3, 95, 117, 119, 127

[25] W. C. Fan, A. Ignatiev, and N. J. Wu. Growth of bismuth on Si(100) surface: AES and LEED study. *Surf. Sci.* **235**, 169 (1990). 3, 72

[26] D. E. Beutler and N. Giordano. Localization and electron-electron interaction effects in thin Bi wires and films. *Phys. Rev. B* **38**, 8–19 (1988). 3

[27] J. Chang, H. Kim, J. Han, M. H. Jeon, and W. Y. Lee. Microstructure and magnetoresistance of sputtered bismuth thin films upon annealing. *J. Appl. Phys.* **98**, 023906–1 – 023906–7 (2005). 3

[28] G. Jnawali, F.-J. Meyer zu Heringdorf, D. Wall, S. Sindermann, and M. Horn-von Hoegen. Stable tungsten disilicide contacts for surface and thin film resistivity measurements. *J. Vac. Sci. Technol. B* **27**, 180 (2009). accepted. 5

[29] G. Jnawali, H. Hattab, B. Krenzer, and M. Horn-von Hoegen. Lattice accommodation of epitaxial Bi(111) films on Si(001) studied with SPA-LEED and AFM. *Phys. Rev. B* **74**, 195340 (2006). 5

[30] G. Jnawali, H. Hattab, F.-J. Meyer zu Heringdorf, B. Krenzer, and M. Horn-von Hoegen. Lattice matching periodic array of misfit dislocations: heteroepitaxy of Bi(111) on Si(001). *Phys. Rev. B* **76**, 035337 (2007). 5

[31] G. Jnawali, H. Hattab, C. Bobisch, A. Bernhart, E. Zubkov, F.-J. Meyer zu Heringdorf, R. Möller, B. Krenzer, and M. Horn-von Hoegen. Nanopattern Formation by Periodic Array of Interfacial Misfit Dislocations in Bi(111)/Si(001) Heteroepitaxy. *MRS Proceedings* **1059-KK07-07** (2007). 5

[32] H. Hattab, E. Zubkov, A. Bernhart, G. Jnawali, C. Bobisch, B. Krenzer, M. Acet, R. Möller, and M. Horn-von Hoegen. Epitaxial Bi(111) films on Si(001): Strain state, surface morphology, and defect structure. *Thin Solid Films* **516**, 8227–8231 (2008). 5

[33] G. Jnawali, H. Hattab, C. Bobisch, A. Bernhart, E. Zubkov, R. Möller, and M. Horn-von Hoegen. Nanoscale dislocation patterning in Bi(111)/Si(001) heteroepitaxy. *Surf. Sci.* (2009). accepted. 5

[34] G. Jnawali, H. Hattab, C. Deiter, C. A. Bobisch, T. Weisemoeller, A. Bernhart, F. Bertram, E. Zubkov, R. Möller, J. Wollschläger, and M. Horn-von Hoegen. Epitaxial growth of Bi(111) on Si(001). *e-J. Surf. Sci. Nanotech.* (2009). accepted. 5

[35] G. Jnawali, H. Hattab, C. A. Bobisch, A. Bernhart, E. Zubkov, R. Möller, and M. Horn-von Hoegen. Homoepitaxial growth of Bi(111). *Phys. Rev. B* **78**, 035321 (2008). 5, 42

[36] G. Jnawali, Th. Wagner, H. Hattab, R. Möller, and M. Horn-von Hoegen. Nucleation and initial growth in the semimetallic homoepitaxial system of Bi on Bi(111). *Phys. Rev. B* (2009). submitted. 5

[37] G. Jnawali, Th. Wagner, H. Hattab, R. Möller, and M. Horn-von Hoegen. Surface conductivity study via surface manipulation in Bi(111) films (2009). in preparation. 6

[38] C. J. Davisson and L. H. Germer. The scattering of electrons by a single crystal of Nickel. *Nature* **119**, 558–560 (1927). 7

[39] C. Davisson and L. H. Germer. Diffraction of electrons by a crystal of Nickel. *Phys. Rev.* **30**, 705–740 (1927). 7

[40] M. P. Seah and W. A. Dench. Quantitative electron spectroscopy of surfaces: A standard data base for electron inelastic mean free paths in solids. *Surf. Interf. Anal.* **1**, 2–11 (1979). 7

[41] M. Henzler. Measurement of Surface Defects by Low-Energy Electron Diffraction. *Appl. Phys. A* **34**, 205–214 (1984). 8, 10

[42] M. Horn-von Hoegen. Spot profile analysis low energy electron diffraction of semiconductor growth. *Z. Kristallogr.* **214**, 591 & 684 (1999). 12, 28, 31, 53, 86, 104, 106

[43] C. S. Lent and P. I. Cohen. Diffraction from sepped surfaces. *Surf. Sci.* **139**, 121–154 (1984). 12, 104, 106

[44] C. S. Lent and P. I. Cohen. Diffraction from stepped surfaces 1. Reversible surfaces. *Surf. Sci.* **139**, 121–154 (1984). 13, 14

[45] J. Wollschläger, E. Z. Luo, and M. Henzler. Thermal roughness of the homogeneous and inhomogeneous Cu(311) surface studied by high-resolution low-energy electron diffraction. *Phys. Rev. B* **44**, 13031–13041 (1991). 14, 90, 91

[46] J. Wollschläger, J. Falta, and M. Henzler. Electron diffraction at stepped homogeneous and inhomogeneous surfaces. *Appl. Phys. A* **50**, 57–68 (1990). 14

[47] M. Henzler. Quantitative evaluation of random distributed steps at interfaces and surfaces. *Surf. Sci.* **73**, 240–251 (1978). 14

[48] M. Horn-von Hoegen, M. Pook, A. Al Falou, B. H. Müller and M. Henzler. The interplay of surface morphology and strain relief in surfactant mediated growth of Ge on Si(111). *Surf. Sci.* **284**, 53–66 (1993). 15, 64, 84

[49] U. Gradmann, and G. Waller. Periodic lattice distortions in epitaxial films of Fe(110) on W(110). *Surf. Sci.* **116**, 539–548 (1982). 15

[50] M. Ritter, W. Ranke, and W. Weiss. Growth and structure of ultrathin FeO films on Pt(111) studied by STM and LEED. *Phys. Rev. B* **57**, 7240–7251 (1998). 15

[51] M. Horn-von Hoegen, A. Al-Falou, H. Pietsch, B. H. Müller, and M. Henzler. Formation of interfacial discolation network in surfactant mediated growth of Ge on Si(111) investigated by SPA-LEED. *Surf. Sci.* **298**, 29–42 (1993). 15, 16, 76, 80, 84

[52] M. Horn-von Hoegen, T. Schmidt, G. Meyer, D. Winau, and K.H. Rieder. Lattice accommodation of low-index planes: Ag(111) on Si(001). *Phys. Rev. B* **52**, 10764 (1995). 16, 62, 64, 76, 84, 96, 98

[53] W. L. Bragg. The Diffraction of Short Electromagnetic Waves by a Crystal. *Proc. Camb. Phil. Soc.* **17**, 43–57 (1913). 19

[54] W. H. Bragg and W. L. Bragg . The Reflection of X-rays by Crystals. *Proc. Roy. Soc.* **A 88**, 428–438 (1913). 19

[55] I. K. Robinson and D. J. Weet. Surface x-ray diffraction. *Rep. Prog. Phys.* **55**, 599–651 (1992). 20

[56] I.K. Robinson and E. Vlieg. X-ray reflectivity study of the Si(111)7x7 surface. *Surf. Sci.* **261**, 123–128 (1992). 20

[57] Th. Schmidt. *Untersuchungen zur Surfactant-modifizierten Epitaxie von Germanium auf Silizium(111).* Ph.D. thesis, Hasylab in DESY, Hamburg (1998). 20

[58] C. Deiter. *Röntgenstrukturanalyse von Halbleiter-Isolator-Schichtsystemen.* Ph.D. thesis, Universität Bremen (2005). 20

[59] Charles Kittel. *Introduction to solid state physics* (John Wiley & Sons, Inc., New York, USA, 1976), 5th edn. 22

[60] M. Ali Omar. *Elementary solid state physics: principles and applications* (Addition-Wesley publishing company, 1975). 23, 24

[61] J. M. Ziman. *Principles of the theory of solids* (Cambridge university press, Cambridge, 1972). 24

[62] T. Heinzel. *Mesoscopic Electronics in Solid State Nanostructures* (Wiley-VCH, New York, 2003). 24

[63] P. Zahl and M. Horn-von Hoegen. Third-generation conical spot profile analyzing low-energy electron diffraction. *Rev. Sci. Instrum.* **73**, 2958–2962 (2002). 29

[64] F. J. Morin, and J. P. Maita. Electrical properties of silicon containing arsenic and boron. *Phys. Rev.* **96**, 28–35 (1954). 35

[65] G. G. Macfarlane, T. P. McLean, J. E. Quarrington, and V. Roberts. Fine Structure in the Absorption-Edge Spectrum of Si. *Phys. Rev.* **111**, 1245–1254 (1958). 35

[66] J. R. Haynes, M. Lax, and W. F. Flood. Analysis of intrinsic recombination radiation from silicon and germanium. *J. Phys. Chem. Solids* **8**, 392–396 (1959). 35

[67] R. E. Schlier and H. E. Farnsworth. *Semiconductor Surface Physics* (Pennsylvania University Press, 1957). 37

[68] R. E. Schlier and H. E. Farnsworth. Structure and Adsorption Characteristics of Clean Surfaces of Germanium and Silicon. *J. Chem. Phys.* **30**, 917–928 (1959). 37, 118

[69] A. Ramstad, G. Brocks, and P. J. Kelly. Theoretical study of the Si(100) surface reconstruction. *Phys. Rev. B* **51**, 14504–14523 (1995). 37

[70] D. J. Chadi. Atomic and electronic structures of reconstructed Si(100) surfaces. *Phys. Rev. Lett.* **43**, 43–47 (1979). 37, 52

[71] W. S. Yang and F. Jona. Atomic structure of Si(001)-(2x1). *Phys. Rev. Lett.* **28**, 2049–2059 (1983). 37

[72] N. Jedrecy, M. Sauvage-Simkin, R. Pinchaux, J. Massies, N. Greiser and V. H. Etgens. Asymmetric versus symmetric dimerization on the Si(001) and As/Si(001)-(2x1) reconstructed surfaces as observed by grazing incidence X-ray diffraction. *Surf. Sci.* **230**, 197–204 (1990). 37

[73] M. Aono, Y. Hou, C. Oshima, and Y. Ishizawa. Low-energy ion scattering from the Si(001) surface. *Phys. Rev. Lett.* **49**, 567–570 (1982). 37

[74] R. M. Tromp, R. J. Hamers, and J. E. Demuth. Si(001) dimer structure observed with scanning tunneling microscopy. *Phys. Rev. Lett.* **55**, 1303–1306 (1985). 37

[75] H. Tochihara, T. Amakusa, and M. Iwatsuki. Low-temperature scanning-tunneling-microscopy observations of the Si(001) surface with a low surface-defect density. *Phys. Rev. B* **50**, 12262–12265 (1994). 37

[76] J. Ihm, D. H. Lee, J. D. Joannopoulos, and J. J. Xiong. Structural Phase Diagrams for the Surface of a Solid: A Total-Energy, Renormalization-Group Approach. *Phys. Rev. Lett.* **51**, 1872–1875 (1983). 37

[77] A. Saxena, E. T. Gawlinski, and J. D. Gunton. Structural phase transitions of the Si(100) surface. *Suf. Sci.* **160**, 618–640 (1985). 38

[78] T. Tabaka, T. Aruga, and Y. Murata. Order-disorder transition on Si(001): c(4x2) to (2x1). *Surf. Sci.* **179**, L63–L70 (1987). 38, 52

[79] Y. Nakamura, H. Kawai, and M. Nakayama. Influence of defects on the order-disorder phase transition of a Si(001) surface. *Phys. Rev. B* **55**, 10549–10560 (1997). 38

[80] T. Shirasawa, S. Mizuno, and H. Tochihara. Electron-beam-induced disordering of the Si(001)-c(4x2) surface structure. *Phys. Rev. Lett.* **94**, 1955021–1955024 (2005). 39

[81] C. A. Hoffman, J. R. Meyer, F. J. Bartoli, A. Di Venere, X. J. Yi, C. L. Hou, H. C. Wang, J. B. Ketterson, and G. K. Wang. Semimetal-to-semiconductor transition in bismuth thin films. *Phys. Rev. B* **48**, 11431–11434 (1993). 41, 130

[82] R. Peierls. *More Surprises in Theoretical Physics* (Princeton University Press, Princeton, 1991). 42

[83] J. Donohue. *The structures of the elements* (JohnWiley & Sons, New York, 1974). 42

[84] F. Jona. Low-energy electron diffraction study of surfaces of antimony and bismuth. *Surf. Sci.* **8**, 57–76 (1967). 42

[85] R. J. Needs, R. M. Martin, and O. H. Nielsen. Total energy calculations of the structural properties of the group-V element arsenic. *Phys. Rev. B* **33**, 3778–3784 (1986). 42

[86] Ph. Hofmann. The surfaces of bismuth: Structural and electronic properties. *Prog. Surf. Sci.* **81**, 191–245 (2006). 42, 43, 62, 68, 157

[87] N. E. Ashcroft and N. D. Mermin. *Solid state physics* (Saunders College, Philadelphia, international edition, 1976). 43

[88] E. Bauer. Phänomenologische Theorie der Kristallabscheidung an Oberflächen. I. *Z. Kristallogr.* **110**, 372–394 (1958). 45, 84

[89] E. Bauer and H. Poppa. Recent advances in epitaxy. *Thin Solid Films* **12**, 167–185 (1972). 45

[90] J. A. Venables. Rate equation approaches to thin film nucleation kinetics. *Philos. Mag.* **27**, 697 (1973). 46, 48, 122

[91] J. A. Venables, G. D. T. Spiller, and M. Hanbücken. Nucleation and growth of thin films. *Rep. Prog. Phys.* **47**, 399–459 (1984). 46, 48, 110, 122

[92] J. A. Venables. Atomic processes in crystal growth. *Surf. Sci.* **299/300**, 798–817 (1994). 46, 48

[93] Z. Y. Zhang and M. G. Lagally. Atomistic Processes in the Early Stages of Thin-Film Growth. *Science* **276**, 377–383 (1997). 46, 47

[94] H. Brune. Microscopic view of epitaxial metal growth: nucleation and aggregation. *Surf. Sci. Rep.* **31**, 121–229 (1998). 46, 112

[95] K. J. Leidler. *Chemical kinetics* (McGraw Hill, London, 1965). 46

[96] D. W. Bassett and P. R. Webber. Diffusion of single adatoms of platinum, iridium and gold on platinum surfaces. *Surf. Sci.* **70**, 520–531 (1978). 47

[97] J. D. Wrigley and G. Ehrlich. Surface Diffusion by an Atomic Exchange Mechanism. *Phys. Rev. Lett.* **44**, 661–663 (1980). 47

[98] R. Gomer. Diffusion of adsorbates on metal surfaces. *Rep. Prog. Phys.* **53**, 917–1002 (1990). 48, 121

[99] P. Hahn, J. Clabes, and M. Henzler. LEED-investigations and work-function measurements of the first stages of epitaxy of tungsten on tungsten (110). *J. Appl. Phys.* **51**, 2079 (1980). 49, 108

[100] G. Meyer, J. Wollschläger, and M. Henzler. Epitaxial growth of thin copper layers on Cu(111) studied by high-resolution low-energy electron diffraction. *Surf. Sci.* **231**, 64 (1990). 49

[101] S. P. Murarka. Refractory silicides for integrated circuits. *J. Vac. Sci. Technol.* **17**, 775–792 (1980). 51

[102] C. Calandra, O. Bisi, and G. Ottaviani. Electronic properties of silicon-transition metal interface compounds. *Surf. Sci.* **4**, 271–364 (1985). 51

[103] F. Mohammadi, and K. C. Saraswat. Properties of sputtered tungsten silicide for mos integrated circuit applications. *J. Electrochem. Soc.* **127**, 450–454 (1980). 51

[104] K. Roh, S. Youn, S. Yang, and Y. Roh. Tungsten silicide for the alternate gate metal in metal-oxide-semiconductor devices. *J. Vac. Sci. Technol. A* **19**, 1562 (2001). 51

[105] V. A. Ukraintsev, and J. T. J. Yates. The role of nickel in si(001) roughening. *Surf. Sci.* **346**, 31–39 (1996). 51

[106] P. Revesz, L. R. Zheng, L. S. Hung, and J. W. Mayer. Morphological degradation of TiSi2 on 100 silicon. *Appl. Phys. Lett.* **48**, 1591 (1986). 51

[107] S. Ogawa, T. Yoshida, and T. Kouzaki. Dependence of thermal stability of the titanium silicide/silicon structure on impurities. *Appl. Phys. Lett.* **56**, 724–727 (1990). 51

[108] L. D. Locker, and C. D. Capio. Reaction kinetics of tungsten thin films on silicon (100) surfaces. *J. Appl. Phys.* **44**, 4366–4369 (1973). 51

[109] M. Horn Von Hoegen, J. Falta and M. Henzler. The initial stages of growth of silicon on si(111) by slow positron annihilation low-energy electron diffraction. *Thin Solid Films* **183**, 213–220 (1989). 51, 101

[110] J. H. Liang, and D. S. Chao. Formation of tungsten silicide films by ion bean synthesis. *Surf. Coat. Technol.* **140**, 116–121 (2001). 51

[111] D. L. Brors, J. A. Fair, K. A. Monnig, and K. C. Saraswat. Properties of low pressure cvd tungsten silicide as related to ic process requirements. *Solid State Technol.* **26**, 183–186 (1983). 52

[112] F. Nava, B. Z. Weiss, K. Y. Ahn, D. A. Smith, and K. N. Tu. Thermal stability and electrical conduction of coevaporated wsi2 thin films. *J. Appl. Phys.* **64**, 354–364 (1988). 52, 58

[113] R. A. Wolkow. Direct observation of an increase in buckled dimers on Si(001) at low temperature. *Phys. Rev. Lett.* **68**, 2636–2639 (1992). 52

[114] R. M. Tromp, R. J. Hamers, and J. E. Demuth. Si(001) dimer structure observed with scanning tunneling microscopy. *Phys. Rev. Lett.* **55**, 1303–1306 (1985). 52

[115] R. M. Tromp and M. C. Reuter. Design of a new photo-emission/low-energy electron microscope for surface studies. *Ultramicroscopy* **36**, 99 (1991). 53

[116] O. Nishikawa, Y. Tsunashima, E. Nomura, S. Horie, M. Wada, M. Shibata, T. Yoshimura, and R. Uemori. Atom-probe study of the early stage of silicide formation. 1. w-si system. *J. Vac. Sci. Technol. B* **1**, 6 (1983). 57

[117] H. Dallaporta, M. Liehr, and J. E. Lewis. Silicon dioxide defects induced by metal impurities. *Phys. Rev. B* **41**, 5075–5083 (1990). 57

[118] R. Tromp, G. W. Rubloff, P. Balk, and F. K. LeGoues. High-temperature sio2 decomposition at the sio2/si interface. *Phys. Rev. Lett.* **55**, 2332–2335 (1985). 57

[119] M. Liehr, H. Lefakis, F. K. LeGoues, and G. W. Rubloff. Influence of thin sio2 interlayers on chemical reaction and microstructure at the ni/si(111) interface. *Phys. Rev. B* **33**, 5517–5525 (1986). 57

[120] A. H. Reader, A. H. van Ommen, P. J. W. Weijs, R. A. M. Wolters, and D. J. Oostra. Transition metal silicides in silicon technology. *Rep. Prog. Phys.* **56**, 1397–1467 (1992). 57

[121] W. T. Lin, and L. J. Chen. Localised epitaxial growth of tetragonal and hexagonal wsi2 on (111)si. *J. Appl. Phys.* **58**, 1515–1518 (1985). 57, 58

[122] H. Mönig, J. Sun, Y. M. Koroteev, G. Bihlmayer, J. Wells, E. V. Chulkov, K. Pohl, and Ph. Hofmann. Structure of the (111) surface of bismuth: LEED analysis and first-principles calculations. *Phys. Rev. B* **72**, 085410 (2005). 62, 68

[123] M. Horn-von Hoegen, A. Al-Falou, H. Pietsch, B. H. Müller, and M. Henzler. Formation of interfacial dislocation network in surfactant mediated growth of Ge on Si(111) investigated by SPA-LEED: Part I. *Surf. Sci.* **298**, 29–42 (1993). 64, 84

[124] G. Springholz. Strain contrast in scanning tunneling microscopy imaging of subsurface dislocations in lattice-mismatched heteroepitaxy. *Appl. Surf. Sci.* **112**, 12–22 (1997). 64, 77, 82, 84

[125] H. Brune, M. Giovannini, K. Bromann, and K. Kern. Self-organized growth of nanostructure arrays on strain-relief patterns. *Nature* **394**, 451–453 (1998). 64, 84

[126] C. Schwennicke, J. Schimmelpfennig and H. Pfnür. Morphology of thin NaCl films grown epitaxially on Ge(100). *Surf. Sci.* **293**, 57–66 (1993). 68, 80

[127] M. Henzler. Growth of epitaxial monolayers. *Surf. Sci.* **357-358**, 809 (1996). 68, 80

[128] L. Dressler, K. Goetz, and J. Kräusslich. X-Ray Double Diffraction (Umweganregung) in SiC Monocrystals. *phys. stat. sol. (b) ,* **200**, 377–383 (1997). 68

[129] H. Kiessig. Interference of Rontgen rays on thin layers. *Ann. Phys.* **10**, 769–788 (1931). 68

[130] K. Häupl and P. Wißmann. Determination of thickness and roughness of thin copper films by x-ray diffraction measurements. *Fresenius Z. Anal. Chem.* **314**, 337–339 (1983). 69

[131] R. M. Goodman and G. A. Somorjai. Low-energy electron diffraction studies of surface melting and freezing of Lead, Bismuth, and Tin single-crystal surfaces. *J. Chem. Phys.* **52**, 6325–6331 (1970). 74, 157

[132] E. A. Murphy, H. E. Elsayed-Ali, and J. W. Herman. Superheating of Bi(0001. *Phys. Rev. B* **48**, 4921–4924 (1993). 74

[133] A. Janzen, B. Krenzer, P. Zhou, D. von der Linde, and M. Horn-von Hoegen. Ultrafast electron diffraction at surfaces after laser excitation. *Surf. Sci.* **600**, 4094–4098 (2006). 74, 157

[134] Th. Schmidt. *Epitaxy von Silber(111) auf Silizium(001).* Master's thesis, Universität Hannover (1994). 74

[135] Horn-von Hoegen, M. and M. Henzler. Lattice matching periodic interfacial dislocation network in surfactant-mediated growth of Ge on Si(111). *Phys. Stat. Sol. (a)* **146**, 337–352 (1994). 76, 80

[136] J. Wollschläger. Diffraction from surfaces with randomly distributed structural defects. *Surf. Sci.* **328**, 323–336 (1995). 76

[137] M. Schmid, A. Biedermann, H. Stadler, and P. Varga. Lattice mismatch dislocations in a preferentially sputtered alloy studied by scanning tunneling microscopy. *Phys. Rev. Lett.* **69**, 925–928 (1992). 76, 84

[138] R. M. Tromp, F. K. LeGoues, and M. C. Reuter. Strain relief during growth: CaF2 on Si(111). *Phys. Rev. Lett.* **74**, 2706–2709 (1995). 76

[139] R. Stalder, H. Sirringhaus, N. Onda, and H. von Känel. Observation of misfit dislocations in epitaxial CoSi2/Si(111) layers by scanning tunneling microscopy. *Appl. Phys. Lett.* **59**, 1960–1962 (1991). 76

[140] C. Bobisch, A. Bannani, M. Matena, and R. Möller. Ultrathin Bi films on Si(100). *Nanotechnology* **18**, 055606 (2007). 78, 95

[141] S. N. Filmonov, V. Cherepanov, N. Paul, H. Asaoka, J. Brona, and B. Voigtländer. Dislocation network in conventional and surfactant-mediated ge/si(111) epitaxy. *Surf. Sci.* **599**, 76–84 (2005). 82

[142] I. N. Stranski and V. L. Krastanow. *Akad. Wiss. Lit. Mainz. Math-Natur. K1 IIb* **146**, 797 (1939). 84

[143] D. J. Srolovitz. On the stability of surfaces of stressed solids. *Acta Metall.* **37**, 621 (1989). 84, 85

[144] D. J. Eaglesham and M. Cerullo. Dislocation-free Stranski-Krastanow growth of Ge on Si(001). *Phys. Rev. Lett.* **64**, 1943–1946 (1990). 84

[145] C. W. Snyder, B. G. Orr, D. Kessler and L. M. Sander. Effect of strain on surface morphology in highly strained InGaAs films. *Phys. Rev. Lett.* **66**, 3032–3035 (1991). 84

[146] M. Horn-von Hoegen, A. Al Falou, B. H. Müller, U. Köhler, L. Andersohn, B. Dahlheimer, and M. Henzler. Surfactant-stabilized strained Ge cones on Si(001). *Phys. Rev. B* **49**, 2637–2650 (1994). 84

[147] M. Horn-von Hoegen, B. H. Müller, and A. Al Falou. Strain relief by microroughness in surfactant-mediated growth of Ge on Si(001). *Phys. Rev. B* **50**, 11640–11652 (1994). 84

[148] J. H. van der Merwe. Crystal interfaces. part ii. finite overgrowths. *J. Appl. Phys.* **34**, 123–127 (1963). 84

[149] J. W. Matthews. Defects associated with the accommodation of misfit between crystals. *J. Vac. Sci. Technol.* **12**, 126–133 (1975). 84

[150] R. People and J. C. Bean. Calculation of critical layer thickness versus lattice mismatch Ge(x)Si(1-x)/Si. *Appl. Phys. Lett.* **47**, 322–324 (1985). 84, 88

[151] P. M. J. Maree, J. C. Barbour, J. F. van der Veen, K. L. Kavanagh, C. W. T. Bulle-Lieuwma, and M. P. A. Viegers. Generation of misfit dislocations in semiconductors. *J. Appl. Phys.* **62**, 4413–4420 (1987). 84

[152] U. Gradmann and G. Waller. Periodic lattice distortions in epitaxial films of Fe(110) on W(110). *Surf. Sci.* **116**, 539–548 (1982). 84

[153] H. Bethe, D. Heuer, Ch. Jensen, K. Reshöft, U. Köhler. Misfit-related effects in the epitaxial growth of iron on W(110). *Surf. Sci.* **331**, 878–884 (1995). 84

[154] W. M. Yim and R. J. Paff. Thermal expansion of AlN, sapphire, and silicon. *J. Appl. Phys.* **45**, 1456–1457 (1974). 85

[155] Y. Okada and Y. Tokumaru. Precise determination of lattice parameter and thermal expansion coefficient of silicon between 300 and 1500 K. *J. Appl. Phys. 56, 314 (1984* **56**, 314–320 (1984). 85

[156] J. Henrion and G.E. Rhead. Leed studies of the first stages of deposition and melting of lead on low index faces of copper. *Surf. Sci.* **29**, 20–36 (1972). 91

[157] J. W. M. Frenken and J. F. van der Veen. Observation of Surface Melting. *Phys. Rev. Lett.* **54**, 134–137 (1985). 91

[158] H.-N. Yang, T.-M. Lu, and G.-C. Wang. Collapsing of thermally induced steps on the Pb(111) surface. *Phys. Rev. Lett.* **62**, 2148–2151 (1989). 91

[159] Y. Cao and E. H. Conrad. Approach to thermal roughening of Ni(110): A study by high-resolution low-energy electron diffraction. *Phys. Rev. Lett.* **64**, 447–450 (1990). 91

[160] K. C. Prince, U. Breuer, and H. P. Bonzel. Anisotropy of the order-disorder phase transition on the Pb(110) surface. *Phys. Rev. Lett.* **60**, 1146–1149 (1988). 91

[161] S. Yaginuma, T. Nagao, J. T. Sadowski, A. Pucci, Y. Fujikawa, T. Sakurai. Surface pre-melting and surface flattening of Bi nanofilms on Si(1 1 1)-7x7. *Surf. Sci.* **547**, L877–L881 (2003). 91

[162] L. G. Parratt. Surface studies of solids by total reflection of x-rays. *Phys. Rev.* **95**, 359–369 (1954). 92

[163] S. Tang and A. J. Freeman. Bi-induced reconstruction on si(100). *Phys. Rev. B* **50**, 1701–1704 (1994). 93

[164] H. P. Noh, Ch. Park, D. Jeon, K. Cho, T. Hashizume, Y. Kuk, and T. Sakurai. Adsorption of Bi on Si(001) surface: An atomic view. *J. Vac. Sci. Technol. B* **12**, 2097–2099 (1994). 93

[165] K. Miki, J. H. G. Owen, D. R. Bowler, G. A. D. Briggs, and K. Sakomoto. Bismuth-induced structures on Si(001) surfaces. *Surf. Sci.* **421**, 397–418 (1999). 93

[166] S. Yu. Bulavenko, I. F. Koval, P. V. Melnik, N. G. Nakhodkin, H. J. W. Zandvliet. STM investigation of the initial adsorption stage of Bi on Si(100)-(2x1) and Ge(100)-(2x1) surfaces. *Surf. Sci.* **482-485**, 370–375 (2001). 93

[167] T. Hanada and M. Kawai. Study of successive phase transition of the Si(001)-Bi surface by RHEED. *Surf. Sci.* **242**, 137–142 (1991). 93

[168] C. Park, R. Z. Bakhtizin, T. Hashizume and T. Sakurai. Ordering of missing-row-defects forming (2xn)-Bi phases on the Si(100)-(2x1) surface studied by the scanning tunneling microscopy. *Jpn. J. Appl. Phys.* **32**, L528–L531 (1993). 93

[169] J. Tersoff and R. M. Tromp. Shape transition in growth of strained islands: Spontaneous formation of quantum wires. *Phys. Rev. Lett.* **70**, 2782–2785 (1993). 95

[170] R. M. Tromp, A. W. Denier van der Gon, F. K. LeGoues, and M. C. Reuter. Observation of buried interfaces with low energy electron microscopy. *Phys. Rev. Lett.* **71**, 3299–3302 (1993). 95

[171] G. Meyer and K. H. Rieder. Low-temperature scanning tunneling microscopy study of nucleation, percolation, and growth of ultrathin Ag films on Si(111)7x7. *Appl. Phys. Lett.* **64**, 3560–3562 (1994). 95

[172] R. Kunkel, B. Poelsema, L. K. Verheij, and G. Comsa. Reentrant layer-by-layer growth during molecular-beam epitaxy of metal-on-metal substrates. *Phys. Rev. Lett.* **65**, 733–736 (1990). 95, 103

[173] G. Rosenfeld, R. Servaty, C. Teichert, B. Poelsema, and G. Comsa. Layer-by-layer growth of Ag on Ag(111) induced by enhanced nucleation: A model study for surfactant-mediated growth. *Phys. Rev. Lett.* **71**, 895 – 898 (1993). 95, 96, 97

[174] Ch. Ammer, T. Schaefer, Ch. Teichert, K. Meinel, and M. Klaua. The multilayer growth mode in the epitaxy of Ag on Ag(111) analysed by SPALEED. *Surf. Sci.* **307-309**, 570–575 (1994). 95

[175] M. Hanbücken and H. Neddermeyer. A LEED-AES study of the growth of Ag films on Si(100). *Surf. Sci.* **14**, 563–573 (1982). 96

[176] M. Horn-von Hoegen, T. Schmidt, M. Henzler, G. Meyer, D. Winau, K. H. Rieder. Epitaxial layer growth ofAg(111)-films on Si(100). *Surf. Sci.* **331-333**, 575–579 (1995). 96

[177] H. A. van der Vegt, H. M. van Pinxteren, M. Lohmeier, E. Vlieg, and J. M. C. Thornton. Surfactant-induced layer-by-layer growth of ag on ag(111). *Phys. Rev. Lett.* **68**, 3335 – 3338 (1992). 96

[178] J. Vrijmoeth, H. A. van der Vegt, J. A. Meyer, E. Vlieg, and R. J. Behm. Surfactant-Induced Layer-by-Layer Growth of Ag on Ag(111): Origins and Side Effects. *Phys. Rev. Lett.* **72**, 3843–3846 (1994). 97

[179] E. Z. Luo, J. Wollschläger, F. Wegner, and M. Henzler. Spa-leed studies of growth of ag on ag(111) at low temperatures. *Appl. Phys. A* **60**, 19–25 (1995). 98, 109

[180] W. F. Egelhoff, Jr. and I. Jacob. Reflection high-energy electron diffraction (rheed) oscillations at 77 k. *Phys. Rev. Lett.* **62**, 921–924 (1989). 101, 103

[181] G. Ehrlich and F. G. Hudda. Atomic View of Surface Self-Diffusion: Tungsten on Tungsten. *J. Chem. Phys.* **44**, 1039–1049 (1966). 102

[182] R. L. Schwoebel and E. J. Shipsey. Step Motion on Crystal Surfaces. *J. Appl. Phys.* **37**, 3682–3686 (1966). 102

[183] H. C. Jeong, and E. D. Williams. Steps on surfaces: experiment and theory. *Surf. Sci. Rep.* **34**, 171–294 (1999). 103

[184] M. Horn and M. Henzler. LEED studies of Si molecular beam epitaxy onto Si(111). *J. Crys. Growth* **81**, 428–433 (1987). 104

[185] R. Altsinger, H. Busch, M. Horn, and M. Henzler. Nucleation and growth during molecular beam epitaxy (MBE) of Si on Si(111). *Surf. Sci.* **200**, 235–246 (1988). 106

[186] V. S. Édel'man. STM observation of twin microlayers on cleaved bismuth surfaces. *Phys. Lett. A* **210**, 105–109 (1996). 106

[187] R. Smoluchowski. Anisotropy of the electronic workfunction of metals. *Phys. Rev.* **60**, 661–674 (1941). 107

[188] P. Bedrossian and B. Poelsema and G. Rosenfeld and L. C. Jorritsma and N. N. Lipkin, and G. Cosma. Electron density contour smoothening for epitaxial Ag islands on Ag(100). *Surf. Sci.* **334**, 1–9 (1995). 107

[189] M. Henzler. LEED studies of surface imperfections. *Appl. Surf. Sci.* **11/12**, 450–469 (1982). 108

[190] J.-K. Zuo, J. F. Wendelken, H. Dürr, and C.-L. Liu. Growth and coalescence in submonolayer homoepitaxy on cu(100) studied with high-resolution low-energy electron diffraction. *Phys. Rev. Lett.* **72**, 3064–3067 (1994). 108

[191] K. Stolt, W. R. Graham, and G. Ehrlich. Surface diffusion of individual atoms and dimers: Re on W(211). *J. Chem. Phys.* **65**, 3206 (1976). 109, 113

[192] Th. Michely and G. Cosma. Temperature dependence of the sputtering morphology of pt(111). *Surf. Sci.* **256**, 217 (1991). 109, 113

[193] M. Hohage, M. Bott, M. Morgenstern, Z. Zhang, Th. Michely, and G. Comsa. Atomic Processes in Low Temperature Pt-Dendrite Growth on Pt(111). *Phys. Rev. Lett.* **76**, 2366 – 2369 (1996). 109, 112, 113

[194] P. Stoltze. Simulation of surface defects. *J. Phys.: Condens. Matter* **6**, 9495–9517 (1994). 111

[195] C.-M. Zhang, M. C. Bartelt, J.-M. Wen, C. J. Jenks, J. W. Evans, and P. A. Thiel. Submonolayer island formation and the onset of multilayer growth during ag/ag/100) homoepitaxy. *Surf. Sci.* **406**, 178–193 (1998). 111

[196] J. Jacobsen, K. W. Jacobsen, P. Stoltze, and J. K. Nžrskov. Island shape-induced transition from 2d to 3d growth for pt/pt(111). *Phys. Rev. Lett.* **74**, 2295–2298 (1995). 111

[197] K. Kyuno, A. Gölzhäuser, and G. Ehrlich. Growth and the diffusion of platinum atoms and dimers on Pt(111). *Surf. Sci.* **397**, 191–196 (1998). 111

[198] Th. Michely, M. Hohage, M. Bott, and G. Comsa. Inversion of growth speed anisotropy in two dimensions. *Phys. Rev. Lett.* **70**, 3943 – 3946 (1993). 112, 113

[199] E. Hahn, E. Kampshoff, N. Wälchli, and K. Kern. Strain driven fcc-bct phase transition of pseudomorphic cu films on pd(100). *Phys. Rev. Lett.* **74**, 1803–1806 (1995). 112

[200] S. Günther, E. Kopatzki, M. C. Bartelt, J. W. Evans, and R. J. Behm. Anisotropy in nucleation and growth of two-dimensional islands during homoepitaxy on "hex" reconstructed au(100). *Phys. Rev. Lett.* **73**, 553–556 (1994). 112

[201] R. Q. Hwang, J. Schröder, C. Günther, and R. J. Behm. Fractal growth of two-dimensional islands: Au on ru(0001). *Phys. Rev. Lett.* **67**, 3279–3282 (1991). 112

[202] H. Brune, Ch. Romainczyk, H. Röder & K. Kern. Mechanism of the transition from fractal to dendritic growth of surface aggregates. *Nature* **369**, 469–471 (1994). 112

[203] H. Röder, K. Bromann, H. Brune, and K. Kern. Diffusion-Limited Aggregation with Active Edge Diffusion. *Phys. Rev. Lett.* **74**, 3217–3220 (1995). 112

[204] K. Takayanagi, Y. Tanishiro, M. Takahashi, and S. Takahashi. Structural analysis of si(111)-7x7 by uhv-transmission electron diffraction and microscopy. *J. Vac. Sci. Technol. A* **3**, 1502–1506 (1985). 118

[205] K. Takayanagi, Y. Tanishiro, S. Takahashi, and M. Takahashi. Structure analysis of si(111)-7x7 reconstructed surface by transmission electron diffraction. *Surf. Sci.* **164**, 367–392 (1985). 118

[206] G. Binnig, H. Rohrer, Ch. Gerber, and E. Weibel. 7x7 reconstruction on si(111) resolved in real space. *Phys. Rev. B* **50**, 120–123 (1983). 118

[207] R. J. Hamers, R. M. Tromp, and J. E. Demuth. Surface electronic structure of si (111)-(7x7) resolved in real space. *Phys. Rev. Lett.* **56**, 1972–1975 (1986). 118

[208] J. T. Sadowski, T. Nagao, S. Yaginuma, Y. Fujikawa, A. Al-Mahboob, K. Nakajima, T. Sakurai, G. E. Thayer, and R. M. Tromp. Thin bismuth film as a template for pentacene growth. *Appl. Phys. Lett.* **86**, 073109 (2005). 119

[209] J. T. Sadowski, T. Nagao, S. Yaginuma, Y. Fujikawa, T. Sakurai, A. Oreshkin, and M. Saito. Stability of the quasicubic phase in the initial stage of the growth of bismuth films on Si(111)-7x7. *J. Appl. Phys.* **99**, 014904 (2006). 119

[210] S. Yaginuma, T. Nagao, J. T. Sadowski, M. Saito, K. Nagaoka, Y. Fujikawa, T. Sakurai, and T. Nakayama. Origin of flat morphology and high crystallinity of ultrathin bismuth films. *Surf. Sci.* **601**, 3593–3600 (2007). 119

[211] Y. W. Mo, J. Kleiner, M. B. Webb, and M. G. Lagally. Surface self-diffusion of Si on Si(001). *Surf. Sci.* **268**, 275–295 (1992). 122

[212] Y. W. Mo, J. Kleiner, M. B. Webb, and M. G. Lagally. Activation energy for surface diffusion of Si on Si(001): A scanning-tunneling-microscopy study. *Phys. Rev. Lett.* **66**, 1998–2001 (1998). 122

[213] R. E. Macfarlane. *The Physics of Semimetals and Narrow Gap Semiconductors* (Pergamon Press, New York, 1971). 122

[214] H. Brune, H. Röder, C. Boragno, and K. Kern. Microscopic view of nucleation on surfaces. *Phys. Rev. Lett.* **73**, 1955–1958 (1994). 123

[215] T. A. Witten and L. M. Sander. Diffusion-limited aggregation. *Phys. Rev. B* **27**, 5686–5697 (1983). 124

[216] H. Brune, Ch. Romainczyk, H. Röder, and K. Kern. Mechanism of the transition from fractal to dendritic growth of surface aggregates. *Nature* **369**, 469–471 (1994). 124

[217] T. Michely and J. Krug. *Islands, Mounds and Atoms*. Springer series in surface sciences (Springer-Verlag, Berlin, 2004). 124

[218] T. Nagao, S. Yaginuma, M. Saito, T. Kogure, J. T. Sadowski, T. Ohno, S. Hasegawa, and T. Sakurai. Strong lateral growth and crystallization via two-dimensional allotropic transformation of semi-metal Bi film. *Surf. Sci. Lett.* **590**, L247–L252 (2005). 127

[219] T. Hirahara, I. Matsuda, S. Yamazaki, N. Miyata, and S. Hasegawa. Large surface-state conductivity in ultrathin Bi films. *Appl. Phys. Lett.* **91**, 202106 (2007). 127, 130, 137, 138, 152, 158

[220] Allen N. Friedman. Some effects of sample size on electrical transport in Bismuth. *Phys. Rev.* **159**, 553–563 (1967). 130

[221] J.-P. Michenaud and J.-P. Issi. Electron and hole transport in bismuth. *J. Phys. C: Solid State Phys.* **5**, 3061–3072 (1972). 130, 138

[222] R. Hartman. Temperature dependence of the low-field galvanomagnetic coefficients of bismuth. *Phys. Rev.* **181**, 1070–1086 (1969). 130

[223] H. Asahi, T. Humoto, and A. Kawaju. Quantum size effects in thin bismuth films. *Phys. Rev. B* **9**, 3347–3356 (1974). 130

[224] Y. F. Komnik and E. I. Bukhshtab and Y. V. Nikitin, and V. V. Andrievskii. Features of temperature dependence of the resistance of thin bismuth film. *Sov. Phys. JETP* **33**, 364–373 (1971). 130

[225] T. Wosiński. Evidence for the electron traps at dislocations in GaAs crystals. *J. Appl. Phys.* **65**, 1566–1570 (1989). 130

[226] O. Yastrubchak, T. Wosiński, A. Makosa, T. Figielski and A. L. Tóth. Capture kinetics at deep-level defects in lattice-mismatched GaAs-based heterostructures. *Physica B* **308-310**, 757–760 (2001). 130

[227] A. V. Ofitserov and V. S. Edel'man. Investigation of the spectrum of surface states in bismuth by scanning tunneling spectroscopy. *J. Exp. Theor. Phys.* **93**, 642–648 (2001). 131

[228] A. Tanaka, M. Hatano, K. Takahashi, H. Sasaki, S. Suzuki, and S. Sato. Bulk and surface electronic structures of the semimetal Bi studied by angle-resolved photoemission spectroscopy. *Phys. Rev. B* **59**, 1786–1791 (1999). 132

[229] F. Patthey, W.-D. Schneider, and H. Micklitz. Photoemission study of the Bi(111) surface. *Phys. Rev. B* **49**, 11293–11296 (1994). 132

[230] M. Hengsberger, P. Segovia, M. Garnier, D. Purdie, and Y. Baer. Photoemission study of the carrier bands in Bi(111). *Eur. Phys. J. B* **17**, 603–608 (2000). 132

[231] E. H. Sondheimer. The mean free path of electrons in metals. *Adv. Physics* **50**, 499–537 (2001). 133

[232] T. Hirahara. *Private communication.* 137, 158

[233] I. Matsuda, T. Hirahara, M. Konishi, C. Liu, H. Morikawa, M. D'angelo, and S. Hasegawa. Evolution of Fermi surface by electron filling into a free-electronlike surface state. *Phys. Rev. B* **71**, 235315 (2005). 137, 138

[234] T. Hirahara, T. Nagao, I. Matsuda, G. Bihlmayer, E. V. Chulkov, Yu. M. Koroteev, and S. Hasegawa. Quantum well states in ultrathin Bi films: Angle-resolved photoemission spectroscopy and first-principles calculations study. *Phys. Rev. B* **75**, 035422 (2007). 138

[235] C. R. Ast and H. Höchst. Fermi Surface of Bi(111) Measured by Photoemission Spectroscopy. *Phys. Rev. Lett.* **87**, 177602 (2001). 138, 158

[236] F. Soria, J.L Sacedon, P. M. Echenique and D. Titterington. LEED study of the epitaxial growth of the thin film Au(111)/Ag(111) system. *Surf. Sci.* **68**, 448–456 (1977). 145

[237] J. H. van der Merwe and E. Bauer. Influence of misfit and bonding on the mode of growth in epitaxy. *Phys. Rev. B* **39**, 3632–3641 (1989). 145

[238] R. J. Culbertson, L. C. Feldman, and P. J. Silverman. Epitaxy of Au on Ag(111) Studied by High-Energy Ion Scattering. *Phys. Rev. Lett.* **47**, 657–660 (1981). 146

[239] T. C. Hsieh, A. P. Shapiro, and T.-C. Chiang. Core-level shifts for Au epitaxial overlayers on Ag. *Phys. Rev. B* **31**, 2541–2544 (1985). 146

[240] G. K. Wertheim and D. N. E. Buchanan. Core-electron binding energies of adsorbed metallic monolayers: Au/Ag(111). *Phys. Rev. B* **33**, 914–918 (1986). 146

[241] T. Miller and T.-C. Chiang. Study of a surface state in a Ag-Au superlattice gap. *Phys. Rev. Lett.* **68**, 3339–3342 (1992). 146

[242] P. Fenter and T. Gustafsson. Bilayer growth in a metallic system: Au on Ag(110). *Phys. Rev. Lett.* **64**, 1142–1145 (1990). 146

[243] S. Rousset, S. Chiang, D. E. Fowler, and D. D. Chambliss. Intermixing and three-dimensional islands in the epitaxial growth of Au on Ag(110). *Phys. Rev. Lett.* **69**, 3200–3203 (1992). 146

[244] C. T. Chan, K. P. Bohnen, and K. M. Ho. Initial growth mode of Au on Ag(110) studied with first-principles calculations. *Phys. Rev. Lett.* **69**, 1672–1675 (1992). 146

[245] U. Lipphardt, H. Engelhard, J. Westhof, A. Goldmann and S. Witzel. Angle-resolved photoemission from Au deposited on Ag(111): evidence for surface alloy formation. *Surf. Sci.* **294**, 84–92 (1993). 146

[246] B. Eisenhut, J. Stober, G. Rangelov, and Th. Fauster. Growth and structure of thin Au films on Ag(111). *Phys. Rev. B* **49**, 14676–14683 (1994). 146

[247] J. Hayoz, Th. Pillo, R. Fasel, L. Schlapbach, and P. Aebi. Experimental evidence for kinetically determined intermixed Volmer-Weber growth in thin-film deposition of Au on Ag(110). *Phys. Rev. B 59* **59**, 15975–15989 (1999). 146

[248] M. I. Haftel, M. Rosen, T. Franklin, and M. Hettermann. Molecular dynamics observations of interdiffusion and Stranski-Krastanov growth in the early film deposition of Au on Ag(110). *Phys. Rev. Lett.* **72**, 1858–1861 (1994). 146

[249] M. G. Goldiner, V. B. Sapozhnikov, M. Klaua and K. Meinel. Experimental evidence of a diffusion size effect in thin Au films on Ag(111). *J . Phys.: Condens. Matter* **3**, 5479–5487 (1991). 146

[250] A. Bannani. *Ladungstransport in dünnen metallischen Filmen.* Ph.D. thesis, Universität Duisburg-Essen (2007). 153

[251] C. Bobisch. *Mikroskopie mit ballistischen Elektronen.* Ph.D. thesis, Universität Duisburg-Essen (2007). 153

[252] J.T. Sadowski, R.Z. Bakhtizin, A.I. Oreshkin, T. Nishihara, A. Al-Mahboob, Y. Fujikawa, K. Nakajima, and T. Sakurai. Epitaxial C60 thin films on Bi(0001). *Surf. Sci.* **601**, L136–L139 (2007). 154

[253] A. Bannani, C. Bobisch, and R. Möller. Ballistic Electron Microscopy of Individual Molecules. *Science* **315**, 1824–1828 (2007). 154

[254] C. R. Ast, J. Henk, A. Ernst, L. Moreschini, M. C. Falub, D. Pacile, P. Bruno, K. Kern, and M. Grioni. Giant Spin Splitting through Surface Alloying. *Phys. Rev. Lett.* **98**, 186807 (2007). 155

[255] P. Cucka and C. S. Barrett. The Crystal Structure of Bi and of Solid Solutions of Pb, Sn, Sb and Te in Bi. *Acta Cryst.* **15**, 865–872 (1962). 157

[256] G. K. White. Thermal expansion of trigonal elements at low temperatures : As, Sb and Bi. *J. Phys. C: Solid State Phys.* **5**, 2731–2745 (1972). 157

[257] P. Fischer, I. Sosnowska and M. Szymanski. Debye-Waller factor and thermal expansion of arsenic, antimony and bismuth. *J. Phys. C: Solid State Phys.* **11**, 1043–1051 (1978). 157

[258] G. E. Smith, G. A. Baraff, and J. M. Rowell. Effective g factor of electrons and holes in bismuth. *Phys. Rev.* **135**, A1118–A1124 (1964). 158

[259] R. A. Hoffman and D. R. Frankl. Electrical transport properties of thin bismuth films. *Phys. Rev. B* **3**, 1825–1833 (1971). 158

List of Figures

List of Tables

Publications and Presentations

A. The present work has so far resulted in the following publications:

Publications which are published till the date of final defense:

1. **G. Jnawali**, H. Hattab, B. Krenzer, and M. Horn-von Hoegen. Lattice accommodation of epitaxial Bi(111) films on Si(001) studied with SPA-LEED and AFM, *Phys. Rev.* B **74**, 1953401 (2006).

2. **G. Jnawali**, H. Hattab, F.-J. Meyer zu Heringdorf, B. Krenzer, and M. Horn-von Hoegen. Lattice matching periodic array of misfit dislocations: heteroepitaxy of Bi(111) on Si(001). *Phys. Rev.* B **76**, 035337 (2007)

3. **G. Jnawali**, H. Hattab, C. A. Bobisch, A. Bernhart, E. Zubkov, R. Möller, and M. Horn-von Hoegen. Homoepitaxial growth of Bi(111). *Phys. Rev.* B **78**, 035321 (2008).

4. H. Hattab, E. Zubkov, A. Bernhart, **G. Jnawali**, C. Bobisch, B. Krenzer, M. Acet, R. Möller, and M. Horn-von Hoegen. Epitaxial Bi(111) films on Si(001): Strain state, surface morphology, and defect structure. *Thin Solid Films* **516**, 8227 (2008).

5. **G. Jnawali**, H. Hattab, C. Bobisch, A. Bernhart, E. Zubkov, F.-J. Meyer zu Heringdorf, R. Möller, B. Krenzer, and M. Horn-von Hoegen. Nanopattern Formation by Periodic Array of Interfacial Misfit Dislocations in Bi(111)/Si(001) Heteroepitaxy. *Mater. Res. Soc. Symp. Proc.* **1059**, 1059-KK07-07 (2008).

6. **G. Jnawali**, F.-J. Meyer zu Heringdorf, D. Wall, S. Sindermann, and M. Horn-von Hoegen. Stable tungsten disilicide contacts for surface and thin film resistivity measurements. *J. Vac. Sci. Technol.* B **27**, 180 (2009)

7. **G. Jnawali**, H. Hattab, C. Deiter, C. A. Bobisch, T. Weisemoeller, A. Bernhart, E. Zubkov, J. Wollschläger, R. Möller and M. Horn-von Hoegen. Epitaxial growth of Bi(111) on Si(001). *e-J. Surf. Sci. Nanotech.* **7**, 441 (2009).

8. **G. Jnawali**, H. Hattab, C. A. Bobisch, A. Bernhart, E. Zubkov, R. Möller, and M. Horn-von Hoegen. Nanoscale dislocation patterning in Bi(111)/Si(001) heteroepitaxy. *Surf. Sci.* **603**, 2057 (2009).

9. **G. Jnawali**, Th. Wagner, H. Hattab, R. Möller, and M. Horn-von Hoegen. Nucleation and initial growth in the semimetallic homoepitaxial system of Bi on Bi(111). *Phys. Rev.* B **79**, 193306 (2009).

Publications which are in preparation:

1. M. Horn-von Hoegen**, G. Jnawali**, and H. Hattab. Interplay of strain state, misfit dislocation array and lattice parameter in heteroepitaxial system: Bi(111) on Si(001). (**under preparation**)

2. **G. Jnawali**, Th. Wagner, H. Hattab, R. Möller, and M. Horn-von Hoegen. Surface conductivity study in Bi(111) films via surface manipulation. (**under preparation**)

Earlier publication:

1. M. Uhlig, A. Bertz, H. Brocke, M. Dobler, C. Flannery, **G. Jnawali**, D. Zeidler, and T. Gessner. Integration of plasma deposited CF polymer in a Copper/Low k Damascene, *Proc. Adv. Met. Conf.* (San Diego 2002).

Not refereed article:

1. C. Deiter, **G. Jnawali**, B. Krenzer, M. Horn-von Hoegen, T. Weisemoeller, L. Boewer, and J. Wollschläger, and M. Horn-von Hoegen. GIXRD and XRR Studies on Thin Bi(111) Films on Si(001). HASYLAB Jahresbericht (2006).

B. Parts of the work in the thesis have been presented in talks/posters presented/contributed by the author at the following conferences:

1. **G. Jnawali**, B. Krenzer, and M. Horn-von Hoegen. Study of conductivity and surface morphology during adsorption of silver atoms on a smooth Ag(111) film *DPG Frühjahrstagung* March 4–9, (2005) Berlin. (Poster)

2. C. Deiter, **G. Jnawali**, B. Krenzer, M. Horn-von Hoegen, T. Weisemoeller, L. Boewer, and J. Wollschläger. GIXRD and XRR Studies on Thin Bi(111) Films on Si(001) *DPG Frühjahrstagung* March 26–31, (2006) Dresden. (Poster)

3. **G. Jnawali**, H. Hattab, B. Krenzer, and M. Horn-von Hoegen. Epitaxial growth of Bi(111) on Si(001) studied by SPA-LEED: Morphology and lattice accommodation. *DPG Frühjahrstagung* March 26-31, (2006) Dresden. (Talk)

4. R. Khanafer, A. Janzen, B. Krenzer, **G. Jnawali**, H. Hattab, and M. Horn-von Hoegen. Surface Debye temperature of thin Bi(111) on Si(001) *DPG Frühjahrstagung* March 26–31, (2006) Dresden. (Talk)

5. C. Deiter, **G. Jnawali**, B. Krenzer, M. Horn-von Hoegen, T. Weisemoeller, L. Boewer, and J. Wollschläger. GIXRD Studies on Thin Bi(111) Films on Si(100) *HASYLAB Usermeeting* (2007) Hamburg. (Poster)

6. **G. Jnawali**, H. Hattab, F.-J Meyer zu Heringdorf, B. Krenzer, and M. Horn von Hoegen. Lattice accommodation by a periodic array of interfacial misfit dislocations in Bi(111)/Si(001) heteroepitaxy. *DPG Frühjahrstagung* March 26–30, 2007 Regensburg (Talk).

7. **G. Jnawali**, H. Hattab, F.-J Meyer zu Heringdorf, C. Bobisch, A. Bernhart, E. Zubkov, R. Möller, B. Krenzer and M. Horn-von Hoegen. Nanopattern Formation by Periodic Array of Interfacial Misfit Dislocations in Bi(111)/Si(001) Heteroepitaxy. *MRS Fall Meeting* November 26 - 30, (2007) Boston MA, USA. (Talk).

8. **G. Jnawali**, H. Hattab, C. Deiter, C. A. Bobisch, T. Weisemoeller, A. Bernhart, E. Zubkov, R. Möller, J. Wollschläger, and M. Horn-von Hoegen. Epitaxial growth of Bi(111) on Si(001). ICSFS-14 (14th International Conference on Solid Films and Surfaces) 29th June–5th July (2008) Dublin, Ireland. (Talk)

9. H. Hattab, **G. Jnawali**, B. Krenzer, and M. Horn-von Hoegen. Resistance of a single atom: scattering of electrons by single adatoms and small islands during homoepitaxial growth of Bi(111) films. *DPG Frühjahrstagung* March 25–29, 2008 Berlin. (Poster)

Acknowledgments

I owe a debt of gratitude to many people who have been involved in the work leading to the present thesis. I awfully regret, however, not being able to explicitly list all the names due to space limitations.

First of all, it has been a great pleasure to be a part of the group. The helpful and lighthearted spirit made the efforts a lot less strenuous. I want to express my deeply-felt thanks to my thesis advisor, Prof. Dr. M. Horn-von Hoegen for accepting me as a PhD student by providing the challenging, interesting, and exciting topic of the thesis. His unique and talented way of looking at a complicated problem from its most simplified case has greatly influenced the way I think. I'm really grateful of having a thesis adviser like him who offered me thoughtful guidance and warm encouragement. His time is shared between many projects but still he has managed to guide my work at the right points with his many ideas. His understanding and continued support are highly appreciated.

I am deeply grateful to Dr. B. Krenzer for his patiently training me using the UHV system at the beginning of my thesis. His continuous support, numerous stimulating discussions and constructive comments throughout this work are highly appreciated. I wish to thank him for the critical reading of this thesis.

I would like to thank all the members in the group of AG Horn-von Hoegen for their ideas and inspiring working atmosphere. In particular, I thank Dipl. Phys. H. Hattab for friendly cooperation to carry out the measurements. His contribution in the lab and intensive data analysis are highly appreciated. I'm grateful to Dr. F.-J. Meyer zu Heringdorf for his contribution performing computer simulation and AFM measurements. I express my gratitude to him for the LEEM/PEEM measurements. His support, guidance and the cooperation during this work are gratefully acknowledged. I thank Dipl. Phys. Th. Payer for his understanding to perform AFM measurements. I really appreciate the electrical measurements of silicide contacts. I would like to thank Dipl. Phys. D. Wall and Dipl. Phys. S. Sindermann for the LEEM/PEEM measurements under the guidance of Dr. F.-J. Meyer zu Heringdorf. That was really a nice example of mutual cooperation. I would like to thank Dipl. Phys. A. Jansen (former staff member) for fruitful discussion and friendly help. I would like to thank Dipl. Phys. C. Wiethoff and Dipl. Phys. R. Khanafer for some of the complementary SPA-LEED measurements.

Collaboration and mutual cooperation plays a vital role in scientific research. During this work I have collaborated with many colleagues for whom I have great regard, and I wish to extend my warmest thanks to all those individuals. Fruitful and nice collaboration with members of the Prof. Dr. R. Möller's group are gratefully acknowledged. In particular, I

would like to thank Prof. Dr. R. Möller, Dr. C. A. Bobisch, Dr. A. Bannani, Dipl. Phys. A. Bernhart and Dipl. Phys. E. Zubkov for the nice team work to study Bi films via STM. I would like to express my sincere gratitude to Prof. R. Möller and Dr. Th. Wagner (Johannes Kepler University Linz) for the second phase of collaboration to carry out STM investigation of early stages of growth in Bi films. Special tanks go to Dr. Th. Wagner for the intensive STM measurements and friendly cooperation.

I wish to express my warm thanks to Prof. Dr. J. Wollschläger (AG Wollschläger, Universität Osnabrück), Dr. C. Deiter (DESY, Hamburg), and Dipl. Phys. T. Weisemöller (AG Wollschläger, Universität Osnabrück) for their contribution performing synchrotron XRD/XRR measurements in HASYLAB. I would like to address my special thanks to Dr. C. Deiter for the XRD data analysis and valuable discussions. Similarly, I would like to acknowledge Prof. Dr. M. Acet for the laboratory XRD measurements in AG Farle in the University of Duisburg-Essen.

Much appreciation to technical staff members of AG Horn-von Hoegen, Dipl.-Ing. Mike Tluk (†), Dip. Ing. H. Wolf, L. Kujawinski and former technical staff D. Tonnes, for the entire technical support in the lab and outside the lab. I have benefited a lot from their friendly attitudes throughout my work in the group.

Furthermore, I would like to acknowledge Prof. Dr. S. Hasegawa (Hasegawa research group, University of Tokyo) and Dr. T. Hirahara (Hasegawa research group, University of Tokyo) for important discussion about the Bi films. I especially wish to express my thanks to Dr. T. Hirahara for providing important information regarding to the electronic properties of Bi films. I also wish to thank Prof. Dr. K. Roos (Bradley University in Peoria, USA) for the fruitful discussion during his visit in our group. My warm thanks are due to Dipl. Phys. E. Akcöltekin (AG Schleberger, Universität Duisburg-Essen) for friendly contribution performing the AFM measurements. Many thanks to Dr. D. A. Kovács (Universität Duisburg-Essen) for correcting and giving comments on the manuscripts. My sincere thanks to Dr. L. Chelaru (former staff member of AG Horn-von Hoegen) for the encouragement and friendly discussion.

I'm very much indebted to Frau A. Podig (Secretary, AG Horn-von Hoegen) who made difficult administrative problems simple. She had been very cordial in all respects throughout my work in the group.

A very special thanks goes to Mrs. Elizabeth Meyer zu Heringdorf for the meticulous correction of English grammar in my thesis and various manuscripts as well.

I would like to acknowledge collaborative research center SFB 616 "Energy Dissipation at Surfaces" for the financial support throughout my thesis work. I wish to express my warm thanks to all the members of SFB 616 for mutual cooperation and intensive discussion during the workshop and a round table seminars. I enjoyed a lot working under this project.

Finally, I offer my sincere appreciation and love to my wife for consistent support and patience during the PhD period. I am forever endebted to my parents for their encouragement and love.